Direct TEM Observation of the Movement of the Austenite-Ferrite Interface in Steels

By:

John Nutter

A thesis submitted in partial fulfilment of the requirements for the degree of Doctor of Philosophy

The University of Sheffield
Faculty of Engineering
Department of Materials Science and Engineering

September 2018

Abstract

The solid-state phase transformation from austenite to ferrite is one of the key transformations in determining the final microstructure of steels, and therefore is an important factor in the versatility of steels. An improved understanding of this process can therefore lead to greater control over final properties in steels.

This thesis presents the results of cyclic partial phase transformation (CPPT) experiments using in situ hot stage TEM in order to directly observed the interface behaviour during thermal cycling in the $\alpha + \gamma$ austenite phase region, for Fe-C-Mn alloys with up to 0.33 wt% C and 1.5 wt% Mn. Hot stage TEM experiments of this type have not been reported in the literature before and are able to provide new information which is not available from other techniques commonly used to carry out CPPT experiments such as dilatometry.

The observation of individual interfaces makes it possible to observe not just the kinetics of the transformation but also the interface morphology and its interaction with microstructural features. Individual interface behaviour could be classified into the three stages expected during CPPT from bulk experiments: the normal transformation, the inverse transformation and the stagnant stage. The TEM observations show that sluggish interface migration continued during the stagnant stage, without the interface becoming completely static for any significant period of time. This migration distance was measured to be <500 nm, making this difficult to detect using other techniques. Furthermore, the observations showed that the interface often displayed an evolving morphology during the normal transformation, but reverted to a more stable, often straight or smoothly curved morphology during the stagnant stage.

TEM observations also showed good reversibility between cycles with the interface migrating along approximately the same path during thermal cycling, with only minor changes. Interaction with microstructural features was also observed, including the segmentation of the interface due to nearby twin boundaries and the pinning of the interface by foreign particles.

Finally, the results of in situ TEM observations of the growth of bainite are presented. Two growing bainite plates were observed and the lengthening and thickening rates

measured. Lengthening occurred in a series of discrete steps with periods of relatively slow or no growth interspersed with periods of rapid lengthening. In contrast it was observed that the subsequent thickening of the plates was a continuous process.

Acknowledgements

I would like to express my sincere gratitude to my supervisors, Professor Mark Rainforth and Professor Sybrand van der Zwaag, for their guidance and advice over the course of this project and for providing some much-needed perspective on the difficulties involved in performing the TEM experiments.

In addition, I would like to thank the staff at the Department of Materials Science and Engineering and the Sorby Centre, particularly Dr Peng Zeng, Dr Cheryl Shaw and Dr Le Ma, for the training and assistance they have provided over the course of this project. I would also like to thank Hussein Farahani at TU Delft, for performing the dilatometry experiments that appear in chapters 4 and 6, and for providing me with the benefit of his experience using the DICTRA software.

Furthermore, I am grateful to the Advanced Metallics Systems Centre for Doctoral Training and the Engineering and Physical Science Research Council for financially supporting this project.

Finally I would like to thank my family for their support and encouragement over the last four years.

Contents

Abstract 2

Acknowledgements 4

1. Introduction 8

2. Literature Review 10

2.1 Phase Transformations in Steels 10

2.1.1 Phase Transformations in Steels: Introduction. 10

2.1.2 The Austenite to Ferrite Transformation. 13

2.1.3 Nucleation. 14

2.1.4 Interface Controlled Growth. 17

2.1.5 Diffusion Controlled Growth. 18

2.1.6 Diffusion Controlled Growth in Ternary Alloys: Para Equilibrium. 20

2.1.7 Diffusion Controlled Growth in Ternary Alloys: Local Equilibrium. 21

2.1.8 The Mixed Mode Model 24

2.1.9 Sharp Interfaces. 25

2.1.10 Wide Interfaces. 26

2.1.11 Additional Factors: Austenite Grain Size and Impingement. 30

2.1.12 Normal Mode and Lateral Mode Growth. 31

2.1.13 Cyclic Partial Phase Transformations. 32

2.1.14 The Bainite Transformation 38

2.2 In Situ TEM Experiments. 41

2.2.1 Heating Holder Types. 41

2.2.2 Electron Beam Heating and Radiation Damage. 43

2.2.3 Thermal Grooving. 45

2.2.4 Other Surface Effects. 47

2.2.5 Annealing in Thin Specimens. 48

2.2.6 Phase Transformations using in situ hot stage TEM. 50

2.2.7 Other Direct Observation Experiments 51

2.3 Concluding Remarks 52

3 Experimental Methods 54

3.1 Materials Examined. 54

3.1.1 Fe-0.1C-0.5Mn 55

3.1.2 Fe-0.1C-1Mn 58

3.1.3 Fe-XC-1.5Mn-0.14Si, X = 0.183, 0.263, 0.330. 60

3.1.4 Fe-0.307-3Mn-1.49Si-0.146Mo. 65
3.1.5 99.8% Pure Fe. 67
3.1.6 Fe-0.1C-1.6Mn-0.5Mo. 69
3.2 Hot Stage Transmission Electron Microscopy. 71
3.2.1 Calibration of Heating Holder. 73
3.2.2 Foil Thickness 75
3.3 Dilatometry. 76
3.4 Optical Microscopy, Scanning Electron Microscopy and Electron Backscatter Diffraction. 76
3.5 Thermodynamic and Kinetic Modelling. 77
3.6 Analysis of Video and Measurement of Interface Velocities. 77
3.7 TEM Artefacts 78
3.7.1 Thermal Grooving and Surface Diffusion. 78
3.7.2 Thermal Radiation. 81
4. Cyclic Partial Phase Transformation Experiments: Fe-0.1C-0.5Mn. 85
4.1 Introduction. 85
4.2 TEM Experimental Outline. 86
4.3 Dilatometry. 88
4.4 Kinetic Modelling. 93
4.5 Initial Ferrite to Austenite Transformation. 96
4.6 Austenitic Microstructure. 98
4.7 Initial Formation of Austenite-Ferrite Interfaces. 99
4.8 Interface Position. 102
4.9 Interface Velocity. 107
4.10 General Observations: The Ferrite to Austenite Transformation. 110
4.11 General Observations: The Austenite to Ferrite Transformation. 115
4.12 General Observations: Lateral Growth. 118
4.13 General Observations: Triple Point Behaviour. 120
4.14 General Observations: Dislocation Motion. 122
4.15 Interface Morphology. 125
4.16 Thermal Grooving. 129
4.17 EBSD and Texture Development. 135
4.18 Discussion 137
4.19 Chapter Summary. 145
5. Cyclic Partial Phase Transformation Experiments: Fe-0.1C-1Mn. 147
5.1 Introduction. 147

5.2 TEM Experimental Outline. 147
5.3 Austenite Microstructures and Initial Austenite-Ferrite Interface Formation. 150
5.4 Interface Position. 154
5.5 Interface Velocity. 158
5.6 General Observations: The Normal and Inverse Transformation. 159
5.7 General Observations: Interface Pinning. 162
5.8 Kinetic Modelling. 166
5.9 Discussion. 167
5.10 Chapter Summary. 170
6. Cyclic Partial Phase Transformation Experiments: Fe-XC-1.5Mn (where X = 0.183, 0.263 & 0.330). 172
6.1 Introduction. 172
6.2 Experimental Outline. 173
6.3 Austenite Microstructure and Initial Interface Formation. 177
6.4 Interface Position. 179
6.5 Interface Velocity. 184
6.6 General Observations. 187
6.7 Kinetic Modelling and Dilatometry. 192
6.8 Discussion. 195
6.9 General Discussion. 198
6.10 Chapter Summary. 203
7. Conclusions. 204
7.1 Hot Stage TEM Experiments. 207
7.2 Cyclic Partial Phase Transformations. 204
7.3 Appendix A: Bainite Transformation. 207
7.4 Future Work. 209
9. References 210
Appendix A: Bainitic Transformation. 224
7.1 Introduction. 224
7.2 Experimental Outline. 224
7.3 Results. 227
7.4 Discussion. 231
7.5 Chapter Summary. 233

1. Introduction

Steels are one of the most important and prevalent materials in use today. The primary reasons for this prevalence are the wide range of microstructures and properties that can be produce through control of the processing and heat treatment of the material [1], combined with the ability to manufacture large quantities for a relatively low cost. The solid-state phase transformations which occur during heat treatment of steels are key to the production of different microstructures and therefore different properties of this widely used alloy [2].

Of particular importance is the transformation from the FCC austenite phase to the BCC ferrite phase, both because these phases are present in a wide range of steels and because it can inform the study other related phase transformations such as the bainite or martensite transformations [2]. There are two proposed models for the austenite to ferrite transformation in ternary Fe-C-M (where M is a substitutional alloying element such as Mn or Ni) steels known as local equilibrium and paraequilibrium. These models are distinguished by the partitioning behaviour of the substitutional alloying elements. Local equilibrium assumes that full equilibrium conditions exist at the migrating interface, whilst paraequilibrium assumes that on the time scale of the transformation there is no partitioning of the substitutional element.

Recently, the use of cyclic partial phase transformations [3, 4, 5] has been applied to the study of the austenite to ferrite and ferrite to austenite transformations. This technique involves austenitising the specimen before reducing the temperature to produce a mixture of austenite and ferrite. Specimens are then thermally cycled between two temperatures, T_1 and T_2, within the $\alpha+\gamma$ two phase region to determine the kinetics of the transformation, primarily using dilatometry and kinetic modelling. There are several advantages to this compared to traditional studies which fully transform the specimen from austenite to ferrite or vice versa. Significantly, the effect of nucleation, which is difficult to measure experimentally [6], on the kinetics is minimised as the specimen starts with already established austenite and ferrite grains with the corresponding interfaces.

A further advantage is that qualitatively different kinetic behaviour is predicted depending on whether local equilibrium or paraequilibrium kinetics are assumed. In

the local equilibrium case the enrichment of substitutional alloying elements at the interface gives rise to a so-called stagnant stage between the austenite to ferrite and ferrite to austenite transformations during cycling. This takes the form of a distinct period in which the transformation either ceases or continues only slowly. The duration of this period is dependent on the local chemistry at the interface and therefore on the composition of the specimen [7] [8].

The aim of this project was to combine the use of cyclic partial phase transformations (CPPT) with the direct observation of individual interfaces using in situ hot stage transmission electron microscopy (TEM). Although hot stage TEM has been used previously to examine phase transformations in steels, the use of hot stage TEM to investigate interface behaviour during CPPT experiments has not been reported in the literature before. The primary purpose of this combination was to determine how the interface behaved during the stagnant stage and in the period immediately before and after it. This includes understanding whether the interface migrated sluggishly or remained completely static as well as any effect on the nature of the interface itself. More general insight could be gained using this technique into the behaviour of the interface during the austenite to ferrite and ferrite to austenite transformation, including how the interface interacts with microstructural features.

This thesis is structured as follows. Chapter 2 contains a review of the literature concerning phase transformations in steels, cyclic partial phase transformations and the use of in situ TEM experiments to study dynamic processes. Chapter 3 gives an account of the experimental procedures and techniques used and the materials examined in this thesis. Chapter 4 presents the results of CPPT experiments performed using hot stage TEM on a Fe-0.1C-0.5Mn (in wt%) steel, with a discussion of those results. Chapter 5 similarly reports the observed behaviour of a Fe-0.1C-1.0Mn steel with the relevant discussion. Chapter 6 reports the results and discussion for experiments performed on Fe-XC-1.5Mn steels (X=0.183, 0.263, 0.330), and contains a general discussion on all the CPPT experiments performed. Chapter 7 reports observations of the growth of bainite using hot stage TEM. Finally Chapter 8 offers the final conclusions on the experimental results and suggests avenues for future work.

2. Literature Review

2.1 Phase Transformations in Steels

2.1.1 Phase Transformations in Steels: Introduction.

It is the solid-state phase transformations which occur during the heat treatment and cooling of steels that are responsible for the wide variety of microstructures that can be produced. Therefore, a better understanding of the mechanisms of these phase transformations can lead to improved control over the final properties in manufacturing, leading to improved performance. This review focuses on the austenite to ferrite phase transformation, including the major models used to describe the kinetics in terms of the conditions and chemistry at the transformation interface, the formal descriptions of the interface itself as well as other factors affecting the kinetic behaviour during phase transformations. The use of cyclic partial phase transformations is reviewed with a focus on how this can be used to investigate the transformation kinetics and probe the local chemistry. Finally, in the second part of this review, the major considerations when undertaking in situ TEM experiments are outlined, with a particular focus on hot stage TEM, and the relevant literature using hot stage TEM to investigate phase transformations in steels is highlighted.

The solid state phase transformations in steels can be divided into diffusion controlled reconstructive phase transformations, in which the crystal structure of the steel is changed by breaking all atomic bonds and rearranging them into a new structure, and diffusionless displacive phase transformations in which atoms change position in a well-ordered fashion to create a new crystal structure [9] [10].

In plain carbon steels, the face centred cubic austenite phase is stable above 723^{o}C, with a maximum carbon concentration of 2.1 wt% at 1147^{o}C. Whilst the eutectoid (Ae_1) temperature remains constant for compositions with more than 0.022 wt% C, the austenite finish, or Ae_3, temperature varies with carbon concentration. This falls from 912^{o}C in pure Fe, down to 723^{o}C for a steel with a carbon composition of 0.8wt% [11] [12].

It should be noted, however, that the Ae_1 and Ae_3 temperatures are the transformation temperatures under equilibrium conditions. Whilst the transformation temperature can be detected using techniques such as dilatometry or differential thermal analysis some hysteresis is observed. Corresponding non-equilibrium values of the transformation temperature can therefore also be measured for both A_1 and A_3 and are denoted Ac and Ar for heating and cooling respectively. These Ac_1, Ac_3, Ar_1 and Ar_3 values are dependent on the composition of the steel as well as on the heating and cooling rates, with the difference between Ac or Ar and Ae becoming smaller at lower heating or cooling rates [11] [13].

During reconstructive phase transformations in Fe-C the phases formed from the decomposition of austenite are ferrite and cementite. The body centred cubic ferrite phase is stable at temperatures below 910^{o}C with low carbon solubility, rising from approximately 0.008 wt% at room temperature to a peak of 0.022 wt% at 723^{o}C [11]. Unlike austenite and ferrite, cementite does not have a cubic crystal structure but is instead orthorhombic, its chemical formula is Fe_3C with a carbon composition of 6.67 wt% [12].

In hypoeutectoid steels, which have a carbon content lower than 0.8 wt%, these reconstructive transformation products typically take specific forms. The ferrite generally is the first to nucleate during slow cooling, forming allotriomorphs on existing austenite grain boundaries, with a preference for locations where multiple grain boundaries meet, and growing along them in an anisotropic fashion. As a result in the initial stages of growth these allotriomorphs have an aspect ratio of with a thickness approximately 1/3 of the length [14].

The low solubility of carbon in ferrite means the carbon atoms are rejected from the ferrite as the transformation progresses, consequently enriching the remaining austenite. Once a concentration of 0.8wt% is reached the mechanism of austenite decomposition changes and involves the cooperative growth of ferrite and cementite. The resulting microstructure, consisting of alternating lamellae of ferrite and cementite exhibiting defined orientation relationships, is known as pearlite [15] [16].

When the austenite decomposes at lower temperatures this leads to the promotion of alternative morphologies which transform through a displacive mechanism. This includes the growth of Widmanstätten ferrite plates, which grow along specific

austenite lattice planes [17] [18]; Bainite, an intermediate morphology consisting of aggregates of ferrite plates with precipitation of cementite [19] [20]; and at the lowest temperatures Martensite, a body centred tetragonal phase in which no diffusion occurs during nucleation or growth [21].

The transformation from austenite to ferrite was the main process studied in this thesis and is therefore the focus of this review. The transformation from austenite to ferrite is one of the major issues in the determination of final microstructures. This is not restricted to microstructures containing ferrite, but has wider implications for non-ferritic microstructures as, for example, the suppression of ferrite growth is important in the formation of Martensite [22].

In practice many steels, even those designated as carbon steels, contain elements other than iron and carbon [23]. This can consist of elements like Mn due to its effect on austenite decomposition and role forming MnS [24], and Si or Al to prevent the evolution of gas during solidification [25]. High Strength Low Alloy steels control the chemical composition to produce superior mechanical properties, often through micro alloying with strong carbide or nitride forming elements such as Nb [26] [24].

When these additional alloying elements are present in steels, the thermodynamic stability of the phases is changed. Alloying elements can be grouped into one of four categories depending on the effect this has on the austenite phase region. Austenite stabilisers are those which increase the range of temperatures over which austenite is stable, whilst those which restrict it are known as ferrite stabilisers. These two groups can be further divided into two subgroups to distinguish what exactly their effect is on the stability of the austenite phase.

The austenite stabilisers can be classified as leading to either an open γ-field or an expanded γ-field. The first of these contains elements such as nickel and manganese, which lower both the A_1 and A_3 temperatures whilst increasing the range of compositions over which the austenite is stable. The expanded γ-field operates in a similar way but the size of the austenite field is restricted by the formation of compounds, with carbon and nitrogen being the most significant examples [27].

In a similar vein the ferrite stabilisers can be divided into those which produce a closed γ-field and a contracted γ-field. The closed γ-field elements include silicon, aluminium and strong carbide formers such as vanadium and increase the A_1 and A_3 temperatures

whilst minimising the compositional range over which the austenite is stable, resulting in a single phase field for α and δ ferrite. The contracted α-field elements, which include boron and niobium, also restrict the stability of the austenite but do so primarily through compound formation [27].

2.1.2 The Austenite to Ferrite Transformation.

The austenite to ferrite transformation begins with the formation of ferrite allotriomorphs on existing austenite grain boundaries at small undercooling [28]. Such allotriomorphs have a defined orientation with one of the austenite grains, of which the most common is the Kurdjumov-Sachs orientation relationship (OR), given below in equation 2.1 [29] [30].

$$\{111\}_\gamma = \{110\}_\alpha$$

$$< 1\bar{1}0 >_\gamma = < 1\bar{1}1 >_\alpha \qquad (2.1)$$

Another commonly encountered orientation relationship is the Nishiyama-Wasserman OR, as shown in equation 2.2 [31] [30].

$$\{\bar{1}11\}_\gamma = \{\bar{1}10\}_\alpha$$

$$< 0\bar{1}1 >_\gamma = < 001 >_\alpha \qquad (2.2)$$

In addition to this defined OR, where the close packed planes are parallel, the allotriomorph typically has a random orientation relationship with adjacent austenite grains. Consequently, there exists both partly coherent and disordered interfaces with the latter migrating more readily at higher temperatures and the partly coherent interface migration becoming more dominant at lower temperatures [32].

This means that the allotriomorph may consist of a curved boundary on one side with a partially coherent, potentially facetted, boundary on the other [18]. Alongside considerations of the relative mobility of the ordered and disordered interfaces, the shape of the allotriomorph is affected by the transport of carbon away from the interface. Discussed in more detail in chapter 2.1.5, the redistribution of alloying elements between the original austenite grain and the growing ferrite grain forms one of the rate controlling factors in the transformation. The ferrite allotriomorph develops

an aspect ratio of 1/3 in Fe-C alloys [14, 33, 34] as growth is facilitated in one direction by shape factors, such as the highly curved regions of the interface [35].

2.1.3 Nucleation.

The transformation from austenite to ferrite begins with the formation of ferrite nuclei, typically on austenite grain boundaries, followed by growth of this newly formed ferrite. As with the nucleation of a solid phase from a liquid the driving force is the difference between the free energy per unit volume of the new phases against the free energy per unit volume of the parent phase [36]:

$$\Delta G_v = \Delta G_v^{\gamma} - \Delta G_v^{\alpha} \quad (2.3)$$

Where α is the nucleating phase and γ is the parent phase, ΔG is free energy per unit volume.

The total energy change of the system is offset by the creation of a new α/γ interface, and in the solid state, by the misfit strain energy required to accommodate new phase. This total energy change is given in equation 2.4 [36]:

$$\Delta G_{hom} = -V\Delta G_v + A\gamma + V\Delta G_s \quad (2.4)$$

Where V is the transformed volume, A is the area of the interface, γ is the interfacial energy and ΔG_s is the strain energy term.

Assuming a spherical nucleus this produces a critical nuclei radius and an energy barrier to nucleation as shown in equations 2.5 and 2.6:

$$r^* = \frac{2\gamma}{(\Delta G_v - \Delta G_s)} \quad (2.5)$$

$$\Delta G^* = \frac{16\pi\gamma^3}{3(\Delta G_v - \Delta G_s)^2} \quad (2.6)$$

Yielding a homogeneous nucleation rate, I_{hom}, as in equation 2.7:

$$I_{hom} = \omega C_0 \exp\left(\frac{-\Delta G^* + \Delta G_a}{kT}\right) \quad (2.7)$$

Where ω is the vibrational frequency of the atoms, C_0 is the number of atoms per unit volume, ΔG_a is the activation energy for migration, k is the Boltzmann number and T the temperature.

However, as with solidification, nucleation tends to be heterogeneous is practice, nucleating on defects including inclusions, grain boundaries and free surfaces [36, 37, 38]. This affects the nuclei shape and the initial microstructural development during the transformation. In this case the free energy change is modified by the destruction of the defect on which the new phase nucleates (equation 2.8):

$$\Delta G_{het} = -V(\Delta G_v - \Delta G_s) + A\gamma - \Delta G_d \qquad (2.8)$$

Where ΔG_d is the defect energy.

The most relevant situation is where nucleation occurs on a grain boundary surface. This results in the reduction of the total grain boundary area with a corresponding reduction in free energy. The nuclei in this case will be a symmetrical lens shape as shown in figure 2.1 [37].

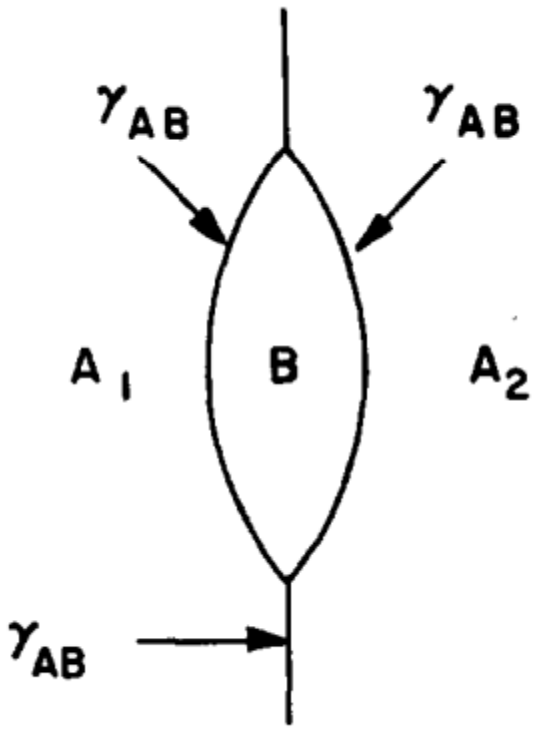

Figure 2.1: Critical nucleus shape of newly formed phase, B. γ_{AB} is energy of the interface between phases A and B. Reprinted from Acta Metallurgica, Vol. 3, P.J. Clemm and J.C. Fisher, "The influence of grain boundaries on the nucleation of secondary phases", pp. 70-73, Copyright (1955), with permission from Elsevier [37].

Consequently the ratio of the activation energy for heterogeneous nucleation (in this case, grain boundary nucleation, ΔG_B^*) to homogeneous nucleation can be expressed as:

$$\frac{\Delta G_B^*}{\Delta G_{hom}^*} = S(\theta) = \frac{1}{2}(2 - 3\cos(\theta) + \cos(\theta)^3) \quad (2.9)$$

Where θ, the contact angle, is given by the ratio of the grain boundary energy, γ_{gb}, to the interfacial energy:

$$\theta = \cos^{-1}(\frac{\gamma_{gb}}{\gamma_{\alpha\beta}}) \quad (2.10)$$

Similarly the nucleation rate at grain boundaries is related to the homogeneous nucleation rate by:

$$\frac{I_B}{I_{hom}} = \frac{\delta_B}{L_B}\exp(\frac{\Delta G_{hom}^* - \Delta G_B^*}{kT}) \quad (2.11)$$

Where δ_B is the grain boundary thickness, and L_B is the mean grain size.

The geometry becomes more complex when more austenite grains meet, but the activation energy at grain edges where three grains meet, ΔG_E^*, is lower than ΔG_B^* and is further reduced when four grains meet at grain corners, ΔG_c^* [39]. Therefore, nucleation is preferred first at grain corners, then grain edges, followed by grain surfaces [28].

However, as discussed in chapter 2.1.2 above, ferrite nuclei often possess specially oriented semi-coherent boundaries with one of the austenite grains. This facetted boundary further reduces ΔG_{het} [36]. This means that the geometries assumed for nucleation at the grain boundary, edge and corner do not account for experimentally observed nucleation rates [38]. The nucleation activation energy can more generally be written as:

$$\Delta G^* = \frac{\Psi}{\Delta G_v^2} \quad (2.12)$$

Where Ψ represents both the interfacial energy and the nucleus geometry.

Ψ is difficult to measure experimentally [6] [5], and there are significant differences between the values predicted by models and experimental measurements. Clemm and Fisher [37] predicted $\Psi = 3.3*10^{-3}$ J^3m^{-6} at grain corners with incoherent boundaries.

The experimentally determined value of Offerman et al. [6] using X-ray diffraction was $\Psi = 5*10^{-8}\ J^3m^{-6}$.

2.1.4 Interface Controlled Growth.

The rate controlling factor for the growth of a new phase can be considered to be processes which occur at the interface between the product phase and the parent phase. This case, known as interface-controlled growth [40], represents one extreme of a continuum of behaviour found primarily when the concentration of alloying elements is low, or when the interfacial processes are slow.

One possibility is for the rate controlling process to be one where the ferrite phase grows by the transfer of atoms across the interface, with those atoms being transferred independently of each other. In this case, the interface can be considered to present a barrier to transfer which requires an activation energy, ΔG to overcome [40].

Therefore, the frequency, U, at which an atom is transferred across the interface will be as shown in equation 2.13:

$$U_{\gamma\alpha} = \nu\ \exp\left(-\frac{\Delta G}{kT}\right) \tag{2.13}$$

Where ν is a characteristic frequency.

Similarly, the frequency of the transfer in the opposite direction (from the ferrite to the austenite phase) is given in equation 2.14.

$$U_{\alpha\gamma} = \nu \exp\left(-\frac{\Delta G^* + \Delta G^{\alpha\gamma}}{kT}\right) \tag{2.14}$$

The difference between equations 2.13 & 2.14 will therefore give the net transfer rate of atoms across the interface, by multiplying this by the width of the interface, d_b, it is possible to derive an expression for the velocity of the interface. When the driving force for the transformation is low (that is, when $\Delta G^{\alpha\gamma} << kT$) this becomes equation 2.15 [40]:

$$V_{interface} = \frac{\nu\, d_b\, \Delta G^{\alpha\gamma}}{kT} \exp\left(-\frac{\Delta G^*}{kT}\right) \tag{2.15}$$

It is possible to simplify this further as in equation 2.16 [41] [42]:

$$V_{interface} = M^B \Delta G(T) \quad (2.16)$$

Where M^B is the interface mobility, and $\Delta G(T)$ is the free energy change per atom.

In this way the velocity of the interface can be considered to be a product of a mobility and a driving force in a similar way to the formal description of diffusion [40].

The interface mobility, M^B, is a temperature dependent quantity expressed in equation 2.17 below:

$$M^B = M_o \exp(\frac{-Q}{RT}) \quad (2.17)$$

Where M_o is a pre-exponential factor, Q is the activation energy for atoms crossing the interface, R is the gas constant and T is the temperature.

Experimentally, attempts to measure the mobility of the interface in steels typically do so by measuring the rate of the massive transformation. Since the massive transformation is partitionless, it is the intrinsic mobility of the interface that represents the rate controlling factor [43]. Comparing with the mobility for α/α grain boundaries (where M_o = 0.035), Hillert and Höglund [43] reviewed existing data on interface mobility. Wits et al. [44], studied the austenite to ferrite transformation in binary substitutional Fe-X alloys and found a mobility several orders of magnitude lower than for grain boundaries, with pre-exponential factor of $M_o = 1.7\times10^{-5}$. Krielaart and van der Zwaag [45], found $M_o = 4\times10^{-7}$ in low manganese Fe-Mn alloys studied using differential scanning calorimetry (DSC). The mobility data derived from dilatometry and differential thermal analysis (DTA) experiments by Liu et al. [46, 47, 48], are in agreement with these lower estimates. More recently, Zhu et al. [49] derived the intrinsic mobility of the interface using dilatometry from the kinetics of the austenite to ferrite and the ferrite to austenite transformation in Fe-X (X= Ni, Mn and Co), determining $M_o = 2.7\times10^{-6}$.

2.1.5 Diffusion Controlled Growth.

When significant quantities of alloying elements or impurities are present, with different levels of solubility in each of the two phases, the rate controlling factor of the transformation is the diffusion of these elements away from the interface [50]. The

original model for diffusion-controlled growth, applied to the growth of a spherical precipitate was developed by Zener [51].

For binary alloys, it is normally assumed that equilibrium is maintained across the interface, and so the tie lines on the phase diagram give the composition of the phases on each side of the interface [52].

The growing ferrite phase can therefore be considered to have a composition equal to c^{α} throughout the grain. The austenite grain which is being transformed on the other hand will have a composition of c^{γ} at the interface but a composition of c^{0} throughout the rest of the grain. Consequently, there is a concentration gradient within the austenite grain. The flux of carbon atoms away from the interface under these conditions is given in equation 2.18 [53]:

$$J = -D \frac{(C^0 - c^\gamma)}{\Delta x} \tag{2.18}$$

Where D is the diffusion coefficient of carbon in austenite.

The rate at which solute is redistributed into the austenite is proportional to the interface velocity and an expression for this is given below in equation 2.19:

$$J = (c^\gamma - c^\alpha)\frac{dz}{dt} \tag{2.19}$$

In order to maintain equilibrium at the interface it is necessary for the rate at which the solute is redistributed to the austenite be equivalent to the flux of carbon away from the interface.

$$(c^\gamma - c^\alpha)\frac{dz}{dt} = -D \frac{(C^0 - c^\gamma)}{\Delta x} \tag{2.20}$$

In parallel to this it is important to consider the conservation of mass in the system as a whole, with the solute rejected from the ferrite (left hand side of equation 2.21) being equal to the solute with which the austenite has become enriched (right hand side of 2.21).

$$(c^0 - c^\alpha)\, z = \frac{1}{2}\,(c^\gamma - c^0)\,\Delta x \tag{2.21}$$

Where z is the position of the interface.

By combining equation 2.21 with equation 2.20 it is possible to derive an equation for the interface velocity as a function of interface position. This is given below in equation 2.22 [53]:

$$\frac{dz}{dt} = D\,\frac{(c^0 - c^\gamma)^2}{2\,z\,(c^\alpha - c^\gamma)(c^\alpha - c^0)} \qquad (2.22)$$

It can be seen by integrating with respect to t that the position of the interface is proportional to $t^{1/2}$ and that therefore the velocity should vary as a function of $t^{-1/2}$ [14] [50].

2.1.6 Diffusion Controlled Growth in Ternary Alloys: Para Equilibrium.

In ternary Fe-C-X alloys the situation becomes more complex as the diffusion of the carbon and species X must be described, which results in a pair of simultaneous equations of the same form as equation 2.20. More generally this can be expressed as equation 2.23 [52] [53]:

$$(c_i^\gamma - c_i^\alpha)\,v = -D_i\,\nabla C_i \qquad (2.23)$$

Where i = C or X.

It is apparent that the diffusion coefficients, D_i, of each species will differ, particularly when one is an interstitial and another a substitutional solute, and that this will affect the selection of appropriate tie lines on a ternary isotherm (figure 2.2) when determining concentrations [52].

Therefore, the simplest situation occurs when one of the alloying elements diffuses much more rapidly than the others, as in the case where the diffusion of substitutional solutes is significantly slower than interstitial solutes over the time scale of the experiment. This condition of partial chemical equilibrium is known as paraequilibrium (PE), and as can be seen in figure 2.2 the tie lines connect compositions of equal Fe/X ratio [54], and with the chemical potential of C remaining constant across the interface [4]. Consequently, the diffusion of the interstitial carbon atoms, will be the rate determining factor and so the situation can be modelled in a similar fashion to binary alloys [55].

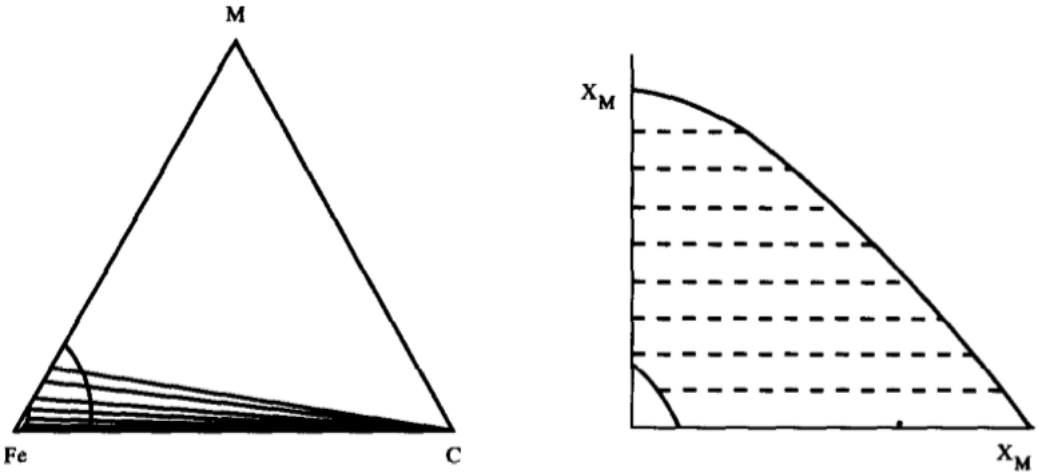

Figure 2.2: Paraequilibrium ties lines on a ternary isotherm. Tie lines correspond to a constant ratio of Fe:M. Reprinted from Progress in Materials Science, Vol. 40(3), A. Van der Ven and L. Delaey, "Models for precipitate growth during the γ → α + γ transformation in Fe-C and Fe-C-M alloys", pp. 181-264, Copyright (1996), with permission from Elsevier [55].

2.1.7 Diffusion Controlled Growth in Ternary Alloys: Local Equilibrium.

In the local equilibrium (LE) model the alloying elements are redistributed at the interface according to local equilibrium assumptions, meaning that the chemical potential of each species is constant on either side of the interface [4, 52, 55]:

$$\mu_i^{\gamma} = \mu_i^{\alpha} \tag{2.24}$$

Where i = C or X

As in the previous cases, it is then necessary to solve Fick's law for each of the alloying elements present in both the austenite and ferrite phases (equation 2.25) [56]. Simultaneously it is also necessary to ensure that there is conservation of mass at the interface [4](equation 2.26):

$$\frac{\partial c_i^{\phi}}{\partial t} = \nabla \left(D_i^{\phi} \nabla C_i^{\phi} \right) \tag{2.25}$$

Where i = C or X

$$J_i^{\gamma} - J_i^{\alpha} = v \left(c_i^{\gamma} - c_i^{\alpha} \right) \tag{2.26}$$

Where i = C or X, v is the interface velocity and c is the concentration at the interface.

Using these equations it becomes possible for the interface concentrations and the migration velocity to be calculated at progressive time steps. As noted above, however, the diffusion coefficients between species will differ with the interstitial carbon having a coefficient several orders of magnitude greater than that of the substitutional elements such as Mn or Ni [57]. Consequently, the need to maintain local equilibrium at the interface requires either that there be a large concentration difference for element X at the interface and throughout the rest of the austenite grain or that there be a low concentration difference for carbon, as can be seen in figures 2.3 and 2.4 [2].

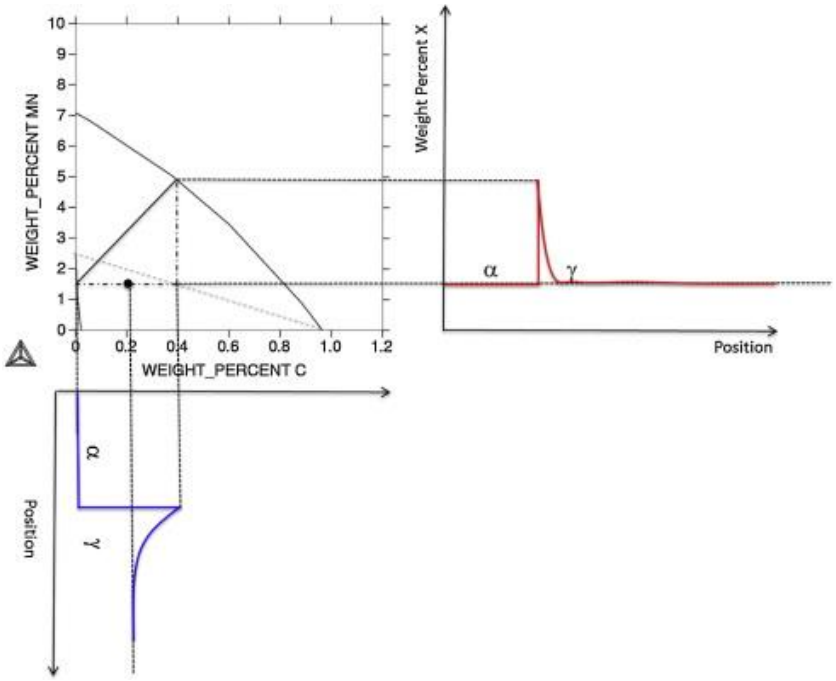

Figure 2.3: Ternary isotherm for Fe-C-Mn at 700°C. The composition profiles for X (Mn in this case) and C are plotted for the situation where the bulk composition is below the zero partition line (dotted line). There is no partitioning of Mn and the transformation is controlled by Local Equilibrium with Negligible Partitioning (LENP) kinetics. Reprinted from Materials Science and Engineering: R: Reports, Vol. 92, Gouné et al., "Overview of the current issues in austenite to ferrite transformation and the role of migrating interfaces therein for low alloyed steels", pp. 1-38, Copyright (2015), with permission from Elsevier [2].

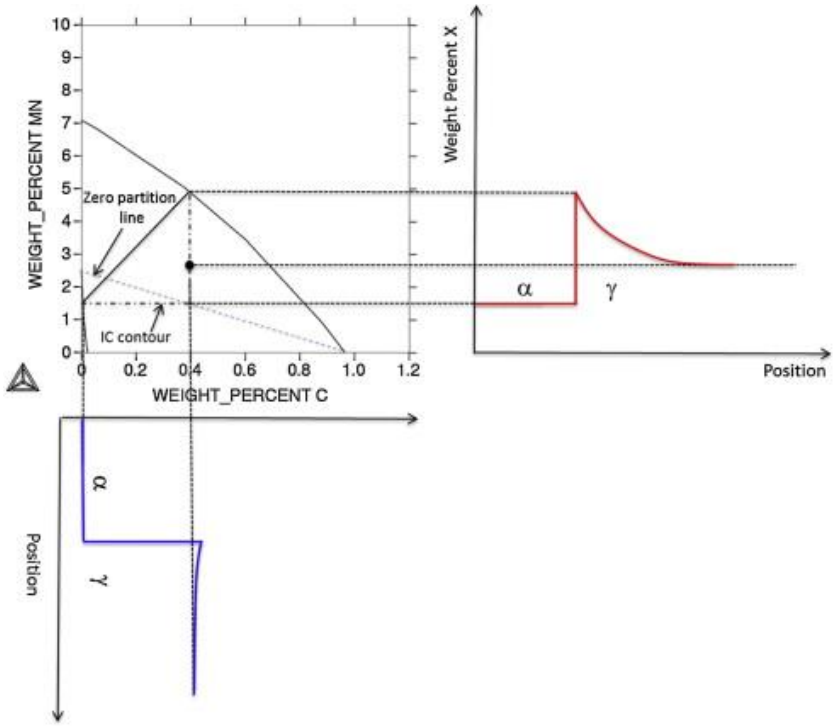

Figure 2.4: Ternary isotherm for Fe-C-Mn at 700°C. The bulk composition is above the zero partitioning line and consequently there is Mn partitioning between phases. The transformation is controlled by Local Equilibrium with Partitioning (LEP) kinetics. Reprinted from Materials Science and Engineering: R: Reports, Vol. 92, Gouné et al., "Overview of the current issues in austenite to ferrite transformation and the role of migrating interfaces therein for low alloyed steels", pp. 1-38, Copyright (2015), with permission from Elsevier [2].

As a result of these different composition profiles at the interface there will be two distinct situations which govern the kinetics under local equilibrium conditions: a partitioning transformation where X is redistributed into the austenite grain (LE-P) and non- or negligible-partitioning transformations (LE-NP) where no such partitioning occurs [53].

Experimentally, the austenite to ferrite transformation is traditionally studied using metallography to determine the thickness of ferrite allotriomorphs during isothermal heat treatments. Limitations of this technique, such as the difficulty of distinguishing nucleation and growth kinetics, led to the development of alternative techniques such as controlled decarburisation [2] [58]. For the Fe-C-Ni, where the interaction of X with the interface and C atoms is negligible, growth kinetics from traditional metallography experiments can be described using a model which begin with para-equilibrium interface conditions before developing into local equilibrium conditions over time [59] [22]. There are some limitations of decarburisation experiments for studying the initial

stages of ferrite formation [60] but produced good agreement with LENP kinetics as the transformation progressed [59].

However, for the Fe-C-Mo system the precision in determining ferrite growth kinetics using decarburisation experiments shows that PE/LENP models overestimated the growth kinetics. Since the interaction of Mo with C and the transformation interface is non-negligible this disparity can be interpreted as the existence of a solute drag effect [59].

For the Fe-C-Mn system, decarburisation experiments showed a transition from LENP to PE kinetics at higher temperatures [61] [62] (for a Fe-0.57C-0.94Mn alloy this transition occurred in the temperature range 775-825^{o}C). To account for this a model involving the introduction of a finite capacity of the interface to accommodate Mn, due to the tendency of Mn to segregate to the interface as a result of Mn-C interactions [62]. Guo et al. [63] in STEM studies of Fe-0.04C-3Mn-1.9Si proposed three growth stages based on the chemistry found across interfaces transformed at 751^{o}C. An initial rapid growth stage with no partitioning or interfacial enrichment of Mn, a second non-partitioning stage with interfacial Mn enrichments, followed by full Mn partitioning.

It can be seen then, that there neither PE or LE kinetics can account for the growth behaviour of all ternary Fe-C-X systems under all conditions.

2.1.8 The Mixed Mode Model.

The cases of diffusion and interface-controlled growth outlined above should be regarded as the limiting cases for the actual kinetics of partitioning phase transformations. Since both the interface mobility and the diffusivity will be finite the transformation will have characteristics which are intermediate between the two extremes [64]. Therefore, such models cannot necessarily predict the correct growth kinetics of actual partitioning phase transformations [65].

For a partitioning transformation the driving force is assumed to be proportional to the difference between the equilibrium concentration of the partitioning element and the actual concentration. The driving force is therefore given by equation 2.27:

$$\Delta G = \chi\left(x^{\beta\alpha} - x^{\beta}\right) \qquad (2.27)$$

Where χ is a proportionality factor, $x^{\beta\alpha}$ is the equilibrium content of the parent β phase and x^{β} is the actual content of the β phase at the interface.

Following the description of interface-controlled growth above, the velocity of the transformation is (equation 2.28):

$$v = M\Delta G = M\chi\left(x^{\beta\alpha} - x^{\beta}\right) \tag{2.28}$$

Where M is the effective interface mobility.

The mixed-mode character of the transformation is defined by the mode parameter, S, which is given in equation 2.29 below [65] [64]:

$$S = \frac{x^{\beta\alpha} - x^{\beta}}{x^{\beta\alpha} - x_0} \tag{2.29}$$

Where x_0 is the total concentration of the element which is partitioned, x^{β} is the interfacial concentration in β and $x^{\beta\alpha}$ is the concentration in β in equilibrium with α.

This parameter varies between 0, where the transformation is diffusion controlled, and 1 where interface control dominates. When x^{β} is close to $x^{\beta\alpha}$ there is a concentration gradient ahead of the interface and so the diffusion of the partitioning element in the β phase is the rate controlling factor. When x^{β} is close to x_0 the concentration gradient is minimal and the lattice transformation is the rate limiting factor.

The model does not make assumptions about the diffusional or interface control of growth or the actual solute concentrations at the interface. For Fe-C binary alloys the transformation begins with interface-controlled growth kinetics before switching to diffusion control as the concentration of solute atoms at the interface increases.

2.1.9 Sharp Interfaces.

One important consideration when developing a model of phase transformations is the formal description of the transformation interface itself. The simplest of these descriptions is to consider the interface to be a discontinuity between the two phase which has zero width [2] [58]. The sharp interface model typically assumes a full chemical equilibrium each side of the interface [58]. The description of diffusion-controlled growth above can therefore be recognised as examples of a sharp interface

model. In practice this assumption of full chemical equilibrium at the interface may not be entirely valid in solid state phase transformations [55, 58, 66].

One way to account for deviations from local equilibrium is to consider an intrinsic drag or interface friction, which acts against the migration of the interface itself and is the reciprocal of the interface mobility [43, 67, 68]. This friction is generally considered to be proportional to the interface velocity [58]. The driving force to overcome this must come from a deviation from equilibrium conditions at the interface and consequently results in lower measured growth rates than expected from considering carbon diffusion alone [43]. It is therefore straightforward to add terms which account for other relevant phenomena including the pressure on a growing particle due to the increased interfacial energy of a curved interface [58] [69]. Therefore, the total chemical driving force is considered to be dissipated by the transinterface diffusion and interface friction [66], as in equation 2.30 [2] [69]:

$$D^{Chem} = \Delta G^{Diff} + \Delta G^{Friction} \quad (2.30)$$

Where D^{Chem} is the driving force, ΔG^{diff} is the transinterface diffusion and $\Delta G^{Fiction}$ is the interface friction.

2.1.10 Wide Interfaces.

The wide interface model assumes that the interface has a defined thickness and that therefore it is possible to describe the composition profile of the solute atoms within the interface. The deviations from local equilibrium in this case were based on work which originally began by examining the drag effects caused by impurities and solute atoms on grain boundaries. It was first assumed that solute atoms will tend to segregate towards grain boundaries in order to reduce the elastic stresses within the grain and that these atoms will be left behind as the grain boundary moves. However, since the boundary tends to attract such atoms, they will diffuse in the direction of grain boundary motion. This force exerted on the solute atoms will also act to retard the motion of the grain boundary. If the attractive force between the grain boundary and the solute atoms is given a value, f, then the velocity at which the solute atoms diffuse

towards the boundary is given by equation 2.31, whilst the solute drag on the boundary is given by equation 2.32 [70]:

$$v = \frac{D}{kT} f \tag{2.31}$$

$$P = n f \tag{2.32}$$

Where D is the diffusion coefficient, k is the Boltzmann constant, T is the temperature, n is the number of atoms and f is the attractive force between the grain boundary and the solute.

Therefore the maximum velocity for a boundary which is experiencing solute drag can be obtained from equation 2.31, provided that the driving force is not greater than the solute drag, P. At higher velocities the boundary can be considered to have broken away from the solute atoms. Furthermore, by combining equations 2.31 & 2.32 it is possible to obtain a relation between the magnitude of the solute drag and the velocity, as in equation 2.33 [71]:

$$P = \frac{n\,k\,T\,v}{D} \tag{2.33}$$

This can be developed further by considering the interaction between the boundary and the solute atoms to vary with the distance from the centre of the boundary. Therefore the solute drag becomes equation 2.34:

$$P = -N \int_{-\infty}^{\infty} (C - C_o) \frac{dE}{dx}\, dx \tag{2.34}$$

Where C_o is the composition away from the boundary.

The term $\int C_0 \frac{dE}{dx} dx$ is zero when grain growth is occurring since C_0 is both the initial solute concentration and the concentration of the growing grain. However, it is non-zero for a phase transformation [72].

As previously noted, moving from a model which assumed a sharp interface to one in which the interface has a finite thickness means that it is necessary to calculate the composition profile for the solute atoms within the boundary itself, and it is this which is necessary to calculate the magnitude of the solute drag from equation 2.33 [68].

If the boundary interaction energy and diffusion coefficient normal to the boundary are functions of the distance from a centre plane of the boundary then the chemical potential of the solute atoms will be given by equation 2.35 below.

$$\mu = kT \ln C(x) + E(x) + const. \tag{2.35}$$

Where the constant is chosen such that E(∞) = 0

The E(x) term describes the interaction energy on either side of the boundary as well as inside it and is often considered to be continuous with discontinuities of its first derivative at the boundary edges and centre. For an interface moving with a steady velocity, v, the concentration profile of the solute atoms must fulfil equation 2.36 [73]:

$$\frac{\partial}{\partial x}\left[D\frac{\partial C}{\partial x} + \frac{CD}{kT}\frac{\partial E}{\partial x} + vC \right] = 0 \tag{2.36}$$

Therefore the concentration profile can be calculated for each of the four distinct regions of the interface. Figure 2.5 below shows the solute concentration profiles for an austenite stabiliser and a ferrite stabiliser at three different interface velocities.

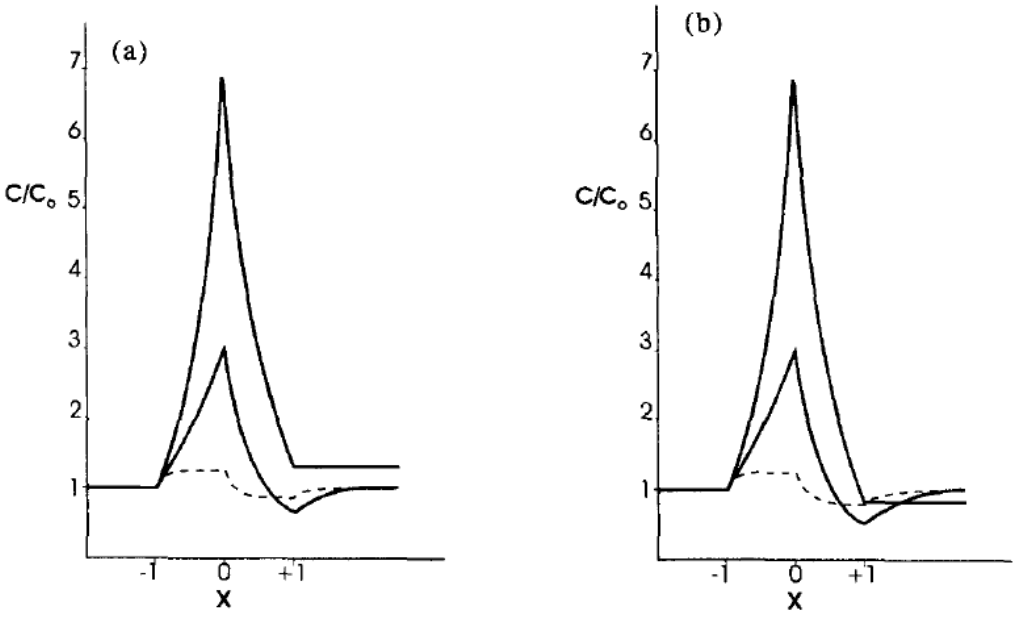

Figure 2.5: Solute profiles at the moving interface, for three dimensionless velocities v = 0.0001, v = 1.8 and v = 10. The profiles are reduced with increased velocity. (a) shows an austenite stabilising alloying element and (b) shows the same for a ferrite stabilising alloying element. Reprinted from Acta Metallurgica et Materialia, Vol. 43(10), G.R. Purdy and Y.J.M. Brechet, "A solute drag treatment of the effects of alloying elements on the rate of the proeutectoid ferrite transformation in steels", pp. 3763-3774, Copyright (1995), with permission from Elsevier [73].

Therefore the forces acting on a steadily migrating interface can be expressed as below in equation 2.37 [67]:

$$P^{sd} + P^{friction} + P^{\sigma} = 0 \quad (2.37)$$

Where P^{sd} is the solute drag, $P^{friction}$ is the resistance to migration which occurs even in pure elements, P^{σ} is the force due to the interfacial energy of a curved interface.

A different approach viewed the problem of solute drag as one where the diffusion of solute caused by boundary motion led to the dissipation of Gibbs energy, thus lowering the driving force for the migration of the boundary [74]. Equation 2.38 gives the energy dissipated by diffusion over the width of the boundary, generalised to multicomponent systems:

$$\Delta G^{diff} = -\int_0^d \sum (x_i - x_i^0) \frac{d\mu_i}{dx} dx \quad (2.38)$$

In this approach the dissipation of Gibbs energy should therefore be equal to the chemical driving force (equation 2.39):

$$D^{chem} = \Delta G^{diff} + \Delta G^{friction} + P^{\sigma} V_m \quad (2.39)$$

By comparing equations 2.39 and 2.37 it is apparent that the two approaches can be considered to be equivalent if the chemical driving force is equal to the difference between ΔG^{diff} and $P^{sd}V_m$. By modifying equation 2.34 so that the solute and solvent atoms are considered in exactly the same way then the solute drag and Gibbs energy dissipation approaches can be considered to be equivalent. Thus equation 2.34 becomes equation 2.40:

$$P^{sd} = \frac{-1}{V_m} \int_0^d \sum x_i \frac{d\mu_i}{dx} dx \quad (2.40)$$

The understanding of this solute drag effect is important for the general reason that deviations from expected experimental results are often attributed to the existence of a solute drag effect.

2.1.11 Additional Factors: Austenite Grain Size and Impingement.

The austenite grain size influences the rate at which the austenite to ferrite transformation progresses. As seen in chapter 2.1.3 above, the grain boundaries provide a low energy site for heterogeneous nucleation. Since grain boundaries provide a preferential site for nucleation, the grain boundary area transformed at any given time in the transformation is greater than the total volume fraction transformed. This, known as site saturation, means that the nucleation rate decreases more rapidly than the untransformed volume [75]. The effect of this site saturation is affected by whether the nucleation occurs preferentially on the grain surface, grain edges or grain corners, in decreasing order of magnitude [39] [75]. The type of nucleation also influences how the time to half transformation is affected by the grain size [75] [39]:

$$t_{1/2}\ \alpha\ D^{m} \tag{2.41}$$

Where $t_{1/2}$ is the time to half transformation, D is the grain diameter and the value of m depends on the type of nucleation (m=1 for site saturation, and 0.25, 0.5 and 0.75 for boundary, edge and corner nucleation respectively).

However, in practice, steels often undergo thermomechanical processing resulting in deformed austenite grains. Therefore, a more general variable is the total area of austenite grain boundaries per unit volume, or S_v. This parameter is related to the austenite grain size as measured by the linear intercept length as in equation 2.42 [76].

$$S_v = \frac{2}{D} \tag{2.42}$$

Where S_v is the total area of austenite grain boundaries per unit volume and D is the austenite grain size determined using the linear intercept method.

In the period immediately following nucleation, each growing ferrite grain grows without being affected by the presence of other growing ferrite grains in the austenite. However, when the ferrite grain becomes larger, it is possible for the carbon diffusion fields ahead of the migrating interfaces of two or more ferrite grains to overlap. This is known as soft impingement and reduces the rate of the transformation [75].

Hard impingement occurs at later stages of growth when the austenite-ferrite interfaces of growing ferrite grains physically collide, leading to the creation of grain

boundaries. This effectively halts growth in certain directions, leading to an overall reduction in the rate of transformation [77].

2.1.12 Normal Mode and Lateral Mode Growth.

The migration of the interface involves the transfer of individual atoms across the boundary from the parent phase to the growing phase. There are two mechanisms by which an incoherent interface can migrate normal to itself in this way.

The first mechanism, often referred to as the normal (i.e. perpendicular) mode, involves the simultaneous and independent transfer of atoms across all points of the interface [78]. This results in continuous growth along the length of the interface.

For the lateral mechanism, the interface is considered to be stepped at an atomic scale. Atoms are no longer transferred across the all points of the interface but are added to the growing phase only at these steps. The migration of the interface therefore proceeds through the lateral migration of each of these steps. In this case, any individual section of the interface remains immobile until the step or ledge grows over it, at which point it undergoes a discrete migration equal to the height of the step [78] [79]. The growth rate normal to the interface for a ledged boundary is given by equation 2.43 [80]:

$$G_t = \frac{hV}{\lambda} \tag{2.43}$$

Where G_t is the growth rate normal to the interface, h is the height of the ledge, V the velocity of the ledge, and λ the inter ledge spacing.

Ledge structure is often more complex with ledges being either singular, often on the scale of one stacking sequence, or a combination of multiple stacking sequences in a single superledge. Such superledges are more commonly encountered than ledges with heights equal to or smaller than the lattice parameter. If a dislocation is associated with the ledge, the defect is known as a disconnection [81].

2.1.13 Cyclic Partial Phase Transformations.

Cyclic partial phase transformations are used to study phase transformation growth kinetics using a heat treatment procedure which involves the cyclic heating and cooling of the specimen between two temperatures, T_1 and T_2. These temperatures are selected to be within the $\alpha+\gamma$ phase region and covering a sufficient temperature range for the interface to migrate with changing temperature [5]. Specimens are first austenitised before cooling down to T_1, the lower cycling temperature, and held isothermally for 20 minutes resulting in the creation of a mixed austenite/ferrite microstructure. Thereafter the specimen is subjected to one of two cyclic phase transformation routes, known as type I (immediate) and type H (holding) experiments. In type I experiments the temperature is cycled between T_1 and T_2 without a period of isothermal holding between each heating or cooling step. In type H experiments, the specimen is held isothermal between each heating or cooling stage. Figure 2.6 illustrates the two heat treatments schematically [4] [2].

This route for producing phase transformations has several advantages. The creation of a mixed austenite and ferrite microstructure prior to cycling means that the transformation can progress through the movement of existing boundaries rather than the nucleation of new grains. Therefore, the potentially complicating effects of nucleation on the measurement of phase transformation kinetics can be avoided [3]. This is important as the parameters used to calculate nucleation rates are typically difficult to measure experimentally [6] [5].

A further benefit is that cyclic phase transformations allow the study of the ferrite to austenite transformation without the complicating effect of pearlite dissolution where the starting stage of the austenite formation is compositionally inhomogeneous. Most relevant to this thesis, however, is that the partitioning behaviour of alloying elements at the transformation interface can be studied.

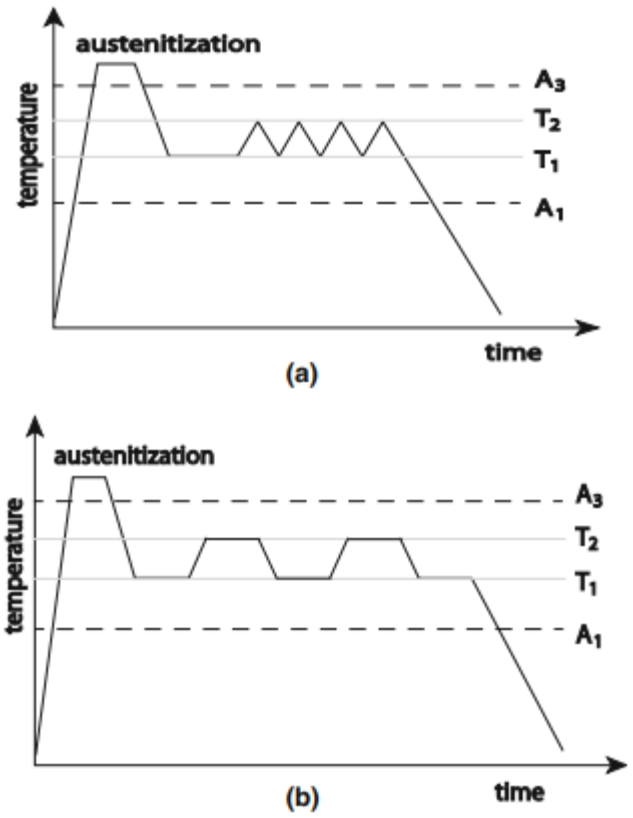

Figure 2.6: Schematic of heat treatment for (a) I-type and (b) H-type CPPT experiments. Reprinted from Acta Materialia, Vol. 59(17), Chen et al., "Application of cyclic partial phase transformations for identifying kinetic transitions during solid-state phase transformations: Experiments and modelling", pp. 6751-6760, Copyright (2011), with permission from Elsevier [4].

The two models for interfacial conditions during phase transformations outlined above, paraequilibrium and local equilibrium, lead to different expectations of interface behaviour. Figure 2.7 shows these rival predictions.

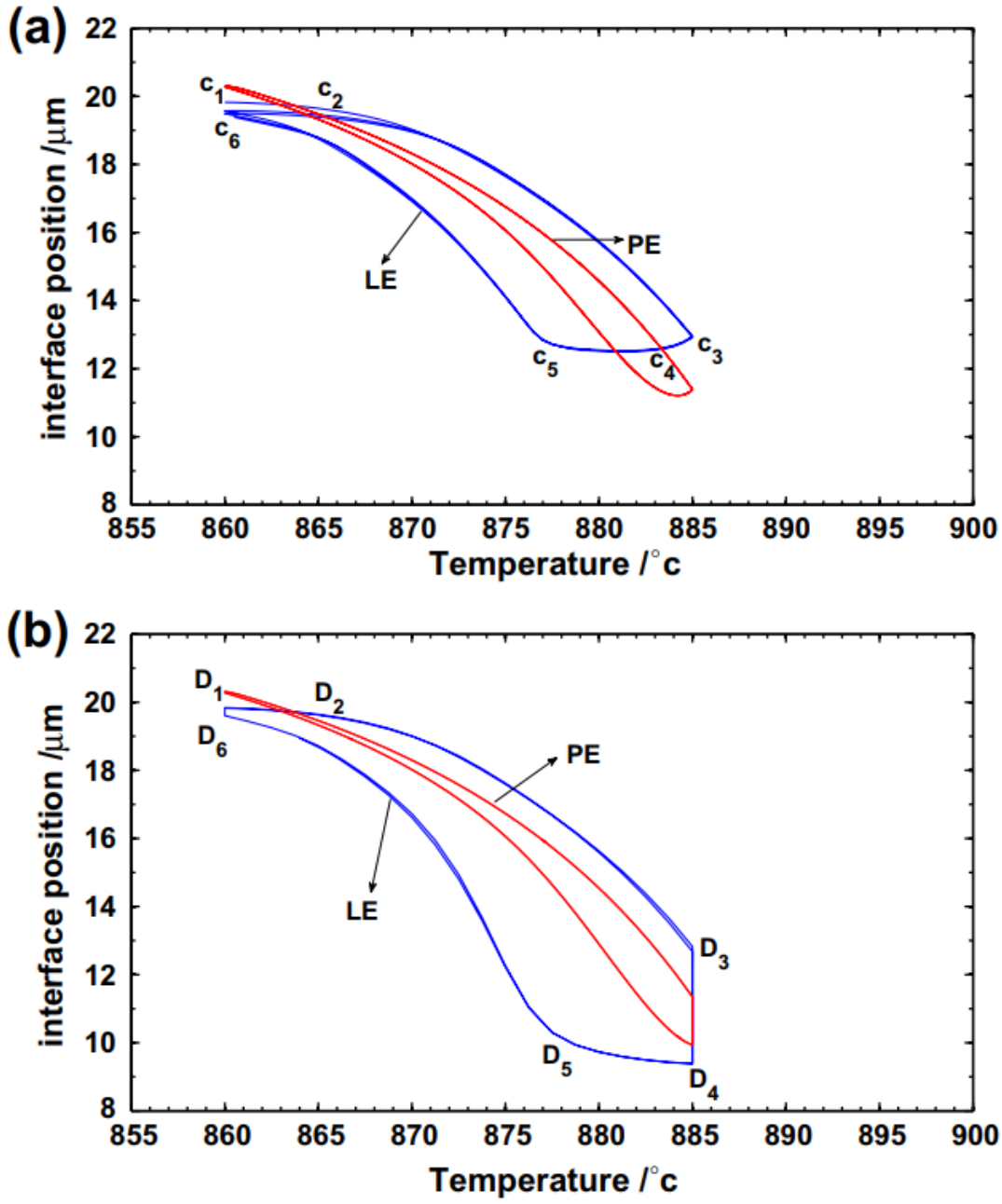

Figure 2.7: The interface position against temperature for (a) I-type and (b) H-type CPPT experiments simulated under local equilibrium (LE) and paraequilibrium (PE) conditions. Reprinted from Acta Materialia, Vol. 59(17), Chen et al., "Application of cyclic partial phase transformations for identifying kinetic transitions during solid-state phase transformations: Experiments and modelling", pp. 6751-6760, Copyright (2011), with permission from Elsevier [4].

For Fe-C-Mn alloys cyclic partial phase transformation heat treatments produce the characteristic curve associated with local equilibrium at the interface when measured using dilatometry. There is a good qualitative match in behaviour [4]. A typical dilatometry curve for a type I heat treatment is shown in figure 2.8(a) in comparison with a normal austenite to ferrite transformation shown in figure 2.8(b).

The curve shows three features, appearing once for the α to γ transformation and once for the γ to α transformation. The majority of the transformation, and therefore interface migration, takes place during the normal transformation stage. This normal transformation stage is "normal" in the sense of expected (γ→α on cooling, α→γ on heating) and is distinct from the "normal mode" growth. Throughout this thesis, the terms "normal transformation" and "normal mode" growth are used to stay in line with the respective terminology, and it should be clear from the context of the usage which form is meant. However, it is the other two features, the inverse transformation and the stagnant stage, which are distinctive features of cyclic experiments.

The inverse transformation involves the continuation of the phase transformation after the inversion of the heating-cooling rate when the T_1 or T_2 temperature was reached. During this time the austenite to ferrite transformation continued for a period during heating, and the same for the ferrite to austenite transformation once cooling had begun. This indicates that the interface was not under equilibrium conditions when the cycle switches from heating to cooling or vice versa [4].

During the stagnant stage, the interface only migrates slowly or not at all, despite continuing change in the temperature. In the case of type H experiments the inverse transformation is not seen due to the isothermal holding between each heating/cooling step, whilst still exhibiting the normal transformation and stagnant stage.

The stagnant stage occurs as a result of the partitioning of substitutional alloying elements in order to establish local equilibrium at the interface. This is in contrast to the normal and inverse transformation stages where only the carbon, and not the substitutional alloying elements are partitioned. Under normal conditions, this LE-NP growth leads to the development of a spike of the substitional element ahead of the migrating interface during the austenite to ferrite transformation. The physical meaning of the interfacial spike in this model has been questioned as it is predicted to be similar to, or smaller than, the interatomic distance [2].

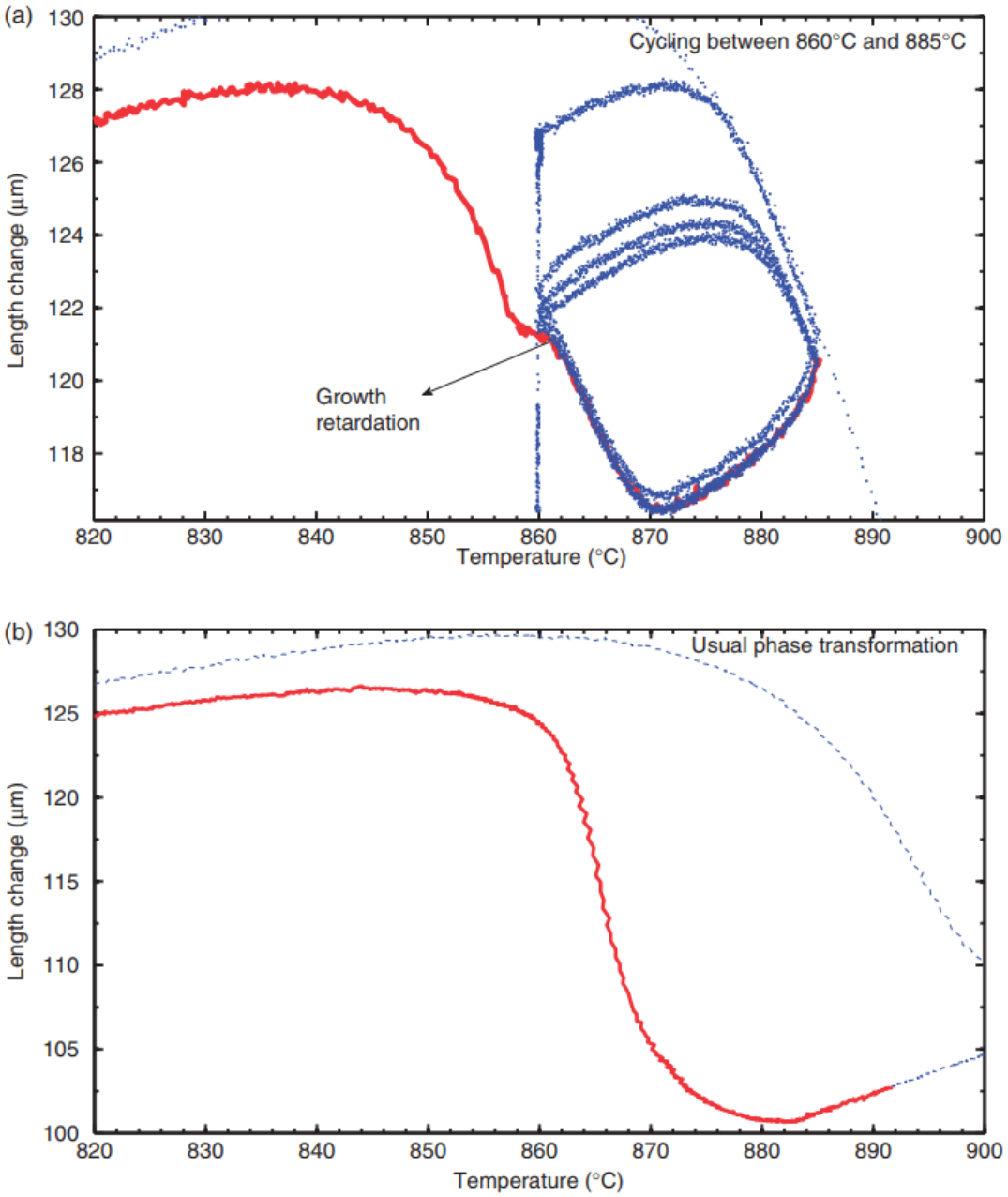

Figure 2.8: Dilation as a function of temperature for (a) a Fe-0.023C-0.17Mn steel subjected to I-type CPPT heat treatment (with final cooling in red) and (b) a Fe-0.023C-0.17Mn steel undergoing the usual γ→α transformation (in red). Reprinted from Philosophical Magazine: Letters, Vol. 92(2), H. Chen and S. van der Zwaag, "Indirect evidence for the existence of the Mn partitioning spike during the austenite to ferrite transformation", pp. 86-92, 2012 [82].

Cyclic partial phase transformations can use the stagnant stage to investigate interfacial chemistry in several ways. Firstly, the temperature range of the stagnant stage is dependent on the composition of the steels being cycled. Simulated cyclic transformations performed by Chen et al. [7] estimated that the temperature range of the stagnant stage in Fe-0.02C-X (where X = Si, Co, Cu, Ni and Mn) steels was

dependent on the partition coefficient of the substitional alloying elements. The applied heat treatment was selected such that T_2-T_1 = 25C, $A_e3 - T_2$ = 5C and dT/dt = ± 10C/min. The stagnant stage ranged from 0C for Co, partitioning coefficient = 1, up to 35C for 1 wt% Mn with a partitioning coefficient of 1.9.

Furthermore, the effect of additional substitutional alloying elements on Fe-C-Mn-X alloys was found to be additive, with the effectiveness at increasing stagnant stage temperature range also influenced by the partitioning coefficient [7].

The temperature range of the stagnant stage is therefore dependent on the composition of the specimen, the tendency of the substitional alloying elements to partition, and therefore the composition at the interface. In addition, Farahani et al. [8] found that the temperature range of the stagnant stage in Mn containing steels is sensitive to the carbon concentration with a predicted increase of approximately 5C when C is increased from 0.1 wt% to 0.3 wt% with a heating/cooling rate of 60C/min.

This increase in stagnant stage temperature range with increasing carbon concentration occurs due to the tendency of Mn to co-segregate with carbon. These C-Mn interactions have also been found by Langelier et al. [83] and by van Landeghem et al. [84] in APT studies of Fe-C-Mn steels transformed through decarburisation. Song et al. [85] also show that C segregation at the interface can attract affects the distribution of Mn in 0.19C-1.42Si-2.02Mn during quench and partitioning. Similarly, Ab initio simulations by Wicaksono and Militzer [86] also show co-segregation of C-Mn to Σ3 grain boundaries in bcc iron.

In addition, on final cooling after thermal cycling a growth retardation stage was observed by Chen and van der Zwaag [82] which was attributed to the interaction of the interface with a residual manganese spike in the austenite left over from a previous cycle in the partial phase transformation. An example of this growth retardation is highlighted in figure 2.8. Using a modified heat treatment Chen and van der Zwaag [87] were able to create two residual spikes in the austenite and show that this did, in fact, lead to the development of two separate growth retardation stages during final cooling. Furthermore, they noted that the two growth retardation stages were not of equal magnitude, attributing this to a combination of the Mn diffusing out of the spike after its creation and by small changes in interface path as a result of initial interaction with the first spike.

Finally Chen et al. [88] carried out in situ high temperature laser scanning confocal microscope (HT-CLSM) experiments on a 0.107C-0.173Mn steel in order to demonstrate that the path of the moving interface is reversible. During these observations, no nucleation of new grains was observed indicating that the cyclic partial phase transformation behaviour observed in dilatometry experiments were the result of moving austenite-ferrite interfaces. During HT-CLSM observations, the interfaces were observed to move in a predominantly planar manner, with only small changes in the orientation of the mobile interface.

In this way the stagnant stage provides information about the concentration of interstitial and substitutional alloying elements at moving austenite-ferrite interfaces, through both the chemistry at the interface in any one cycle and through residual spikes, where the substitutional alloying element concentration deviates from $c_{o,}$ which are left in the austenite after the end of the inverse transformation.

2.1.14 The Bainite Transformation

Bainite is a ferrite and cementite microstructure produced at intermediate temperatures between the pearlite and martensite reactions [89]. Bainite primarily consists of sheaves of bainitic ferrite separated by other phases such as retained austenite or cementite. These sheaves are made up of lenticular plates or laths of bainitic ferrite, which share a common crystallographic orientation. This gives the sheaf as a whole a wedge-shaped morphology with the thick end at the nucleation site [90].

Two different forms of bainite can be distinguished based on the precipitation of cementite around the bainitic ferrite plates. Upper bainite, the variant formed at higher temperatures, the carbon is partitioned into the austenite before carbide precipitation between the ferrite plates. In lower bainite, the reduced transformation temperature means that the carbon is not sufficiently partitioned and results in carbide precipitation in the ferrite [19]. This is illustrated schematically in figure 2.9.

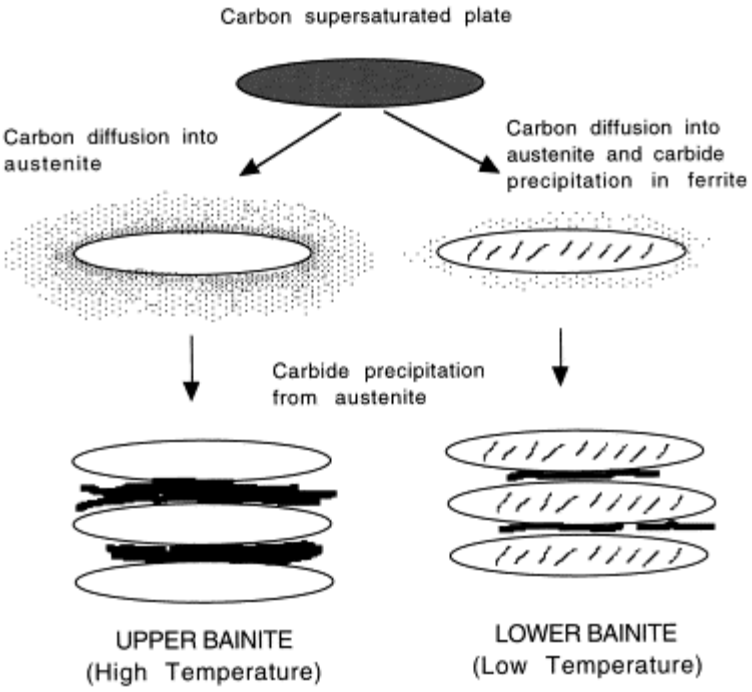

Figure 2.9: Schematic illustration of the development of upper and lower bainite. Reprinted from Materials Science and Engineering A, Volume 273, H.K.D.H Bhadeshia, "The bainite transformation: unresolved issues", pp. 58-66, Copyright (1999), with permission from Elsevier [19].

There are two approaches to describing the kinetics of the bainite transformation, one in which the growth rate of the bainite plates is diffusion controlled, whilst the other proposes the growth of sub-units through a displacive mechanism with the rate controlling factor being the nucleation of new sub-units [91] [20].

In the diffusion-controlled model, the nucleation and growth of bainite occurs through a reconstructive mechanism, with the ferrite and cementite growing cooperatively [20]. The lengthening rate is higher than the thickening rate and so migration occurs through a ledge mechanism.

According to the nucleation-controlled model, a sub-unit of bainitic ferrite nucleates at an austenite grain boundary (or another heterogeneous nucleation site). Carbon is partitioned during this nucleation stage. Lengthening of each sub-unit occurs through a displacive mechanism until further lengthening is halted by plastic deformation [20] [92]. Growth of the sheaf is continued through the autocatalytic nucleation of new sub-units at its tip [93] [94]. Whilst the growth of individual sub-units is fast, significantly faster than expected under para-equilibrium conditions [95], the overall kinetics is

reduced by the time between nucleation of sub-units. This time is expected to increase over the course of the transformation due to the changing austenite composition [93].

In addition to a description of the kinetics, there are several features which any theory of the bainite transformation must account for. These are the distinct forms of upper and lower bainite, the existence of a bainite start temperature, and the incomplete reaction phenomenon in isothermally transformed steels [20] [96].

Multiple studies have been carried out to directly observe the growth of bainite in steels, using hot stage TEM, hot stage scanning laser confocal microscopy and photoemission electron microscopy. Bhadeshia measured sub-unit growth rates of 75 $\mu m \cdot s^{-1}$ at 380^{o}C [95], significantly higher than the 0.083 $\mu m \cdot s^{-1}$ expected from calculations assuming paraequilibrium conditions at the interface. Hu et al. [97] [98] found lengthening rates in the range of 1-10 $\mu m \cdot s^{-1}$ for bainite sheaves transformed during cooling to 330^{o}C of a Fe-C-Mn-Si superbainitic steel, with the lengthening rates varying with nucleation site. They also found smaller, <1 $\mu m \cdot s^{-1}$, lengthening rates during isothermal holding at 330^{o}C. They concluded that this supported a diffusional mechanism of the bainite growth rate.

Yada et al. [99] examined a Fe-XC-6Ni (where X=0.29-0.71) finding an average growth rate of 0.135 $\mu m \cdot s^{-1}$. Mao et al. [100] analysed the nucleation and growth of bainite in reheated metal welds finding a wide range of growth rates from 2 $\mu m \cdot s^{-1}$ up to >2000 $\mu m s^{-1}$. Kolmskog et al. [101] found growth rates of around 7 $\mu m \cdot s^{-1}$ for bainite growth below the M_s temperature in a Fe-0.51C-2.055Mn-2.287Si steel. Sainis et al. [102] for a Fe-0.2C-1.5Mn-2.0Cr steel transformed isothermal between 450^{o}C and 650^{o}C observed nucleation rates in qualitative agreement with classical nucleation theory, but with rather different rates between austenite grains. Measured growth rates varied from <1 $\mu m \cdot s^{-1}$ at higher temperatures to 10-100 $\mu m \cdot s^{-1}$ at the lowest temperatures.

These direct observation studies found a number of nucleation sites for the bainite in addition to austenite grain boundaries. These nucleation sites included inclusions, twin boundaries and other bainite sheaves or laths [102] [100] [98]. Furthermore, several growth modes were identified. As well as the growth of singular laths or plates, the fast and slow growth of multiple parallel laths, the simultaneous growth of bainite

laths in multiple directions forming a latticed structure and the growth of laths into a triangular frame was also observed [100].

2.2 In Situ TEM Experiments.

2.2.1 Heating Holder Types.

The primary distinction between heating holder types is whether the mechanism for heating the specimen is direct or indirect. Early direct heating methods typically involve attaching the specimen to a grid and the system undergoes Joule heating by the application of an electric current. The close contact of the specimen with the heater leads to rapid response times with low applied current. However, this was often accompanied by significant specimen drift and poor reproducibility between experiments [103]. More recently, MEMS devices have come into use and specimens are mounted upon consumable microheaters and by isolating the specimen and heater from the frame image displacement on heating and cooling is reduced [104] [105]. The use of MEMS heating chips also introduces problems related to the bulging of the membrane on which the microheater is mounted. This can create movement of the specimen that requires manual adjustment of the focus or a shift of the specimen if the holder is tilted [105]. An example of the configuration of a MEMS based heating holder can be seen in figure 2.10

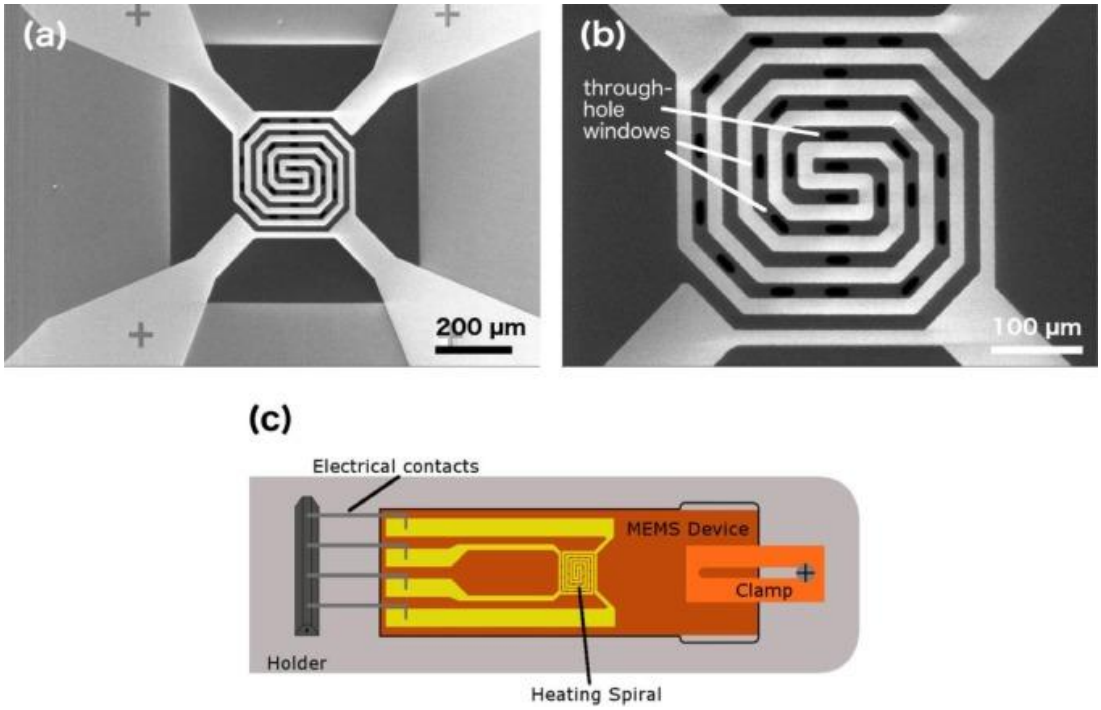

Figure 2.10: (a) and (b) SEM images of MEMS device showing heating spiral and through-hole windows and (c) schematic diagram of heating holder and MEMS device. Reprinted from Ultramicroscopy, Volume 190, Canavan et al. "Novel in-situ lamella fabrication technique for in-situ TEM", pp. 21-29, Copyright (2018), with permission from Elsevier [106].

Indirect heating holders are also known as furnace type holders, due to the presence of a miniaturised coil furnace around the holder. Specimens are inserted normally and so can include thin foils, films and FIB lamellar mounted on copper grids. These heaters typically have a less rapid thermal response than direct heating methods [103], and there is some uncertainty about the actual specimen temperature due to the thermal contact between the specimen and furnace [104]. Image drift can be controlled by the design of the hot stage to ensure high temperature stability and can be further reduced through the employment of water cooling [107]. An example of a furnace type heating holder can be seen in figure 2.11.

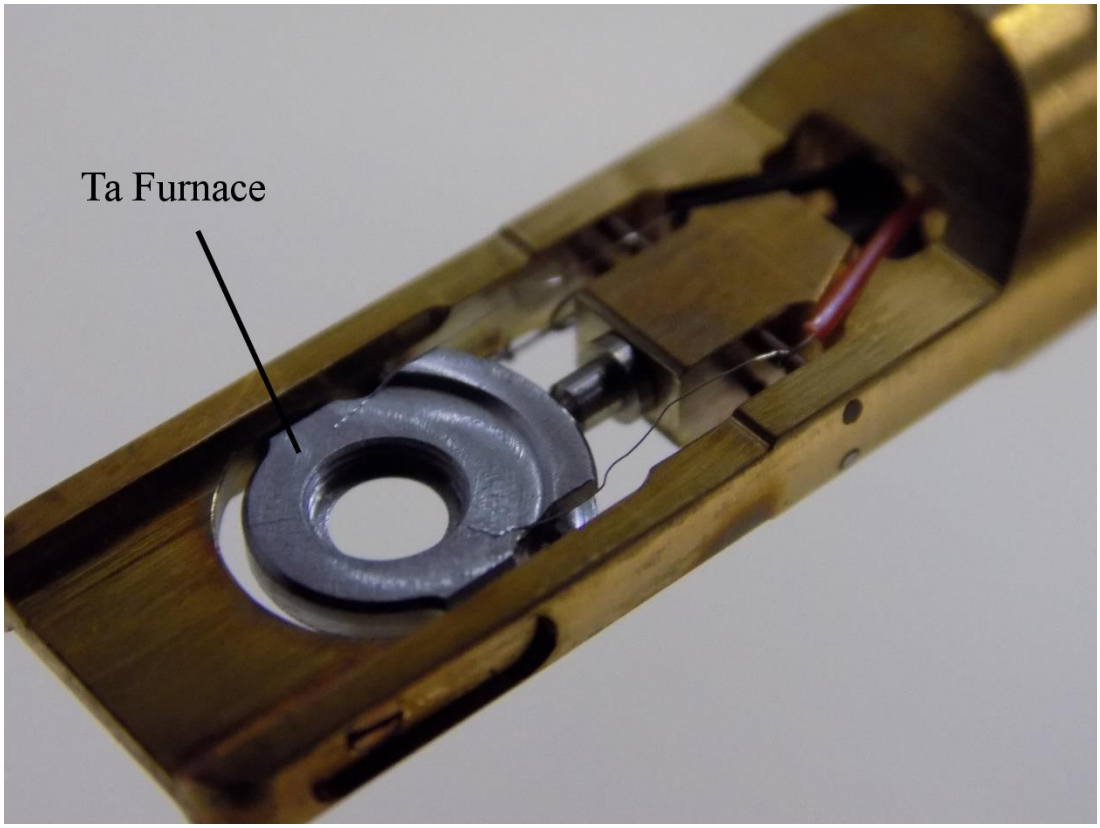

Figure 2.11: Gatan Model 628 Single Tilt Heating Holder with Ta furnace.

2.2.2 Electron Beam Heating and Radiation Damage.

One significant factor to consider during in situ TEM experiments of any kind is the interaction of the specimen with the electron beam. This raises the possibility that experiments of this kind can affect the process being observed through localised heating or radiation damage of the specimen.

In the case of specimen heating this arises from inelastic scattering of the electron beam. This heating is primarily through the generation of phonons within the specimen, either as a result of direct electron-atom interactions or through the absorption of X-rays or Auger electrons [108].

Gale and Hale [109] developed a simplified model for the localised heating caused by the electron beam. This model assumes that the foil is bounded by a conductor of infinite conductivity held at temperature T_0, with the rate of heat generation per unit volume assumed to be independent of the penetration depth of the beam. If the heat

lost due to radiation is neglected then the temperature of the specimen as a function of r (the distance from the beam axis) is given by:

$$T(r) = T_0 + \frac{H_0 a^2}{4k}[Ei\{-(r/a)^2\} - Ei\{-(b/a)^2\} + \ln(b/r)^2] \qquad (2.44)$$

Where b is the radius of the conductor, H_0 the maximum heat flux, k is the thermal conductivity, d is the thickness of the foil, a is a measure of the extent of the irradiated area, T_o is the temperature at the periphery and Ei are standard exponential integrals.

Gale and Hale also investigated the temperature increase experimentally, in order to determine H_0, using a 100 kV TEM with a beam current of 50 μA, 600 μm condenser aperture and a 17 μm beam diameter. It was found that for Fe foils of 300 nm thickness the α→γ transformation (at 910°C) could be induced, and that the asymmetrical heat conduction near the edge made it possible in some cases to melt the foil edge. This was not seen in gold or copper foils, a fact attributed to the lower thermal conductivity of iron. For beam diameters closer to those used during normal work, the temperature increase was calculated to be on the order of 70C for Fe, 30C for Al and 20C for Au [109]. However, this can be reduced significantly by reducing the beam current and size of the condenser aperture [110].

Fisher modified this to account for the relativistic nature of the electron beam, showing the temperature increase to be proportional to the density of the specimen and the electron beam flux, and inversely proportional to the thermal conductivity of the specimen. Furthermore, the heating effect was smaller for higher kV and smaller electron beam radii [110].

Other estimates of the heating caused by the electron beam indicate that for Cu and Al the temperature increase is on the order of 1-10C. Using HVEM the temperature increase of stainless steels has been estimated between 30-60C [110] [111].

Ultimately, this localised heating can have several effects including accelerating the transformation kinetics and inducing stress/strain in the foil. The generation of phonons by inelastic processes can also affect image quality due to electron-phonon interactions.

A second effect of the electron beam is to induce radiation damage by displacing individual atoms and creating a Frenkel pair in the specimen if the accelerating voltage

of the microscope exceeds a certain threshold [112]. In order to produce an atomic displacement in the material, the energy transferred from an electron colliding with the atom must exceed the displacement energy, E_d. The threshold voltage is related to the displacement energy by equation 2.45 below [113]:

$$eU_d = m_o c^2 \{ \sqrt{1 + \frac{m_A}{2{m_o}^2 c^2} E_d} - 1 \} \quad (2.45)$$

Where e is the electron charge, c is the speed of light, m_o is the rest mass of the electron, m_A the atomic mass and U_d is the threshold accelerating voltage.

For BCC Fe the threshold voltage is in the 300-400 kV range [114].

2.2.3 Thermal Grooving.

One potentially serious detrimental effect arising from the use of thin foils is the development of thermal grooves [115]. It is well known that polycrystalline materials will develop grooves on the free surface of the material, appearing where existing grain boundaries intersect with the surface [116] [117]. These grooves form in order to minimise the free energy of the system, rapidly establishing a groove with an equilibrium angle in the area immediately adjacent to the grain boundary [116] [118]. This equilibrium angle is given in equation 2.46:

$$2\gamma_s sin\beta = \gamma_b \quad (2.46)$$

Where γ_s is the surface energy, β the equilibrium angle and γ_b is the grain boundary energy.

Figure 2.12 shows a schematic profile of thermal grooving at a grain boundary. The establishment of a groove with angle β, leads to the development of ridges on either side of the interface. Since the equilibrium angle is determined by the ratio of the surface energy to the grain boundary energy, the shape profile of the groove is time independent. However, the grooves subsequently widen to reduce the sharp variations in the surface profile [117], which in turn drives the deepening of the groove to maintain the equilibrium angle [116].

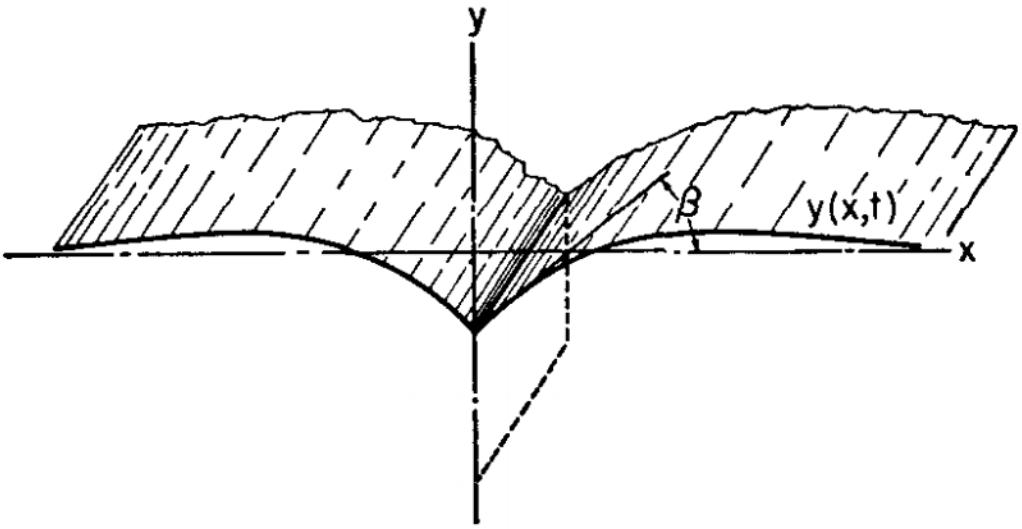

Figure 2.112: Schematic showing a thermal groove on a free surface. Reprinted from W. W. Mullins, "The effect of thermal grooving on grain boundary motion," Acta Metallurgica , vol. 6, pp. 414-427, 1958, with the permission of AIP Publishing [116].

In general, the development of the groove occurs through surface diffusion [119, 120, 117, 118]. On this assumption, the width and depth of the thermal groove can be expressed as a function of time, as in equations 2.47 and 2.48 below [116]:

$$d = 0.973m(Bt)^{\frac{1}{4}} \tag{2.47}$$

Where d is the depth of the groove, defined as the distance from the maxima of the surface profile to the grain boundary; m is tan(β), B is $D_s\gamma\Omega^2 v/kT$, t is time.

$$s = 4.6(Bt)^{\frac{1}{4}} \tag{2.48}$$

Where s is the separation between the two maxima, and B and t are as defined above.

The development of thermal grooves presents two main problems to hot stage TEM experiments. The most straight forward is that in thin film specimens the grooving of the surface can lead to the breakup of the film into individual grains as the grooves will eventually penetrate through the entire thickness of the specimen. For 38nm thick Au thin films after 5 minutes and 650^{o}C Goodhew and Smith, measured that the groove depth was approximately 10 nm [120], a similar process is likely to occur in the thinner areas of thin foil specimen. This imposes limitations on time, temperature and specimen thickness for any hot stage TEM experiment. If non-isothermal heat

treatments are used, the breakup of the foil may be accelerated by the stresses caused by thermal expansion and contraction of the specimen.

However, the more significant effect is the potential for thermal grooves to inhibit the motion of grain boundaries and interfaces. This is because, for a stationary grain boundary, the development of a thermal groove causes a shortening of the grain boundary within the foil. Therefore, for the grain boundary to migrate the boundary must lengthen along the z direction, requiring additional energy for the creation of a boundary or interface of increased area [121].

2.2.4 Other Surface Effects.

The free surface of the TEM specimens can also have an effect on the movement of dislocations, representing a significant problem for in situ deformation experiments. However, Onink et al. [122] observed dislocation movement during in situ observations of the austenite to ferrite transformations and suggested that they may play a role in the relief transformation stresses. In situ studies have also demonstrated a role played by dislocations in precipitate dissolution [112]. This indicates that hot stage TEM observations of phase transformations may also be affected.

The dislocation interaction with the foil surface takes two forms with a different effect on the dislocation. In the first case, dislocations that intersect the foil surface can experience a pinning effect inhibiting further movement. In the second dislocations experience an image force [123] which attracts it to the free surface, which can result in the loss of the dislocations at the surface.

The pinning effect arises because the dislocation creates a step at the free surface [124], the height of which is proportional to the Burgers vector. This involves an increase in the energy and so the frictional force, F_f, experienced by the dislocation is as given in equation 3.49 [114]:

$$F_f = \frac{\boldsymbol{b}.\boldsymbol{n}}{\sin\varphi}\gamma \qquad (2.49)$$

Where **b** is the Burgers vector, **n** is a unit vector normal to the foil, φ is the angle between the foil surface and the slip plane and γ is the surface energy.

Dislocations also experience an image force in a grain which has an inhomogeneous stress field, often resulting in the attraction to or repulsion from grain boundaries [125], for a free surface the stress field at the boundary is zero [114] [124]. A screw dislocation experiences a force equivalent to a symmetrically placed image dislocation with opposite Burgers vector, and so the force experienced is given by equation 2.50 [114]:

$$F = \frac{Gb^2}{4\pi l} \tag{2.50}$$

Where G is the shear modulus and l the distance between the surface and the dislocation.

The free surfaces can also act as preferential sites for the nucleation of new phases. This effect is particularly pronounced when the nucleation has a significant strain energy component. This can lead to atypical microstructures, precipitate morphologies, crystallography and kinetics.

The atypical microstructures occur due to the greater ability of the foil surface to accommodate the strain energy of nucleation and to act as heterogeneous nucleation sites, leading to the formation of precipitates at the surface [126]. As such the growth of the precipitate is affected by the intersection of the precipitate with free surface, this can prevent the full three-dimensional morphology of the precipitate from developing. This may also alter the mechanism and crystallography of the reaction, as in the case of Al-Cu alloys which decompose directly to the equilibrium θ phase in thin foils, without the precipitation of metastable phases as found in bulk materials [127] [128]. Although such difficulties could be partially circumvented by nucleating θ´ in the bulk before the thinning of thin foil specimens, Laird and Aaronson [127] found that the kinetics were accelerated as a result of diffusion across the surfaces of the foils. An experimental measurement of the FCC surface diffusion coefficient in steels using thermal groove width, obtained a value of D_s as high as 10^{-4} $cm^2 \cdot s^{-1}$ at 1250°C [129].

2.2.5 Annealing in Thin Specimens.

Annealing experiments using hot stage TEM are affected by the necessary creation of free surfaces in the thin specimens, and therefore by the thickness of the specimen

itself. In bulk materials, it is well known that grain growth near the metal surface is impeded [130].

In early recrystallisation experiments performed using hot stage TEM, a clear difference was observed between bulk and thin foil behaviour. In particular, foils in the region of 1-300nm thick underwent recrystallisation at higher than expected temperatures [131]. When TEM's with higher accelerating voltages (~1MV) were used to study recrystallisation behaviour in a range of materials (including mild steel, Cu and Al), it was found that the recrystallisation ceased at a well-defined front, which corresponded to a critical thickness (on the order of 500 nm) below which recrystallisation could not take place [132].

This was originally attributed to the effect of thermal grooving preventing further grain boundary motion below this thickness. However, later experiments by Hutchinson and Rey showed that when the specimen is prepared from sections normal to the rolling plane, recrystallisation continued to the very thinnest regions [112]. In Al alloys, Sehgal et al. showed that if the cooling rate was sufficiently high to minimise thermal grooving the specimens from rolling plane sections could likewise be completely recrystallised.

The reduction in grain boundary area provides the driving force for grain growth. Consequently, normal grain growth ceases and the process becomes dominated by surface effects once the grain size becomes greater than the foil thickness [133]. As with the case of recrystallisation, the boundary becomes immobile due to the presence of thermal grooves on the specimen surface.

Under these conditions, Mullins [121] described a mechanism responsible for the promotion of abnormal grain growth. He showed that, in a scenario where two grains share a grain boundary but have different surface energies, thermal grooving will not hinder the abnormal grain growth that results from this difference so long as it is more than several percent. A second proposed mechanism is that normal growth is inhibited by the formation or dissolution of secondary phase and precipitates [121] [134]. For this reason in situ TEM studies of grain growth behaviour require that the grain size of the specimen be small relative to the thickness. Even in studies of nanocrystalline materials growth was inhibited in the thinnest regions of the film [135].

2.2.6 Phase Transformations using in situ hot stage TEM.

In situ hot stage TEM has been used to investigate multiple phase transformations in steels including the austenite to ferrite transformation, the austenite to pearlite, and the growth of bainite and martensite.

Darken and Fisher made early observations of the formation of pearlite in evaporated thin films of eutectoid steel [136]. They noted morphological similarities between the pearlite produced in the thin film with that found in bulk specimens, with the interlamellar spacing decreasing when the transformation temperature decreased. However, they also noted that the cementite plates in the pearlite were not necessarily connected to a common nucleus.

Purdy used high voltage electron microscopy to observe the dynamic interface behaviour in Fe-C-Mo alloys [137]. Mobile austenite-ferrite interfaces were found to be smoothly curved and responsive to temperature change on the order of 3^{o}C, with no observable hysteresis. In addition a small number of facetted interfaces were observed, often with a simple orientation relationship between the austenite and ferrite phases, which showed restricted mobility. It was suggested that the results be considered only in a qualitative fashion, particularly regarding kinetics and precipitate morphology, due to experimental artefacts. However, the experiments provided direct evidence of anisotropy in the mobility of the interface due to changes in structure.

Purdy also observed the ferrite formation in Fe-C-Si and a commercial low alloy steel [138]. Ledge migration during the thickening of Widmanstätten ferrite was observed. Ledge heights were estimated to be 3nm or less with varying interledge spacings. Smooth, synchronous movement of ledges was observed.

Onink et al. [122] used 120 kV and 300 kV microscopes to perform hot stage TEM experiments, capturing the austenite to ferrite transformation in Fe-0.36 wt% C and Fe-0.71 wt% C steels. The migration rates of normal and lateral mode growth were determined from the captured video of the phase transformation. In this case the highest values of the measured normal mode migration rate was typically lower than that predicted from diffusion-controlled growth. Several potential reasons for this disparity were suggested including the influence of stress, the advanced stage of the transformation, the overall mobility of the interface and an incorrect classification of

the growth mode. The lateral mode growth rates were comparable to that predicted by diffusion-controlled migration.

Nemoto used HVEM to observe the growth of bainite in an Fe-C-Ni alloy [139] at 380^{o}C. Acicular bainite was observed to grow continuously with an average lengthening rate of 0.05 $\mu m \cdot s^{-1}$. The austenite and bainitic ferrite were oriented close to the Kurdjumov-Sachs orientation relationship, with the growth direction close to the $[121]_{\alpha}$ direction. Growth was observed to be accompanied by the formation of high densities of dislocations. Non-acicular bainite growth was also observed and showed a similar structure to that found in the bulk.

Kang et al. [140] used hot stage TEM to observe the growth of bainitic embryos nucleated in the bulk for a range of steel, iron and copper alloys. Bainite was observed to nucleate and thicken through a shear mechanism in solute depleted regions, developing into a convex lens shape. Lengthening occurred by the formation of new bainite units at the tip of the bainite laths.

2.2.7 Other Direct Observation Experiments.

High Temperature Confocal Scanning Laster Microscopy (HT-CLSM) is a widely used experimental technique that allows the direct observation of phase transformations in steel. Schmidt et al. [129] observed curved austenite-ferrite and austenite-pearlite interface during non-isothermal austenite formation in Fe-C-Mn alloys. They estimated a high surface diffusion coefficient of 10^{-4} cm^2s^{-1} at 1250^{o}C, and qualitative agreement between the measured migration rates and models in the literature. In interstitial free, ultra-low alloy steels, Schmidt et al. [141] observed austenite formation and measured the migration rate during heating. Austenite was seen to nucleate at grain corners, but without achieving site saturation. Most interfaces were planar, but more complex “jagged” interfaces were also observed. The interface mobility was determined to be in good agreement with previous studies of the ferrite to austenite transformation.

Hamada et al. [142] used HT CLSM to observe ferrite growth in Fe-Ni and Fe-Mn alloys. Smoothly curved boundaries were observed to migrate, probably in a massive

manner, with boundary mobility calculated to fall between the equations proposed by Hillert [43] and Wits et al. [44]. The disparity between Wits et al. was partly attributed to the measurement of individual boundaries by Hamada et al. in contrast to the mean boundary mobility under certain assumed austenite microstructure parameters in the case of Wits et al.

2.3 Concluding Remarks.

There are some remaining issues relating to the exact conditions prevailing at migrating austenite-ferrite interfaces, and in particular about the physical nature of the Mn spike during LENP growth.

The use of cyclic partial phase transformations has been able to probe the interfacial conditions by linking the temperature range of the stagnant stage to the local chemistry at the interface. This can be further illuminated through the observation of the interaction of the interface with residual spikes left in the material from a previous cycle causing a non-trivial growth retardation.

Typically phase transformations are studied either using dilatometry or by comparing the final microstructures and chemistry with that predicted by models. The use of in situ hot stage TEM provides an opportunity to directly observe the behaviour of individual interfaces. By combining TEM observation with a CPPT heat treatment further information on aspects of the phase transformation can be gained. Firstly, it can confirm that there is no new nucleation and only the behaviour of existing interfaces gives rise to the stagnant stage. Secondly, it can determine in more detail how the interface behaves during the stagnant stage, for example by confirming that the stagnant stage really is “stagnant” rather than “static”, and how the transition from partitioning to non-partitioning kinetics affects interface behaviour. Finally, and more generally, direct observations can determine the growth mode of the transformation and how the interface interacts with microstructural features.

However, use of in situ TEM presents a number of challenges, which makes it important to compare TEM results with data from modelling or bulk experiments. However, existing studies suggest that quantitative agreement between TEM

experiments and calculation or bulk data are obtainable. The results of Onink et al. [122] indicate a minimal role of surface diffusion alone in affecting the kinetics as measured velocities were below that expected for diffusion-controlled growth. Since Onink et al. were unable to observe the ferrite nucleation (likely due to electron beam heating) they could not precisely establish the start time of the transformation. Since interface velocity in diffusion-controlled growth is inversely proportional to $\sqrt{t}$ slower growth at later times is not unexpected. Similarly the effect of surfaces on nucleation does not necessarily represent a significant problem since in the current thesis cyclic phase transformations are planned, and it is expected that the mobile interface under observation should exhibit a random orientation between the austenite and ferrite phases.

3 Experimental Methods

3.1 Materials Examined.

Five steel compositions were chosen for cyclic partial phase transformation experiments, with a composition based on Fe-C-Mn. Three concentrations of Mn were selected 0.5, 1.0 and 1.5 wt % and for the 1.5 wt % Mn alloys different carbon concentrations of 0.183, 0.263 and 0.330 wt % were also examined. These compositions were selected for several reasons. First, by using different of Mn and C, the effect of these alloying elements on interface behaviour during thermal cycling could be investigated. Second, the transformation of steels with similar manganese content have been previously studied using CPPT experiments and these compositions have real world relevance, with Mn being a common alloying addition to steels. The materials used for thermal cycling and in the bainitic steel were obtained from ArcelorMittal, where the composition was analysed using Spark-OES. They were homogenised with hot and cold work before being machined into dilatometry sized specimens (with the exception of the bainitic steel).

The T_1 and T_2 temperatures were selected in conjunction with thermodynamic modelling using the Thermo-Calc software. Both the low (T_1) and high (T_2) temperatures were selected to be within the two-phase $\alpha+\gamma$ region for each composition. Furthermore, the temperatures were chosen such that at the T_1 and T_2 temperatures the $\alpha \rightarrow \gamma$ or $\gamma \rightarrow \alpha$ transformation would be expected to progress through LENP kinetics. The change in the equilibrium volume fraction of ferrite was estimated to be approximately 0.35-0.4 for all compositions.

Table 3.1 contains the major constituents for each of the materials investigated in this thesis and the corresponding chapter in which the results for each composition appear.

Table 3.1: Table of specimen compositions (in wt%, with the exception of Fe) and the chapter in which the results are reported.

Alloy Tag	C	Mn	Si	Mo	Fe	Chapter
0.1C-0.5Mn-0.03Si	0.0848	0.47	0.03	-	Balance	4
0.1C-1.0Mn-0.026Si	0.095	1.0	0.026	-	Balance	5
0.183C-1.5Mn-0.14Si	0.183	1.464	0.14	-	Balance	6
0.263C-1.5Mn-0.14Si	0.263	1.458	0.14	-	Balance	6
0.330C-1.5Mn-0.14Si	0.330	1.457	0.14	-	Balance	6
0.307C-3Mn-1.49Si	0.307	3.00	1.49	0.146	Balance	A
99.8% Pure Fe	<200 ppm	<800 ppm	<150 ppm	-	Balance	3
Fe-0.1C-1.6Mn	0.1	1.6		0.5		3

3.1.1 Fe-0.1C-0.5Mn.

Figure 3.1 show images of the starting microstructure obtained from optical microscopy after etching in 2% Nital. The microstructure consists of a mixture of allotriomorphic, Widmanstätten and bainitic ferrite. Backscattered electron micrographs in figure 3.2 show the distribution of inclusions and particles in the as polished material and secondary electron micrographs show the microstructure after etching with Nital.

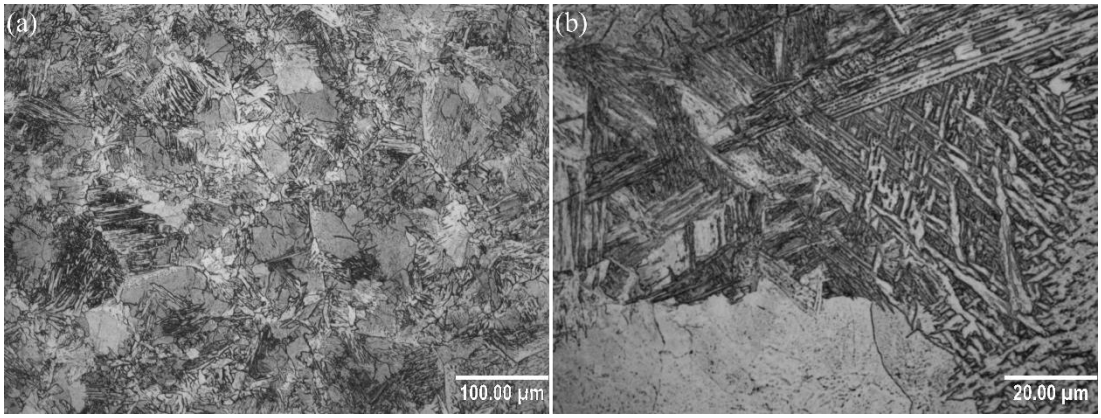

Figure 3.1: Optical micrographs of the starting microstructure for Fe-0.1C-0.5Mn.

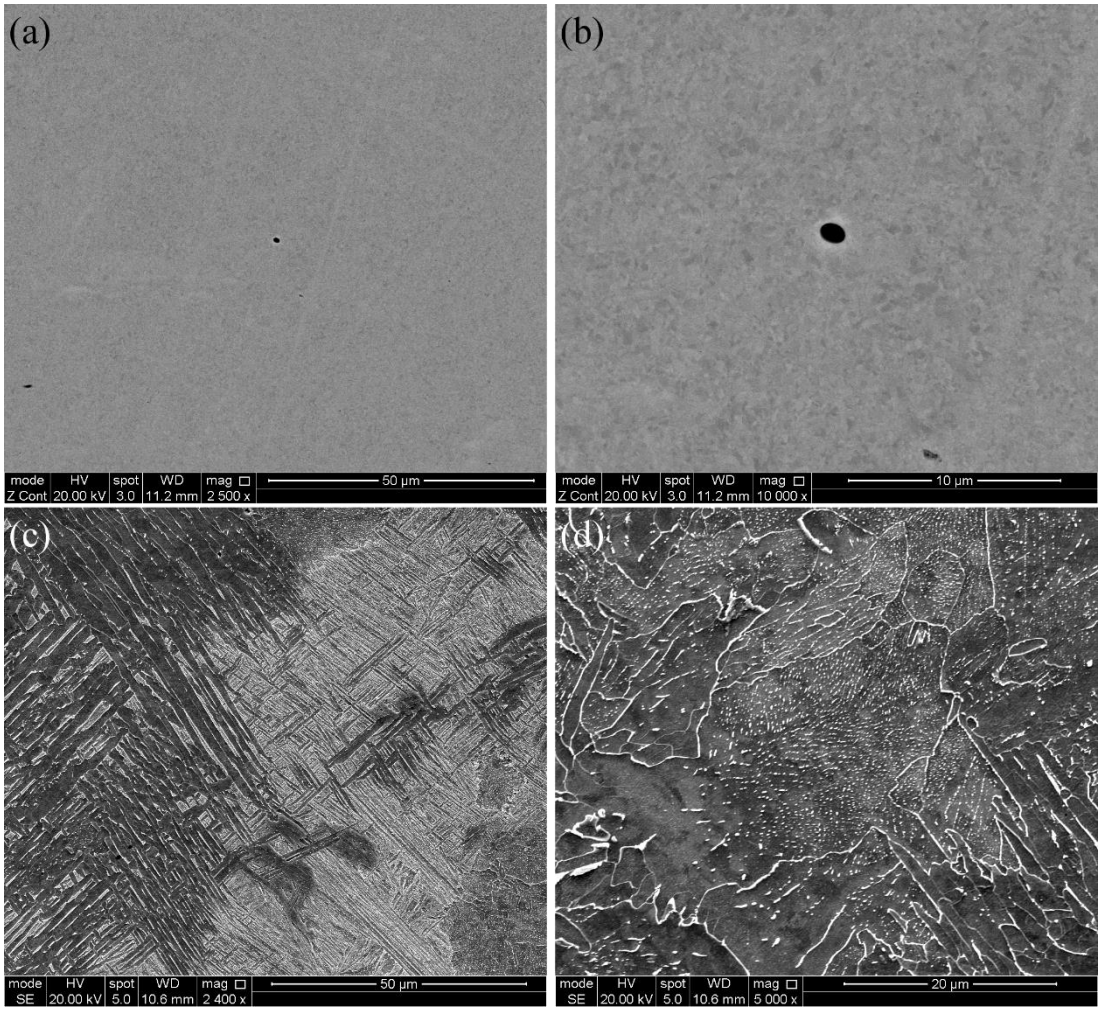

Figure 3.2: (a-b) Backscattered electron micrographs showing the distribution of particles in the as-polished material, (c-d) Secondary electron micrographs of the microstructure revealed by etching with nital.

Bright field TEM images can be found in Chapter 4, figure 4.2. The microstructure consisted of regions of bainitic ferrite alongside allotriomorpic ferrite grains, some of which contained Fe_3C precipitates within the grain, in agreement with the Optical and SEM images. All thin foil specimens displayed a similar microstructure, with no significant differences between foils.

The identity of the inclusions in the Fe-0.1C-0.5Mn was determined using STEM-EDS. Table 3.2 shows that the larger inclusions, figure 3.3(b), contained both high levels of Mn and O as well as elevated concentrations of Al, Si and to a lesser extent S in comparison to the matrix. The smaller particles, figure 3.3(a), were enriched with Al and O compared to the nominal composition, indicating that these were likely oxide

particles. However, the EDS also displayed a prominent Fe signal indicating that the particles were embedded in the foil without penetrating the full thickness of the foil.

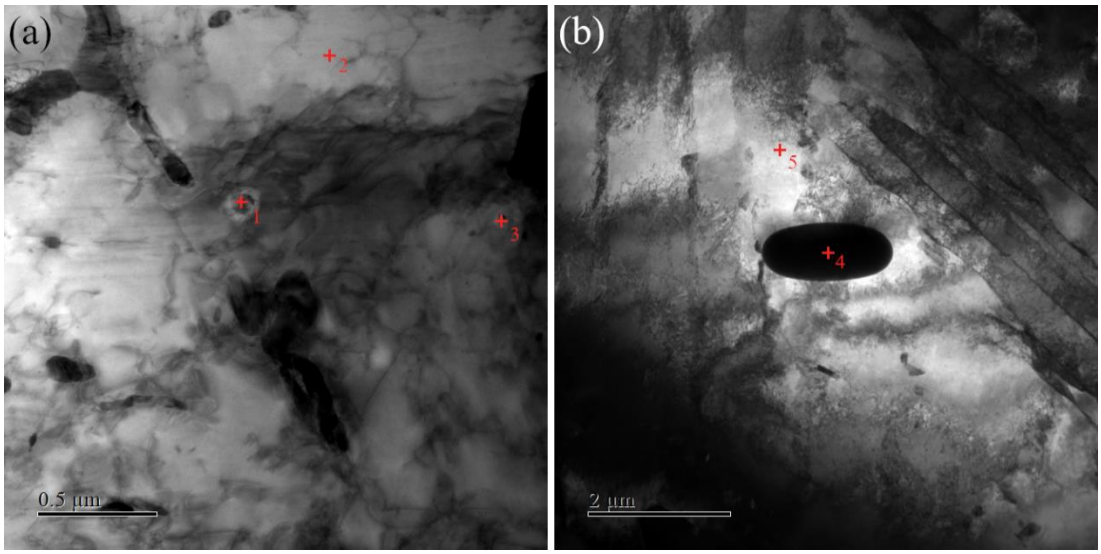

Figure 3.3: (a) small inclusions in the Fe-0.1C-0.5Mn steel and (b) larger inclusions found in the thin foil. The locations of the STEM point analysis are indicated by red crosses.

Table 3.2: Table of EDS point analysis results for figure 3.7, in wt%. Note that the high levels of carbon are the result of contamination on the foil surface.

No.	C	O	Al	Si	S	Mn	Fe
1	8.39	1.81	1.63	0.05	0.06	2.63	85.69
2	6.78	ND	0	0.04	0.02	0.52	92.64
3	5.25	3.06	2.57	0.04	0.53	1.75	86.8
4	6.43	ND	0.02	0.02	ND	0.54	92.99
5	3.42	16.27	3.76	4.38	0.31	29.08	42.78

Figure 3.4 shows the austenite volume fraction against temperature as calculated using Thermo-Calc. The T_1 and T_2 temperature selected for the heat treatment are 790^{o}C and 840^{o}C respectively.

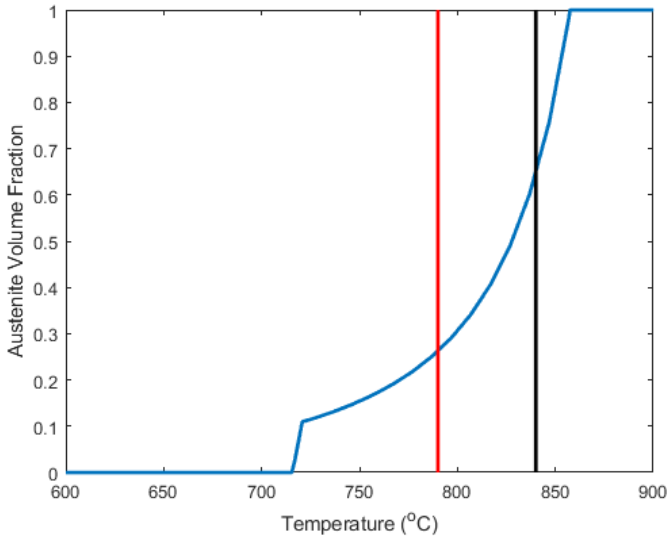

Figure 3.4: Graph of austenite volume fraction against temperature for Fe-0.1C-0.5Mn. The red and black lines indicate the T_1 (790°C) and T_2 (840°C) temperatures respectively.

3.1.2 Fe-0.1C-1Mn.

Figure 3.5 shows the starting microstructure for this composition as revealed after etching with 2% Nital. It consists primarily of equiaxed ferrite grains, with a smaller fraction of bainite, which can be seen in more detail in the secondary electron micrographs found in figure 3.6

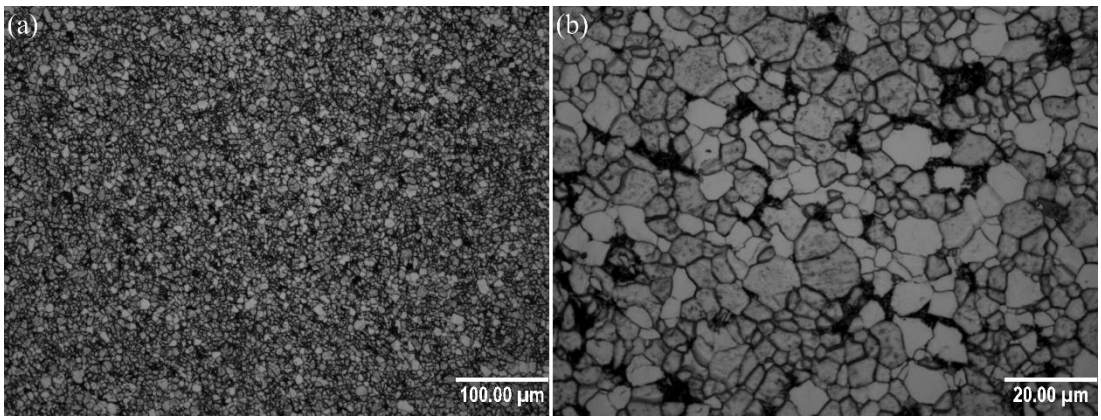

Figure 3.5: Optical micrographs of the starting microstructure for Fe-0.1C-1Mn.

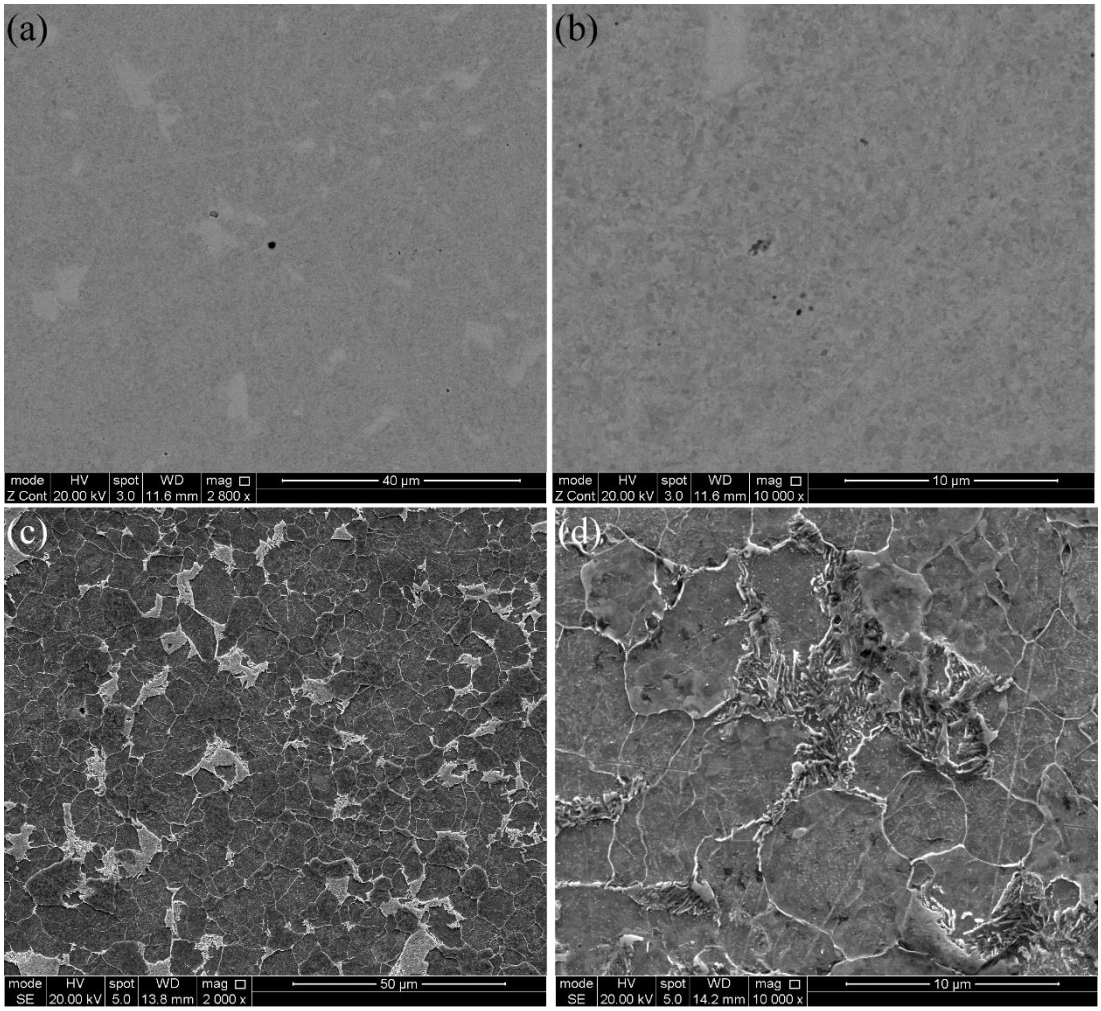

Figure 3.6: (a-b) Backscattered electron micrographs showing the distribution of particles in the as-polished material, (c-d) Secondary electron micrographs of the microstructure revealed by etching with nital.

Bright field TEM images of the starting microstructure can be found in Chapter 5, figure 5.2. This confirms that the microstructure consisted primarily of equiaxed ferrite grains with a small amount of bainitic ferrite. Carbides were also found to be present in the ferrite grains, these were identified as Fe_3C carbides through selected area diffraction. The microstructure was consistent for all specimens of this composition.

Figure 3.7 shows the austenite volume fraction against temperature as calculated using Thermo-Calc. The T_1 and T_2 temperature selected for the heat treatment are 770^{o}C and 820^{o}C respectively.

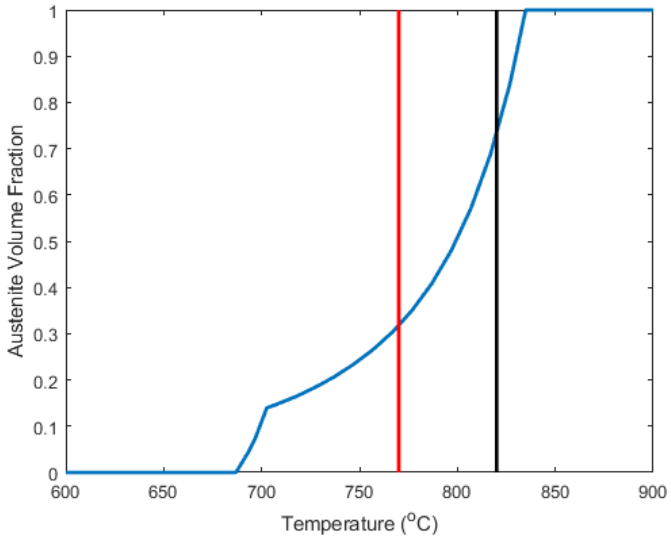

Figure 3.7: Graph of austenite volume fraction against temperature for Fe-0.1C-1M. The red and black lines indicate the T_1 (770°C) and T_2 (820°C) temperatures respectively.

3.1.3 Fe-XC-1.5Mn-0.14Si, X = 0.183, 0.263, 0.330.

The microstructure consists of a mixture of ferrite and pearlite, with an increasing volume fraction of pearlite as the carbon concentration is increased. Figure 3.8 shows optical micrographs of the starting microstructures which are characterised by ferrite idiomorphs within an increasing volume fraction of pearlite. For Fe-0.263C-1.5Mn-0.14Si and Fe-0.330C-1.5Mn-0.14Si allotriomorphic ferrite formed on the prior austenite grain boundaries can be distinguished. Figure 3.9-3.11 contain backscattered electron and secondary electron images of the as-polished material and microstructure after etching with nital. Alongside the pearlite, idiomorphic and allotriomorphic ferrite found in all three compositions, the Fe-0. 263C-1.5Mn-0.14Si material also contains some acicular ferrite as in figure 3.10(d).

Figure 3.12 shows the austenite volume fraction against temperature as calculated using Thermo-Calc for each of the three compositions. The T_1 temperature selected for the heat treatment is 734°C, 729°C, 720°C for 0.183 wt% C, 0.263 wt% C and 0.330 wt% C respectively. The corresponding T_2 temperatures are 789°C, 779°C and 760°C.

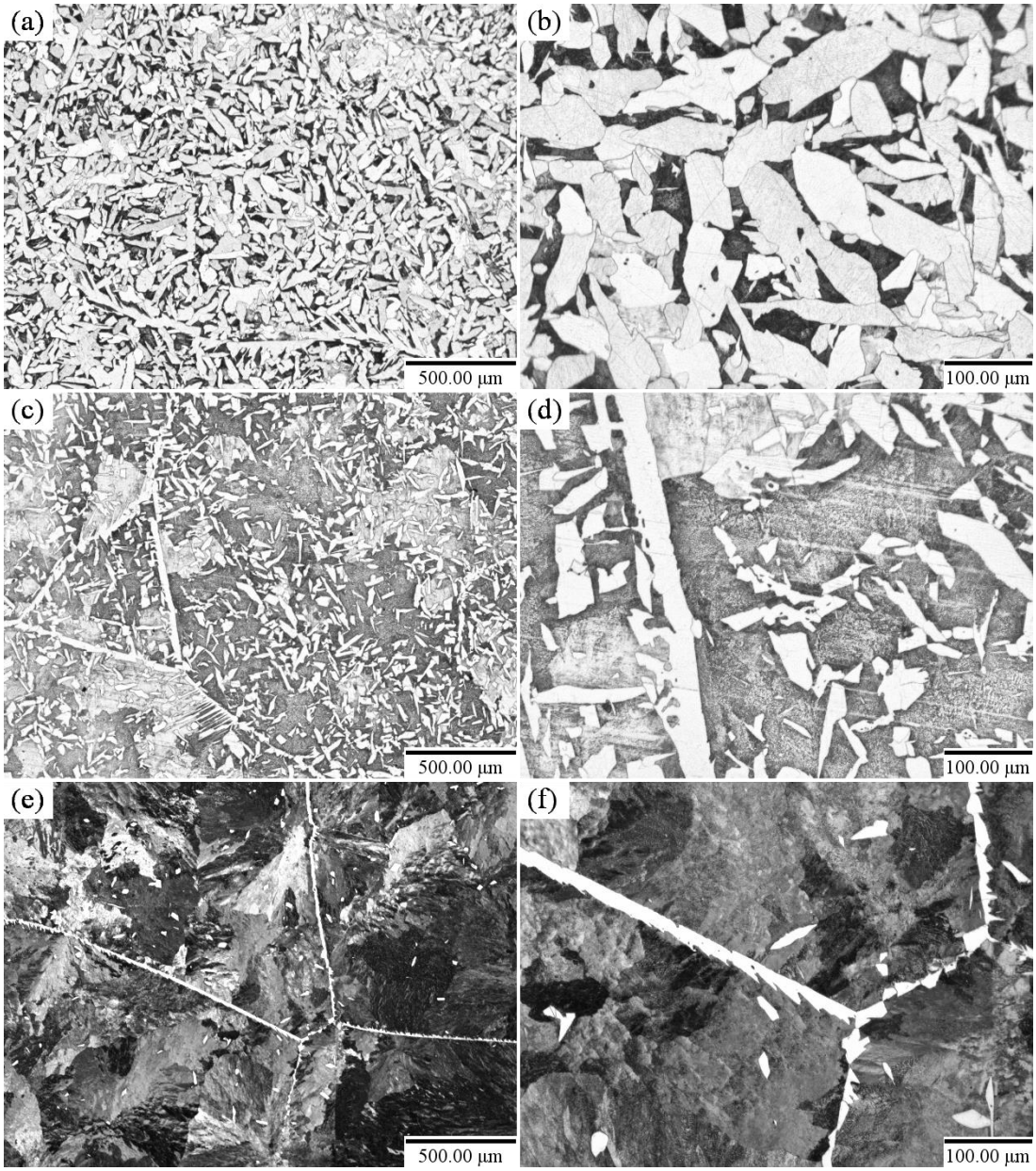

Figure 3.8: Optical micrographs of the starting microstructures for (a-b) Fe-0.183C-1.5Mn-0.14Si (c-d) Fe-0.263C-1.5Mn-0.14Si and (e-f) Fe-0.330C-1.5Mn-0.14Si. For the Fe-0.263C-1.5Mn-0.14Si and Fe-0.330C-1.5Mn-0.14Si microstructures, the presence of pro-eutectoid ferrite is clearly visible along prior austenite grain boundaries. In addition idiomorphic ferrite grains can also be seen.

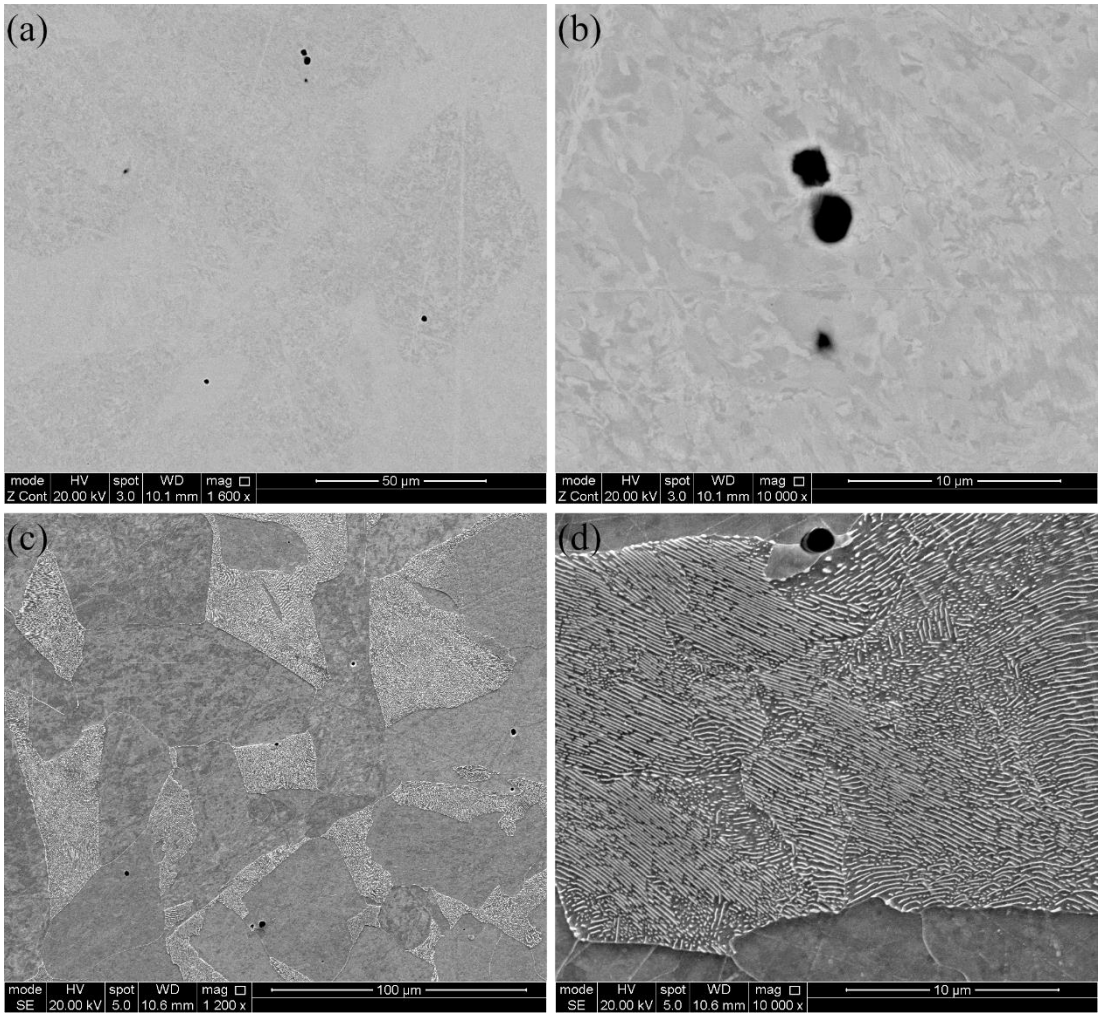

Figure 3.9: (a) and (b) Backscattered electron micrographs showing the distribution of inclusions in the Fe-0.183C-1.5Mn-0.14Si material. (c) and (d) secondary electron micrographs of the microstructure as revealed by etching with Nital. The microstructure is a mixture of ferrite grains and pearlite colonies.

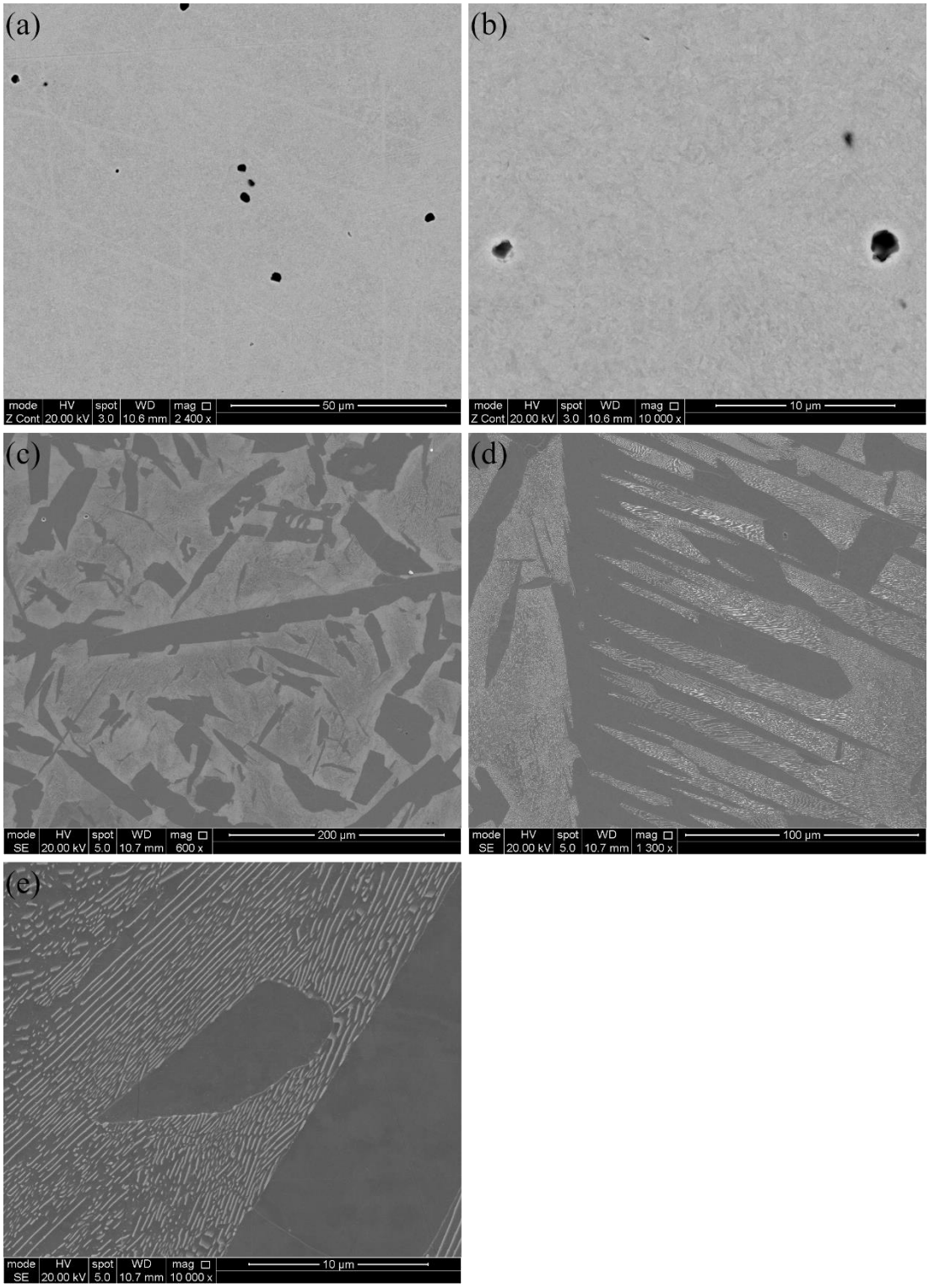

Figure 3.10: (a) and (b) Backscattered electron micrographs showing the distribution of inclusions within the 0.263C-1.6Mn-0.14Si material. (c)-(e) Secondary electron micrograph of the microstructure after etching with Nital. The microstructure was a mixture of ferrite grains and pearlite colonies. In (a) allotriomorphic ferrite can be seen along the prior austenite grain boundary, along with idiomorphic ferrite grains, which are also shown in (e). (d) shows Acicular ferrite distributed along prior austenite grain boundaries.

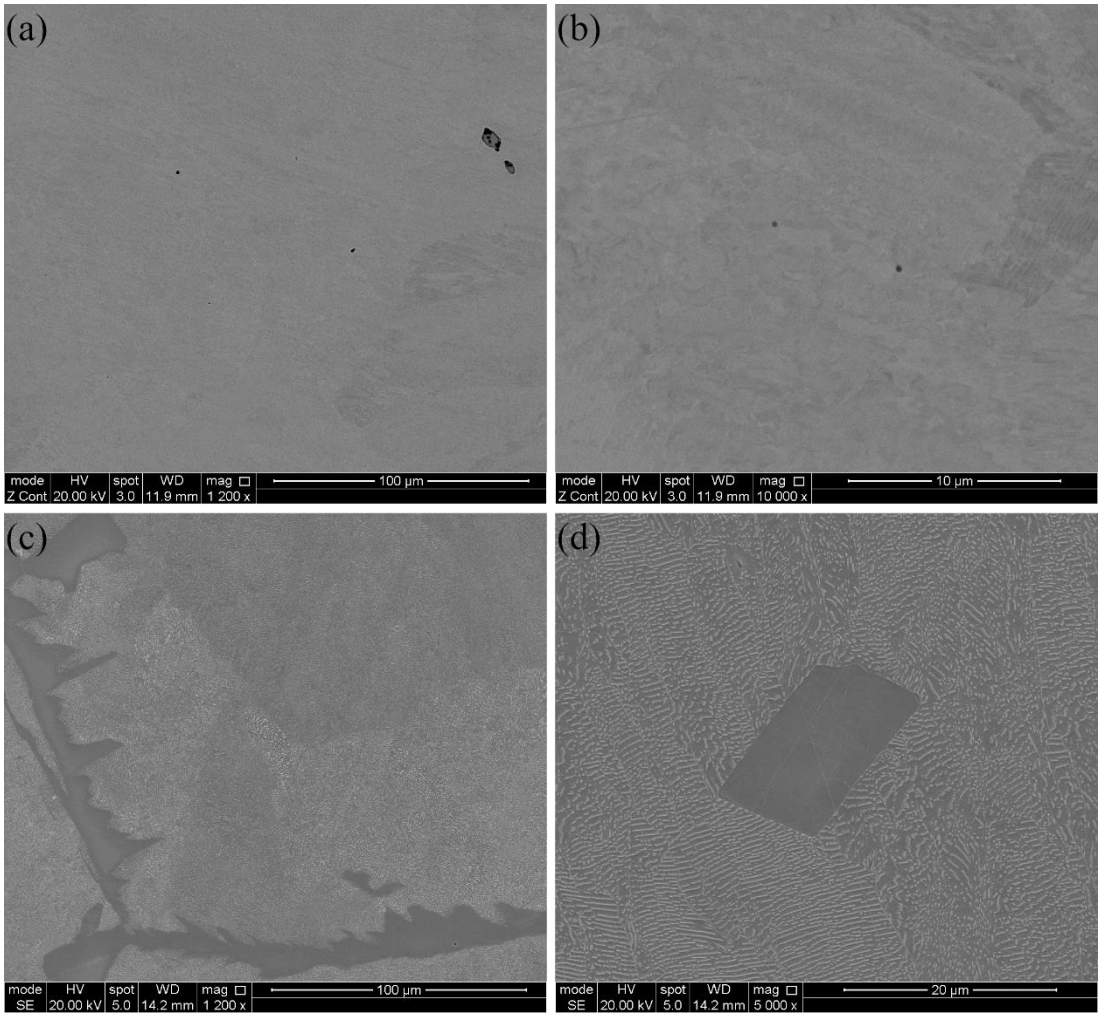

Figure 3.11: (a) and (b) Backscattered electron micrographs showing the distribution of inclusions within the 0.33C-1.5Mn-0.14Si material. (c) and (d) Secondary electron micrographs of the starting microstructure after etching with Nital. Pro-eutectoid ferrite can be seen distributed along prior austenite grain boundaries alongside pearlite colonies and small quantities of idiomorphic ferrite, seen in (d).

Bright Field TEM images of the starting microstructures of can be found in Chapter 6, figure 6.2. As with the lower magnification SEM and Optical images, the microstructure was found to consist of a mixture of allotriomorphic and idiomorphic ferrite, alongside pearlite. The quantity of pearlite was observed to increase with increasing carbon concentration. The microstructure was consistent between different foils of the same composition.

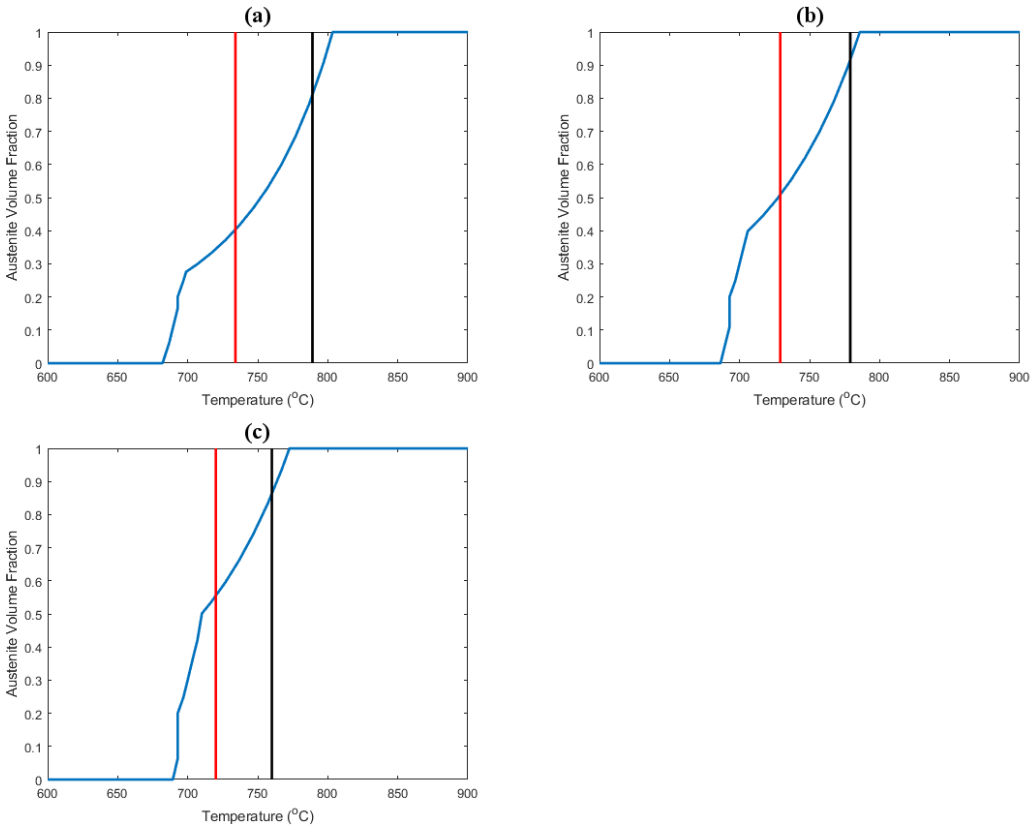

Figure 3.12: Graph of the austenite volume fraction against temperature for (a) Fe-0.183C-1.5Mn-0.14Si (b) Fe-0.263C-1.5Mn-0.14Si and (c) Fe-0.330C-1.5Mn-0.14Si. The red and black lines indicate the T_1 and T_2 temperatures respectively. T_1 temperatures are 734°C, 729°C and 720°C for (a), (b) and (c). The respective T_2 temperatures are 789°C, 779°C and 760°C.

3.1.4 Fe-0.307-3Mn-1.49Si-0.146Mo.

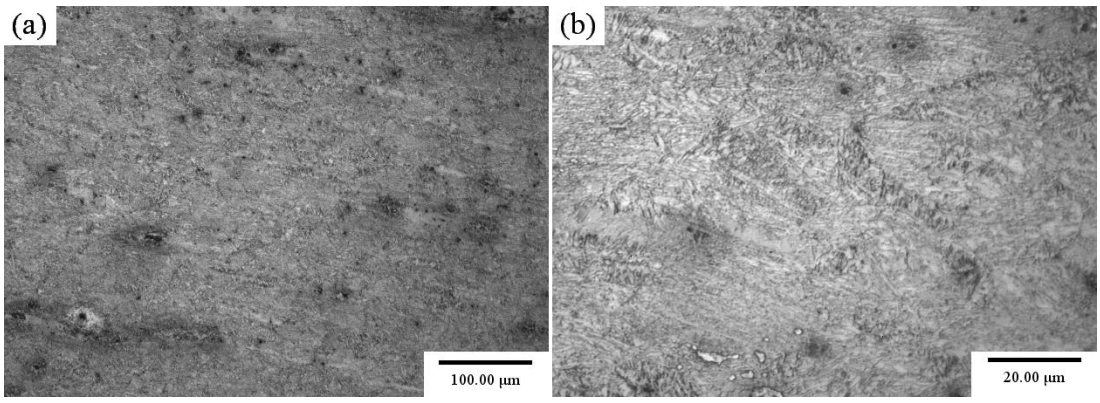

Figure 3.13: Optical micrographs of the starting microstructure for Fe-0.307-3Mn-1.49Si-0.146Mo.

The optical micrographs of the initial bainitic microstructure is shown in figure 3.13, with secondary electron micrographs, showing the microstructure in more detail and demonstrating that it is upper bainite in figure 3.14. Figure 3.14 also contains backscattered electron micrographs showing the distribution of inclusions in the material.

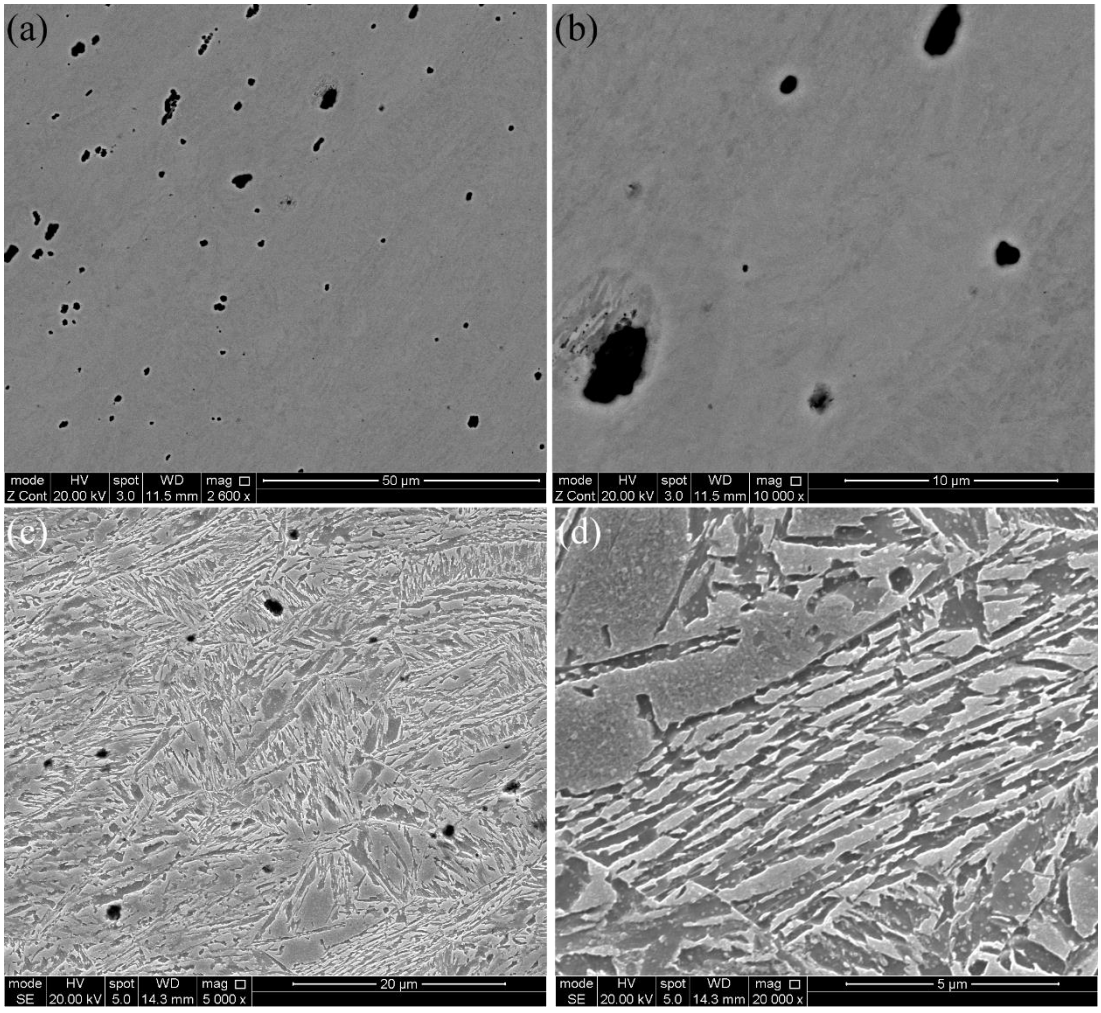

Figure 3.14: (a-b) Backscattered electron micrographs showing the distribution of particles in the as-polished material, (c-d) Secondary electron micrographs of the upper bainite microstructure revealed by etching with nital.

Bright field TEM images of the starting microstructure can be found in Apendix A, figure A.2 and confirms that the nature of the banitic microstructure, which was found in all observed thin foils of this composition.

Figure 3.15 shows the austenite volume fraction against temperature as calculated using Thermo-Calc. The Bainite and Martensite start temperatures were calculated using equations 3.1 [146] and 3.2 [147].

$$B_s(°C) = 830 - 270C - 90Mn - 37Ni - 70Cr - 83Mo \quad (3.1)$$

Where C, Mn, Ni, Cr and Mo is composition of the steel in weight percent for each alloying element.

$$M_s(K) = 764.2 - 302.6w_c - 30.6w_{Mn} - 16.6w_{Ni} - 8.9w_{Cr} + 2.4w_{Mo} - 11.3w_c + 8.58w_{Co} + 7.4w_W - 14.5w_{Si} \quad (3.2)$$

Where w_i is the steel content in weight percent for each alloying element, i.

The calculated B_s temperature was 465°C, and the calculated M_s temperature was 284°C (557K).

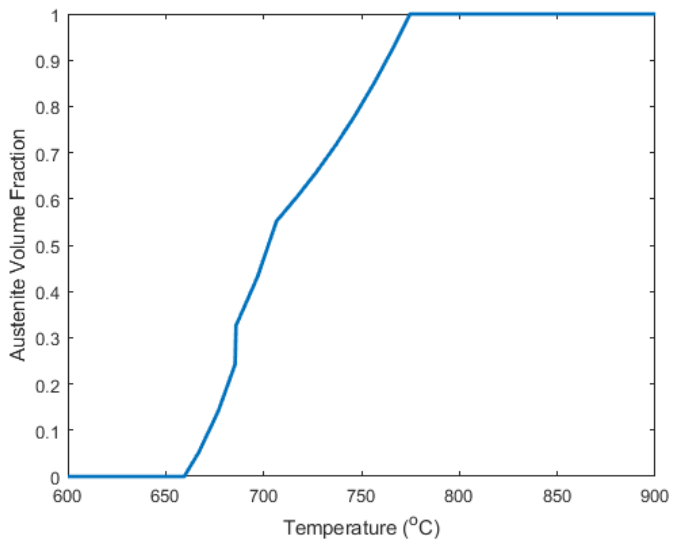

Figure 3.15: Graph of the austenite volume fraction against temperature for Fe-0.307-3Mn-1.49Si-0.146Mo.

3.1.5 99.8% Pure Fe.

Specimens of 99.8% pure Fe, obtained from Goodfellow Cambridge Ltd, were used in the calibration of the heating holder. Figure 3.16 shows the starting microstructures observed with optical microscopy. The as-polished surface, showing the distribution of inclusions and precipitates in the material, and the microstructure as observed under SEM are displayed in figure 3.17. The microstructure primarily consisted of equiaxed ferrite grains, as was also observed in the SEM images.

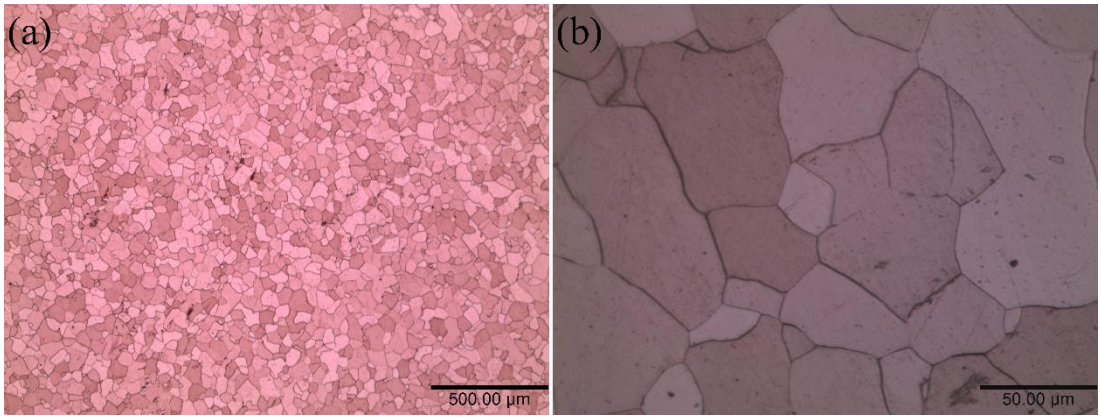

Figure 3.16: Optical Micrographs of the Fe microstructure, consisting of equiaxed ferrite grains.

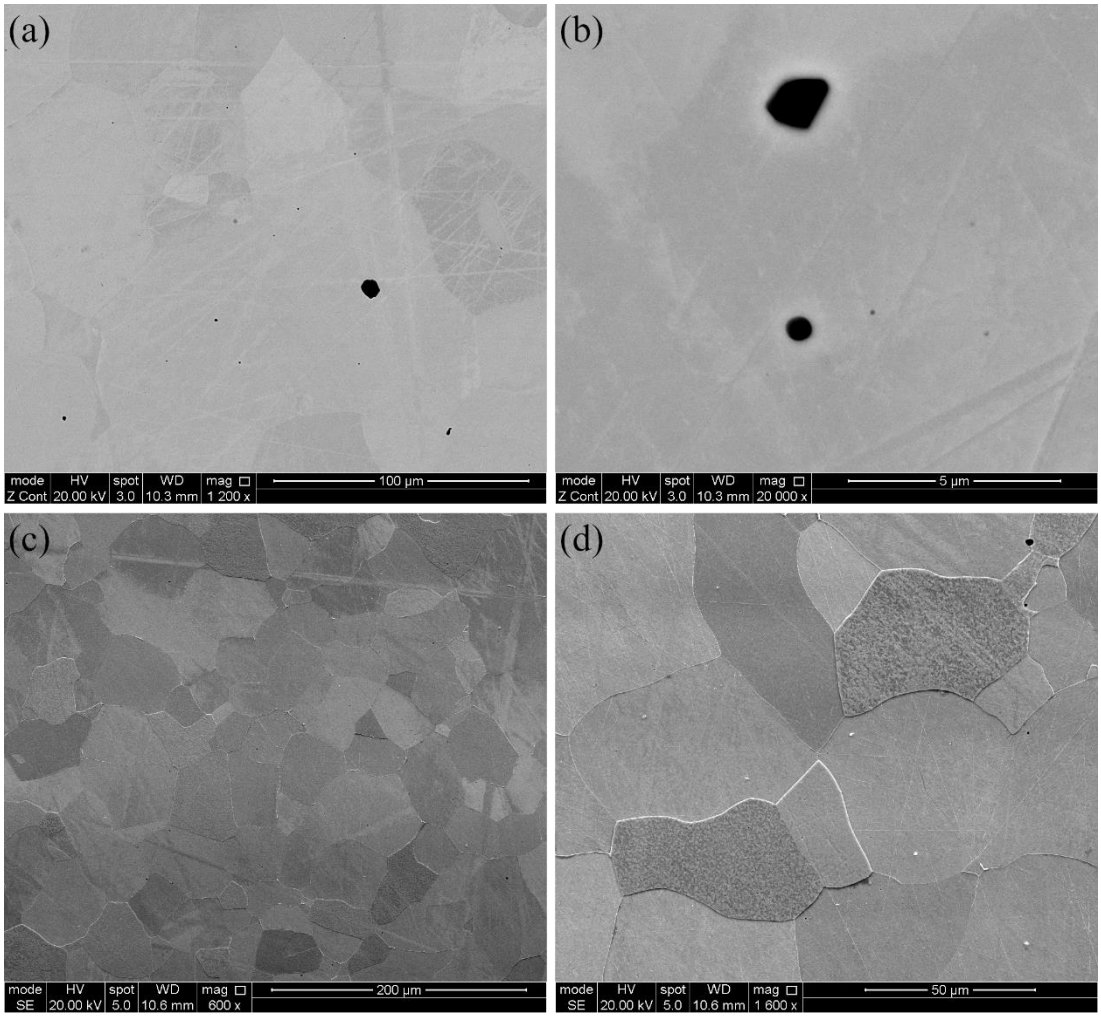

Figure 3.17: (a) and (b) Backscattered electron micrographs showing the distribution of particles in the Fe specimen. (c) and (d) the microstructure of the Fe specimens as revealed by etching with Nital, primarily consisting of equiaxed ferrite grains.

3.1.6 Fe-0.1C-1.6Mn-0.5Mo.

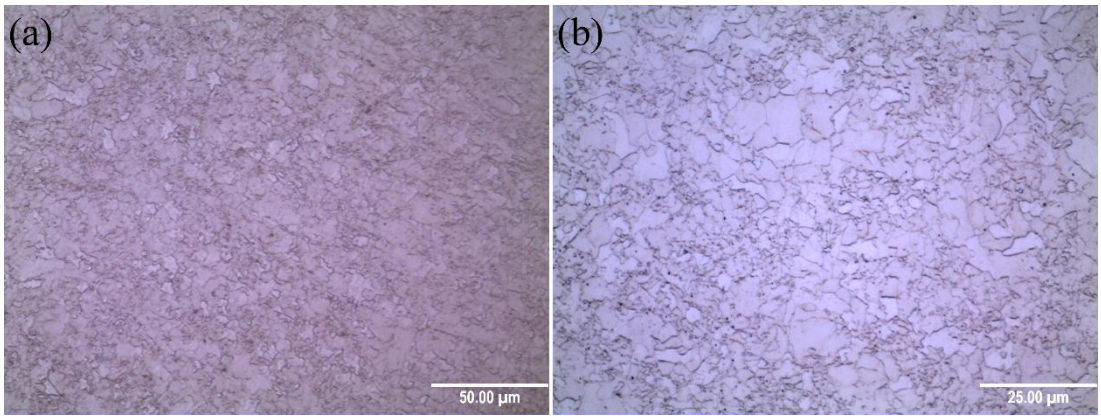

Figure 3.18: Optical Micrographs of the Fe-0.1C-1.6Mn-0.5Mo starting microstructure, primarily consisting of fine equiaxed ferrite grains.

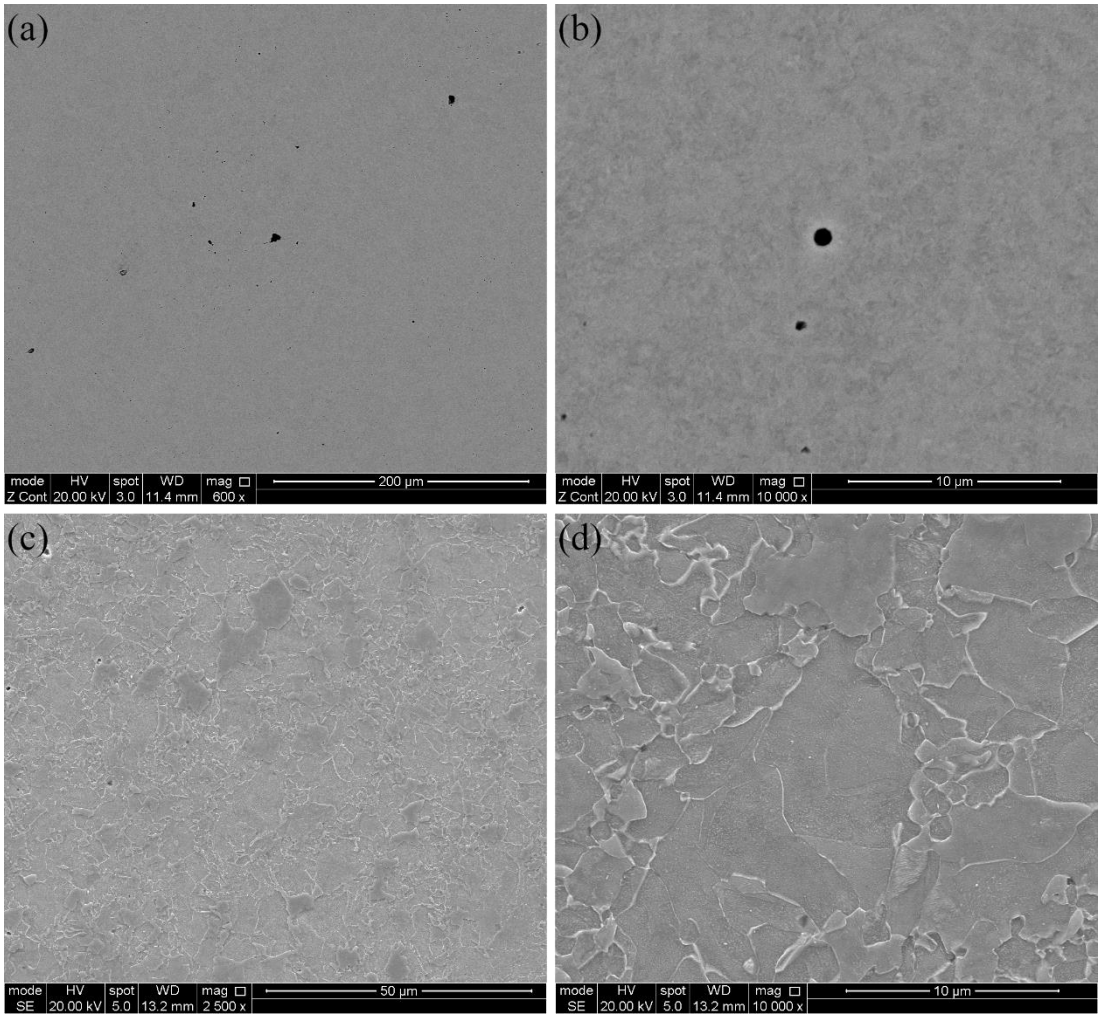

Figure 3.19: (a) and (b) Backscattered electron micrographs showing the distribution of inclusions, (c) and (d) the ferrite microstructure after etching with Nital.

Figure 3.18 and 3.19(c-d) show the microstructure of the Fe-0.1C-1.5Mn-0.5Mo steel after etching with Nital. It primarily consists of equiaxed ferrite grains of under 25 μm. Bright Field TEM images, as in figure 3.20, revealed that the ferrite grains contained a dispersion of fine carbides, on the order of 10's nm in diameter, within the ferrite grains. The distribution of larger particles within the material is shown in the as-polished surface in figure 3.19(a-b).

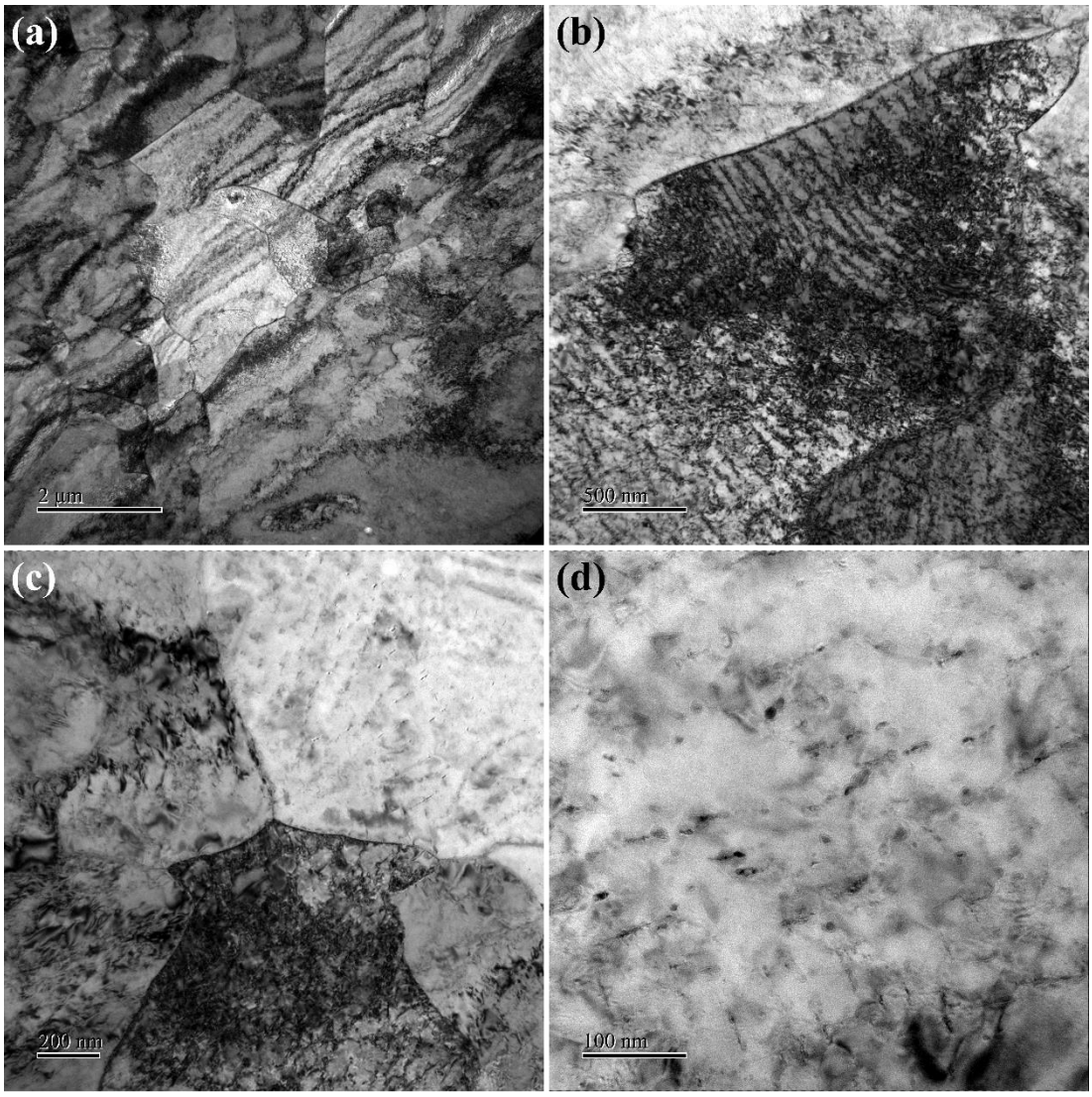

Figure 3.20: Bright field TEM micrographs showing the microstructure of the Fe-0.1C-1.6Mn-0.5Mo steel, with a dispersion of fine carbides within the ferrite grains.

3.2 Hot Stage Transmission Electron Microscopy.

Hot stage TEM was carried out in a JEOL JEM 3010 UHR TEM equipped with a LaB_6 filament, operated at 300 kV in spot size 1 with a 100 µm condenser aperture. 3.0mm discs were mechanically thinned to approximately 100 µm before being electropolished. Electropolishing was carried out in a STRUERS Tenupol-5 electropolishing unit, equipped with a Julabo FP-50 refrigerated circulator operating at -40^{o}C, using a 5% perchloric acid, 35% 2-butoxyethanol, 60% methanol solution.

Immediately after electropolishing, the thin foils were thoroughly rinsed with methanol and examined using optical microscopy. Foils with minimal etching and with smooth central holes were selected for TEM to avoid tearing of the specimen during heating.

The hot stage was a GATAN model 628 Single Tilt Heating Holder, with a tantalum furnace. A schematic diagram of the heating holder and a photograph of the holder when a specimen is loaded are shown in figure 3.21. When loaded into the hot stage, specimens were held between two Ta spacers and secured with a hex ring. The hex ring was tightened by hand, using minimal force, ensuring that there was no movement of the specimen when the hot stage was tilted. However, there was likely to be some variation in the quality of the thermal contact between holder and specimen across multiple samples. The temperature was measured with a platinum – 13% rhodium/platinum thermocouple spot welded to the side of the furnace. The relative position of the thermocouple and the area of observation is depicted in figure 3.1. Upon insertion into the microscope the model 628.09J water recirculator was attached and switched on for a minimum of 20 minutes before the heat treatment began.

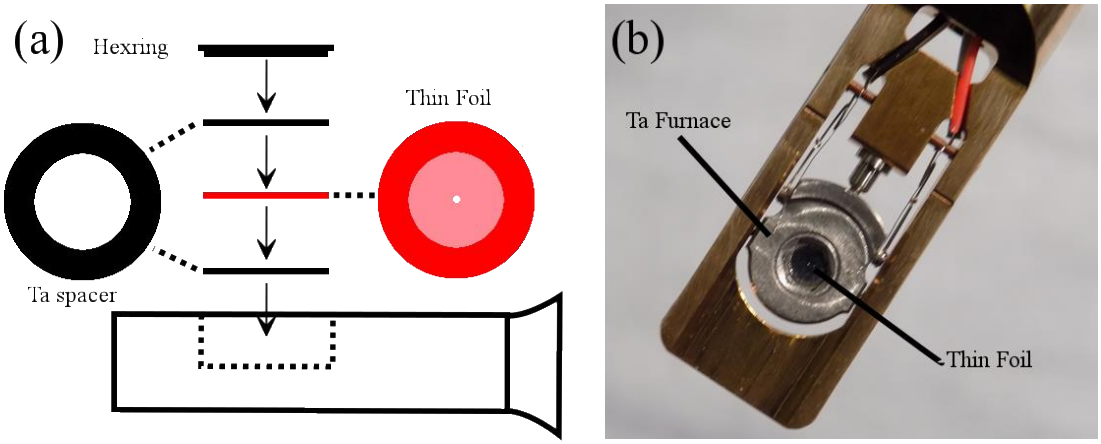

Figure 3.21: (a) Schematic diagram of the insertion of the thin foil specimens into the heating holder. The geometry of the thin foil and Ta spacers is shown in profile and from above (b) Photograph showing the heating holder with a specimen inserted.

The hot stage was controlled using the GATAN model 901 SmartSet Hot Stage Controller. This controller allows the hot stage to be manually controlled via the control unit or by PC via a serial connection. The heat treatment was programmed using Python with the PySerial library. This used the SMART heating mode to adjust the temperature at regular intervals, whilst simultaneously collecting the measured temperature from the holder. The temperature data contained the time (in hh:mm:ss format), the measured temperature (in ^{o}C) and the heater current (in mA).

An example of the programmed heat treatment is shown below in figure 3.22. The specimen was first heated to 870^{o}C, before being cooled to the selected T_2 temperature (in this case 840^{o}C). The cooling rate of this initial temperature drop was 0.7-1.6C/s the temperature was then cycled between T_1 and T_2 with achieved heating and cooling rates of 0.14-0.143C/s (8.4-8.6C/min), before cooling to room temperature.

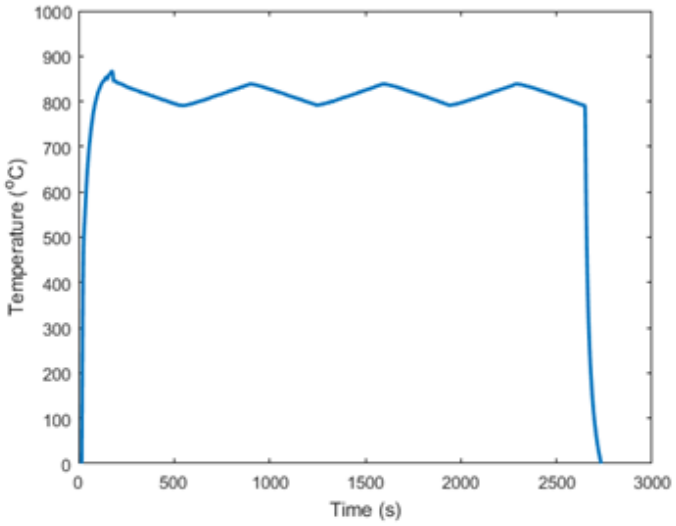

Figure 3.22: Example of the applied CPPT heat treatments. In this case the selected T_1 and T_2 temperatures were 790°C and 840°C respectively and the heating/cooling rate was ±8.6°C/min.

Video was recorded using the TVIPS CCD camera attached to the JEOL 3010 microscope. During recording the exposure time was set to 100ms. .TIF files of the individual frames were exported from the TVIPS software and assembled into a .AVI file using the FIJI (FIJI is just ImageJ) software. The final frame rate of the video was approximately 6fps, with a 45-minute heat treatment corresponding to around 16,000 individual frames.

Selected images of the starting microstructures were obtained using the JEOL JEM-F200 Transmission Electron Microscope operated at in TEM mode 200kV, spot size 1 with a 200 µm condenser aperture. TEM-EDS analysis was carried out using spot size 7 and a 10 µm condenser aperture. STEM-EDS analysis and EELS thickness measurements were made using the JEM-F200 operated in STEM mode at 200kV, probe size 6 and with a 40 µm condenser aperture. The F200 was equipped with a GATAN OneView camera and a GATAN Quantum K2 GIF.

3.2.1 Calibration of Heating Holder.

An initial attempt was made to estimate the temperature at which the ferrite to austenite phase transformation occurred using 99.8% pure Fe. For a furnace type hot stage, calibration using a single point to check the accuracy of the read out is generally

considered sufficient [143]. The temperature was increased to 1000°C using both controlled heating rates of 100-200C/min and using the maximum achievable heating rate of 330C/min. In addition, a stepwise heat treatment was applied where the temperature was increased with 5 minutes between each increment. However, no transformation was seen to occur even at the maximum temperature of the heating holder, this suggested that there was a difference between the specimen temperature and the nominal temperature on the order of 100C.

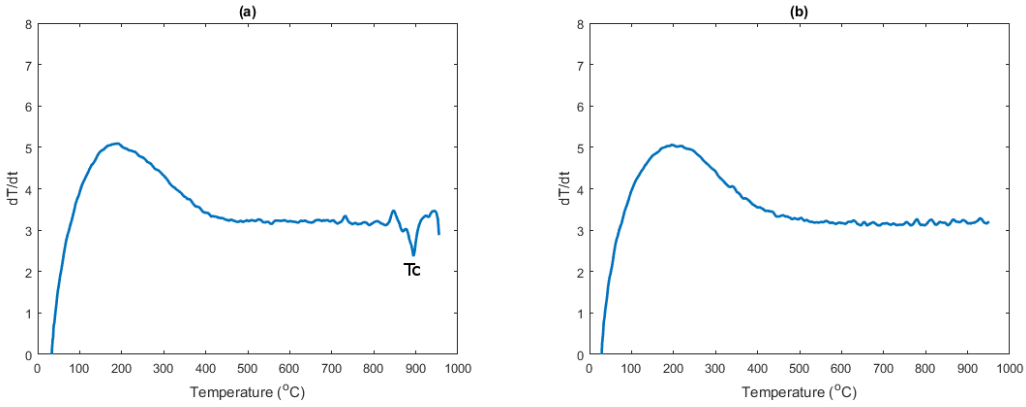

Figure 3.23: Graph of dT/dt against Temperature for (a) Fe and (b) Ni.

Figure 3.23(a) shows the temperature data, with a highly localised reduction in the rate at which the temperature increased during the controlled heating. There is a large increase in heat capacity around the Curie temperature in Fe of 27 $Jmol^{-1}K^{-1}$ [144] (from 45 $Jmol^{-1}K^{-1}$ at 950K to approximately 72 $Jmol^{-1}K^{-1}$ at 1043K). Given the low thermal mass of the holder system, T_c was therefore expected to manifest as a drop in the rate at which the temperature was increasing. The difference between the nominal temperature and the actual temperature of the specimen could therefore be estimated by comparing the temperature at which the rate of heating decreased and T_c. 7 thin foils were subjected to heating at a constant rate to 950°C at heating rates of 100-200C/min. The average temperature difference calculated was 130 ± 7°C (standard errors). Throughout this thesis, unless otherwise indicated temperatures have been adjusted such that $T = T_{nominal} - 130$.

To ensure that this was a property of the specimen and not of the heating holder, pure Ni specimens were also prepared and subjected to the same heat treatment. An

example of the outcome of one such heat treatment is shown in figure 3.2(b). No localised decrease in dT/dt was found.

The difference was confirmed using Fe-0.1C-0.5Mn specimens. Experiments performed assuming no difference between the specimen temperature and the nominal temperature did not result in successful cyclic experiments. Furthermore, by manually adjusting the temperature in the 970-980^{o}C range, it was possible to observe static austenite-ferrite interfaces. This indicates that there was a significant difference in temperature (>100C) between the specimen and the holder.

3.2.2 Foil Thickness

The thickness of the thin foils with a composition of Fe-0.1C-0.5Mn was measured using EELS in the JEM-F200 TEM, operated in STEM mode, probe size 6, a 40 µm condenser aperture and a camera length of 150 mm. Under these conditions the convergence semi-angle, α, was 5 mrad and the collection semi-angle, β, was 12 mrad.

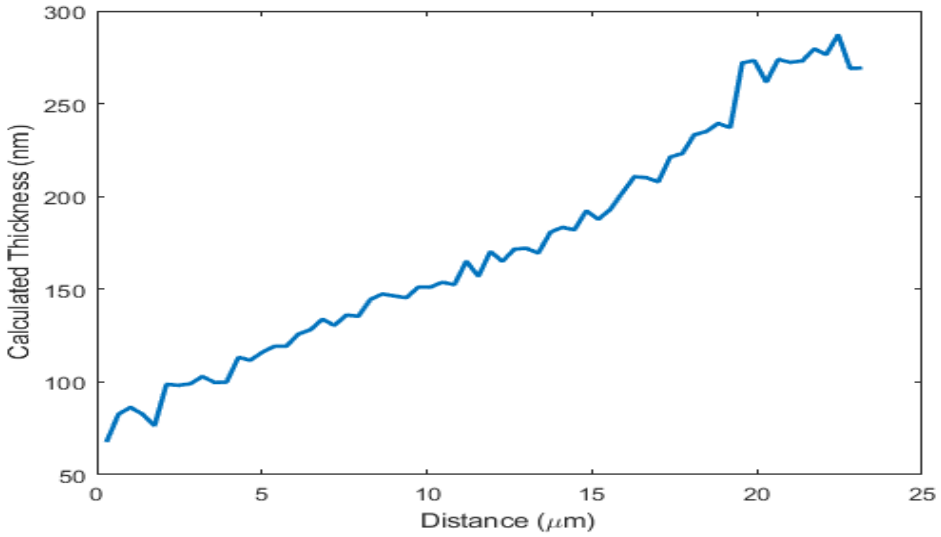

Figure 3.24: Thickness profile for a typical region. Step size is 0.363 µm.

A profile of the calculated thickness against length is shown in figure 3.24 for a typical region in a pre-heat treated specimen. The thickness was measured along a length of 22.8µm, comparable to the migration distance during intercritical annealing reported

in chapter 4, in a direction more or less normal to the hole in the foil. The log ratio measurement, t/λ, where t is the specimen thickness and λ is the inelastic mean free path of electrons in the material, increased from 0.67 to 2.7 along this length. The mean free path of the electrons was calculated given by equation 3.3 below.

$$\lambda = \frac{106F(\frac{E_0}{E_m})}{\ln(\frac{2\beta E_0}{E_m})} \quad (3.3)$$

Where F is a relativistic factor (0.618 for 200kV), E_0 is the incident energy, and E_m is the mean energy loss approximated by $E_m = 7.6Z^{0.36}$ where Z is the atomic number.

3.3 Dilatometry.

Cylindrical specimens with a length of 10mm and diameter of 4-5mm were heat treated using a DIL 805D dilatometer, in vacuum. The temperature difference across the specimen was monitored by spot welding thermal couples at the end and centre of the sample. In all cases, the temperature difference between the two thermocouples was less than 3C. Heat treatments were selected to match those which were used during hot stage TEM.

3.4 Optical Microscopy, Scanning Electron Microscopy and Electron Backscatter Diffraction.

Bulk specimens were prepared for optical and SEM imaging using standard grinding and polishing techniques, with a final polishing stage of colloidal silica, before etching with 2% Nital. Thin foils, examined after heat treatment, were mounted on pin stubs using carbon stickers.

FEI Nova NanoSEM 450 and InspectF scanning electron microscopes, operated at 20kV, spot size 3 and 5, were used for secondary electron and back scattered electron imaging. The NovaNano450 was also equipped with an Oxford instruments NordlysMax^3 EBSD detector and was used for EBSD analysis of texture. For the post heat treatment foils, a step size of 0.7μm was used and the total area was 160 x 120 μm immediately adjacent to the hole in the foil. For the pre heat treatment, a 500 x

400 μm region from the centre of specimen, in the same plane as the thin foil sections, was selected.

3.5 Thermodynamic and Kinetic Modelling.

The well-known Thermo-Calc and DICTRA software package [145] was used for the calculation of the thermodynamic and kinetic data of the materials under examination. The TCFE8 and MOBFE3 databases were used.

For the DICTRA simulations an austenite grain size of 25 μm was chosen to simulate a 50 μm austenite grain size. The T_1 and T_2 temperatures and the heating/cooling rates (0.143 C/s or 8.6 C/min) were selected to match those of the TEM experiments. For Fe-0.1C-0.5Mn T_1 and T_2 temperatures were 790°C and 840°C respectively. For Fe-0.1C-1Mn the T_1 and T_2 temperatures were 770°C and 820°C. The corresponding T_1 and T_2 temperatures for the Fe-XC-1.5Mn-0.14Si alloys were 734°C and 789°C, 729°C and 779°C, and 720°C and 760°C for X= 0.183C, 0.263 and 0.330 respectively.

3.6 Analysis of Video and Measurement of Interface Velocities.

The two phases of interest, austenite and ferrite, were distinguished both during TEM operation and from analysis of the video after heat treatment. The most reliable method of determining the phase of a particular grain was selected area electron diffraction (SADP). An initial judgment could be made due to differences in the observed diffraction patterns. Even in cases where austenite and ferrite grains were both oriented with the same crystallographic direction parallel to the electron beam, the two phases could be visually differentiated due to differences in spacing of the diffraction spots. In all cases, the identity of the phase was subsequently confirmed by indexing the diffraction patterns captured on video. However, a judgement could also be formed on phase identity from the presence of large numbers of twin boundaries in the austenite, in contrast to ferrite grains where such twins were absent.

Still frames from the video were then sampled at intervals with a particular focus on extracting the position of the interface with reference to immobile features. No

processing of the images was carried out except for changes to the contrast and brightness. Alignment of these frames was carried out using the *Linear Stack alignment with SIFT* plugin for FIJI. The quality of this alignment was examined and if necessary manual alignment was carried out by importing frames into the GNU Image Manipulation Program (GIMP) as layers and aligning them with reference to any immobile features identified. Stepped twin boundaries, or multiple inclusions were preferred. Interface velocities were determined by measuring the distance travelled more or less normal to the interface migration between frames. This was done for a single observed section of interface at regular intervals of 500nm along the visible section.

Due to the migration distances involved it was necessary to move the stage in order to track the moving interface. Throughout this thesis features that were observed to be immobile from the video, such as inclusions or twin boundaries, are highlighted where possible using black arrows in the figures. These black arrows therefore indicate common positions between frames and provide an indicate of how the image has been translated between frames.

3.7 TEM Artefacts.

3.7.1 Thermal Grooving and Surface Diffusion.

As seen in chapter 2, it is likely that thermal grooves will develop at locations where the grain boundaries intersect the foil surface during high temperature experiments. Potentially these grooves can have an impact on the experimental observations by pinning boundaries. However, they can also be used to estimate the surface diffusion coefficient for Fe.

Thin foils with a composition of Fe-0.1C-1.6Mn-0.5Mo were prepared by electropolishing in the same way as described in chapter 3.1. This material was selected as no phase transformation was observed during isothermal holding at 870^{o}C. Foils were inspected using an optical microscope to ensure that there was no significant etching of the surface. Each foil was examined using a ContourGT

scanning interferometer to measure the roughness average of the surface at multiple random locations.

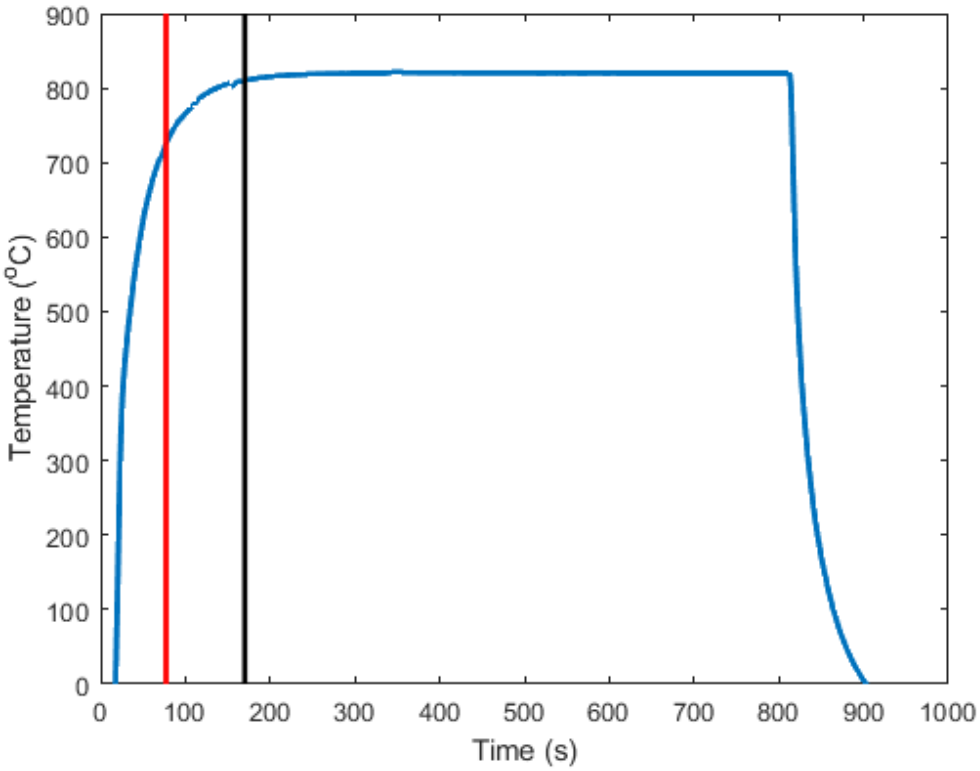

Figure 3.25: Graph of temperature against time for a typical heat treatment used to estimate the surface diffusion coefficient. Vertical red and black lines indicate the time at which the temperature had reached within 10% and 1% of the target temperature respectively.

Samples were heat treated in the TEM using the GATAN model 628 heating holder. To ensure that there were no additional sources of heat, the microscope filament was not switched on and the objective aperture was not inserted. Specimens were heated at the maximum heating rate of approximately 5 C/s to nominal temperatures of 770, 820 and 870°C, held at this temperature for 10 minutes before the heater was switched off and the sample was allowed to cool. A typical heat treatment of this kind is shown in figure 3.25. For the experiments in chapter 4 and 5, 10 minutes corresponds approximately to one T_1-T_2-T_1 cycle.

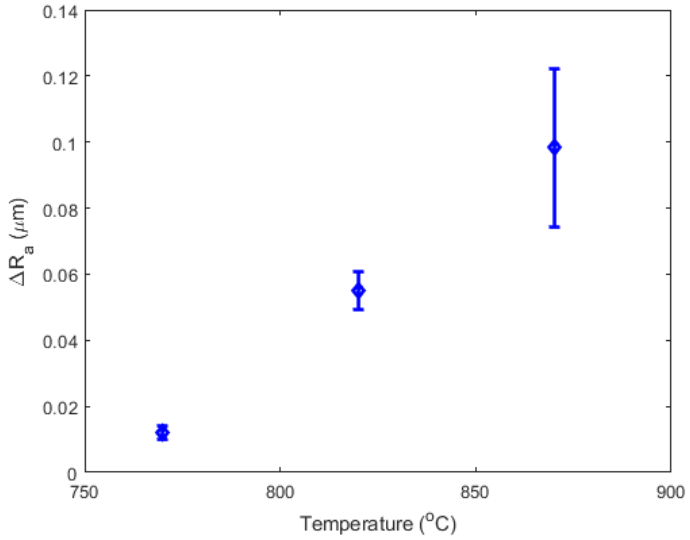

Figure 3.26: Graph of the increase in the roughness average against target temperature during isothermal holding for 600 seconds.

Post-heat treatment foils were then examined using the scanning interferometer to assess the width of those thermal grooves that had developed and the overall effect this had on surface roughness.

Figure 3.26 shows the average roughness (in μm) increase after 10 minutes holding at 770-870ºC. It can be seen that for specimens where there is no phase transformation and grain boundaries or interfaces remain static, thermal grooving on the surface was significant.

The distance between peaks was determined at 770, 820 and 870ºC for multiple thermal grooves. This was used to calculate the average surface diffusion coefficient for Fe using equations 3.4 and 3.5:

$$s = 4.6(Bt)^{1/4} \tag{3.4}$$

Where s is the peak spacing of the groove, t is time. B is given by equation 3.5:

$$B = D_s \gamma \Omega^2 \frac{v}{k_b T} \tag{3.5}$$

Where D_s is the surface diffusion coefficient, γ is the surface energy, Ω the molecular volume, v is the surface atom density, k_b is the Boltzmann constant and T is the

temperature. For the present calculation, it is assumed that the surface is parallel to the (001) plane, and that the surface energy is 2.1 $J \cdot m^{-2}$ [148].

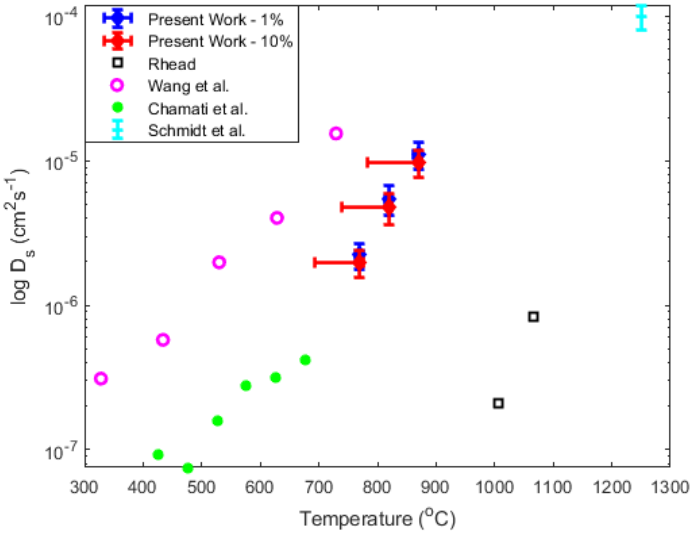

Figure 3.27: Graph of the estimated surface diffusion coefficient of Fe against temperature.

The time, t, used to calculate the surface diffusion coefficient was the time that the temperature was within 1% and 10% of the isothermal holding temperature. Figure 3.27 shows the surface diffusion coefficient for Fe. In this temperature range the surface diffusion coefficient is on the order of 10^{-5}-10^{-6} cm^2s^{-1}. This is compared with the surface diffusion coefficient for Fe in Rhead [149], diffusion of adatoms on Fe (100) in molecular dynamics simulations by Wang et al. [150] and Chamati et al. [151] and as estimated from thermal grooving of Fe in HT-CLSM by Schmidt et al [129]. The current estimates are within the range expected from literature values.

3.7.2 Thermal Radiation.

During hot stage TEM, the heat loss in the specimen is primarily due to radiation from the foil surface. Consequently, this may result in a thermal gradient across the specimen from the unpolished surface which is in contact with the heating holder and the thin areas around the hole, due to the changing surface to volume ratio.

A first order assessment of this temperature difference was made using the finite element analysis software package ANSYS. The profile of the simulated foil is shown in figure 3.28 below. The maximum and minimum thicknesses are 100 μm and 0.1 μm respectively. These were then rotated about the central axis to create a 3 mm disc.

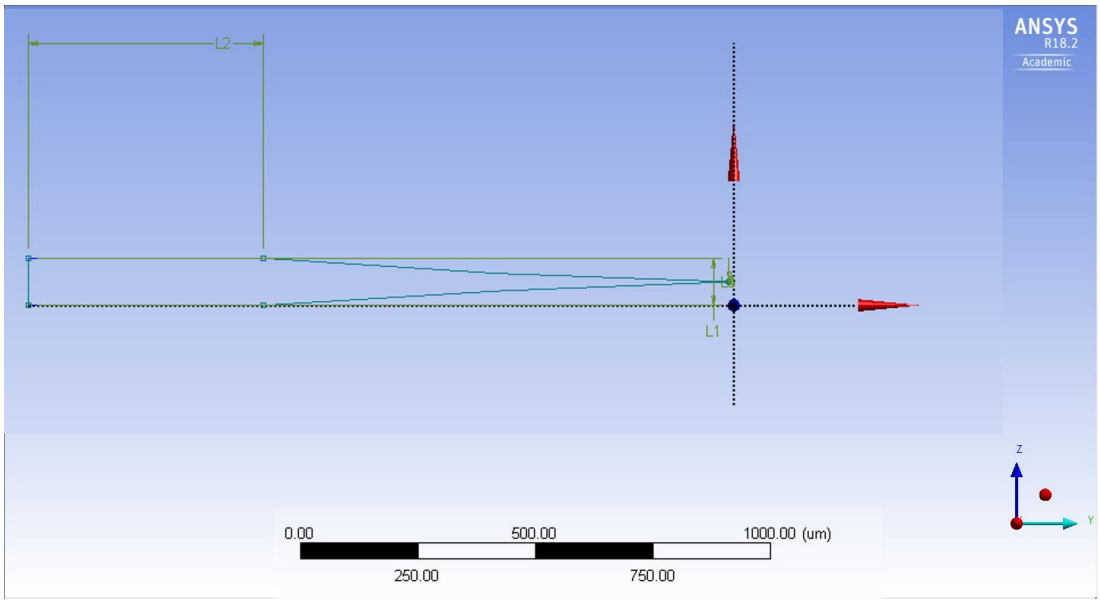

Figure 3.28: The dimensions of the simulated thin foil.

Simulations were carried out assuming no heat loss due to convection, that the thick (unpolished) regions of the foil were all at temperature, and assuming either that the material in question was a black body radiator or using a lower emissivity. Švantner et al. [152] found an emissivity of 0.17 at 250°C for an unoxidized AISI 1015 surface at wavelengths of 2.5-20μm. The composition range of AISI 1015 is close to the Fe-0.1C-0.5Mn used in this thesis. For an oxidised surface at 250°C emissivity was approximately 0.83. For wavelengths between 7.5 μm and 13 μm there was only a small (0.02) increase in emissivity for an oxidised surface at 1020°C compared to 250°C. An emissivity of 0.17 was chosen for the ANSYS simulations. This is a valid choice under two assumptions. First that the total emissivity of the thin foil surface varies with temperature in a comparable manner to an oxidised surface in the 7.5-13 μm range. Second that the surface roughness does not affect emissivity. The electropolished thin foil specimens used in the TEM experiments are likely to be significantly smoother than the billets used by Švantner et al. A thermal conductivity

of 30 $Wm^{-1}k^{-1}$ was selected for the material [153]. The ambient temperature was assumed to be 22°C, a higher ambient temperature would result in a smaller temperature difference across the specimen.

The results of the simulations are shown in figure 3.29 below. The high (assuming a black body) emissivity simulation produced a temperature difference of 37.4C between the thickest and thinnest regions at 840°C (the highest selected T_2 temperature). The low emissivity simulations produced a temperature difference of 6.9C.

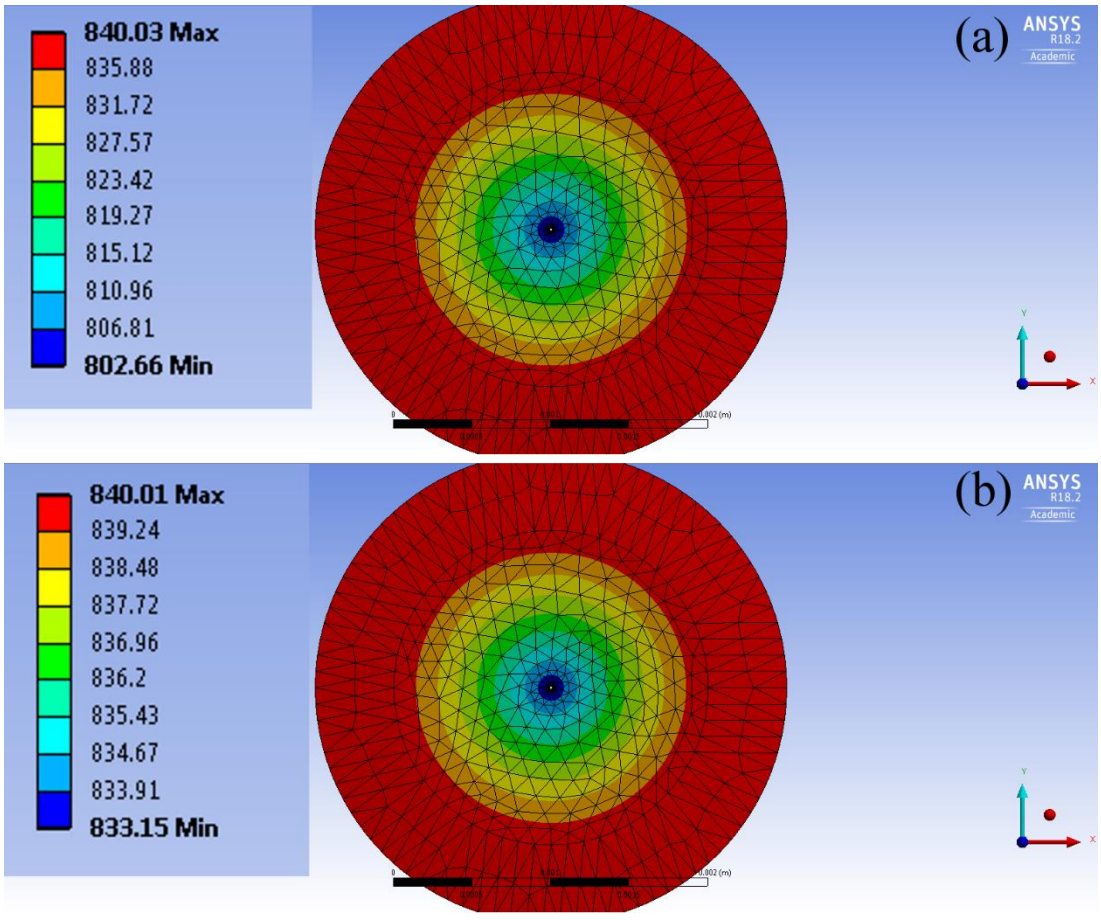

Figure 3.29: Showing the temperature difference across a thin foil modelled using ANSYS assuming (a) an emissivity of 1 and (b) an emissivity of 0.17.

These simulations provide an upper limit for any temperature difference which occurs during in situ TEM experiments as a result of the changing surface area to volume ratio of the thin foils and an indication of the likely magnitude of any thermal gradient

in the observed regions of the specimen. The upper limit, assuming the specimen acts as a black body, implies a ~40C difference. At a lower emissivity, the difference is reduced to less than 10C. This occurs over a distance of approximately 1 mm, indicating that the change in temperature experienced by a migrating interface (predicted migration distances are <50 μm) is likely to be negligible.

4. Cyclic Partial Phase Transformation Experiments: Fe-0.1C-0.5Mn.

4.1 Introduction.

The first composition on which cyclic experiments were performed was the Fe-0.1C-0.5Mn steel. In the past, phase transformations in steels with this composition have been the subject of multiple studies using both modelling and experiments [154] [155]. Transformation behaviour of 0.1C-0.5Mn steels during cyclic partial phase transformations was also a focus of previous studies [156, 87].

Experiments were performed on a total of 5 specimens. Of these, three were successfully cycled within the two-phase region. In the case of one of these experiments the results were only partially valid because of the effect of thermal grooving on the interface behaviour, discussed in greater detail below. The remaining specimens became fully austenitic on heating to 840^{o}C, the higher T_2 temperature in the cycle, indicating that there was some variation in temperature between individual specimens.

The primary intended outcomes of these experiments were to confirm the reversible motion of the interface and to observe the interface behaviour during cycling. Of particular interest is how the interface morphology developed over the course of the thermal cycle, and how the interface behaved during and immediately after the stagnant stage.

It was expected that this composition would display the highest interface velocities and the shortest inverse transformation and stagnant stage. This is because, of the alloys for which observations are report in this thesis, this composition contains the lowest levels of manganese.

In this chapter the results of the *in situ* TEM experiments are presented along with data from dilatometry and kinetic modelling. Interface migration was captured for multiple interfaces throughout the cycle, and behaviour corresponding to the normal transformation, inverse transformation and stagnant stage in dilatometry was identified.

4.2 TEM Experimental Outline.

Table 4.1 shows the experiments performed. Experiments 4.2 and 4.4 are considered failures. In both cases the heat treatment did lead to the formation of austenite-ferrite interfaces, however, the electron transparent regions of the specimens became austenitic on heating to the T_2 temperature. Consequently, the specimens did not undergo a partial phase transformation with the programmed heat treatment. This may be due to variations in the quality of the thermal contact between the holder and the specimen. As noted in chapter 3, the hot stage measured the temperature through a thermocouple spot-welded to the furnace body. Furthermore, some temperature differences were observed between the pure Fe specimens in chapter 3.1.1. Some variation in temperature between specimens is therefore expected in the present experiments. For this composition, where the temperature difference between the A_3 and T_2 temperature is approximately 15C, this variation could be reasonably expected to result in the electron transparent area becoming austenitic. This does not necessarily mean, however, that the entire specimen (including the non-electron transparent region) was completely austenitic.

Table 4.1: Table of the number of experiments performed, indicating whether the specimen was successfully cycled in the two-phase region.

Experiment Number	Success/Failure	Notes
4.1	Partial Success	Experimental Artefacts
4.2	Failure	Fully γ at T_2
4.3	Success	
4.4	Failure	Fully γ at T_2
4.5	Success	

Experiments 4.3 and 4.5 were both successes. The video obtained from experiment 4.5 was superior in terms of image quality and ability to consistently measure interface position. Finally, experiment 4.1 was considered partially successful as the cooling stage of the cycle was affected by experimental artefacts, in this case thermal grooving, discussed in more detail in chapter 4.16.

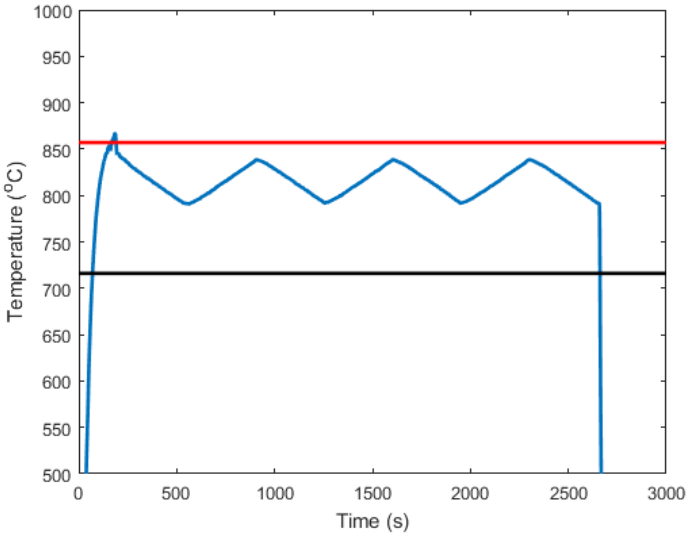

Figure 4.1: Graph of the imposed heat treatment used for all specimens of this composition, with the upper and lower limits of the two phase region depicted by red and black lines respectively.

The programmed heat treatment which was used for all 5 specimens is shown in figure 4.1. Throughout this chapter, unless otherwise noted, all temperatures from the TEM are adjusted in line with the calibration carried out in chapter 3.1 where $T = T_{nominal} - 130$. The T_1 and T_2 temperatures used as the lower and upper temperatures during thermal cycling were 790°C and 840°C respectively. These temperatures were selected because they are both within the two phase α+γ region and because the respective transformations on heating and cooling are expected to be governed by LE-NP kinetics. The change in equilibrium volume fraction of ferrite between these two temperatures was approximately 0.4, as determined from Thermo-Calc. The same programmed heat treatment, including the same T_1 and T_2 temperatures and the heating/cooling rate, was used in dilatometry experiments presented in chapter 4.3.

Bright field TEM images of the starting microstructures are shown in figure 4.2. The microstructure consisted of regions of bainitic ferrite alongside allotriomorpic ferrite grains, some of which contained a carbides precipitates within the grain. The diffraction pattern in figure 4.2(d) identifies these particles as Fe_3C, and shows that the foil surface is otherwise clear of oxides.

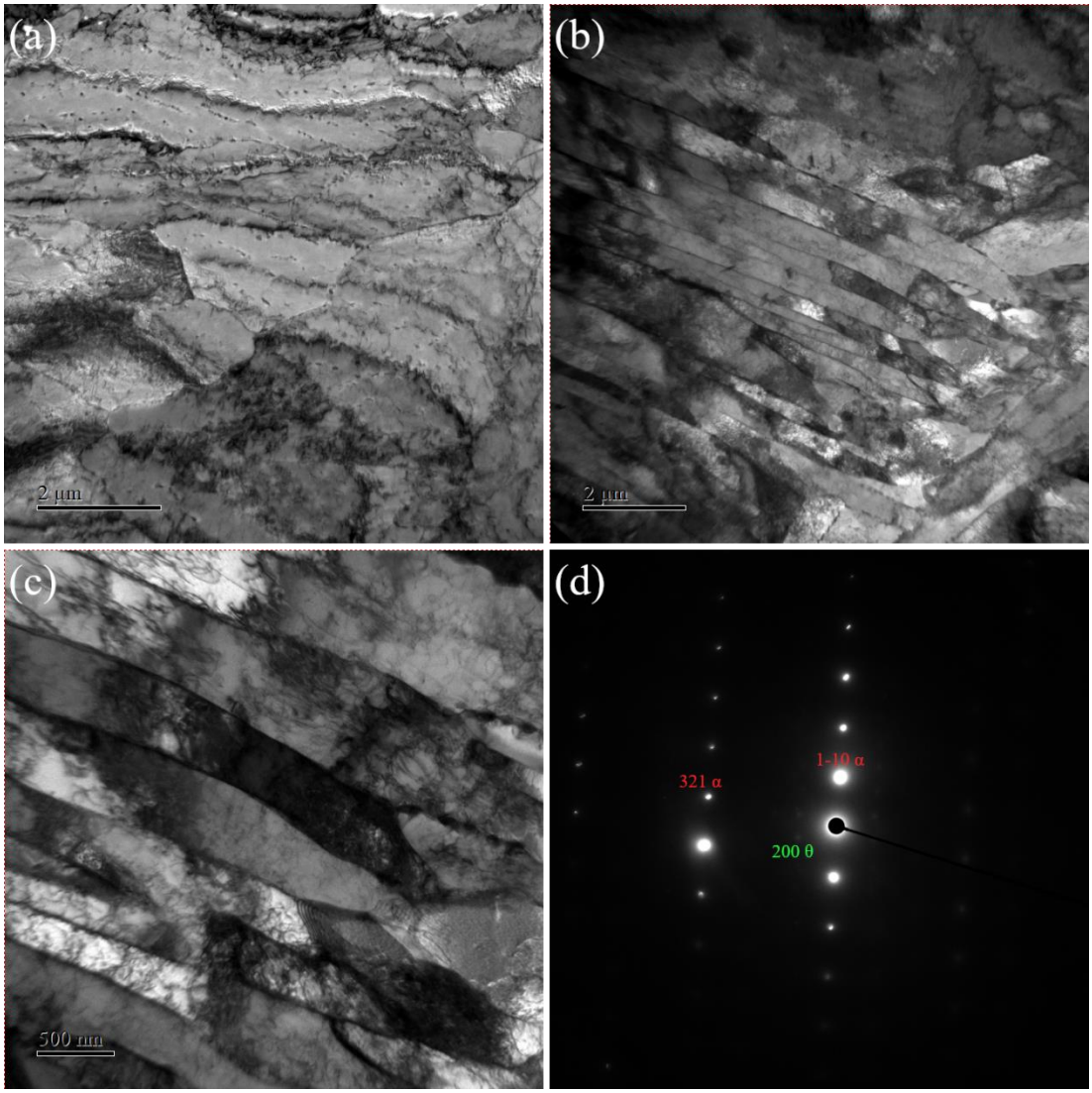

Figure 4.2: Bright Field TEM images of the starting microstructures of the Fe-0.1C-0.5Mn foils, showing the ferrite regions, with Fe_3C precipitates within the ferrite grains (a), bainitic ferrite regions (b-c) and (d) selected area diffraction pattern showing spots only for ferrite and Fe_3C, but otherwise free of surface oxidation.

4.3 Dilatometry.

The thermal profile from the TEM experiments was also used with dilatometry in order to put the TEM observations into perspective. Dilatometry experiments using cyclic partial phase transformations are easier to interpret, as the transformation behaviour of the entire specimen during CPPT experiments can be analysed from the dilation. Furthermore, this can be compared with previous studies and modelling.

Figure 4.3 shows the results of the dilatometry experiments. The dilation curve shows all the expected features of a cyclic partial phase transformation including the normal

transformation (blue arrow), the inverse transformation (green arrow) and the stagnant stage (red arrow). The three cycles match relatively well, although there is some persistent change in the length of the sample as the heat treatment progresses. On cooling the length of the specimen had changed compared to the starting length and this, along with the change between cycles, is attributed to transformation plasticity. In the case of cyclic partial phase transformation experiments, it is assumed that the interface migrates over the same region in each cycle, and that no nucleation occurs. This assumption is supported by HT-CLSM experiments [88].

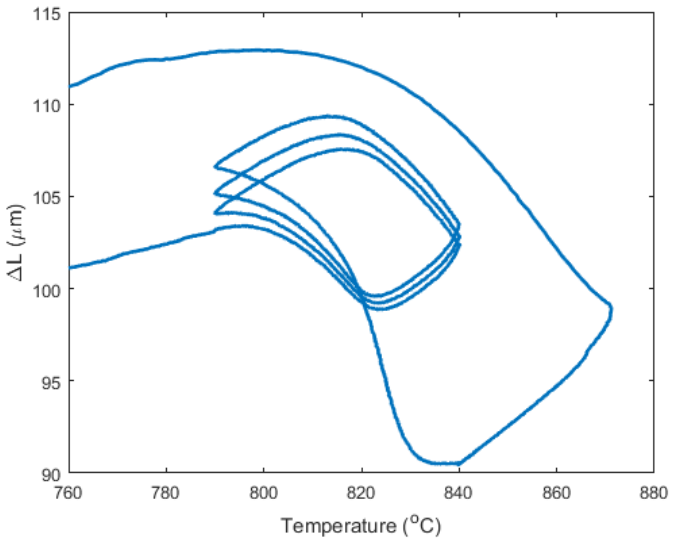

Figure 4.3: Graph of Dilation against Temperature for Fe-0.1C-0.5Mn steel undergoing cyclic heat treatment.

A first approximation of the volume fractions of austenite and ferrite at each point can be extracted from the dilatometry curve using the Lever rule. Some caution is necessary when interpreting this as the steel is a ternary alloy, the dilatometry curve is not a closed loop and some transformation plasticity is apparent in the curve. However, the volume fraction can be used to provide an indication of how far the interface can be expected to migrate in the TEM. This estimate is compared with the migration expected from simulations performed using the DICTRA software package.

For a direct comparison with the TEM velocities it is also useful to use the volume fraction information to estimate the expected velocities of interface migration during

the cycle. Equation 4.1 [46] below, shows how the average interface velocity is related to the change of the volume fraction:

$$\frac{df_\alpha}{dt} = 3(N^* g)^{\frac{1}{3}}(1 - f_\alpha^2)v_\alpha arctanh^{\frac{2}{3}}(f_\alpha) \quad (4.1)$$

Where v_α is the interface velocity, df_α/dt is the rate of change in the volume fraction over time, f_α is the volume fraction, N^* is the nuclei density and g is a geometric factor (where g=1 for cubic nuclei and g = 4π/3 for spherical).

This kinetic model assumes interface-controlled growth, site saturation and includes a hard impingement correction for a situation intermediate between periodic and randomly dispersed particles. A similar equation can be derived for diffusion-controlled growth [157], which in this situation yielded the same results.

The nuclei density was obtained from metallography using the standard linear intercept method to calculate grain size [158]. However, this technique is known to underestimate the grain size, with the true grain size being a factor of 1.5x larger [159] [160]. A ferrite grain size of 40 ± 2 μm was used resulting in a nuclei density of N* = $1.61*10^{13}$.

Using the lever rule, the change in the volume fraction was from approximately 0.65 to 0.3, a change of 0.35, as shown in figure 4.4(a). Figure 4.4(b) and (c) shows the change in interface position, estimated using equation 4.1, assuming cubic (b) and spherical (c) geometry. The average change in the interface position across all cycles was 9 μm for cubic geometry and 5.6 μm when spherical nuclei are assumed. For comparison, a 1-D ferrite grain growing into an austenite grain 40 μm long and undergoing a similar change in ferrite fraction would have a change in position of 14 μm.

Estimates of the temperature range of each feature is made from figures 4.3 and 4.4. These are presented in table 4.2 below. One of the stagnant stages occurs on heating and another on cooling. The small difference in the temperature range of the normal transformation is due to differences in carbon diffusivity in the ferrite and austenite phases.

Table 4.2: Table of the estimated temperature interval for each feature of a cyclic partial phase transformation on heating and cooling.

Feature	Heating	Cooling
Normal transformation	32C	31C
Inverse Transformation	2C	4C
Stagnant Stage	16C	15C

The estimated velocity for cubic and spherical growth is shown in figure 4.5. The maximum velocity was estimated as 52 $nm \cdot s^{-1}$ (cubic geometry) and 32 $nm \cdot s^{-1}$ (spherical geometry) for the austenite to ferrite transformation. This velocity occurred between 814-816^{o}C, shortly after the end of the stagnant stage, but with over 40% of the cooling cycle remaining. Thereafter the temperature steadily decreased for the remainder of the normal and inverse $\gamma \rightarrow \alpha$ transformations. Conversely, for the ferrite to austenite transformation the velocity steadily increased to a peak of -66 $nm \cdot s^{-1}$ and -40 $nm \cdot s^{-1}$ (for cubic and spherical growth respectively) at the T_2 temperature. It then decreased rapidly during the inverse $\alpha \rightarrow \gamma$ transformation.

This provides a first order estimate of the position and velocity of the average interface in the bulk specimen for comparison with the TEM observations. It shows that on heating the driving force for the ferrite to austenite transformation continually increases with increasing temperature. In comparison, on cooling there is an initial period of rapid migration caused by the increased driving force for the austenite to ferrite transformation as a result of the sluggish interface movement during the stagnant stage.

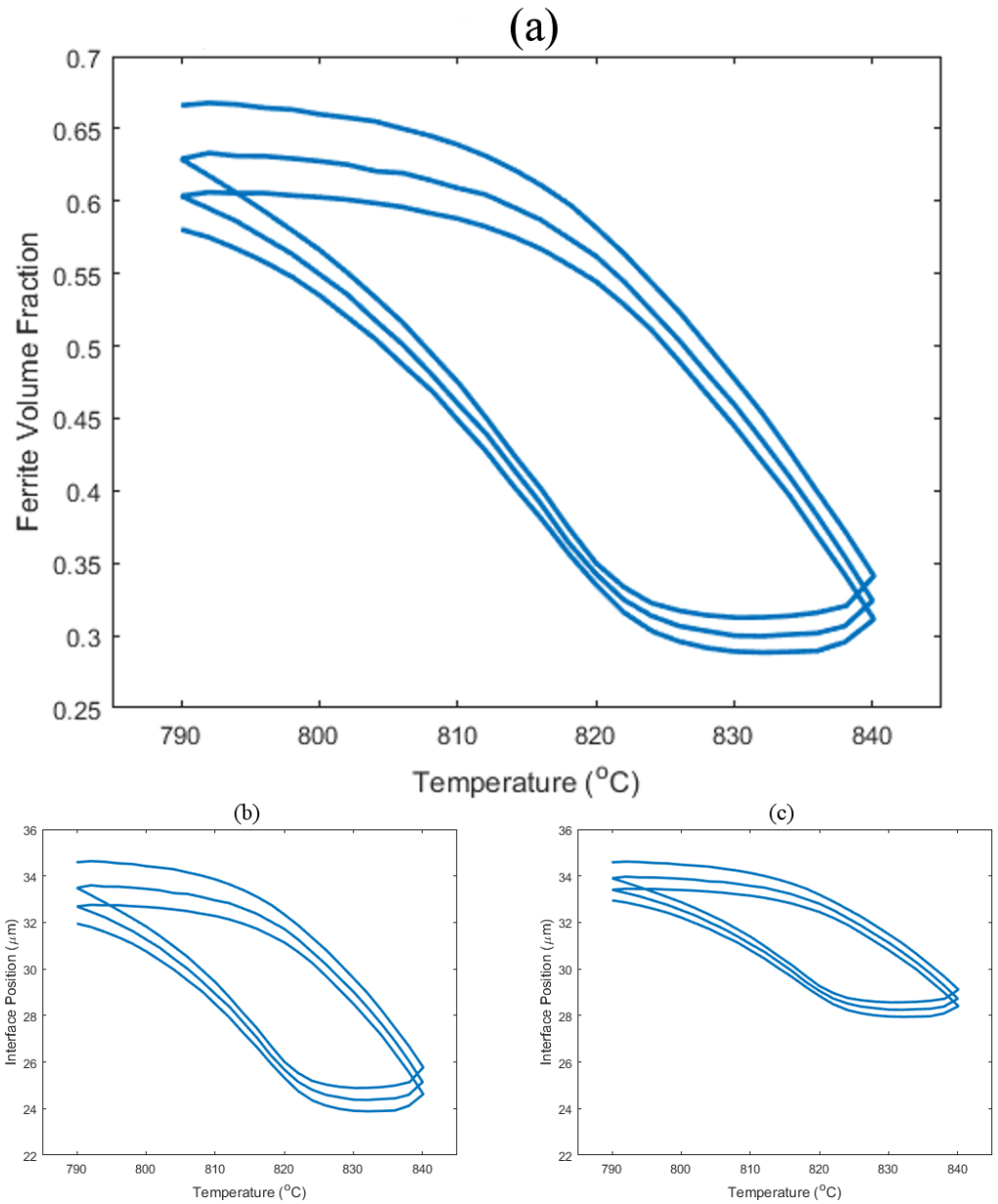

Figure 4.4: Graphs of (a) Ferrite Volume Fraction against Temperature (b) Interface Position against Temperature (cubic geometry) and (c) Interface Position against Temperature (spherical geometry).

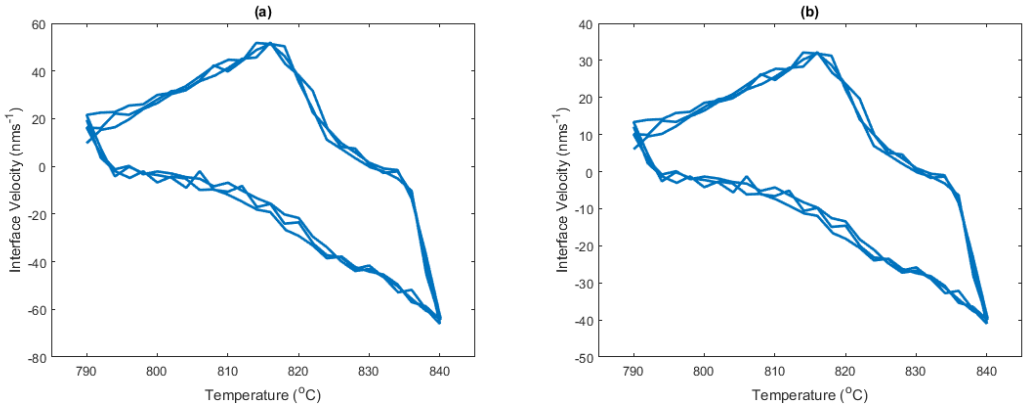

Figure 4.5: Graphs of the interface velocity against temperature for (a) cubic geometry and (b) spherical geometry. Note: the interface velocity for the ferrite to austenite transformation are negative.

4.4 Kinetic Modelling.

The cyclic partial phase transformation heat treatment was also modelled using the well-known DICTRA software [145]. The transformation was modelled using the standard local equilibrium assumptions, with a total austenite grain size of 25 µm and 40 µm. For comparison, this is equivalent to a real grain size of 50 and 80 µm when spherical geometry is assumed. The interface velocities and positions are shown in figure 4.6 below.

For the 25µm austenite grain, the peak velocity for the austenite to ferrite transformation of ~58.2 nm·s^{-1} occured at 814.9^{o}C. In the case of the ferrite to austenite transformation the peak velocity of 45.8 nm·s^{-1} occurred at the T_2 temperature. There is good agreement between the temperatures of the peak velocity between DICTRA and the dilatometry study for the ferrite to austenite transformation. Likewise, the peak velocity for the austenite to ferrite transformation shows a good match.

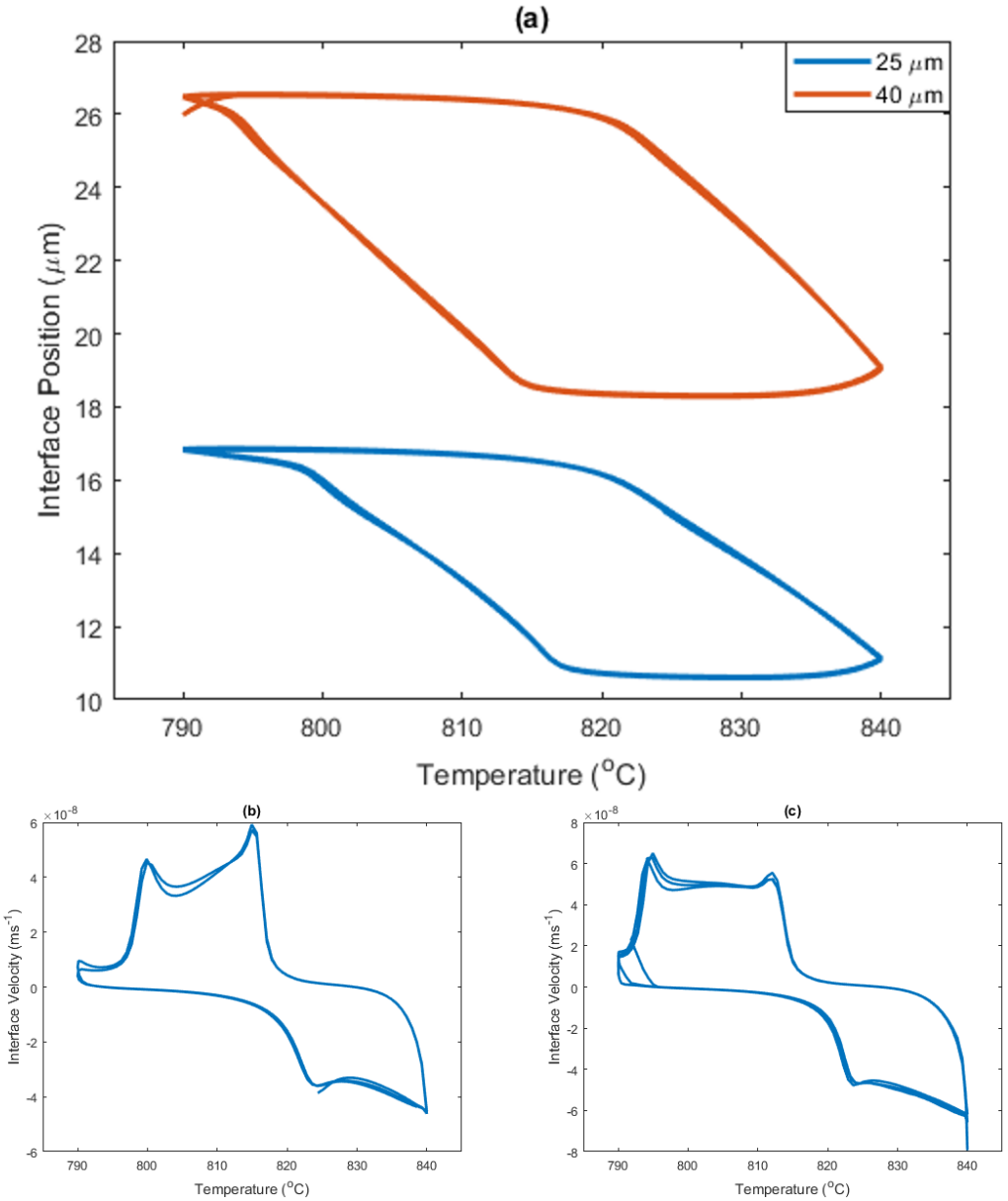

Figure 4.6: Graphs of (a) the interface position against temperature and the interface velocity against temperature for (b) a 25 micron austenite grain and (c) a 40 micron austenite grain simulated using DICTRA. Note: Ferrite to Austenite transformation velocities are negative.

The total change in position of the interface over the course of the cycle is 6.3μm, for the 25 μm case, and 8.7 μm for the 40 μm case. This is slightly smaller than that predicted by dilatometry for the cubic case. This is unexpected as previous studies have found that dilatometry typically produced lower migration distances than that predicted from kinetic modelling [4]. A key difference is that the motion of the interface is calculated only on the basis of diffusion-controlled growth. As noted in chapter 2, diffusion-controlled growth is one extreme of a behaviour ranging from

purely diffusion controlled to purely interface controlled growth [64]. In practice, therefore, the transformation will proceed with characteristics of both diffusion and interface-controlled growth [65]. This means that during experiments the limited mobility of the interface [43] can be expected to influence the kinetics.

The temperature range of each stage estimated from the DICTRA results is shown in table 4.3

Table 4.3: Table of the estimated temperature range of cyclic partial phase transformation features on heating and cooling

Feature	Heating	Cooling
Normal Transformation	33C	30C
Inverse Transformation	1C	4C
Stagnant Stage	16C	16C

Figure 4.7 shows the distribution of Mn at the interface during thermal cycling predicted by DICTRA. This depicts the differences in interfacial chemistry in the case of the two stagnant stages. During the austenite to ferrite transformation the interface is preceded by a Mn spike ahead of the interface [82], compared to a local depletion ahead of the interface during the ferrite to austenite transformation. These dissimilarities in interfacial chemistry are partly responsible for the different interface behaviour during the two stagnant stages.

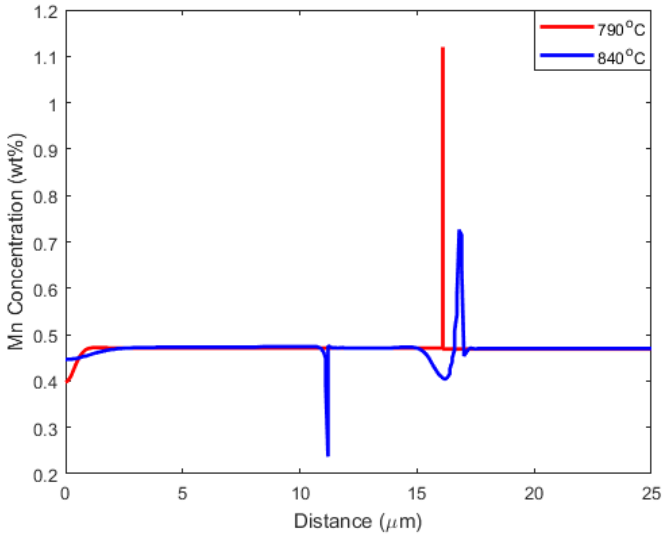

Figure 4.7: Graph of the Mn concentration (in wt%) at the interface for the T_1 and T_2 temperatures.

4.5 Initial Ferrite to Austenite Transformation.

Figure 4.8 shows the ferrite to austenite transformation during the initial heating of specimen 4.1. This part of the heating cycle is not analysed in detail as it is outside of the main topic of interest, and because the high heating rate made it difficult to acquire images of sufficient quality. The sequence is representative of other samples, although the velocities differed between samples. Figure 4.8(a) shows the relative position of the video frames 4.8(b-d). 4.8(b) shows the interface shortly after it appeared. 4.8(c) shows the interface after 11.8 seconds, and 4.8(d) the final position of the interface 19.6 seconds after it first appeared.

In each case, the austenite nucleated outside of the field of view before growing into the observed region. Figure 4.9 contains a plot of the temperature at which the austenite first became visible within the field of view for all samples, and when the transformation was completed in the observed region, alongside the thermodynamic range of the 2-phase region obtained from Thermo-Calc [145] using the TCFE8 database. As the specimen was being heated, the Ac_1 and Ac_3 temperatures were increased above the Ae_1 and Ae_3 temperatures. In addition, the limited field of view means that the ferrite to austenite transformation could be observed for only a relatively small region of the specimen, rather than the specimen as a whole. Considering this, the observed regions show the expected behaviour on initial heating.

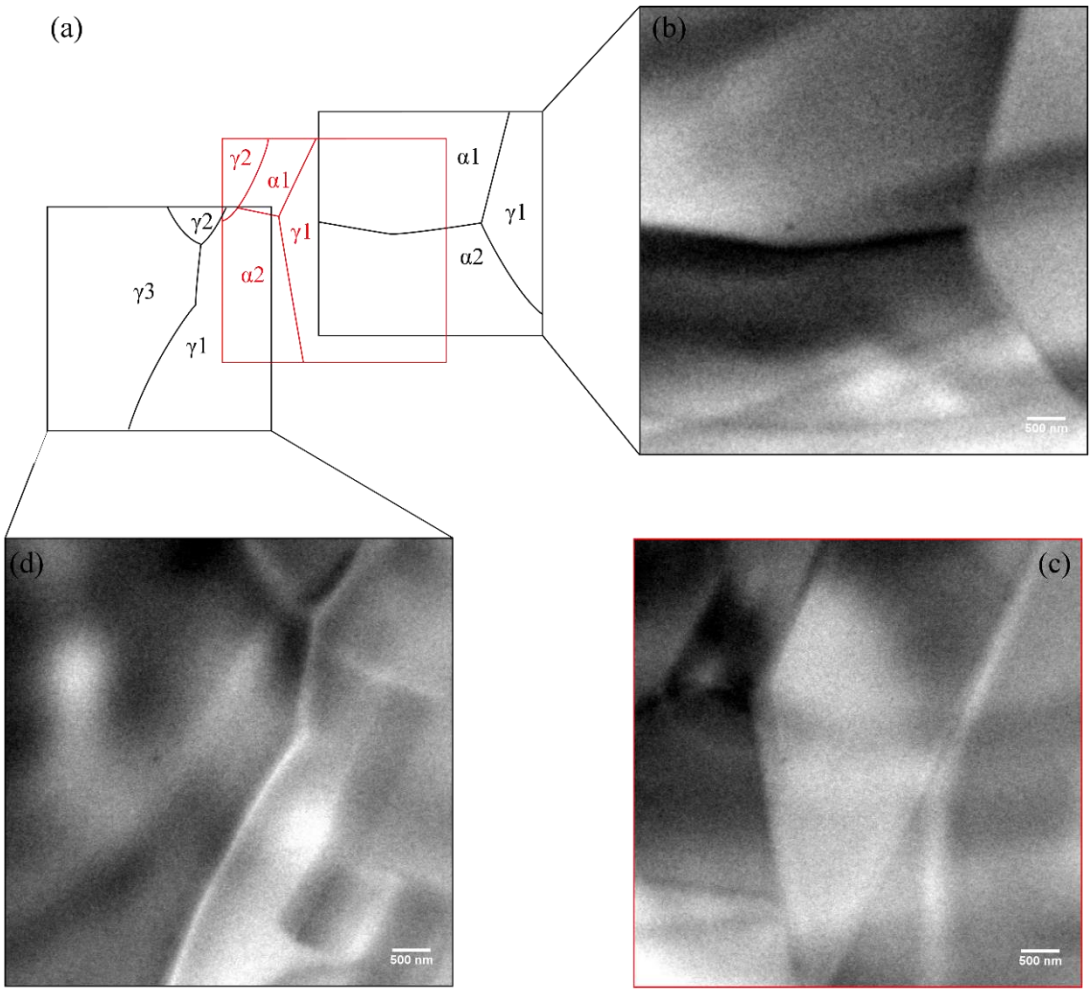

Figure 4.8: Bright Field TEM of the ferrite to austenite transformation showing (a) the relative positions of each frame (b) the first observation of the growing austenite grain at 97.0 seconds (805°C) (b) the interface at 108.8 seconds at 822°C and (d) the region after the transformation was complete, at 116.6 seconds (831°C). (Specimen 4.1).

The first austenite-ferrite interfaces were observed above the Ae_1 temperature and most of the observed regions had completely transformed into austenite by the time the temperature reached the Ae_3 temperature. For the remaining region, the transformation was completed less than 10°C above it. As noted above, this does not necessarily indicate that the specimen became fully austenitic at this temperature, as the field of view was a relatively small area (~25 μm^2).

There is clear variability between each specimen for both the start and finish temperatures. This may indicate not only some variation between specimens but also local differences within the specimen. Overall, however, most of the observed ferrite to austenite transformation took place within the predicted 2-phase region.

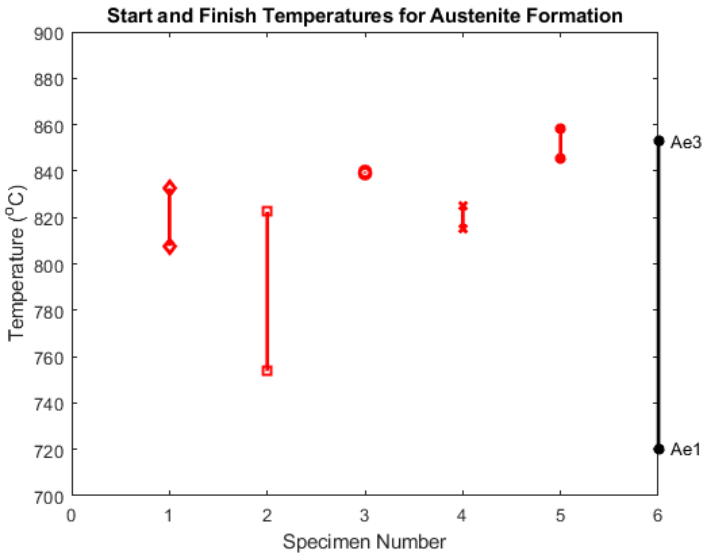

Figure 4.9: Graph of the start and finish temperatures of austenite formation within the field of view across all samples. The temperature range of the 2-phase region, as estimated using Thermo-Calc, is indicated in black at 6. Most of the observed austenite formed within the two phase region.

4.6 Austenitic Microstructure.

Between 820 and 860°C, the observed regions of all samples had fully transformed into austenite with a stable microstructure. The heating of the specimens continued until 870°C. No significant grain growth was observed in the fully austenitic region, even whilst heating to 870°C.

Figure 4.10 shows that the interfaces between the austenite grains consist of both curved and straight boundaries. The austenite grains were often clearly distinguishable from the ferrite because of the different contrast conditions, although final phase identification was carried out using selected area diffraction. These conditions made the observation of features within the austenite more difficult, and consequently it was rare to see dislocations in the austenite, although their presence can be confirmed from figure 4.10(b). In addition, the austenite can be seen to contain numerous growth twins.

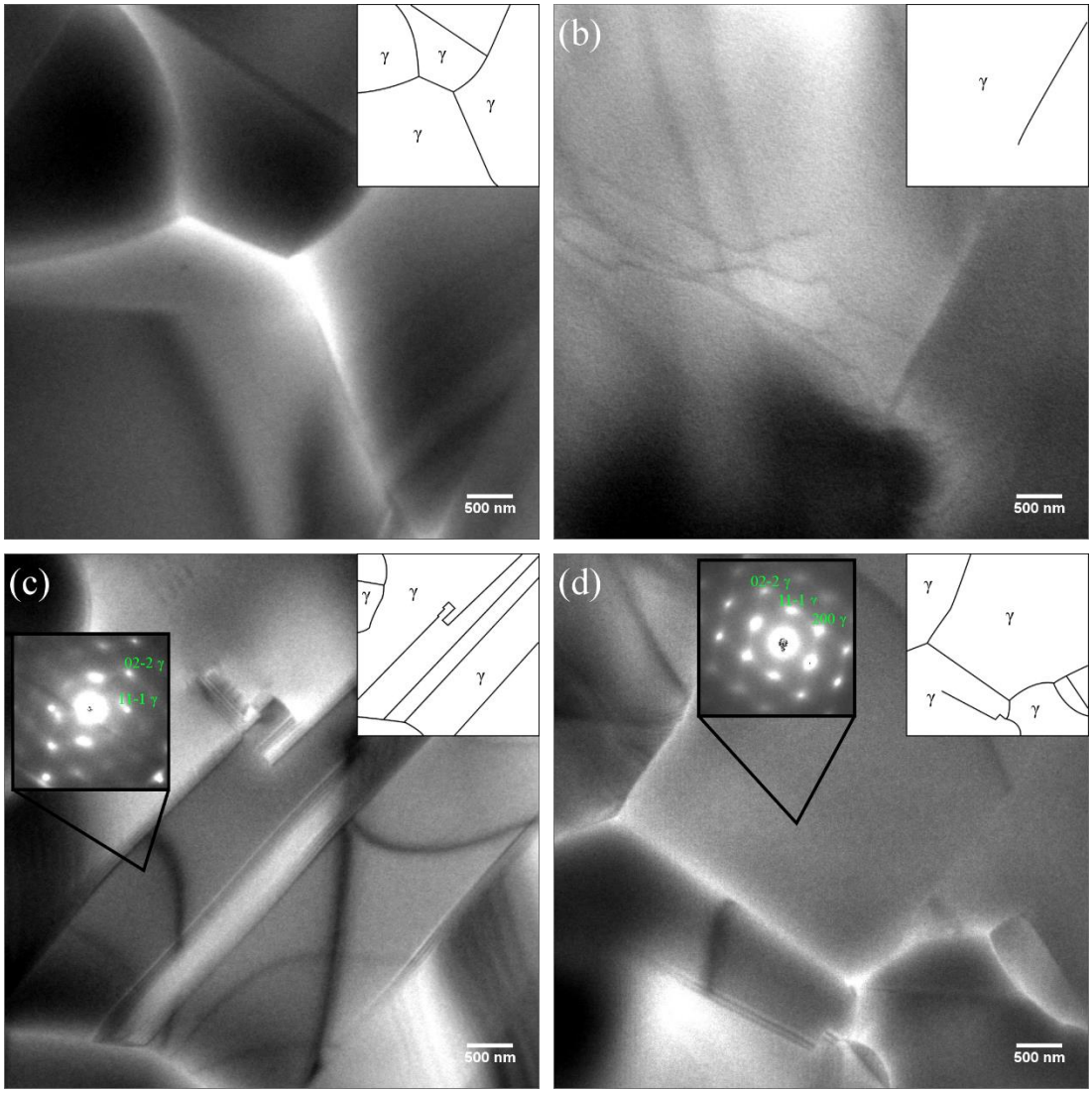

Figure 4.10: Selected bright field TEM images of the fully austenitic microstructure showing (a) specimen 4.1 at 807°C (b) specimen 4.3 at 848°C (c) specimen 4.4 at 845°C, with the selected area diffraction pattern show, and (d) specimen 4.5 at 866°C, with selected area diffraction pattern shown. Bend contours are visible in all four images. Note: (a) shows the microstructure during initial cooling, but before ferrite nucleation was observed.

4.7 Initial Formation of Austenite-Ferrite Interfaces.

Specimens were then cooled to 790°C, the lower (T_1) temperature used during thermal cycling for this composition to produce austenite-ferrite interfaces for observation. As with the austenite, the initial nucleation and growth of the ferrite grains took place outside of the field of view. This was expected on the assumption of the electron beam causing a local temperature increase. Figure 4.11(a-e) shows the first ferrite grains observed during the first cooling stage across for specimens 1-5 respectively, whilst Figure 4.11(f) plots the temperature at which each grain was first observed. The field

of view in each case was moved from the starting location, both to examine the austenitic microstructure and to locate and identify newly formed ferrite grains. The green arrows indicate where two grains shared the N-W orientation relationship.

Ferrite grain size varied between samples, indicating that they were first observed after having had different growth times. The grain in figure 4.11(a) was particularly small, however, it should be noted that after only a short time spent observing this grain, a much larger ferrite grain grew into the field of view. In contrast, the other grains grew for a considerable distance into the austenite.

From Figure 4.11(a-e) several qualitative differences between the interfaces can be noted. The ferrite grain in figure 4.11(a) has interfaces with three separate austenite grains, of which two are predominantly straight, the final interface (on the right) being slightly curved. Whilst the growth of the ferrite grain was being observed there did not appear to be a clear difference in mobility between the three interfaces.

Amongst the remaining grains there are some clear differences. The ferrite grains in 4.11(d&e) were also observed relatively soon after their nucleation. These had begun to grow along the existing austenite grain boundaries, either a grain boundary as in the case of 4.11(d) or, as in the 4.11(e) case, from a triple point which resulted in an "L" shaped grain. In both cases a complex interface was observed with both smoothly curved and relatively straight sections apparent.

The α grain in figure 4.11(b) had interfaces with two austenite grains in the field of view. There is an easily visible interface which is smoothly curved with one γ grain, whilst the interface with the leftmost γ grain were difficult to distinguish but appear much straighter. The grain in figure 4.11(c) displayed the most complex pair of interfaces. The upper/leftmost interface forms a predominantly "L" shaped interface with the left-hand austenite grain. The base of the "L" also shows a small kink in the interface. This may be the result of the interface being temporarily pinned by an inclusion or some other particle which cannot be seen under the current conditions. The lower interface in figure 4.11(c) was curved overall, with a local wavelike quality to the interface.

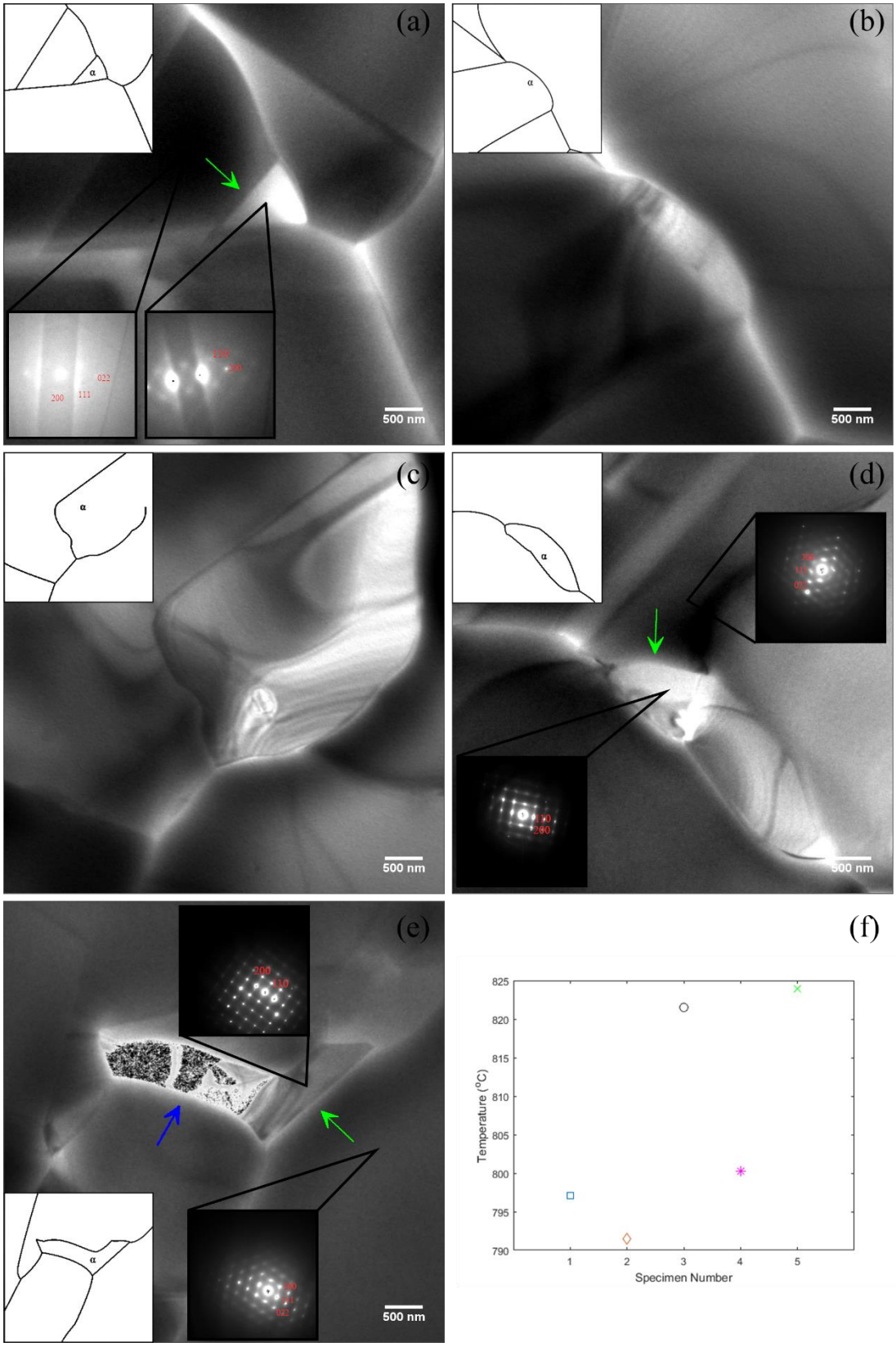

Figure 4.11: Bright field TEM of the first ferrite grains observed for (a) Specimen 4.1, (b) Specimen 4.2, (c) Specimen 4.3, (d) Specimen 4.4 and (c) Specimen 4.5. The temperature at which each grain was first observed is given in (f). Unlabelled grains are austenite. Green arrows indicate the interface between ferrite and austenite grains where a N-W orientation relationship was identified, the blue arrow indicates an interface close to the N-W OR. Note: that the stage was moved to locate the ferrite grains at the earliest opportunity.

The oversaturation of the image in figure 4.11(e) is due to the differing contrast conditions between the ferrite and the austenite grains. This different contrast is the result of the different crystal structure and orientation with respect to the electron beam of the two phases.

The relative orientation of the main migrating interfaces under observation was determined from the SAD pattern. This misorientation is defined as the rotation angle necessary to bring the austenite and ferrite grains into the N-W orientation relationship [31]. The misorientation of the main interface under observation in specimen 5 was 41.3^{o}. This was significantly higher than the main interfaces observed in specimens 1-4 which were all in the range 10.3^{o} to 19.2^{o}.

4.8 Interface Position.

The most complete observations of the interface position were captured for specimen 4.5. This occurred during the final half of the heat treatment and is shown in figure 4.12. There is good qualitative agreement with the evolution of interface position with temperature when compared with the behaviour measured using dilatometry. The stagnant stage and normal transformations can be clearly distinguished, with the inverse transformation also seen.

Interface 1 was primarily observed during cooling, capturing the end of the stagnant stage followed by the normal and inverse $\gamma \rightarrow \alpha$ transformation. Interface 2 was primarily followed during the final T_1-T_2 heating stage, and part of the final T_2-T_1 cooling stage. This captured both stagnant stages and the ferrite to austenite transformation (both normal and inverse).

The total displacement of the interface measured over the course of the full cycle is 19.4 ± 0.3 μm. This was based on the measurement of six positions along the interface as described in chapter 3, with standard errors. This is a factor of ~2 higher than that predicted from dilatometry assuming cubic geometry. Although other interfaces could not be followed as completely, this displacement of approximately 20 μm is consistent with other interfaces observed in this specimen and in the other successful specimens.

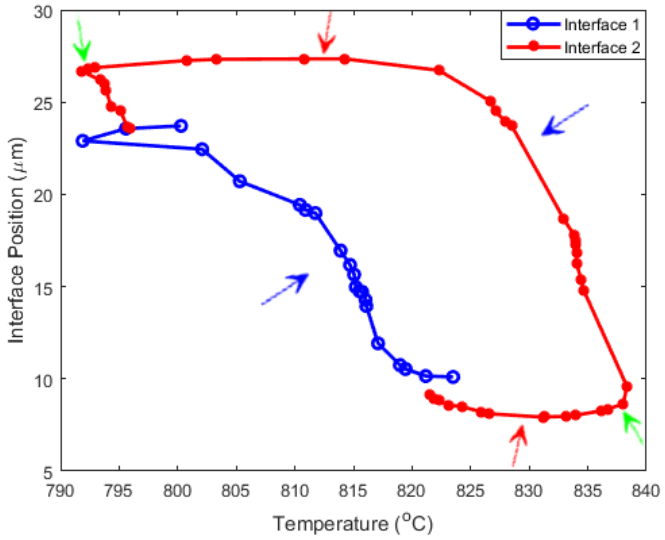

Figure 4.12: Graph of the interface position against temperature throughout a complete cycle, with arbitrary starting position. The normal transformation, inverse transformation and stagnant stage are market with blue, green and red arrows respectively.

The temperature range of the stagnant stage was estimated from figure 4.12. For the stagnant stage during cooling the total temperature range of the stage was estimated to be 15C. For other cycles, the stagnant stage temperature range was 15C and 16C. The average stagnant stage temperature range is therefore 15C, lasting for 119 seconds.

For the stagnant stage during heating the temperature range was estimated to be 21C, significantly longer than the stagnant stage estimated from the previous cycle, 11C. The average temperature range for this stagnant stage is 16C. This disparity may partly be because changing contrast conditions, particularly in thicker regions of the specimen, meant that not all frames were suitable for measuring the interface position, leading to variation in the estimated temperature range of the inverse $\gamma \rightarrow \alpha$ transformation. However, the average of the two cycles is consistent with estimates from other specimens. The average time of the stagnant stage was 127 seconds.

In both cases the estimated stagnant stage temperature range is within 2C of the temperature range estimated by dilatometry. The interface demonstrated different behaviour in the stagnant stage on heating compared to that on cooling. On heating the migration of the interface continued smoothly into the austenite and showed a predominantly straight or curved morphology. The direction of the migration only reversed at the end of the stagnant stage and the interface established a more irregular wave-like morphology as the normal transformation began and it migrated away from

the region it occupied during the stagnant stage. Figure 4.13 shows a composite image of the interface at the end of the stagnant stage and shortly after the normal α→γ transformation had begun, illustrating the change from a nearly straight interface to an increasingly irregular morphology.

On heating, the interface displacement between the beginning and end of the stagnant stage was 0.48 ± 0.06 μm. Throughout the stagnant stage the interface continued to migrate into the austenite.

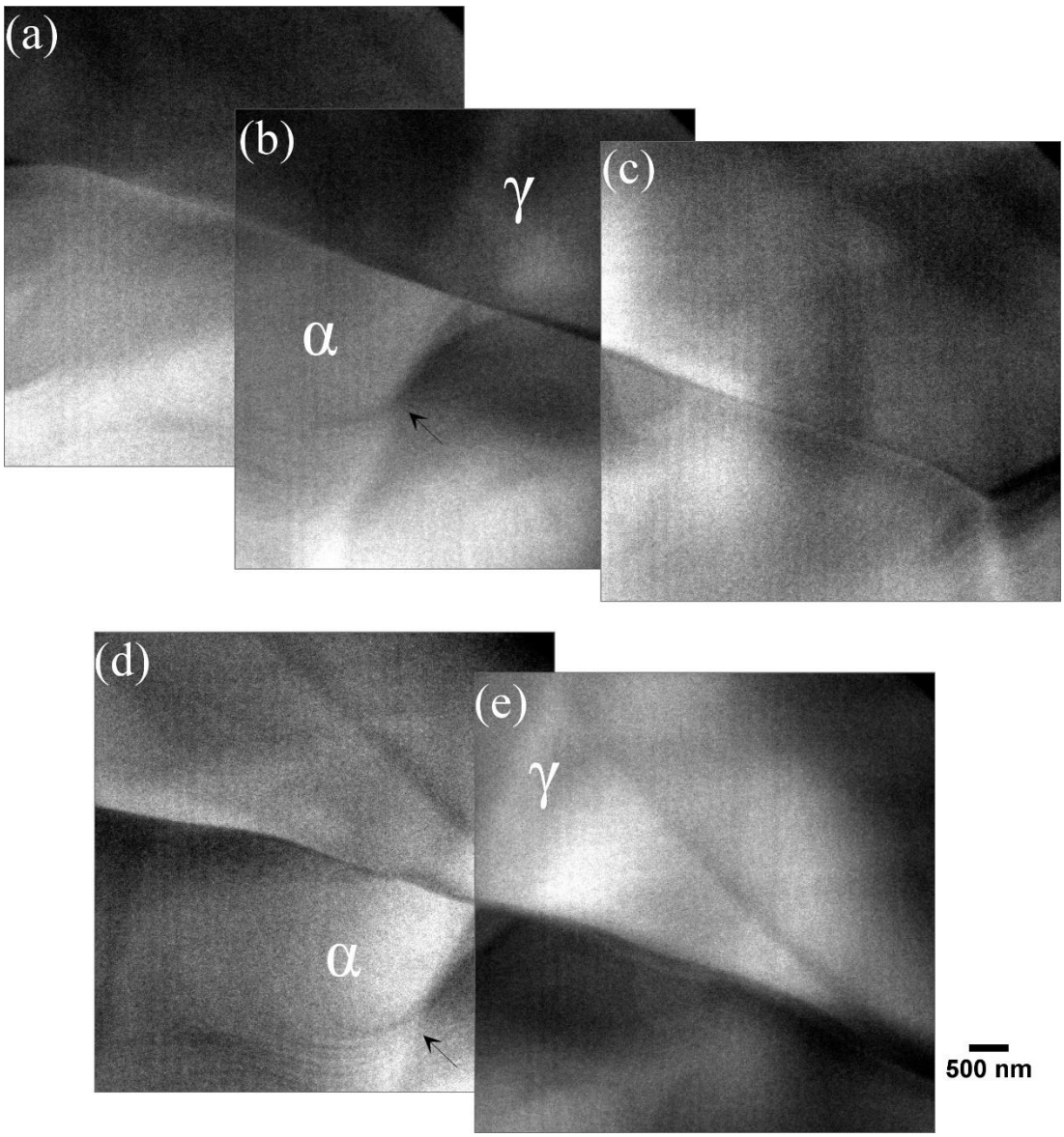

Figure 4.13: Composite bright field TEM image of the interface at (a-c) the end of the stagnant stage (814°C) and (d-e) after the normal α→γ transformation had begun (822°C). Black arrow indicates features immobile between (b) and (d). (Specimen 4.5).

The behaviour during the stagnant stage on cooling was characterised by an initially straight or curved interface which continued to migrate into the ferrite. However, the direction of migration reversed earlier than in the heating case, leading to a lower overall displacement of the interface. This also affected the morphology of the interface which developed over the course of the stagnant stage by becoming curved into the new direction of motion, as illustrated in figure 4.14. This became more pronounced until the migration accelerated with the onset of the normal γ→α transformation. As with the previous transformation the interface morphologies became more irregular or wave-like.

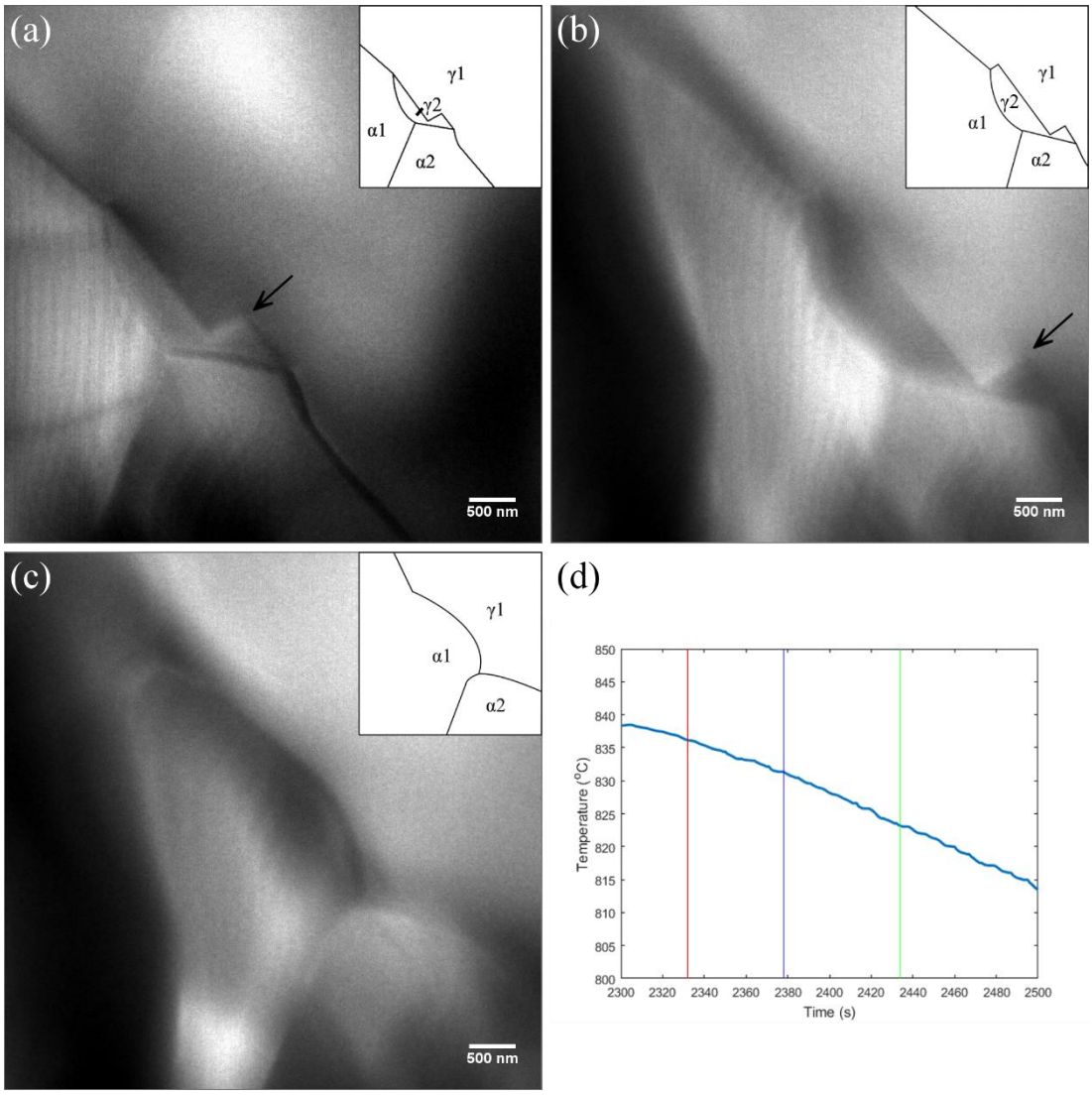

Figure 4.14: Bright field TEM of the interface position during the stagnant stage (a) at 2332.1 seconds (836°C), the start of the stagnant stage (b) at 2378.4 seconds (831°C) (c) at 2434 seconds (823°C), the end of the stagnant stage and (d) showing the time-temperature position of each frame. Vertical lines, from left to right, indicate the time depicted in frames (a)-(c). Black arrows indicate features which are immobile between frames. The field of view was translated between each image. (Specimen 4.5).

For this stagnant stage the displacement was 0.2 ± 0.1 μm, and the total distance migrated 1.07 μm. At the slowest measured velocity, the interface migrated approximately 25 nm. In the case of the α→γ transformation, the inverse α→γ transformation was estimated to have finished by 836°C, lasting 2.4°C, for the interface observed during cycle 3. This is in good agreement with the estimate for the main interface observed during cycle 1 of 837°C. Figure 4.15 shows the interface position against temperature for several interfaces observed during the inverse α→γ transformation. All these interfaces had undergone a significant decrease in velocity by 834°C. Two interfaces where the decrease was particularly pronounced were cycle 2-interface 2 and cycle 3-interface 2 and were associated with observed microstructural features. The former section of interface was adjacent to a rapidly moving triple point, whilst cycle 3-interface 2 was associated with the development of a growth twin in the austenite behind the interface. The interfaces in the cycle 1 track well, because each interface is part of a single segmented interface. This segmentation occurred due to interaction with twin boundaries in the austenite grain.

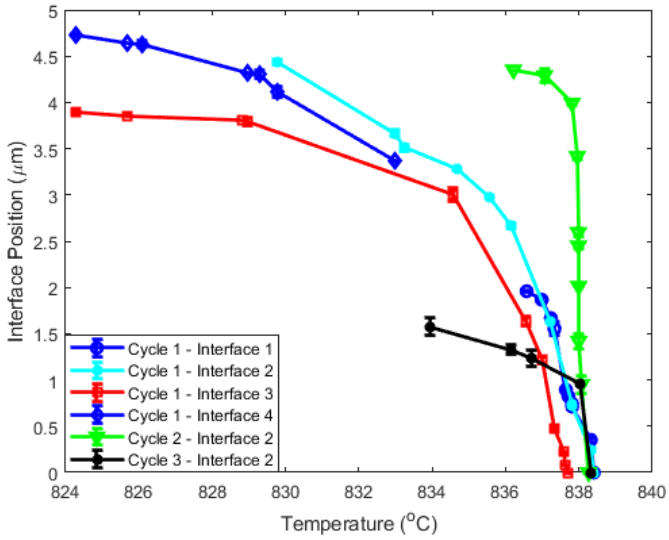

Figure 4.15: Graph of interface position against temperature. The Interface migration taking place during the ferrite to austenite transformation and subsequent stagnant stage. This was based on the measurement of six positions along the interface as described in chapter 3, with standard errors.

The distance migrated by the interface during the inverse α→γ transformation, as estimated from figure 4.12 was 1.3 ± 0.2 μm for 838-836°C. For the γ→α transformation the inverse γ→α transformation was estimated from interface 1 in figure 4.12, to end at 796°C, lasting for 4C. During this period the interface migrated

0.66 ± 0.04 μm. If interface 2 is used, the inverse γ→α transformation was estimated to end at 793ºC, lasting 1C and migrating 0.17 ± 0.02 μm. However, as discussed above this is likely to be an underestimate caused by the difficulty of determining the interface position under changing contrast conditions (and therefore contributes to an overestimate of the stagnant stage temperature range). The averages for temperature range and migration distance during the inverse γ→α transformation are therefore 2.5C and 0.42 μm respectively.

4.9 Interface Velocity.

Figure 4.16(a) shows the interface velocities corresponding to the interfaces in figure 4.12. There are a few unexpectedly high velocities measured, which are associated with specific interface behaviours, for example, the highest velocities on heating were measured close to a rapidly moving α-γ-α triple boundary.

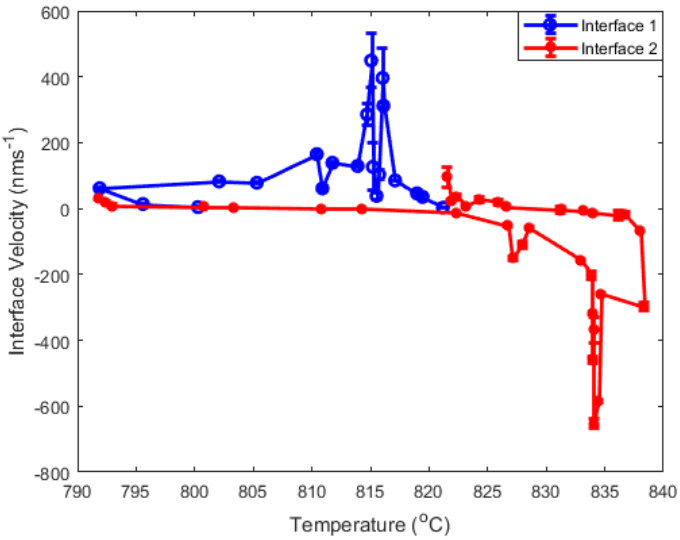

Figure 4.16: Graph of Interface velocity against temperature. Note: the ferrite to austenite velocities are negative.

Excluding these exceptionally high measurements of growth velocity, which because they are atypical, would be averaged out in a technique like dilatometry, the behaviour of the interface over the ferrite to austenite transformation is clearer. The interfaces show an increase in velocity with increasing temperature, velocity of 300 nm·s^{-1} at the maximum temperature of the cycle. Once the specimen began to cool the inverse α→γ

transformation is characterised by a consistent decrease in velocity for all interfaces as in figure 4.15. This is consistent with the bulk observations, but with a peak velocity approximately 5 times higher in the case of the TEM measurements.

In the case of the austenite to ferrite transformation, there is also good semi-quantitative agreement between the bulk and the TEM measurements as shown in figure 4.17. Once significant movement of the interface began, around 820-825°C, the velocity increased rapidly to a peak around 814-816°C. Although this peak measurement is significantly higher, approximately 500 $nm \cdot s^{-1}$ against 52 $nm \cdot s^{-1}$, there is excellent agreement in the temperature at which it occurred. Thereafter, the interface velocity continued to decrease for the rest of the normal $\gamma \rightarrow \alpha$ transformation and for the inverse $\gamma \rightarrow \alpha$ transformation. In general, the interface behaved as expected based on the calculated and bulk kinetics, and there is no deviation from this expected behaviour as the interface migrated into thicker or thinner regions of the specimen.

Overall the interface velocities also show good agreement between cycles, although there is some variation between individual interface segments. The velocities also show that there is not necessarily a smooth acceleration of deceleration of the interface over the course of the cycle. Instead, within a general trend of increasing or decreasing velocity individual interfaces or sections of interface undergo periods of acceleration or deceleration which were not necessarily linked to any features observed in the thin foil specimens.

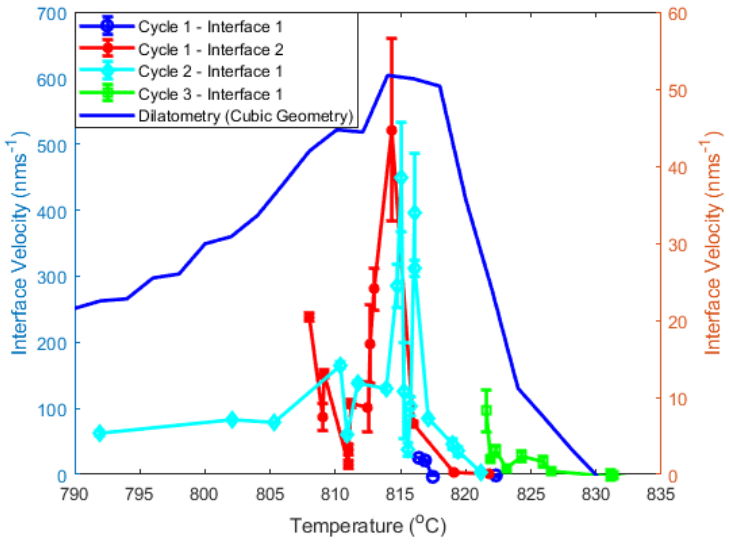

Figure 4.17: Graph of the Interface Velocity against Temperature for the TEM observations and from dilatometry. The velocity estimated from dilatometry corresponds to right hand scale and the TEM to the left hand scale.

The inverse transformation interface velocities are shown in figure 4.18 for multiple interfaces. Since there was no significant period during which the interface was completely static, it was difficult to establish the temperature at which the inverse transformation could be considered to have stopped, and the stagnant stage to have begun.

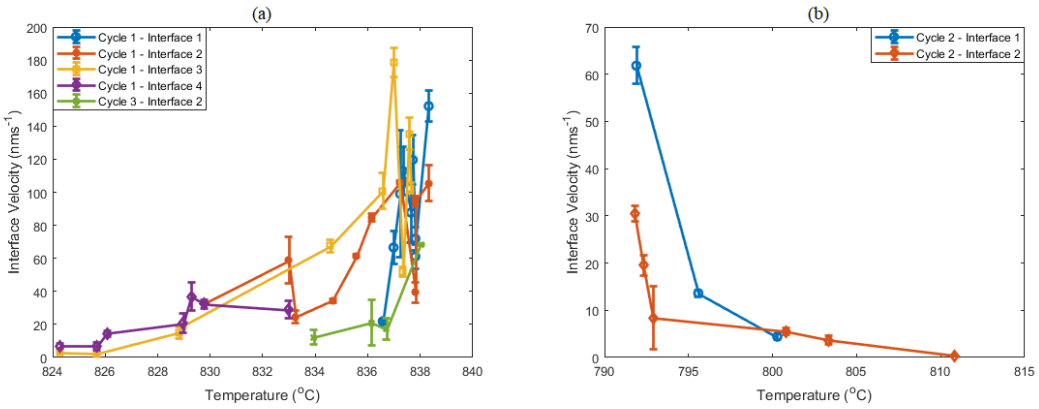

Figure 4.18: Graph of interface velocities against temperature for (a) the inverse ferrite to austenite transformation and the start of the stagnant stage and (b) the inverse austenite to ferrite transformation and the start of the stagnant stage.

As with the interface position the velocities measured are higher than that found in the bulk. The peak velocities are a factor of 5 and 11 higher in the TEM measurement for the α→γ and γ→α transformations respectively. It should be emphasised, however, that the results from dilatometry are an average of all grains in the specimen. Since it is not necessarily the case that each grain attains the maximum velocity at the same nominal temperature, there will be some tendency to average out the maximum velocities.

To an extent this can be seen by comparing the velocities extracted from dilatometry with the TEM velocities. The peak γ→α velocity is much more well defined in the TEM data. Velocities drop significantly (in excess of 100 nm·s^{-1}) 1-2^{o}C from the peak velocity. In contrast the velocities in figure 4.2(b) show that over a range of 2-4^{o}C velocities remain close (within ~10%) of the peak velocity.

Furthermore, the good agreement between the temperatures at which the maximum velocity is found for the γ→α transformation indicates that interface conditions in the TEM at this point are representative of the bulk. The velocity behaviour during this

part of the transformation is attributed to increased driving force as a result of deviation from local equilibrium during the stagnant stage. If the kinetics were being affected by surface diffusion, it would be expected that the temperature at which the peak velocity occurred would change.

4.10 General Observations: The Ferrite to Austenite Transformation.

During thermal cycling multiple interfaces or sections of interface were observed. Some of the observed interfaces formed the boundary between a single austenite and ferrite grain and were distinguished from one another either by distance or twin boundaries. In other cases, the boundaries were close to a well-defined γ-γ-α or γ-α-α triple point. Interfaces with a range of morphological characteristics were observed, including smoothly curved or predominantly straight interfaces traditionally described in most models of the transformation, to those interfaces which were more wave-like and moved with a more undulating motion.

As shown in figure 4.19 multiple interface segments form the interface between a single austenite (γ_1) and ferrite grain (α_1), are positioned closely together and made distinct by the formation of twin boundaries in the austenite. The presence of such twin boundaries was seen to influence the structure of the entire interface between γ_1 and α_1, with a complex development of the individual segments.

Interface A can be seen to switch between a straight and curved morphology over the period of observation, alongside a slight rotation of the interface which affects the direction of migration. A similar process is seen in interface B which is initially curved before becoming (and remaining) straight, a process which is also accompanied by a small rotation in the interface. Interface C on the other hand maintained its straight morphology and migration direction throughout this period, with its more rapid migration as the specimen cooled accommodated by the development of a well-defined corner close to where the twin boundary where it meets interface A.

In the final period of observation, the development of growth twins/twin boundaries eliminated most of the original interfaces. These new interfaces D-E show a much more wave-like morphology.

This behaviour, with the development of growth twins and twin boundaries which led to well defined subsections of interface with differing morphology, was observed across cycles and across specimens as shown in figure 4.20(a).

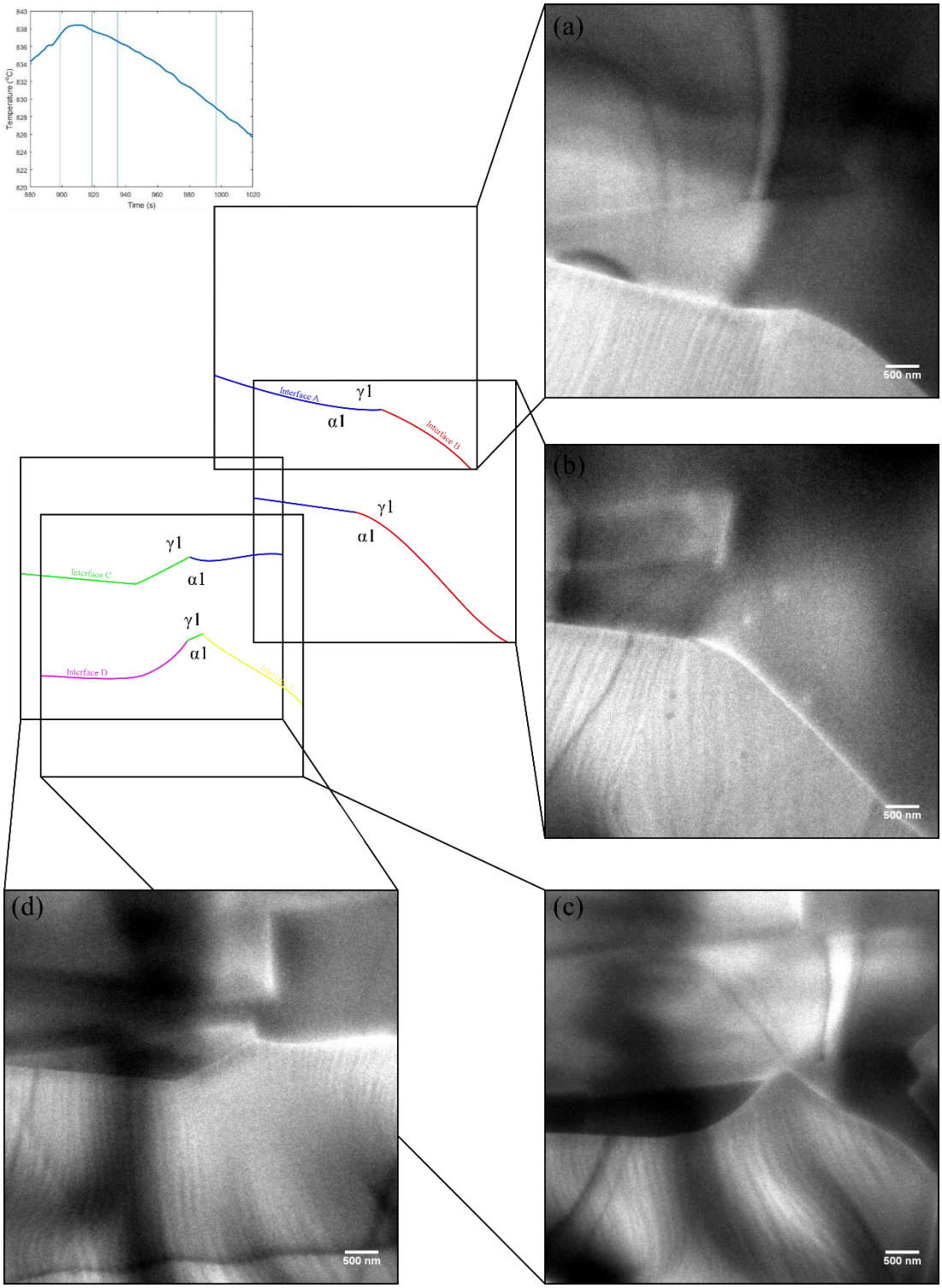

Figure 4.19: Bright field TEM of the interface (a) at 899.2 seconds (837°C) (b) at 919.0 seconds (838°C) (c) at 935.1 seconds (837°C) and (d) at 996.5 seconds (829°C). (Specimen 4.5).

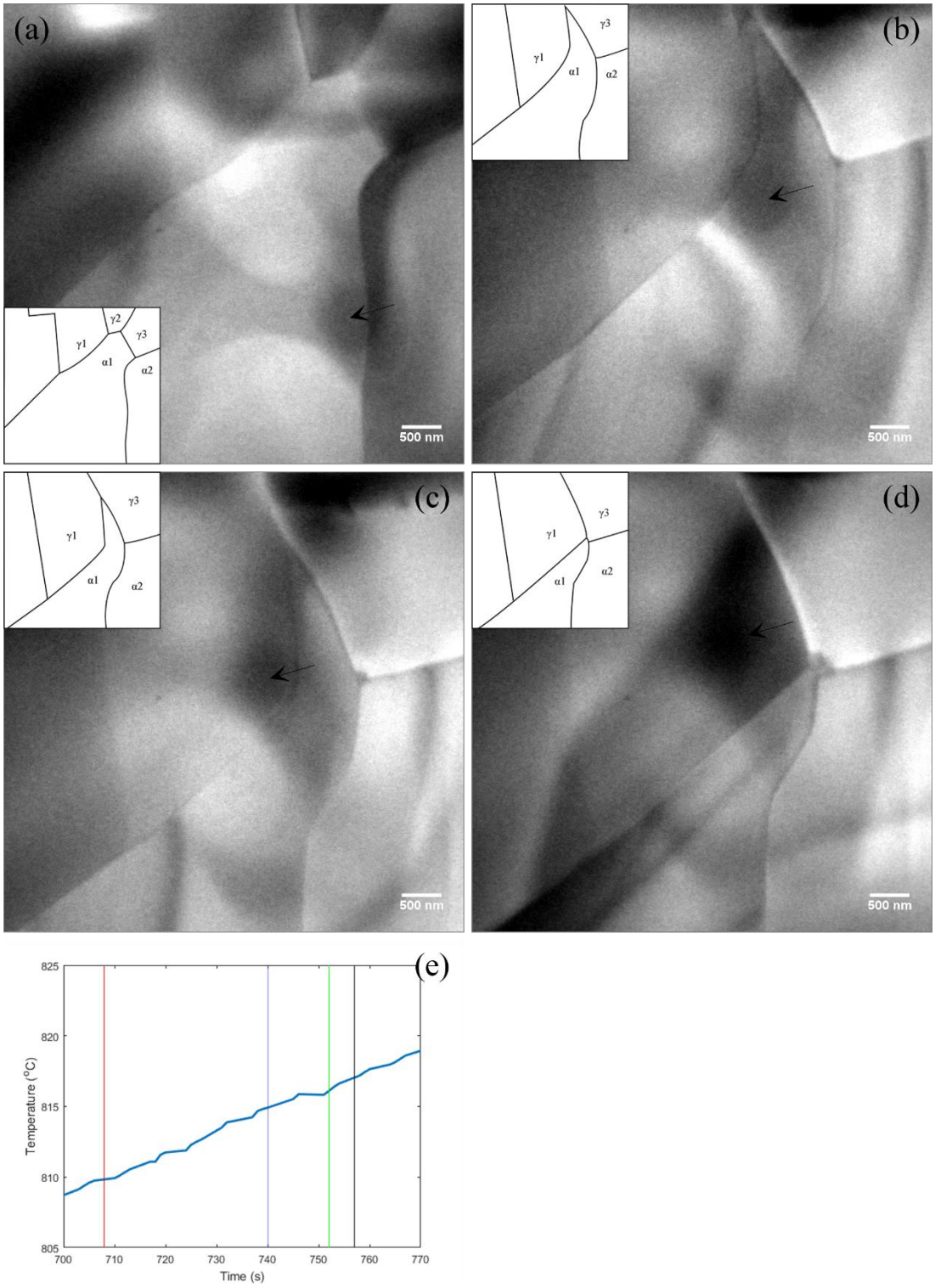

Figure 4.20: Bright field TEM of the interface position during the ferrite to austenite transformation (a) at 708.3 seconds (811°C) (b) at 740.1 seconds (816°C) (c) at 751.9 seconds (818°C) (d) at 756.9 seconds (819°C) and (e) Showing the time-temperature position of each frame. Arrows indicate common positions between frames. Vertical lines, from left to right, indicate the time depicted in frames (a)-(d). (Specimen 4.1).

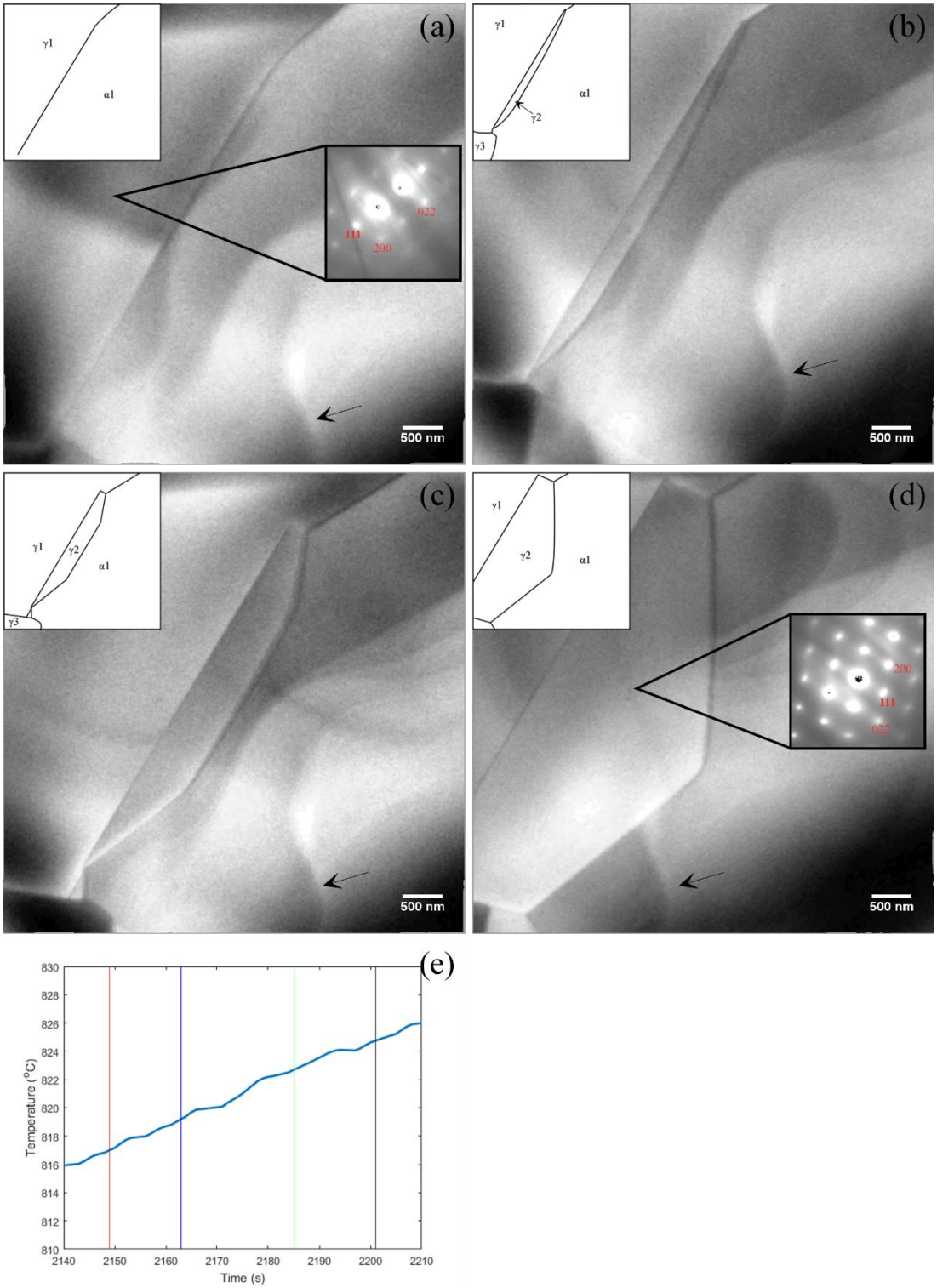

Figure 4.21: Bright field TEM of the formation of a new austenite grain, γ2, (a) at 2148.9 seconds (818°C) (b) at 2162.7 seconds (821°C) (c) at 2185.4 seconds (824°C) (d) at 2201.2 seconds (826°C) and (e) showing the time-temperature position of each frame. Vertical lines, from left to right, indicate the time depicted in frames (a)-(d). Black arrows indicate a "ghost" boundary which is immobile between frames. (Specimen 4.1).

In the case of the interfaces shown in figure 4.20 it was also observed that there was local, zip-like, acceleration of the interface at times when the α/γ interfaces between

two growing austenite grains came into proximity. As shown in figure 4.20(b-c), this led to the rapid elimination of the remaining ferrite between the two austenite grains and the formation of a γ/γ grain boundary.

On one occasion it was also observed that a twin boundary in the austenite did not lead the development of a well-defined growth twin, but rather a large austenite grain that continued to migrate for into the ferrite. In both cases the [011] direction was parallel to the beam direction, with a 70^{o} rotation of the newly formed grain around this axis. Consequently, the close packed (111) planes were parallel. This process is shown in figure 4.21. As in most cases where the formation of a twin boundary was observed at the interface, the interface began with an initially straight section which forms one side of the twin, as in 4.21(a). Subsequent migration of the interface occurred from the new twin growing readily into the ferrite, shown in 4.21(b). This migration continued into the austenite, as in 4.21(c-d), with no formation of a second twin boundary within the austenite. Instead this new grain continued to migrate, forming a coherent facetted boundary with the parent austenite. The subsequent behaviour of the triple point thus formed is describe in more detail in chapter 4.13.

Averaged across all cycles the normal α→γ transformation took place between 812^{o}C and 838^{o}C, a temperature range of 26^{o}C. During cycle 3 the interface migrated a distance of 17.7 ± 0.2 μm. In comparison, the displacement extracted from dilatometry 8.1 μm (cubic geometry) or 5 μm (spherical geometry).

4.11 General Observations: The Austenite to Ferrite Transformation.

Valid observations of the austenite to ferrite transformation could not be made in specimen 4.1, which was influenced by the presence of thermal grooves on the foil surface, discussed in more detail below. As with the ferrite to austenite transformation separate interfaces or segments of interface were distinguished by distance from where the measurements were taken or made distinct by twin boundaries in the austenite.

There was clear interaction between the advancing transformation interface and the pre-existing twin boundaries in the austenite. This occurred when the boundary and the interface were parallel or close to being parallel. When the austenite-ferrite interface reached the boundary, the interface developed a straight section at the

position of the twin boundary, before migration continued. This is shown in figure 4.22. This slight pinning effect may have been due to some grooving at the site of the previous twin boundary. In contrast to the case discussed in chapter 4.16, it did not have a significant effect on the overall kinetics. This is because, as discussed in chapter 2, the groove profile is dependent on the boundary energy, and so the low energy twin boundary will result in less severe grooving compared to the incoherent transformation interface considered in chapter 4.16. Another reason is that the groove was never able to capture the entire interface, and therefore most of the interface continued to migrate unaffected.

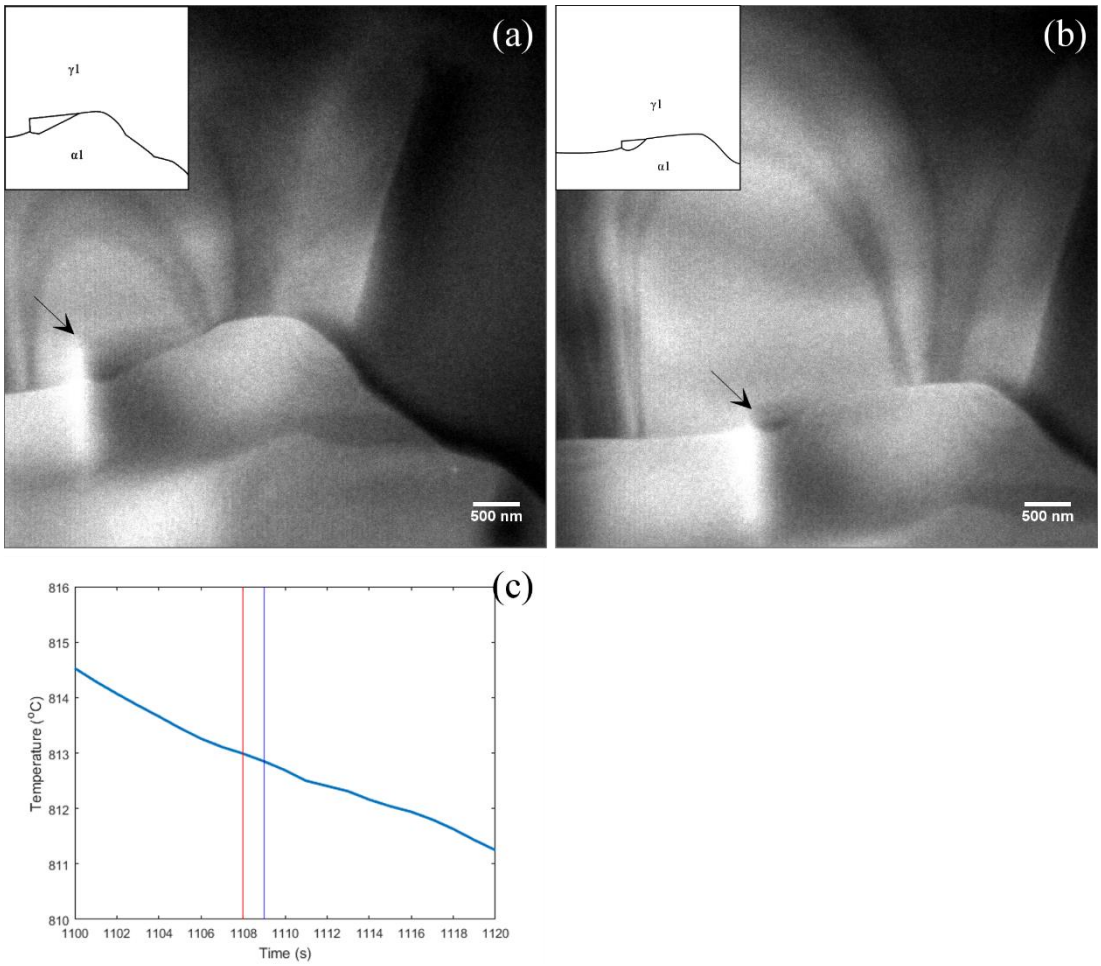

Figure 4.22: Bright field TEM of the interaction of the migrating transformation interface with an existing twin boundary (a) at 117.8 seconds (813.0°C) (b) at 1109.2 seconds (813°C) and (c) showing the time-temperature position of each frame. Vertical lines, from left to right, indicate the time depicted in frames (a)-(b). Black arrows indicate features which are immobile between frames. (Specimen 4.5).

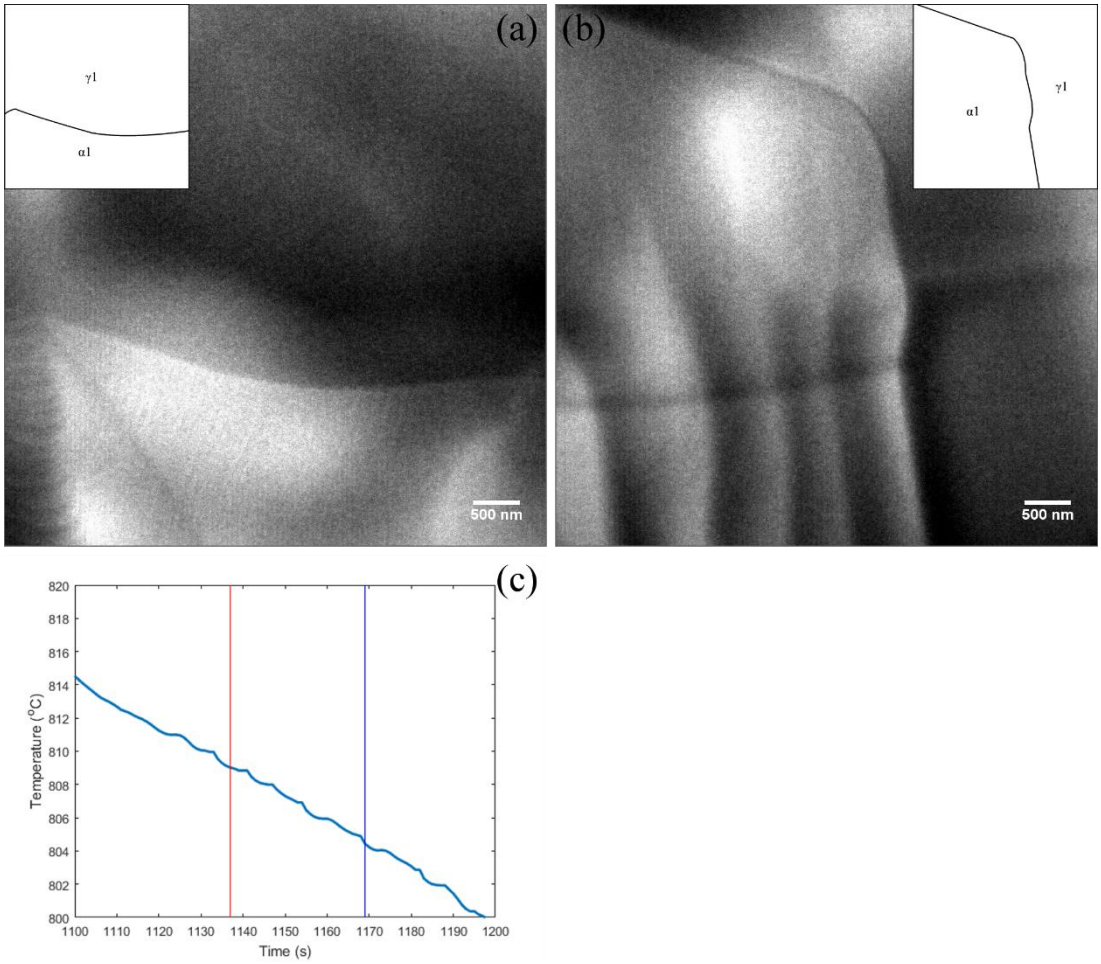

Figure 4.23: Bright field TEM of the morphology of the interface during the austenite to ferrite transformation (a) at 1136.9 seconds (809°C) (b) at 1168.7 seconds (804°C) and (c) showing the time-temperature position of each frame. Vertical lines, from left to right, indicate the time depicted in frames (a)-(b). Note the "ghost boundaries" visible in the ferrite in (b). (Specimen 4.5).

As the transformation progressed, particularly past the region with a high density of twin boundaries, the distinction between segments of interface caused by the twins was eliminated. Instead of sharp discontinuities dividing the interface, the interface was a continuum, with morphology varying between a straight and wavelike morphology, as shown in figure 4.23. The curvature of individual lengths of the interface was seen to vary throughout the rest of the transformation. Although attempts were made to measure the thickness of the bands seen in figures 4.21 and 4.23 after thermal cycling was complete they could not be located in the specimen at room temperature.

Overall, the temperature range of the normal γ→α transformation was 29C, between 821°C and 792°C. The migration of interface 1 during the normal transformation from

figure 4.9 was 12.8 ± 0.2 μm. From dilatometry, the equivalent distance was 7.9 μm (cubic geometry) or 4.9 μm (spherical geometry).

4.12 General Observations: Lateral Growth.

Throughout the thermal cycling, the transformation interface was seen to change between a straighter and a more curved shape. In one specimen, during the α→γ transformation in cycle 2, the interface became straight before developing a ledge which grew parallel to the interface. This migration continued until it reached an existing α/α grain boundary, at which point normal interface motion was resumed, although at a slower rate. A second ledge began to move in the opposite direction followed by a period of rapid growth and the formation of a third ledge, the largest of the three. The growth of this third ledge was accompanied by continued movement of the interface at the bottom of the step. Figure 4.24 shows the migration of these ledges.

Where the first and third ledges appeared, the austenite showed a dislocation structure at the tip of the ledge. Such a feature was not seen in the case of the second ledge, nor in the cases of ferrite growth where the primary direction of interface motion is parallel to the interface. The dislocation travelled with the migrating point of the interface, and in the case of the third ledge, could be seen to persist in the austenite grain after the ledge has stopped growing. Comparing with the selected area diffraction pattern acquired before the development of the ledges, both the broad interface of the ledge and the interface immediately prior to the development of the ledge was approximately parallel with the (420) plane.

The velocity of the interface at the formation of the ledge was much higher than the velocity of normally behaving interfaces when the ledge was initially formed. As can be seen from figure 4.37 it is of the order of 1 $\mu m \cdot s^{-1}$. Subsequent migration of the ledge in the lateral mode took place at velocities consistent with normally migrating interfaces at the same temperature.

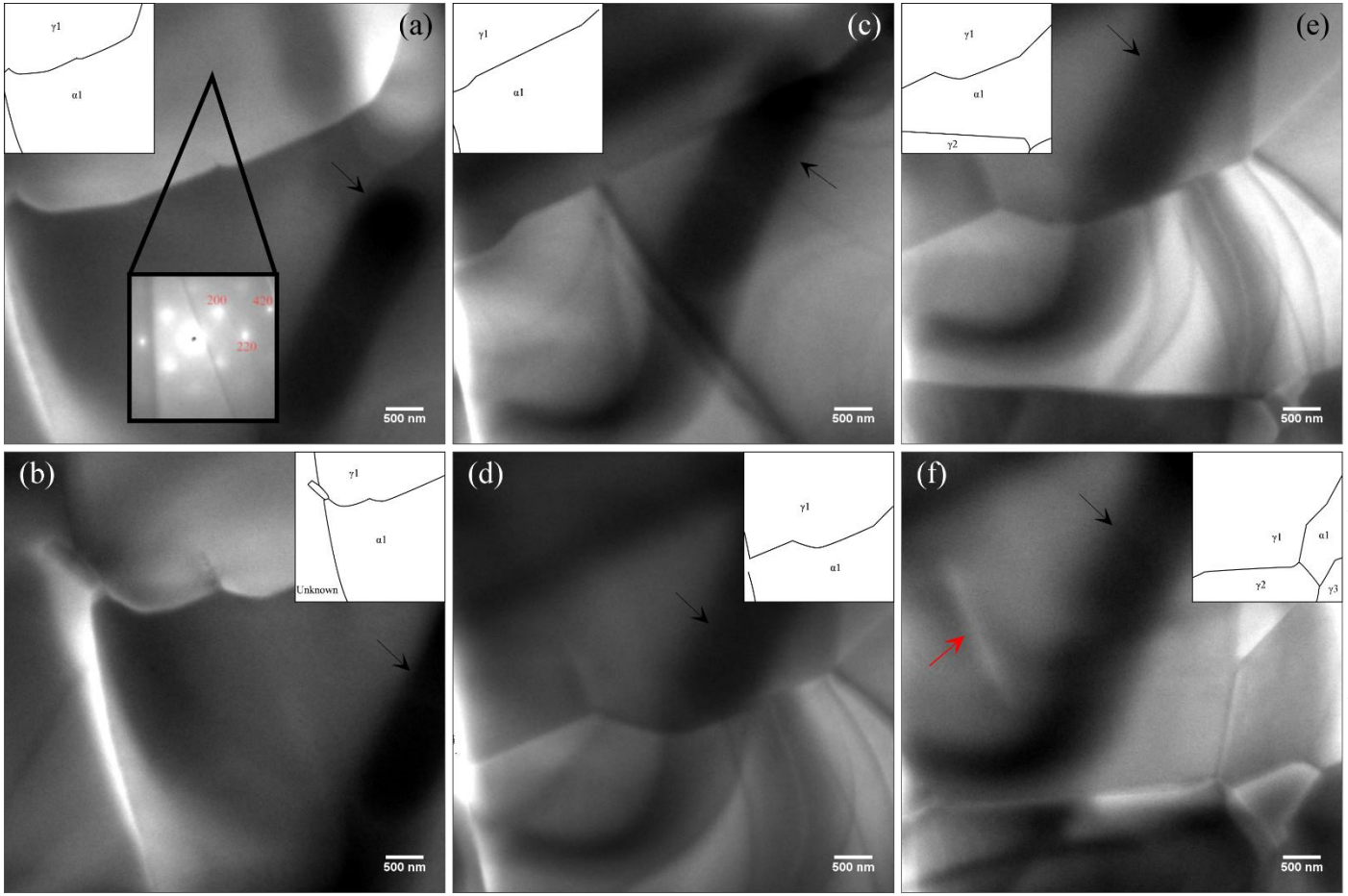

Figure 4.24: Bright field TEM of the development of ledges and subsequent lateral growth of austenite (a) at 1478.9 seconds (822oC) (b) at 1484.5 seconds (823oC) (c) the appearance of the second ledge at 1589.0 seconds (839oC) (d) shortly after the development of the third ledge at 1592.3 seconds (839oC) (e) at 1594.2 seconds (838oC) (f) the dislocation (red arrow) left in the austenite grain at 1601.8 seconds (838oC) and (g) showing the time-temperature position of each frame. Vertical lines, from left to right, indicate the time depicted in frames (a)-(f). The black arrows indicate a region of dark contrast, likely one of the thermal grooves discussed below, that shows the relative position of the frames. (Specimen 4.1).

4.13 General Observations: Triple Point Behaviour.

During the transformations, several triple points were observed. These points consisted of either two ferrite grains growing into a single austenite grain or a pair of austenite grains growing into a single ferrite grain. As such two α/γ transformation interfaces were observed alongside a grain boundary (α/α or γ/γ).

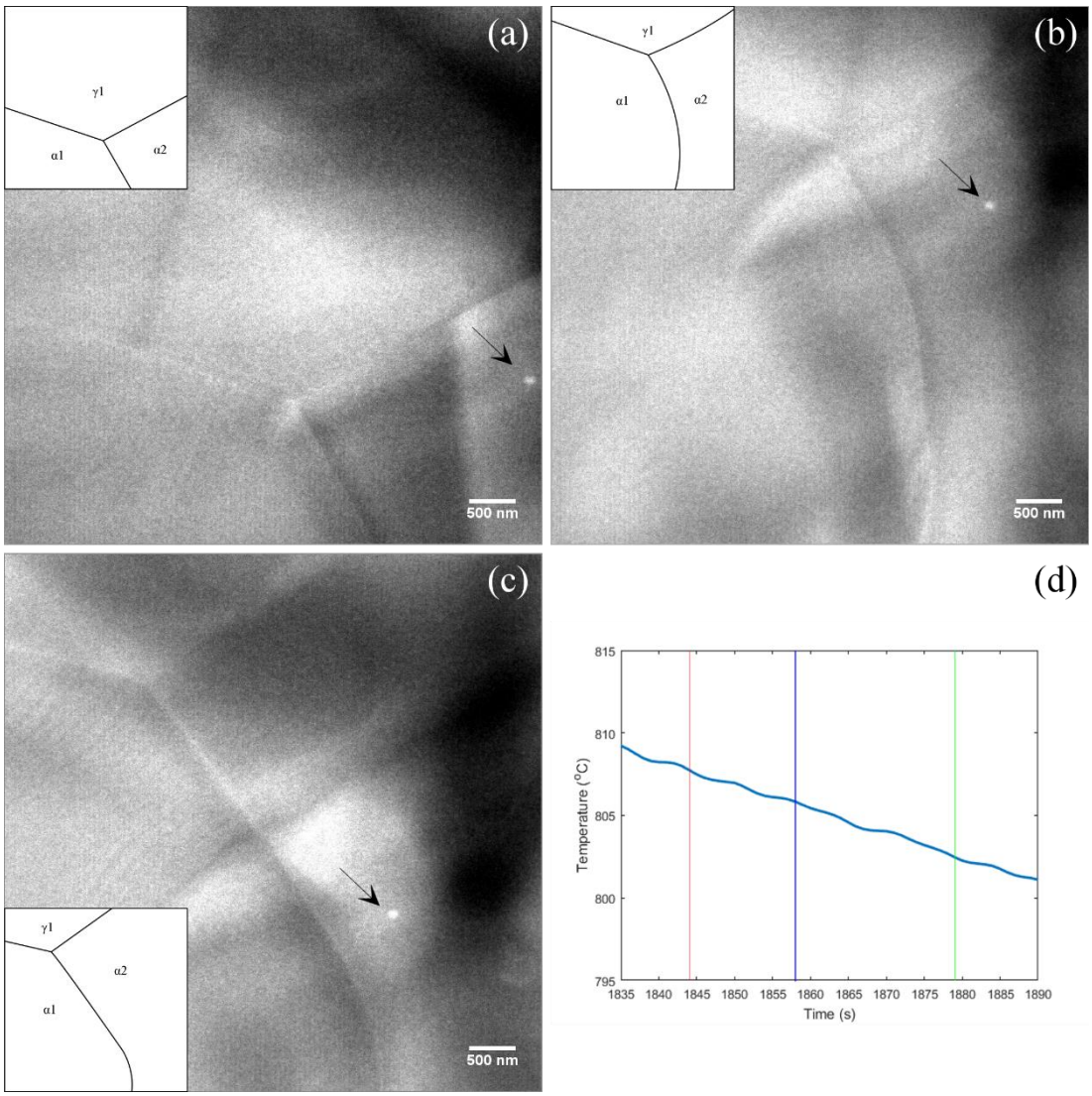

Figure 4.25: Bright Field TEM of the movement of a triple point during the austenite to ferrite transformation (a) at 1844.1 seconds (808°C) (b) at 1858.1 seconds (806°C) (c) at 1879.0 seconds (803°C) and (d) showing the time-temperature position of each frame. Vertical lines, from left to right, indicate the time depicted in frames (a)-(c). The black arrow indicates a feature which is immobile between frames, likely an Al oxide inclusion as identified in chapter 3. (Specimen 4.5).

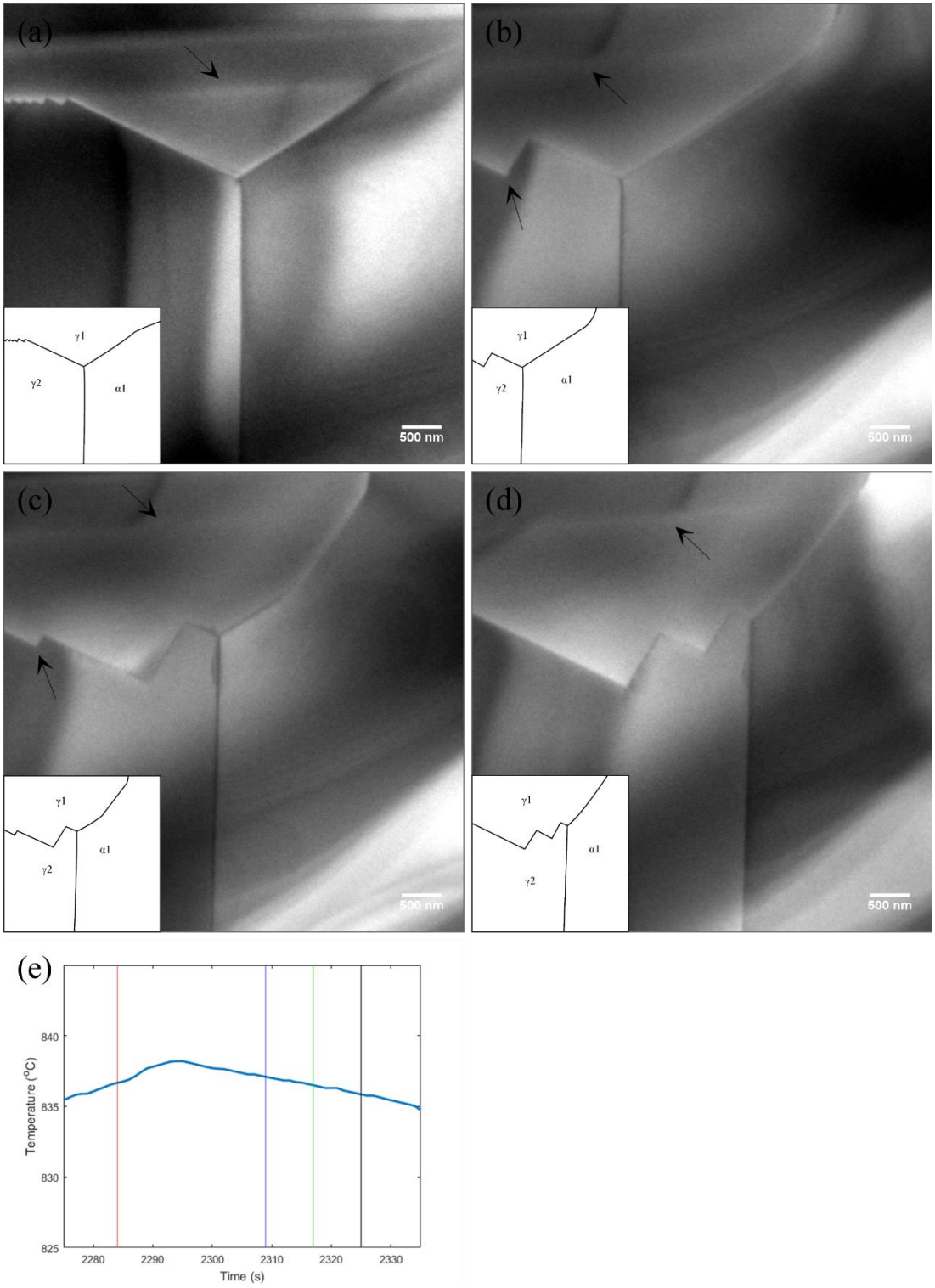

Figure 4.26: Bright field TEM of the movement of a triple point during the ferrite to austenite transformation (a) at 2283.5 seconds (838.2°C) (b) at 2308.8 seconds (836°C) (c) at 2317.3 seconds (836°C) (d) at 2324.6 seconds (835°C) and (e) showing the time-temperature position of each frame. Vertical lines, from left to right, indicate the time depicted in frames (a)-(d). The black arrows indicate features in the austenite which are immobile between frames. (Specimen 4.1).

During observation, these triple points did not migrate in a straightforward manner but showed considerable competition between the two grains of the growing phase. In the case of the growing ferrite grains, displacement of the triple point in a lateral direction was frequently seen. This occurred when the interface of one ferrite grain migrated more rapidly than the other, resulting in that grain containing a greater volume of the transformed austenite than the other ferrite grain. This process is illustrated in figure 4.25. In some cases, a section of the pre-existing grain boundary was observed to move concurrently with the transformation interface to accommodate the new location of the triple point whilst minimizing the length of the boundary.

This contrasts with the behaviour of the triple points where the grain boundary was facetted, observed during periods of austenite growth and illustrated in figure 4.26. In this case, whilst similar behaviour was observed in terms of the competition between the two grains, the lateral displacement of the triple point was not accommodated by movement of the grain boundary. Instead, the pre-existing boundary remained static and the displacement of the triple point was accommodated by a series of steps in the newly-created sections of the grain boundary. This was followed by the steps in the interface moving to create a grain boundary containing fewer ledges.

4.14 General Observations: Dislocation Motion.

The transformation was accompanied by foil bending and dislocation motion around the interface, but these were most clearly visible on the ferritic side of the interface and in thinner regions of the sample. Dislocations were observed to move towards and annihilate with the transformation interface and with grain boundaries during the phase transformation. In some cases, sections of the interface also appeared to act as sources for the moving dislocations. Figure 4.27 shows the movement of dislocations during the austenite to ferrite transformation.

Other dislocation behaviours were also observed. On one occasion, during the final stage of austenite growth, dislocations which had been moving ahead of the interface were seen to coalesce and form a low angle boundary in what had previously been a single ferrite grain. This process is shown in figure 4.28.

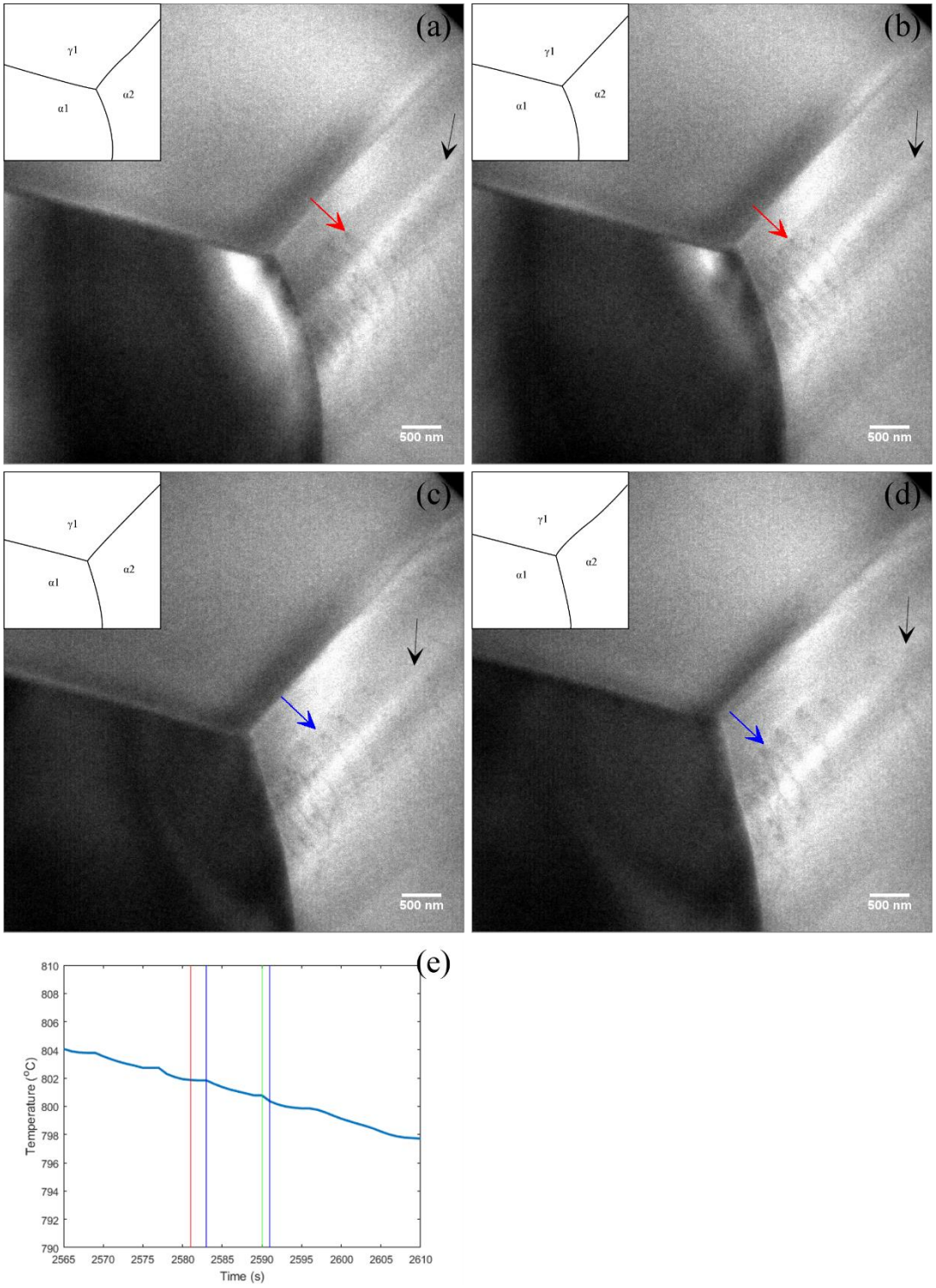

Figure 4.27: Bright field TEM of the movement of dislocations in the ferrite during the austenite to ferrite transformation (a) at 2581.4 seconds (802°C) (b) at 2583.4 seconds (802°C) (c) at 2589.7 seconds (801°C) (d) at 2590.8 seconds (800°C) and (e) showing the time-temperature position of each frame. Vertical lines, from left to right, indicate the time depicted in frames (a)-(d). Black arrows indicate region of banded contrast which is immobile between frames. Red and Blue arrows indicate the movement of individual dislocations. (Specimen 4.5).

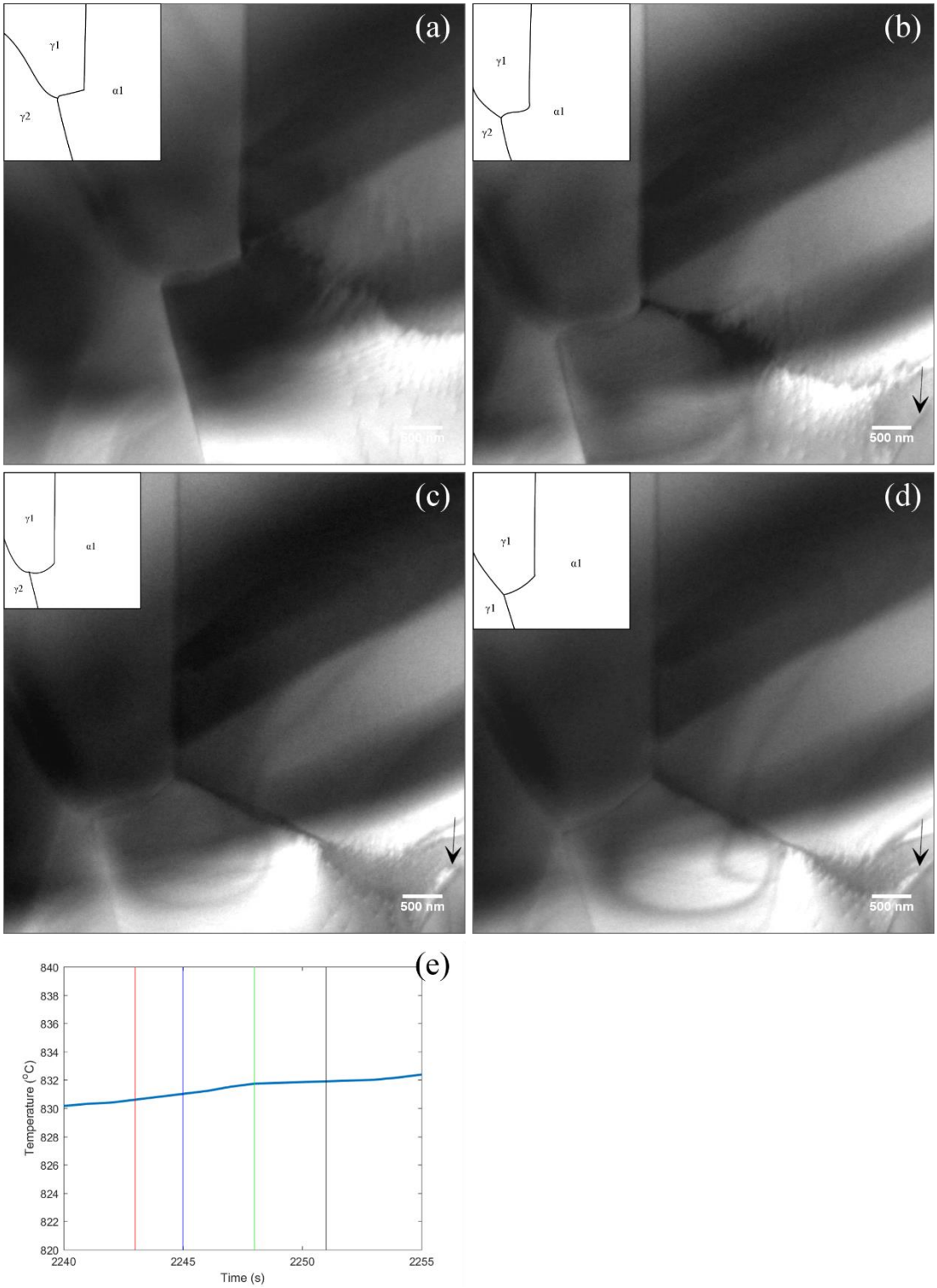

Figure 4.28: Bright field TEM of the formation of a low angle grain boundary ahead of the moving interface during the ferrite to austenite transformation (a) at 2242.8 seconds (832°C) (b) at 2244.8 seconds (832°C) (c) at 2247.8 seconds (833°C) (d) at 2250.7 seconds (833°C) and (e) showing the time-temperature position of each frame. Vertical lines, from left to right, indicate the time depicted in frames (a)-(d). (Specimen 4.1). Black arrows indicate features which are immobile between frames.

4.15 Interface Morphology.

Figure 4.29 and 4.30 show the interface under observation at intervals during the ferrite to austenite transformation. Figure 4.29(a-b) shows the rightmost part of the interface at the outset of the normal $\alpha \rightarrow \gamma$ transformation for cycles 2 and 3. In both cases the interface which was under observation was that between grains γ_1 and α_1. The microstructure is similar between the two cycles with a triple point formed by the presence of a second ferrite grain, α_2. The γ_1-α_1 interface in both cases forms is slightly curved into the austenite, most strongly in cycle 2. The interface is also at a similar angle within the frame indicating a similar path travelled during the transformation.

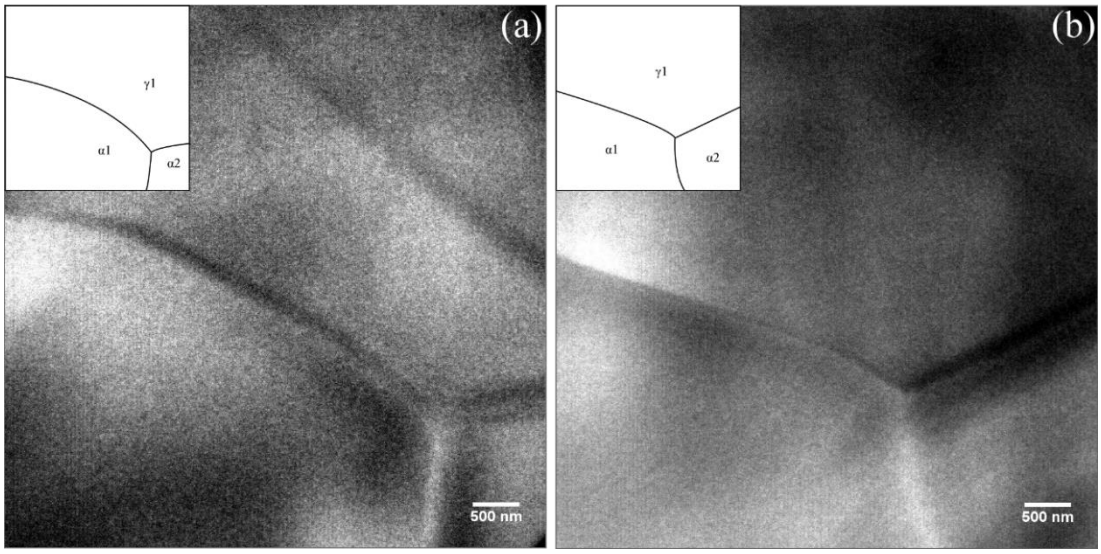

Figure 4.29: Bright Field TEM of the interface morphology at the beginning of the normal ferrite to austenite transformation, for (a) cycle 2 at 1404.8 seconds (810°C) and (b) cycle 3 at 2137.8 seconds (815°C). (Specimen 4.5). Note that for (a) the focus is poor and is included only to qualitatively assess the morphology of the interface at the triple point – it was not used for kinetic measurements of interface position or velocity.

Figure 4.30 (a-c) shows the rightmost observed interface at the end of the normal $\alpha \rightarrow \gamma$ transformation (that is, at the peak temperature of the cycle). Cycle 1 and 2 both show that the interface has been broken up into distinct segments by the formation of a growth twin in the austenite. These segments are only slightly curved or are entirely straight. The austenite in cycle 3 did not show a nearby twin, even outside of the field of view. For each equivalent segment, the angle formed by the interface is within 10° across all three cycles.

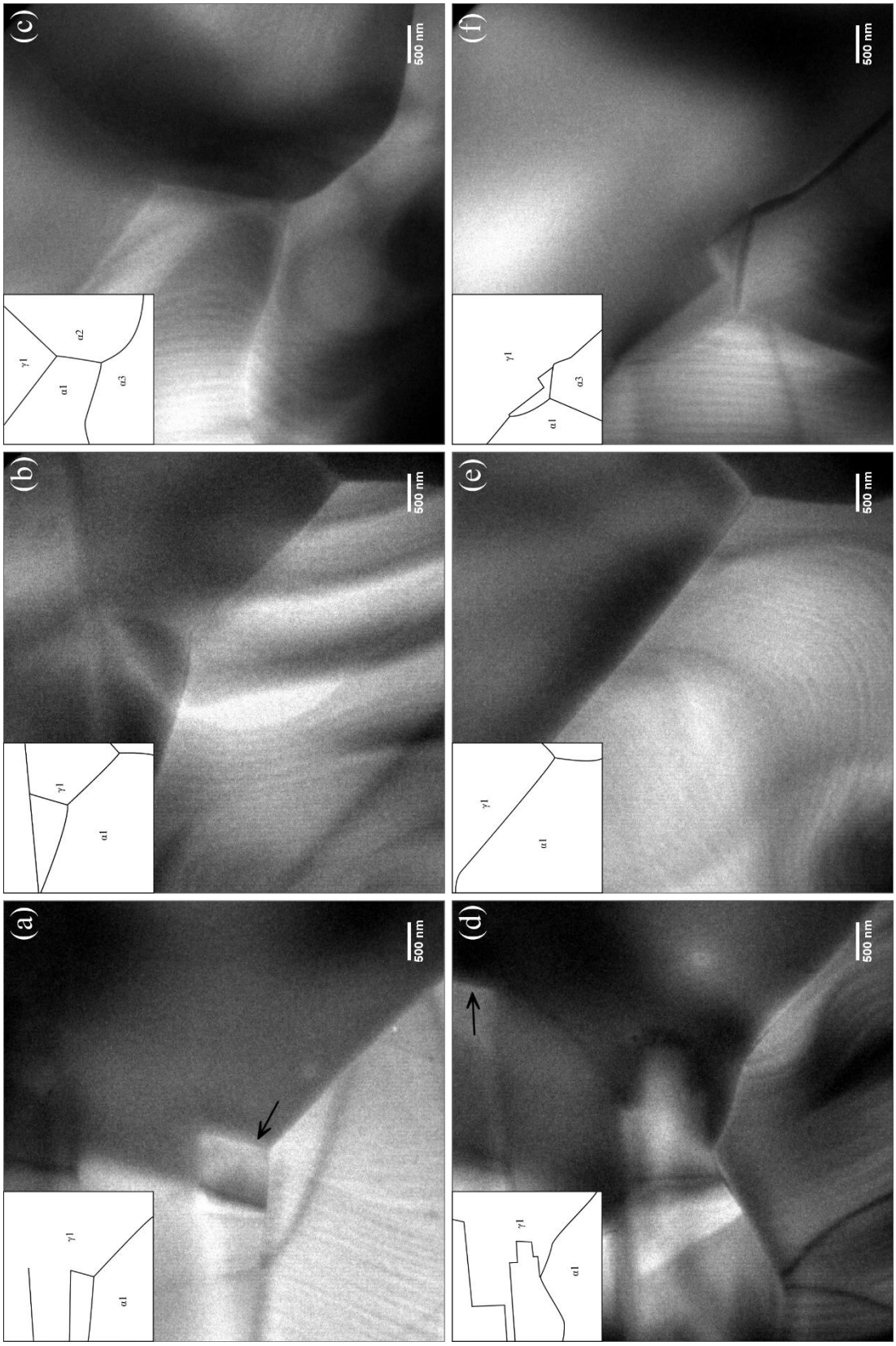

Figure 4.30: Bright field TEM of the interface morphology at the end of the normal ferrite to austenite transformation in (a) at 909.0 s (838°C) (b) 1609.8 s (838°C) and (c) 2304.2 s (839°C). The morphology at the end of the inverse α→γ transformation is shown (d) at 954.1 s (835°C) (e) 1634.4 s (836°C) and (f) 2332.3 s (836°C). black arrows indicate immobile features between (a)-(d), no common features could be identified for (b)-(e) and (c)-(f) in both cases, however, the stage was moved between frames. (Specimen 4.5).

The end inverse α→γ transformation, as seen in Figure 4.30(d-f), shows the greatest dissimilarities between cycles. Firstly, there is a difference in the number and orientation of the twin boundaries in the austenite, and this had an effect on how the interface itself is oriented. There are also differences in the growth of α3.

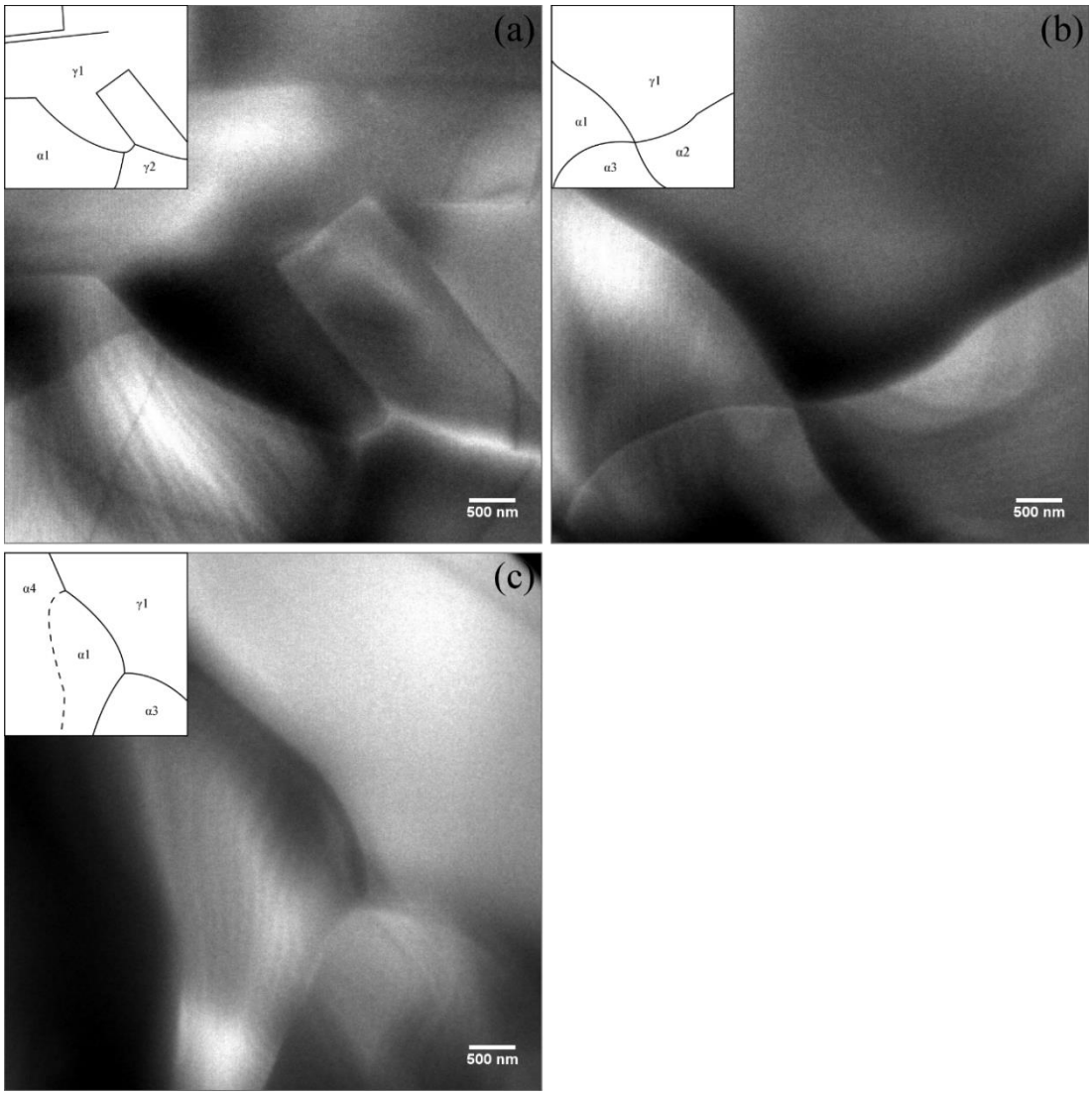

Figure 4.31: Bright field TEM of the interface at the beginning of the normal austenite to ferrite transformation for each cycle (a) at 1065.7 seconds (820°C) (b) 1749.1 seconds (821°C) and (c) 2435.1 seconds (823°C). Note that the specimen stage has been moved between each image to track the interface throughout the thermal cycle. (Specimen 4.5).

An equivalent series is shown for the austenite to ferrite transformation in figure 4.31 and 4.39. Figure 4.31(a) shows the start of the normal γ→α transformation, and so

shows the microstructure as it has developed during the stagnant stage from that shown in figure 4.30(d-f). The interface was curved in all three cases, although it is only in the first cycle that it was curved into the ferrite grain.

At the end of the normal γ→α transformation, figure 4.32(a-b), the similarities between cycles are much stronger with each forming a triple point with the α_2 grain. The interfaces themselves had become straight and have a very similar angle within the frame (<3^o difference across cycles).

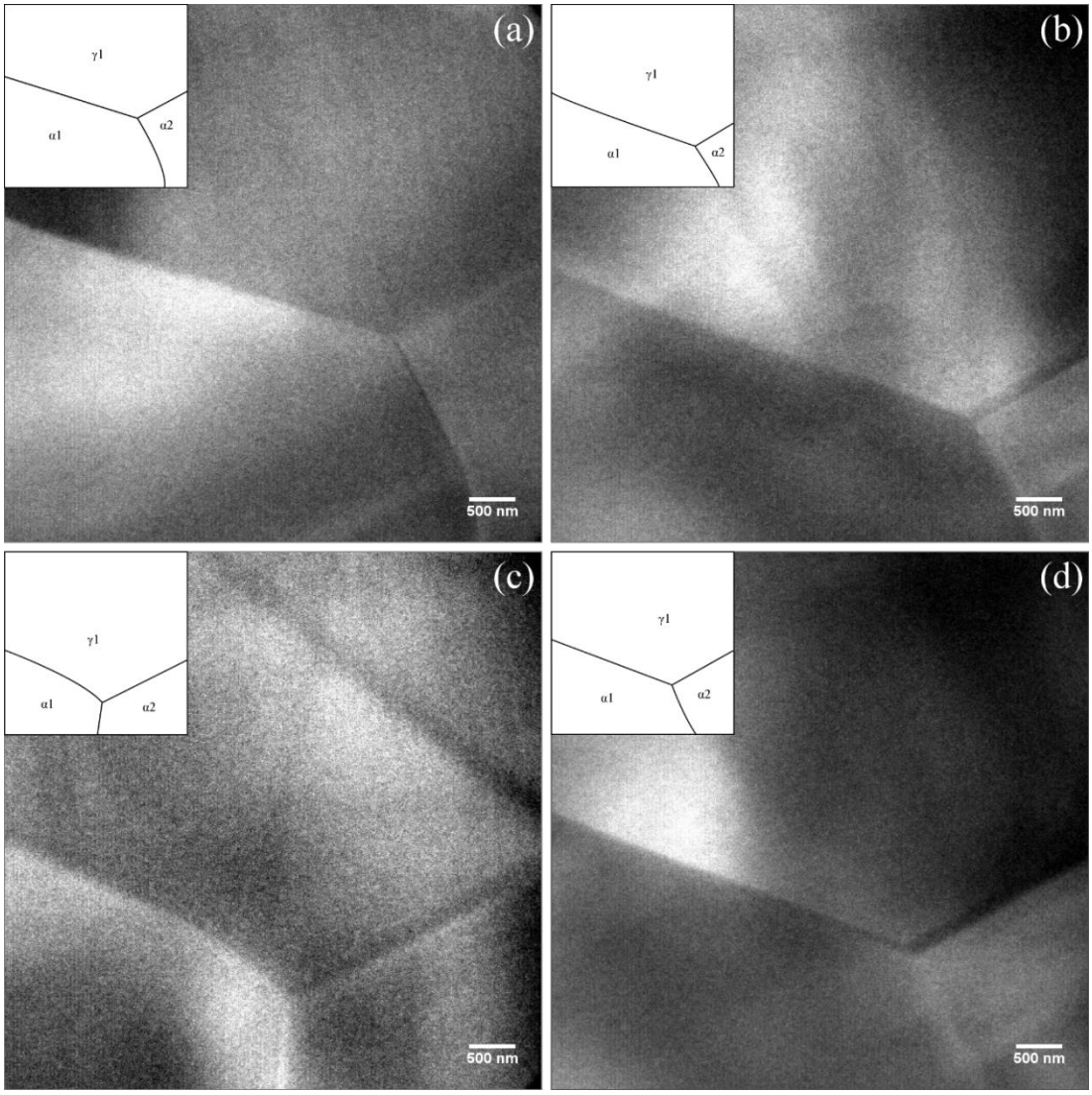

Figure 4.32: Bright field TEM of the interface at the end of the normal γ→α transformation for (a) cycle 1 at 1265.4 seconds (793^{o}C) (b) cycle 2 at 1951.1 seconds (792^{o}C) and the end of the inverse γ→α transformation for (c) cycle 1 at 1318.0 seconds (797^{o}C) and (d) cycle 2 at 1981.7 seconds (794^{o}C). Note that in (c) the focus is poor, resulting in a lower quality image – it is included only to qualitatively assess the interface morphology at the triple point and was not used in the kinetic measurements reported in chapters 4.8 and 4.9. No features were identified between frames (a)-(c) and (b)-(d) to indicate common positions, in both cases the stage has been moved manually. (Specimen 4.5).

The end of the inverse γ→α transformation, figure 4.32(c-d), does not show any significant changes compared with figure 4.30(d-e), although the interface in cycle 1 has developed a slight curve near the triple point. Likewise, compared with figure 4.26(a) the development of a more curved interface appears to be the only change over the austenite to ferrite stagnant stage.

Considered together these results show that there are some broad similarities in the microstructure and interface morphology between cycles when observed at equivalent stages. This indicates that there is, as expected, some reversibility in the transformations but that this is not perfect. Some of the greatest differences between cycles appeared in locations within the γ_1-α_1 interface where there were two or more grains of the growing phase competing, particularly during the ferrite to austenite transformation. For the interface itself, there was also seen to be significant changes to the morphology introduced by the presence or absence of growth twins in the austenite behind the interface.

4.16 Thermal Grooving.

The development of grooves on the surface of the specimen and its potential to affect the outcome of *in situ* TEM experiments was discussed in chapter 2. During the cyclic experiments the interface behaviour of one of the specimens was found to have been dominated by the presence of thermal grooves for part of the cycle. To eliminate such unrepresentative interfaces, it is important to consider how interface behaviour is affected by thermal grooving.

In the present set of experiments, thermal groove dominated behaviour was identified in specimen 4.1 during the stagnant stage which followed the α→γ transformation and then in the initial stages of the subsequent γ→α transformation. This interface is shown in figure 4.33 below. There are three reasons why thermal grooving presents the biggest problem during this part of the thermal cycle. Firstly, the development of thermal grooves is a temperature dependent phenomenon as it is surface diffusion controlled [116] [119]. Therefore, grooves will form and deepen most rapidly at the start of the cooling stagnant stage as this is close to the peak temperature of the cycle.

Secondly, during the α→γ transformation the interface was migrating towards the central hole and into a thinner region of the thin foil. This means that any shortening of the austenite-ferrite interface by thermal grooves will account for a proportionally larger reduction in surface energy. Finally, the interface is migrating slowly during the stagnant stage, giving a potential thermal groove more time to develop in any given area.

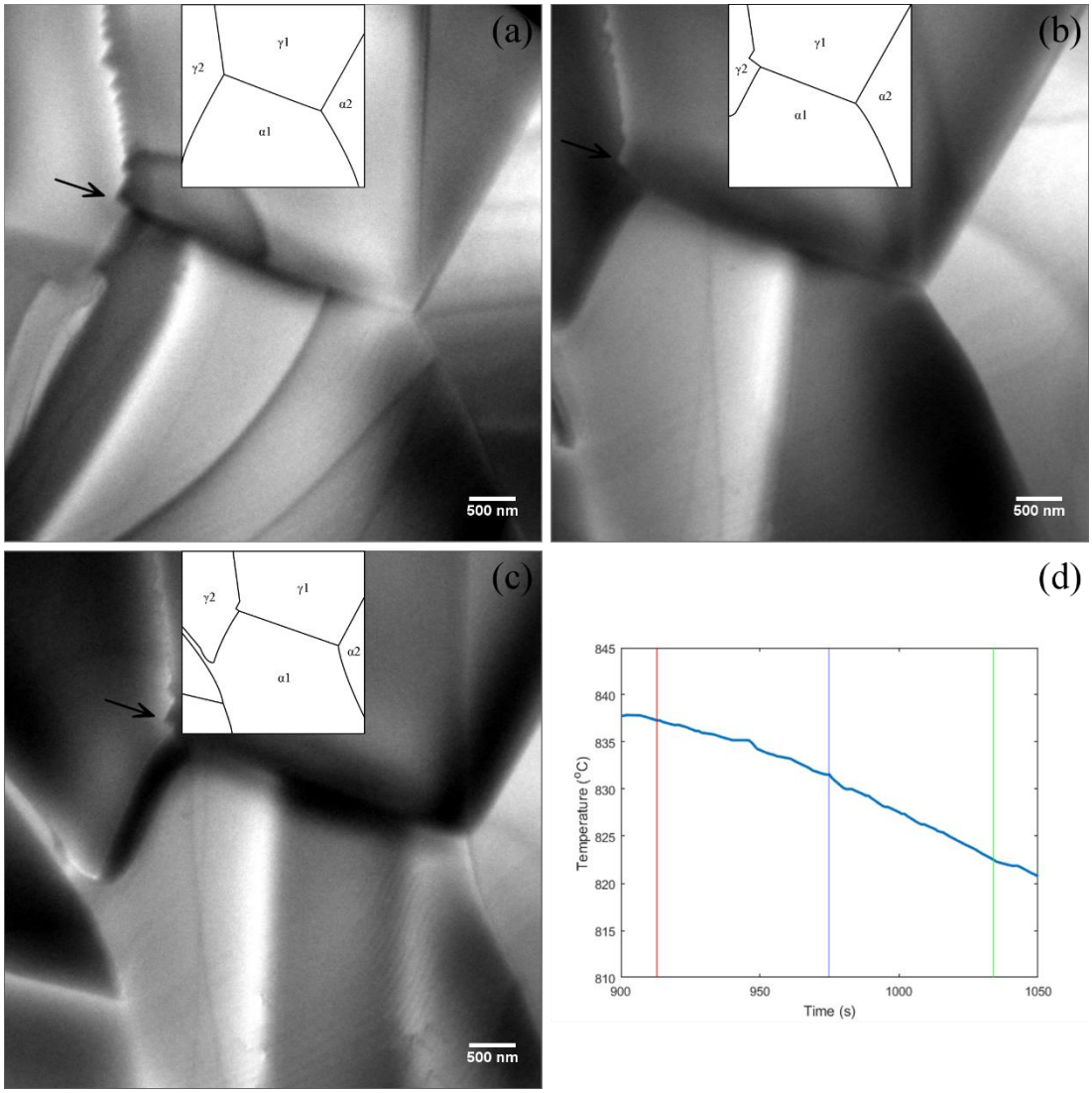

Figure 4.33: Bright field TEM of the development of thermal grooves at the austenite-ferrite interface at (a) 912.6 seconds (837°C) (b) 974.7 seconds (830°C) (c) 1034.1 seconds (822°C) and (d) showing the time-temperature position of each frame. Vertical lines, from left to right, indicate the time depicted in frames (a)-(c). Black arrows indicate features which occupy common positions between frames. (Specimen 4.1).

The development of the thermal groove over time, as it appeared under TEM observation, is shown in Figure 4.33(a-c). It is worth noting that the presence of a

thermal groove in the area around the interface is directly observable from figure 4.33(b) onwards. This takes the form of regions of dark contrast on either side of the interface. From the discussion in Chapter 2, it is clear that although the thickness of the foil should be reduced at the interface, this would be accompanied by the thickening of the foil on either side. This thickening resembles the thickening of the foil edges, figure 4.34, which is the result of a similar process where material is transported to thicker regions from the very thinnest parts of the foil [161].

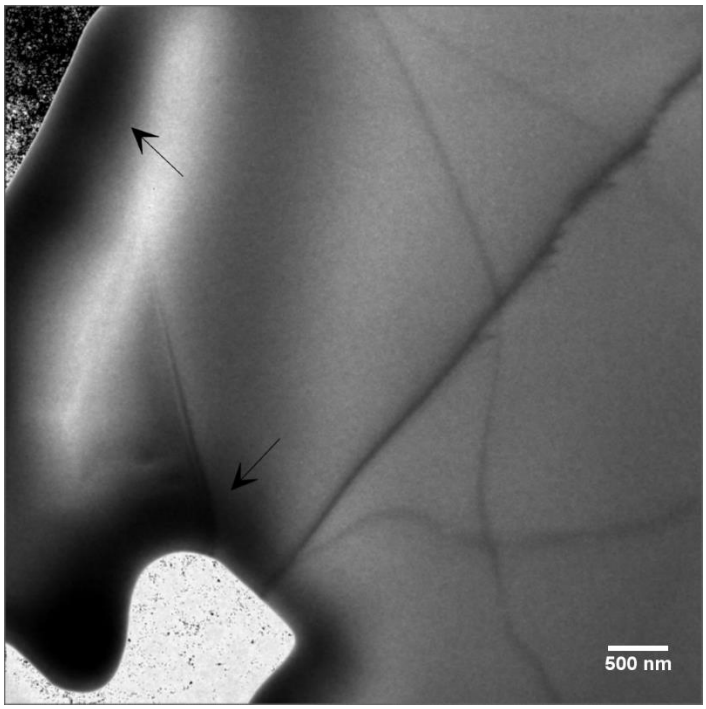

Figure 4.34: Bright field TEM of the appearance of thickening at the foil edges, indicated with black arrows, at 823°C after 288.4 seconds of heating. The oversaturated region visible in the image is the hole in the foil.

Unlike the stagnant stages seen in other specimens, as well as the heating stagnant stage in this specimen, the interface behaviour was not characterised by slow change in morphology or position but remained entirely static. The interface remained static after the specimen had been cooled sufficiently that the austenite to ferrite transformation was expected to have commenced. When the interface did begin to move, it was initially at a relatively small section of the interface. This is shown in figure 4.35(a-c) and suggests that initially there was a localised escape of the interface from the thermal groove, which then makes it possible for progressively larger sections of the interface to move.

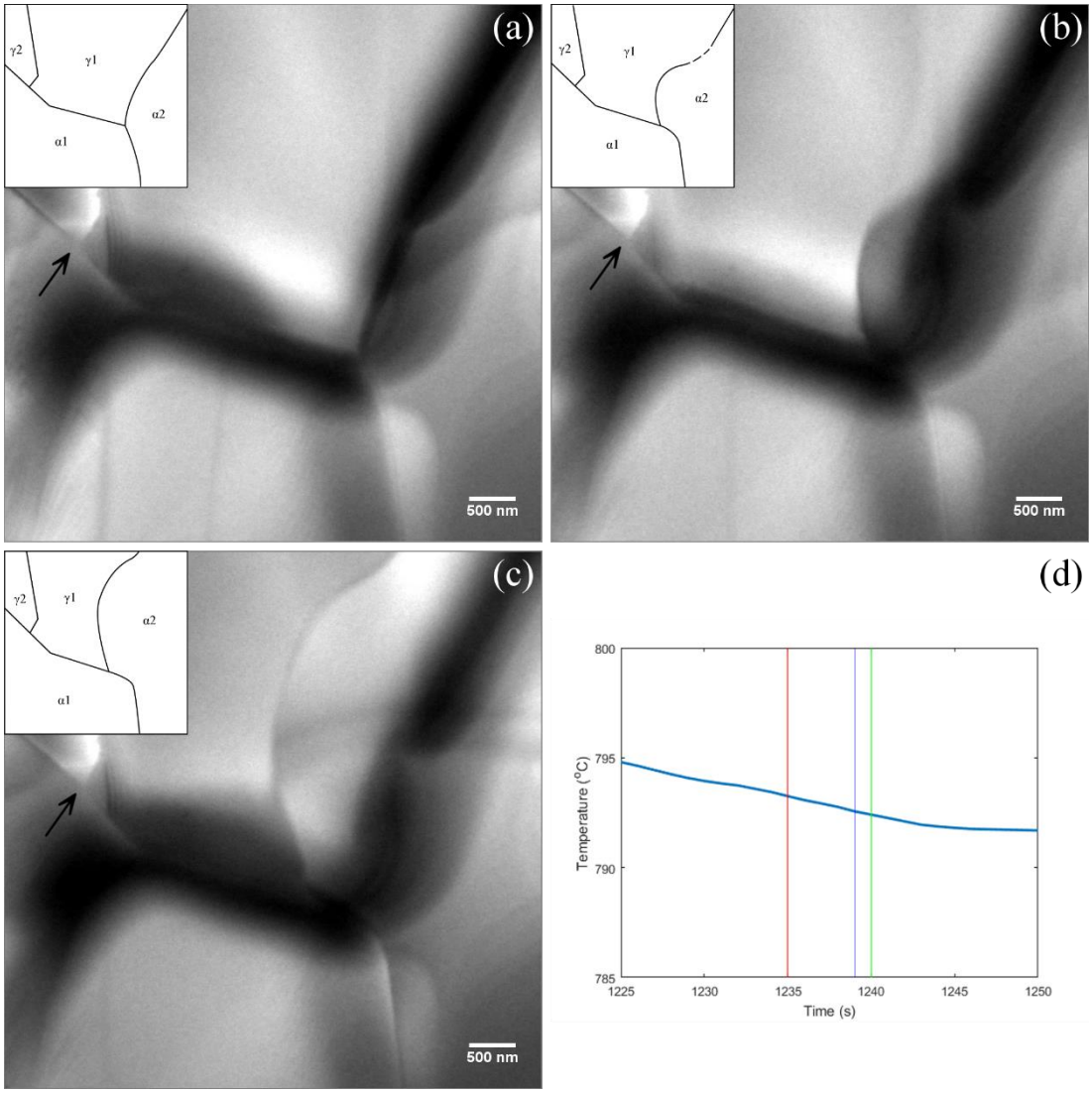

Figure 4.35: Bright field TEM of the austenite-ferrite interface escaping thermal grooves during cooling at (a) 1235.4 seconds (792°C) (b) at 1238.8 seconds (792°C) (c) at 1239.4 seconds (792°C) and (d) showing the time-temperature position of each frame. Vertical lines, from left to right, indicate the time depicted in frames (a)-(c). (Specimen 4.1).

Having escaped, the interface migrated rapidly before slowing down to more normal interface velocities. This is shown in figure 4.36. Movement of the interface was suppressed to lower temperatures, leading to a build-up in the driving force, resulting in more free energy available for the transformation when it finally became unpinned.

However, once the specimen had cooled to the T_1 temperature the interface migration returned to the expected behaviour during heating. The temperature at which the stagnant stage end and the normal ferrite to austenite transformation began is estimated to be 804-810°C, close to that estimated in other specimens. The interface velocities also display behaviour consistent with other specimens, increasing with increased

temperature and generally below 200 nm·s^{-1}. As can be seen from figure 4.37 there are two measured velocities significantly higher than this, which are associated with the development of the ledges shown in figure 4.24.

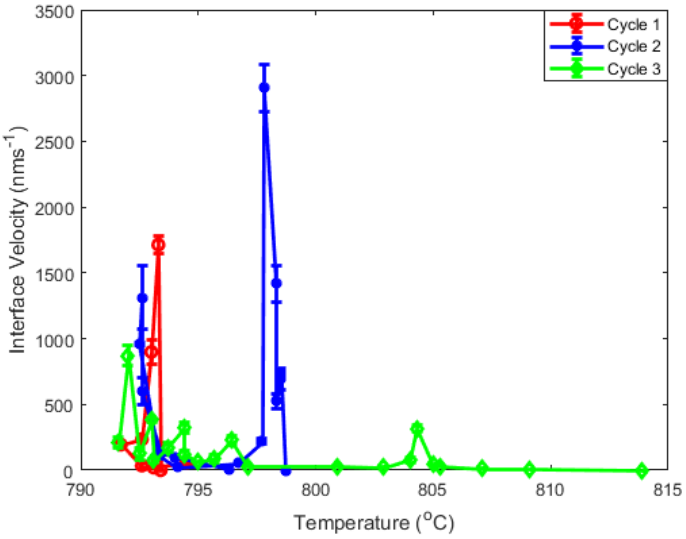

Figure 4.36: Graph of Interface velocity against temperature for the austenite to ferrite transformation in specimen 1. The movement of the interface began at lower temperatures due to pinning by thermal grooves.

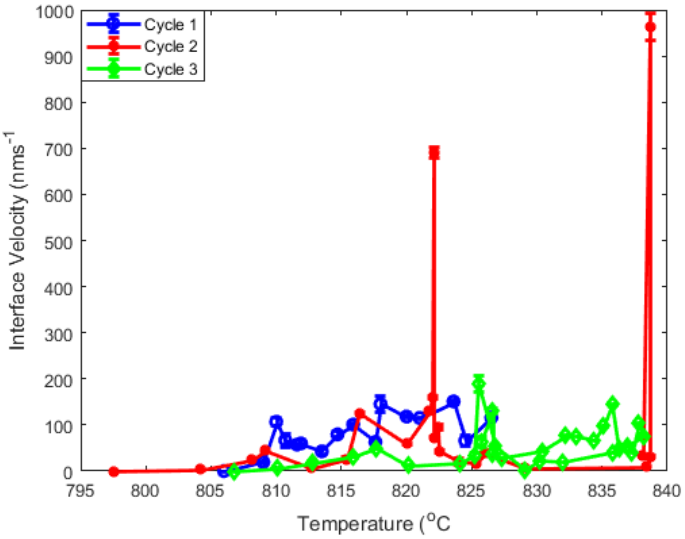

Figure 4.37: Graph of Interface Velocity against Temperature for the normal ferrite to austenite transformation in specimen 4.1.

The room temperature specimen was examined to confirm that the dark grooves in the bright field TEM images from the in situ videos are due to thickening of the foil. A bright field STEM image of the thermal grooves at room temperature shows that the

distinctive shape of the grooving had been retained on cooling, whilst EELS thickness measurements demonstrate that there is a significant change in foil thickness which corresponds with the changing contrast.

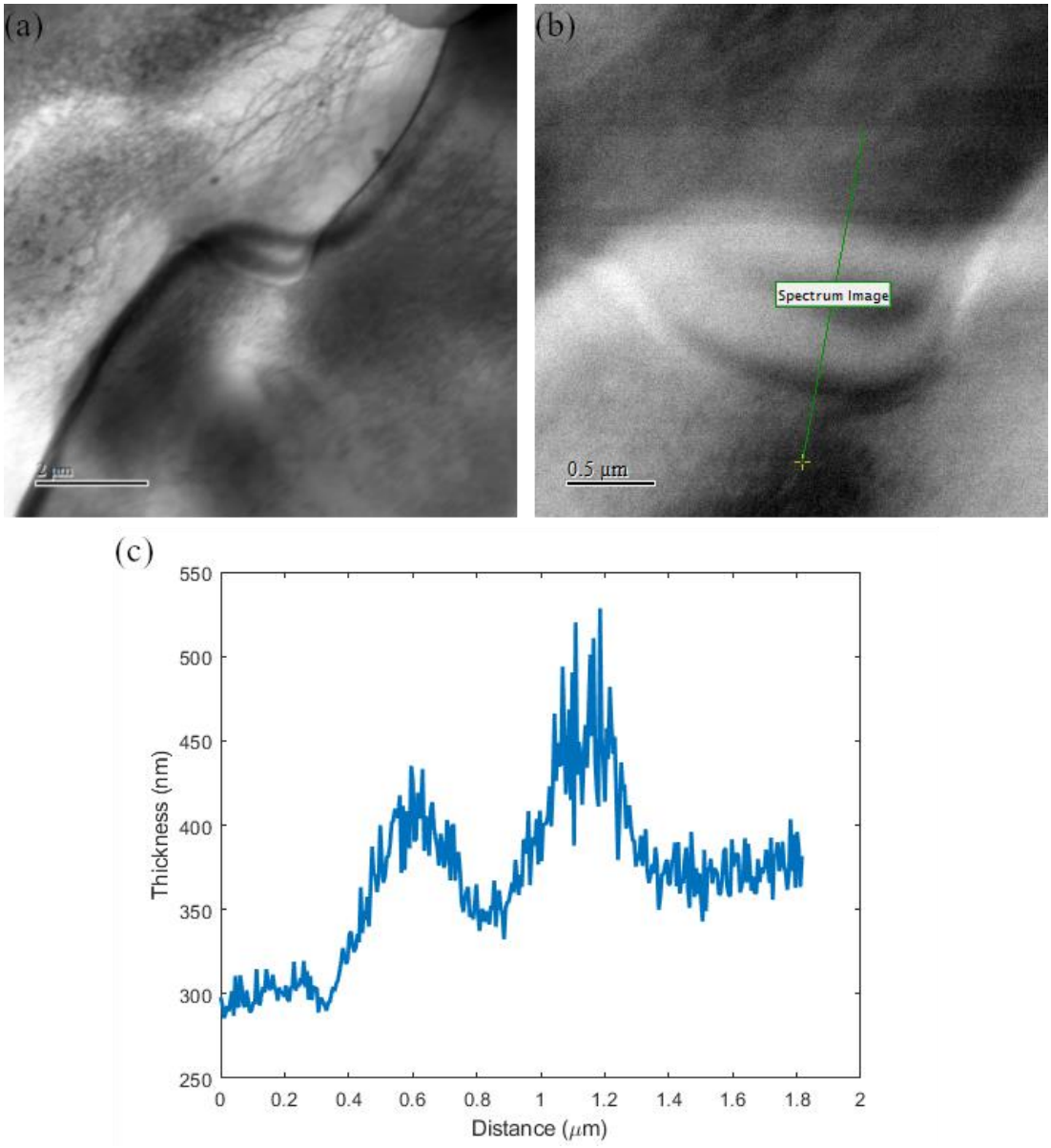

Figure 3.38: (a) Bright field STEM image of bands of dark (as in BF TEM) contrast in room temperature specimen, (b) Dark field STEM image showing the location of the EELS linescan and (c) the measured foil thickness demonstrating that the bands correspond to regions of increased thickness.

In summary, when the interface was pinned by a thermal groove this produced a characteristic effect to behaviour which can be identified by measuring the interface velocity. Furthermore, the presence of thermal grooves can be directly observed in the

TEM where they appear as regions of dark contrast either side of the interface and their nature has been confirmed using EELS thickness measurements. This ease of identification means that affected interfaces can be eliminated from further analysis resulting in a high degree of confidence in the validity of the remaining experimental observations.

4.17 EBSD and Texture Development.

As previously noted, it was possible to acquire selected area diffraction patterns for many of the grains under observation. During thermal cycling ferrite grains were most commonly seen with the [001] direction parallel to the electron beam. The use of TEM makes it difficult to sample a sufficiently substantial number of grains to ensure that this was properly representative of the texture. Therefore, EBSD was used to determine the orientation of ferrite grains in the foil after heat treatment. Figure 4.39 shows the pole figure for the as received material and for sample 4.2 after heat treatment.

The specimens had developed a clear cube texture after heat treatment, indicating that the observations in the TEM were representative of the overall orientation of grains within the thin foil.

In the case of assessing any texture in the austenite grains, it was not possible to carry out EBSD at temperature. Figure 4.40 shows how the austenite grains observed in the TEM were oriented with respect to the electron beam.

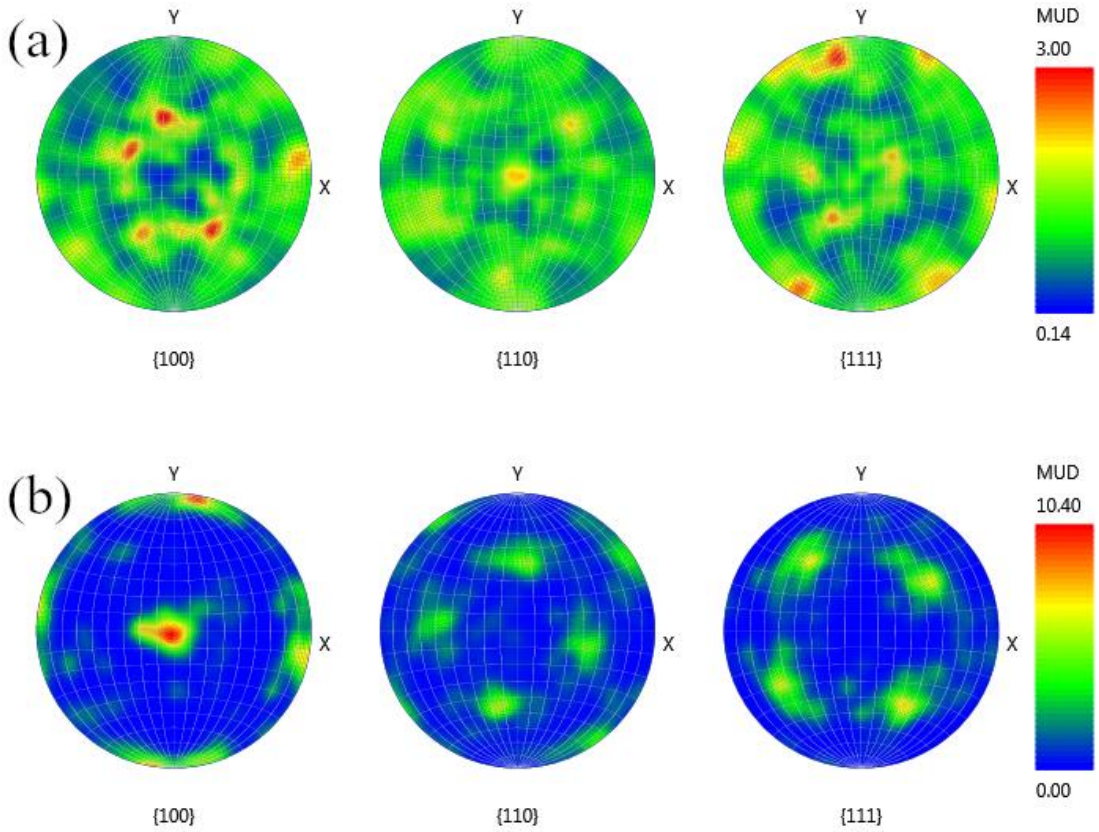

Figure 4.39: Pole figures for specimen 4.2 (a) before and (b) after heat treatment, showing a change to cube texture.

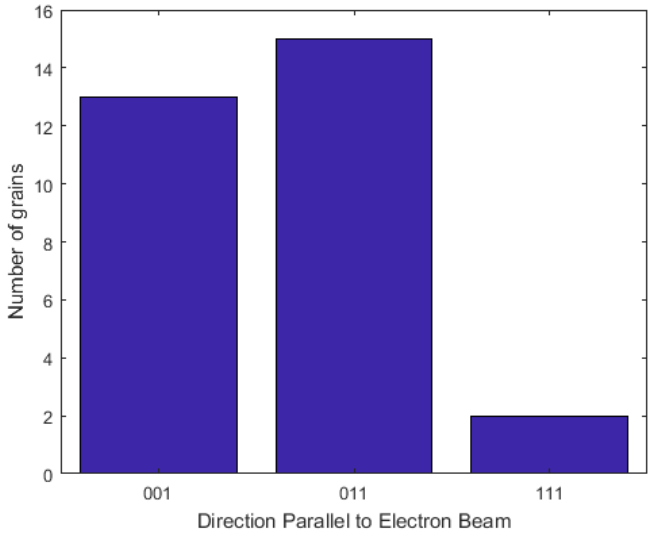

Figure 4.40: Graph of the number of grains with the [001], [011] and [111] directions parallel to the electron beam.

Overall, it appears that the interfaces observed did not have a completely random orientation between the austenite and ferrite phases. As such, the observed interfaces seen during *in situ* TEM may represent only a subset of the total population of interfaces which were being measured using dilatometry.

4.18 Discussion.

The expected transformation behaviour was observed and the distinct transformation stages associated with CPPT heat treatments could be identified. On cooling the expected, normal transformation from austenite to ferrite was observed. Immediately after reaching the T_1 temperature, when heating of the specimen began, the austenite to ferrite transformation was observed to continue – the so-called inverse $\gamma \rightarrow \alpha$ transformation. Finally there was a period in which the interface moved only slowly, without ever becoming completely static, which continued on heating, and this corresponds to the stagnant stage identified from dilatometry. The same process can be observed for the ferrite to austenite transformation. There is good semi-quantitative agreement between the behaviour of the interface in the TEM and in the dilatometry as can be seen by comparing figure 4.12 with figure 4.4.

There is reasonably good reversibility of the interface between cycles as can be seen in figures 4.29-4.32. This applies not just to the position of the interface, but there are also broad similarities in terms of the interface structure between cycles.

The temperature range of the stagnant stages were estimated to be 15C for the stagnant stage which occurs on cooling and 16C for the stagnant stage which occurs on heating. The corresponding inverse transformations were estimated to last 2.4C and 2.5C. In each case this is within 2C of the estimate for dilatometry. Part of this discrepancy can be attributed to the difficulty in estimating the end of the inverse transformation and the stagnant stage.

Chen et al. [7] estimated the effect of nominal Mn concentration on the stagnant stage as 35C per wt% Mn, by modelling the behaviour of Fe-0.02C-XMN (X= 0.1, 0.2, 0.3) during cyclic partial phase transformations. For a 0.5Mn steel this would correspond to a stagnant stage of 17.5C. Adjusting for the different heating and cooling rates used

(10°C/min against 8.6°C/min) the present experiments would be expected to exhibit a stagnant stage of approximately 15C. This is in good agreement (<1°C) with both stagnant stages as measured in TEM and indicates that similar conditions prevail at the interface in each case. This level of agreement provides a good indication that interfacial conditions are similar in both the TEM and the bulk.

The agreement in the temperature at which the peak $\gamma \rightarrow \alpha$ velocity occurs also provides an indication that interface conditions in the TEM is representative of bulk behaviour. In both cases, the temperature at which the peak velocity occurred during the austenite to ferrite transformation was 814-816°C.

Although nucleation of both the ferrite and austenite occurred outside the field of view, it was possible to capture images of the ferrite grains before they had grown significantly, as shown in figure 4.11. In each case the ferrite grain was first observed at austenite grain boundaries or triple points, this agrees with bulk observations [162, 28]. The grains in figure 4.11(d) and 4.11(e) show some evidence of having grown preferentially along the austenite grain boundaries and had an aspect ratio of roughly ~1/4, slightly lower than the expected 1/3 [28], although this is probably not significant due to the small number of grains measured in the present study.

Where the orientation relationship (OR) between the austenite and newly nucleated ferrite grains could be obtained, these were found to be close (within 3° and therefore within the maximum achievable accuracy using selected area diffraction [163]) to the Nishiyama-Wassermann OR [30]. Interfaces between grains with the N-W OR are indicated in figure 4.11 with the green arrow. Greater curvature of the interface was seen as the interface deviated from well-defined orientation relationships. In figure 4.11(e), for example, the interface indicated with the blue arrow was close to the N-W relationship differing by a ~7° rotation of the ferrite around the [001] direction.

Throughout the transformation the interface showed a shifting morphology changing between straight, smoothly curved and wave-like for the portions within the field of view. The interface between the main ferrite and austenite grains under observation was frequently seen to differentiate into distinct segments through the presence of twin boundaries which intersected with the interface, as in figures 4.19 and 4.20. On a more limited scale the influence of other grains of the growing phase affected the

morphology and growth direction of the interface adjacent to interface-grain boundary triple points, illustrated in figures 4.25 and 4.26.

The fastest moving sections of interface were those adjacent to rapidly migrating triple points, forming a localised "V" shape to the interface, as in figure 4.25 and 4.26, followed by the curved interfaces. During the normal transformations the interface displayed a (relatively) rapidly evolving morphology. The interface often shifted between a straight, curve or wave-like morphology. In the first two cases the migration was smooth, with little change in the shape of the interface. However, when the morphology shifted to a wavelike morphology, the migration became more undulating with a less constant interface shape, as in figure 4.23. Overall, parts of the interface could be seen to switch between these competing morphologies over the course of the transformation, particularly in figure 4.19.

The evolution of the morphology also displayed a long-term trend over the course of a single T_2-T_1-T_2 cycle. On cooling, the stagnant stage was characterised by the slow migration of the boundary accompanied by the reshaping of the interface, which had the effect of inverting the curvature of the interface. This was not the case across all cycles. For example, this did not occur in the evolution of the interface during cycle one, as can be seen by comparing figure 4.32(d) and 4.33(a). In this case, this may be due to the complex twin structures behind the interface. In the case of the stagnant stage on heating the inversion of this curvature did not occur until the ferrite to austenite transformation had commenced.

In both cases, the interface became more irregular when the normal transformation commenced, displaying the dynamic behaviour outlined above. As the temperature approached the T_1 or T_2 temperature, the interface became more regular, becoming straighter or smoothly curved, which continued into the inverse transformation.

The morphological observations during the normal transformation are similar to those of Onink et al. in Fe-C alloys isothermally transformed between 710-770^{o}C [122]. In this case interfaces were also found to vary between curved and nearly straight morphologies and interfaces were also found to undergo segmentation. Smooth, gently curved interfaces were also observed in Fe-C-Mo steels by Purdy [137] alongside a small number of facetted interfaces. Observations using HT-CLSM also found curved α/γ transformation interfaces [129] [142], and interfaces containing a mixture of

smooth and jagged regions [141]. In the mixed-mode model the changing morphology of the interface contributes to a gradual change in the nature of the transformation [64].

The observed migration during the stagnant stage contrasts with the HT-CLSM observations of Chen et al. [88] where the interface was found to be immobile. This difference is attributed to the fact that the migration is less than 1 micron and would therefore be difficult to observe using confocal microscopy.

During the slowest period of the stagnant stage, the interface migration was small and within the error of measurement for the interface position. From bulk studies, the thickness of the Mn enriched region found from atom probe tomography (<5nm) in a Fe-0.6C-1.43Mn steel [83, 84] or predicted from DICTRA (1nm) [164]. However, for the magnification used in the present experiments, measurements of this magnitude could not be made with confidence.

General observations during the normal transformation captured a range of behaviour including dislocation movement and low angle grain boundary formation, the formation and lateral migration of growth ledges, and dynamic triple point behaviour.

Dislocation movement was observed in the foils both during interface migration, as in figures 4.27 and 4.28, and in the period before migration began. Dislocations were most clearly visible on the ferrite side of the interface, although dislocations were also observed in the austenite. Periods of increased dislocation activity often corresponded with the austenite to ferrite transformation, indicating that the build-up of stress due to differences in specific volume between the two phases was potentially the cause of this activity. These dislocations moved towards the transformation interface before being eliminated.

Dislocation movement was also observed during austenite growth, as in figure 4.28, one notable example being the formation of a new boundary in the ferrite ahead of the α/γ interface The process by which this occurs appears similar to traditional descriptions of recovery where large numbers of dislocations align to form low angle grain boundaries [165].

The triple point behaviour indicated that in cases where there are two grains of a growing phase, there is competition between these two grains, resulting in the lateral displacement of the triple point. For the normal grain boundaries this took the form of

a continual readjustment of the boundary behind the migrating transformation interfaces, to accommodate the lateral displacement of the interface, as illustrated by figure 4.25.

In contrast, the facetted boundary shown in figure 4.26, the lateral displacement of the triple point was initially accommodated by the creation of a stepped boundary. This was subsequently offset by the migration of the boundary minimising the number of steps. It can be inferred that the driving force for this boundary migration was low, due to the similar surface energies of the two grains (as they were both oriented the same with respect to the foil surface) and because the migration did not result in a reduction in the overall length of an already facetted interface.

In addition to this competitive behaviour, in pairs of growing austenite grains which were in partial contact, the nearby α/γ interfaces were observed to accelerate towards each other. An example of this is shown in figure 4.20, where the facing interfaces formed a single γ/γ grain boundary with a zip like motion. This may occur for small separations, due to the overall reduction in interface energy of a single grain boundary relative to two α/γ interfaces.

Quantitatively, the agreement between the behaviour was poorer for the interface velocities and the change in position compared to the good agreement in stagnant stage temperature range. Comparing the velocities, the peak TEM measurements were a factor of 11 times higher than those obtained in dilatometry for the austenite to ferrite transformation, and a factor of 5 times higher for the ferrite to austenite transformation (excluding specific behaviour such as the development of ledges at the interface). This is not attributed to artefacts such as local beam heating, as this would be expected to enhance one transformation whilst retarding the other. The good agreement at which the peak temperature occurs in the austenite to ferrite transformation, as well as the temperature ranges of the inverse and stagnant stages, indicates that interfacial conditions are similar in both the TEM and dilatometry.

Furthermore, the difference in velocities can be partly attributed to the existence of a thermal gradient between the two thermocouples spot welded to the specimen during the dilatometry experiments on the order of 3C. As grains along the length of the specimen reach the peak velocity at different nominal temperatures, the peak velocity would be averaged out resulting in a lower overall estimate. On heating, the ferrite to

austenite transformation retains a well-defined peak as this remains the maximum temperature reached by all parts of the specimen. Over the entire cycle, the difference in the overall migration distance is a factor of ~2-3, indicating that average velocities over the course of the cycle are closer than a comparison of the peak velocities might imply.

It is important to consider that there is a contribution from the assumed geometry of the specimen when calculating the migration distance from dilatometry. Changing from spherical to cubic geometry increased the predicted migration distance by 3.4 μm. For this reason the migration distance is not well defined when comparing the 3D dilatometry case with the 2-dimensional TEM observations (as well as the 1D modelling performed using DICTRA).

Van Leeuwen et al. [166] compared the kinetics of a more realistic model for the austenite grain geometry to the spherical model. The grain geometry was assumed to be a tetrakaidekahedron, which possesses grain edges and corners, unlike a spherical grain and so could incorporate more realistic nucleation. For a transformation which proceeds at constant velocity and with ferrite nucleating on each grain corner, a tetrakaidekahedron predicts a slower transformation than the equivalent spherical austenite grain. If fewer nuclei were assumed to form within the grain, the transformation rate became even slower.

In the present case, it is the rate of transformation that is fixed, and so the spherical model would be expected to underestimate the migration velocity and distance. Cubic growth is assumed by Liu et al. [159] [157] and Kempen et al. [160]. In the present study closer agreement, a factor of ~2, is achieved assuming cubic growth.

The thin foil did not appear to have undergone any significant decarburisation over the timescale of the experiment. Had the foil decarburised, this would have been accompanied by an increasing quantity of ferrite remaining at the T_2 temperature. However, the position of the interfaces at the beginning and end of each cycle were similar in each case, indicating that the nominal composition of the foil remained largely unchanged.

It is well known that polycrystalline materials develop surface grooves at grain boundaries at elevated temperatures and as discussed in chapter 4.16 the present experiments were no exception. This thermal grooving represents a hazard during

cyclic partial phase transformations as the pinning of the interface by such grooves could be mistaken for the stagnant stage. However, the presence of thermal grooving can be directly observed from TEM images as shown in figure 4.33 and 4.35.

It is also possible for thermal grooves to form on moving boundaries [117], which may be responsible for the "ghost" boundaries [167] which can be seen in the ferrite grains in, for example, figures 4.23. However, Lillo et al., in an in-situ study of strain induced grain boundary migration in Al, indicate that the foil thickness changes which give rise to the appearance of ghost boundaries is also affected by the stress state of the migrating boundary [168].

In a thermionic emission study of proeutectoid ferrite growth in Fe-C-Mo steels Kinsman and Aaronson [169] found that during isothermal holding between 875-725^{o}C surface effects such as thermal grooving had no retarding effect on the transformation. However, it should be noted that this technique is different to HT-TEM and used a bulk specimen with one free surface, in contrast to a thin foil.

Likewise, in a HVEM study of transformation interfaces in Fe-C and Fe-C-Mo steels, Purdy [137] found that incoherent interfaces held between 700-800^{o}C were sensitive to temperature changes of 3C. This suggests that in this case thermal grooving was not severe enough to exert a pinning effect on the interface within that temperature range. This would agree with the behaviour of specimen 4.1 in the present work, where the stagnant stage at the T_2 temperature (~840^{o}C) suffered from severe pinning but the stagnant stage at the T_1 temperature (~790^{o}C) did not.

As shown in chapter 4.16 the effect of thermal grooving can be identified and eliminated from further analysis, increasing confidence that the remaining interface behaviour is unaffected.

The effect of the electron beam also needs to be accounted for. Potential radiation damage of the specimen can be ruled out as the accelerating voltage of the microscope (300 kV) is below the threshold voltage for iron [114]. In terms of localised heating, under normal imaging conditions the temperature of an Fe foil observed at 100 kV can be expected to increase by 70C [109]. However, in the present experiments beam heating did not appear to influence the transformation behaviour. The estimate of the holder-specimen temperature difference made in chapter 3.1 was made with the electron beam turned off.

In the current experiments an increase of 70C would have been expected to increase the T_1 temperature to the fully austenitic region. Even a smaller increase of 20C would have increased the T_2 temperature to above the A_3 temperature. This did in fact occur in two of the five specimens, but it is not attributed to the effect of the electron beam. This is because the entire specimen had become fully austenitic, not just the area under observation at the time. Furthermore, in all specimens, when a ferrite grain or austenite-ferrite interface first came under observation the motion of the interface was not reversed, as would be expected had significant heating occurred. For this reason, the heating effect of the electron beam is considered to be smaller than the temperature differences between specimens.

It is therefore unlikely that experimental artefacts like decarburisation, local heating or thermal grooving were responsible for the discrepancies between the TEM and dilatometry. One factor which may be responsible for this discrepancy is the difference in interface density. The maximum measured displacement of the interface over a single cycle in the TEM was 19.5 ± 0.3 μm (in 2 dimensions) against a measured average ferrite grain size of 40 μm in the dilatometry specimen (in 3 dimensions). This implies that the interface density may be lower in the area observed with TEM compared to that assumed for the bulk and so the interfaces observed during TEM experiments will be less affected by soft impingement. Chen et al. [88], during cyclic HT-CLSM experiments on a lean Fe-C-Mn steel, found that the enhanced impingement caused by a smaller γ grain reduced the interface migration by ~4 μm.

This effect may be increased by the fact that the ferrite was seen to form in the thinnest regions of the thin foil. This meant that migration of the observed interfaces took place towards or away from the central hole. Consequently, the carbon concentration gradients ahead of a growing ferrite grain would be, as a general tendency, parallel to those of nearby ferrite grains. The overlap of those concentration gradients would therefore have a smaller effect on the interface than in the case of a similar pair of interfaces with no constraints on the direction of migration.

A further possibility is that the microstructure produced by this initial heating is not truly representative of the bulk. There is a clear surface effect favouring γ grains with the [001] and [011] directions, and α grains with the [001] direction, parallel to the electron beam. An increase in the area fraction of [001] and [111] grains was observed

for grain growth in Ni and Cu thin films [133], with a corresponding reduction in [011]. Typically, for FCC metals the surface energy of the planes is lowest for the close packed {111} planes, increasing for the {100} then {110} planes [170]. For bcc metals, the close packed {110} plane has the lowest surface energy followed by {100} and {111} [171]. Gautam et al. [172] found a <100>//ND and <110>//ND fibre texture in a surface monolayer for a Fe-C-Mn-Al steel after a α-γ-α transformation in vacuum. This development was attributed to surface energy minimisation, noting that elastic stress relaxation models predict only a <100> orientations.

This indicates that the texture found in the present experiments cannot necessarily be attributed exclusively to surface energy minimisation, as the ferrite grains observed in the TEM were all found to have the [001] direction parallel to the beam. The presence of an additional free surface may have enhanced the role of stress relaxation in selecting grain orientation.

One consequence of this is that the interfaces observed in TEM experiments will not be randomly oriented. As such the TEM observations may represent only a subpopulation of all interfaces found in bulk materials. For these interfaces the [001] direction was parallel to the beam direction in both phases.

Finally, even amongst the successful experiments the behaviour was not necessarily identical, as can be seen from the range at which the local area became fully austenitic in figure 4.6. This indicates that there is some variability between the areas under observation in certain specimen's. This variability may also manifest during thermal cycling in the two-phase region.

4.19 Chapter Summary.

This chapter presents the results of cyclic partial phase transformation experiments performed using in-situ hot stage TEM. The observed interface behaviour shows good semi-quantitative agreement between the behaviour found in the TEM and the behaviour in the bulk as measured using dilatometry. The stagnant stage was found to be between 15C and 16C, for heating and cooling respectively, showing reasonable agreement with the bulk, kinetic modelling and previous studies.

The evolution of the interface morphology was observed throughout the thermal cycling. During normal transformation, the interface was seen to switch between a straight, curved or wavelike morphology with no observed microstructural cause. There were also long-term trends in the interface morphology over the course of the entire cycle, with the interface becoming straighter or more smoothly curved towards the T_1 and T_2 temperatures and during the inverse transformation. The interface continued to migrate during the stagnant stage with some differences in behaviour between heating and cooling. During cooling the interface morphology gradually changed, generally inverting the curvature of the interface. During the stagnant stage which occurred on heating the morphology remained more stable until the normal ferrite to austenite transformation began. The interface showed equivalent behaviour and morphology during each of the T_1-T_2-T_1 cycles.

The interface was observed to interact with dislocations within the ferrite, with dislocations typically annihilating at the interface or nearby grain boundaries. Growth twins in the austenite were observed to have a significant effect on interface behaviour, primarily by causing the interface between an austenite and ferrite grain to segment into multiple subsections with distinct behaviour, morphology and migration paths.

Quantitatively, agreement with bulk or kinetic modelling data was less satisfactory with the observed interfaces migrating a factor of 2-3 times further in the TEM than expected. Some experimental artefacts potentially responsible for this were considered and appear to have either a negligible effect, in the case of decarburisation or electron beam heating, or could be easily identified and eliminated from further analysis as with thermal grooving. Potentially this disparity could arise from changed soft impingement conditions in the TEM compared to the bulk, or from the assumptions made about 3D grain geometry for the dilatometry experiments.

5. Cyclic Partial Phase Transformation Experiments: Fe-0.1C-1Mn.

5.1 Introduction.

Cyclic experiments were performed on a ternary steel with a composition of Fe-0.1C-1Mn. By increasing the Mn content, the effect that substitutional alloying elements can have on the interface behaviour can be compared with the Fe-0.1C-0.5Mn experiments reported in chapter 4. Furthermore, steels of similar composition have been studied using modelling and dilatometry [87].

The transformation behaviour of this composition was expected to differ from the 0.5Mn steel, with lower rates of interface migration and a smaller distance migrated by the interface overall. It was also expected that the interface should have a longer stagnant stage approximately twice that of the 0.5Mn steel.

Two successful experiments were performed demonstrating comparable interface behaviour, with all of the expected features of cyclic partial phase transformations identifiable from the TEM recordings. However, more than 10 attempts were made to record cyclic transformation with specimens of this composition.

The primary outcome of these experiments is to assess how the interface morphology is affected by the increased levels of Mn present in the steel, with a consequent increase in the enrichment at the interface during phase transformations.

5.2 TEM Experimental Outline.

Table 5.1 outlines the experiments that provided images used in this chapter. There were also multiple failed specimens. Generally, the reasons for failure were due to the electron transparent region of the specimen becoming completely ferritic during thermal cycling. This may not necessarily indicate that the specimen itself was fully ferritic, but potentially that any cyclic transformations that were occurring took place within the thicker regions of the specimen.

Table 5.1: Table of Specimen number and outcome.

Specimen number	Success/Failure
5.1	Success
5.2	Partial Success

Figure 5.1 shows the heat treatment that both specimens were subjected to. The T_1 and T_2 temperatures were 770°C and 820°C. These temperatures are both within the two phase α+γ region, and were selected such that the transformation was expected to be governed by LE-NP kinetics. In addition, the temperature range is the same as that for Fe-0.1C-0.5Mn (50C), with a similar change in the equilibrium volume fraction of ferrite (0.4).

Figure 5.2 shows examples of the starting microstructure. As shown at lower magnification in chapter 3, the microstructure consisted primarily of equiaxed ferrite grains with a small amount of bainitic ferrite. Carbides were also found to be present in the ferrite grains, these were identified as Fe_3C carbides through selected area diffraction (5.2(d)). The zone axis diffraction pattern in 5.2(e) shows that the ferrite is free from oxides on the surface.

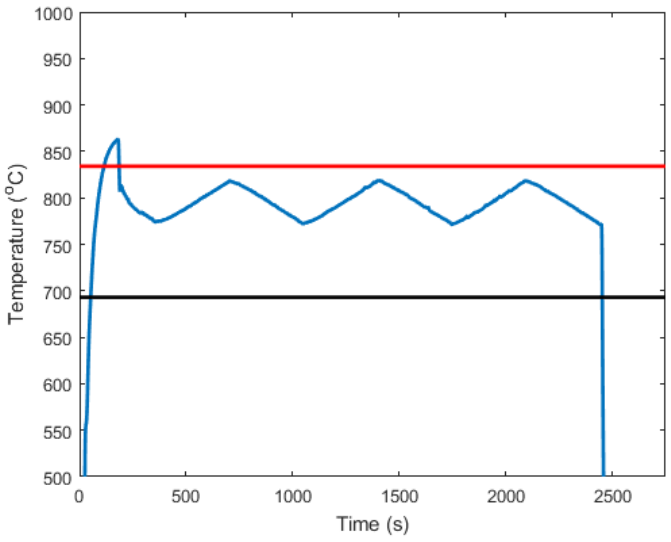

Figure 5.1: Graph of temperature against time showing the applied heat treatment for Fe-0.1C-1Mn specimens, with the upper and lower temperature of the two phase region marked by the red and black lines respectively.

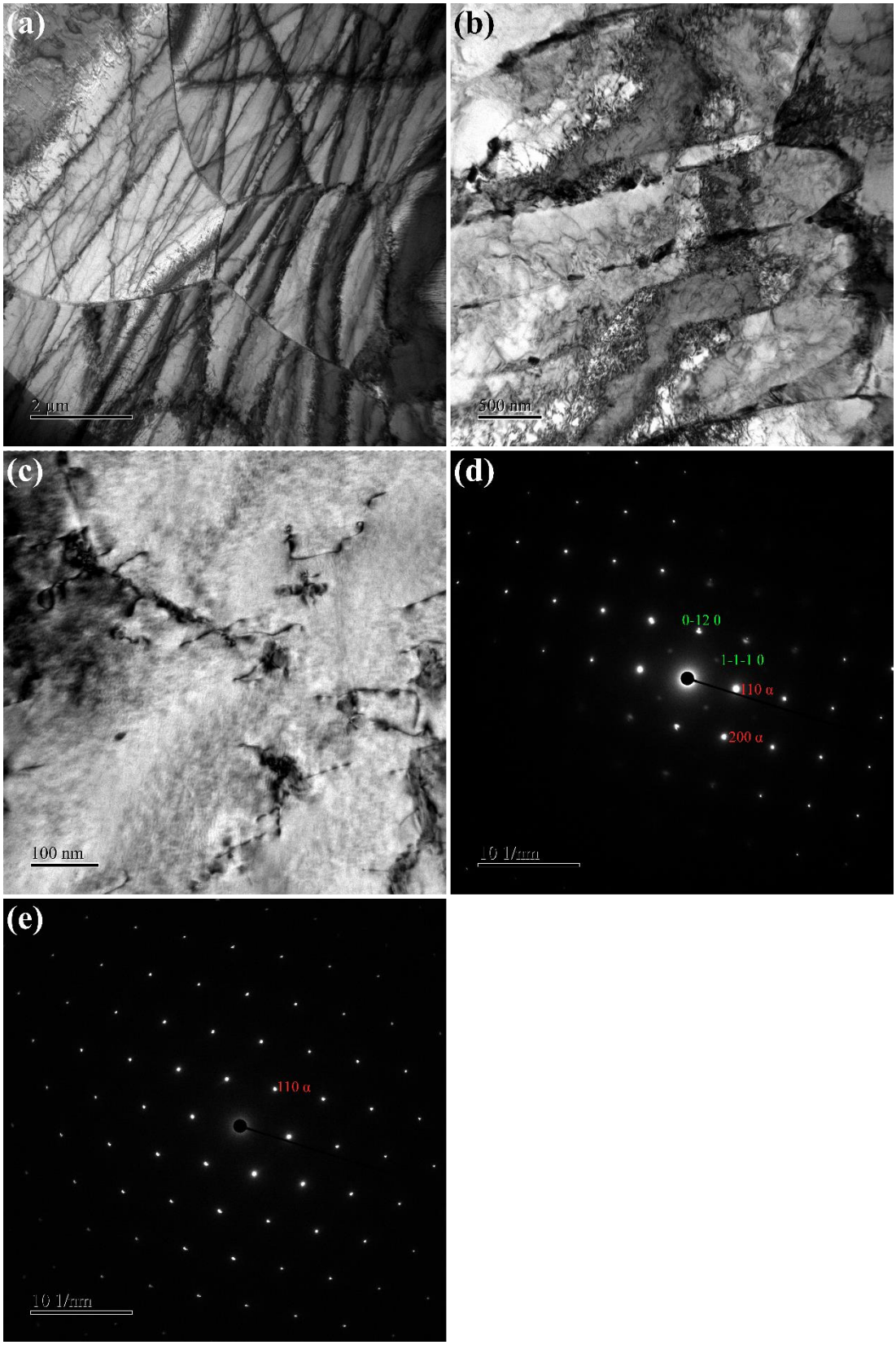

Figure 5.2: Bright field TEM of the microstructure immediately prior to heat treatment (a) ferrite grains, (b) bainitic ferrit, (c) carbides within the ferrite grains, (d) selected area diffraction pattern obtained from the ferrite grains and cementite precipitates and (e) Zone axis diffraction pattern showing the ferrite free from surface oxides.

5.3 Austenite Microstructures and Initial Austenite-Ferrite Interface Formation.

As in the case of the 0.1C-0.5Mn steel the austenitic microstructure displayed predominantly smoothly curved grain boundaries, with austenite grains containing significant number of growth twins. Figure 5.3 shows examples of the growth twins found in the austenite.

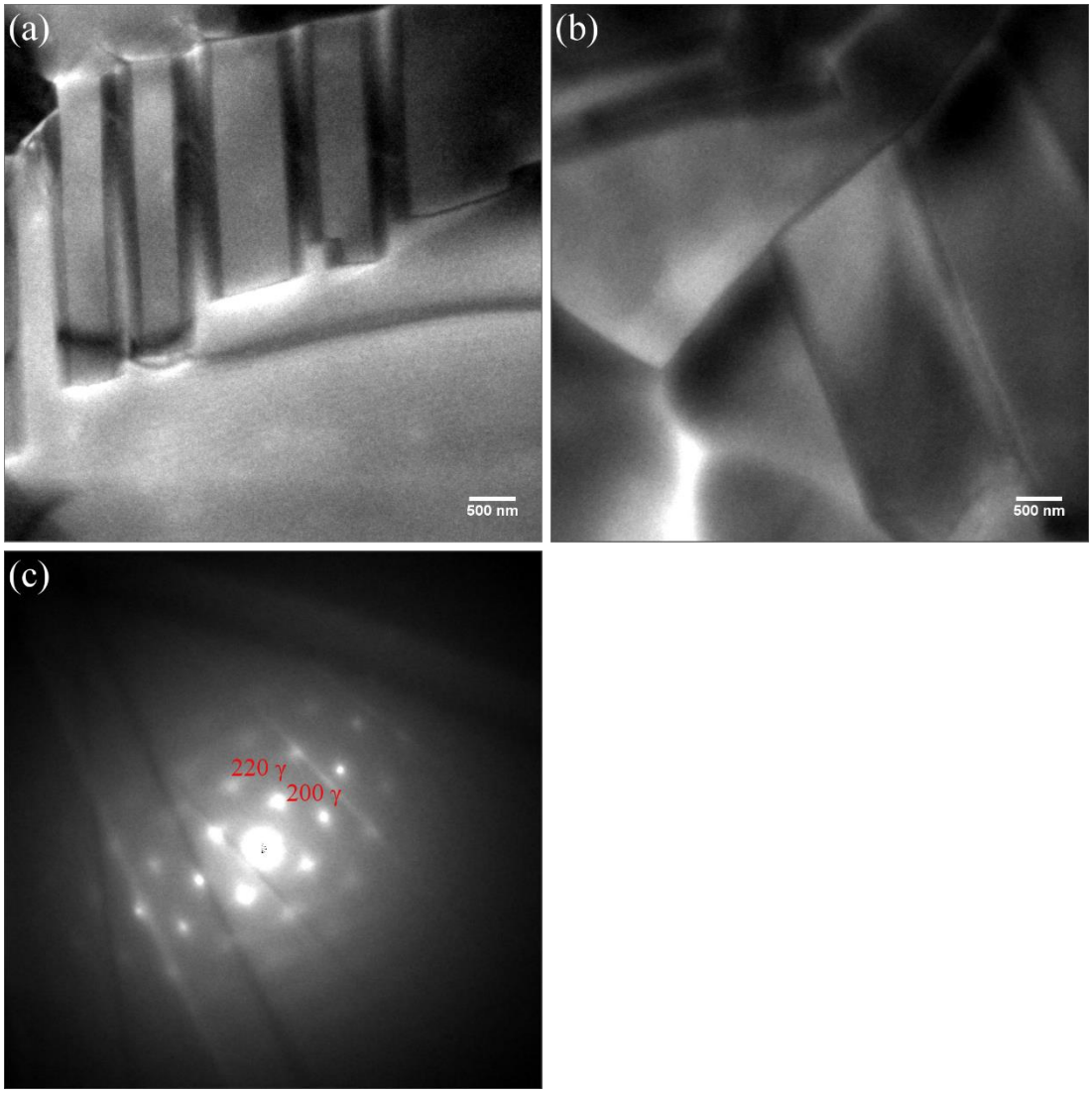

Figure 5.3: Bright field TEM of the austenite microstructure in regions with a high density of twin boundaries. At (a) 855°C and (b) 811°C. Smoothly curved grain boundaries are also apparent in (b). (c) Selected area diffraction pattern of the austenite along the [001] zone axis, at 835°C. From specimen 5.2.

Figure 5.4 shows early ferrite grains captured in specimens 5.1 and 5.2. The austenite-ferrite interfaces consisted of curved boundaries with no specific orientation relationship between the ferrite and surrounding austenite grains.

Figure 5.5 shows the initial austenite-ferrite interface in specimen 5.1. No orientation relationship was identified from the SAD patterns obtained. There was clear interaction of the interface with existing twin boundaries in the austenite. Initially interface migration temporarily halted close to a twin boundary which was normal to the growth direction. This temporary stagnation stage was followed by the rapid migration of the interface across the twin boundary. A second set of boundaries, this time parallel to the growth direction, could be seen to interact with the growing interface leading to a wave-like morphology in the segment that intersected the twin boundaries.

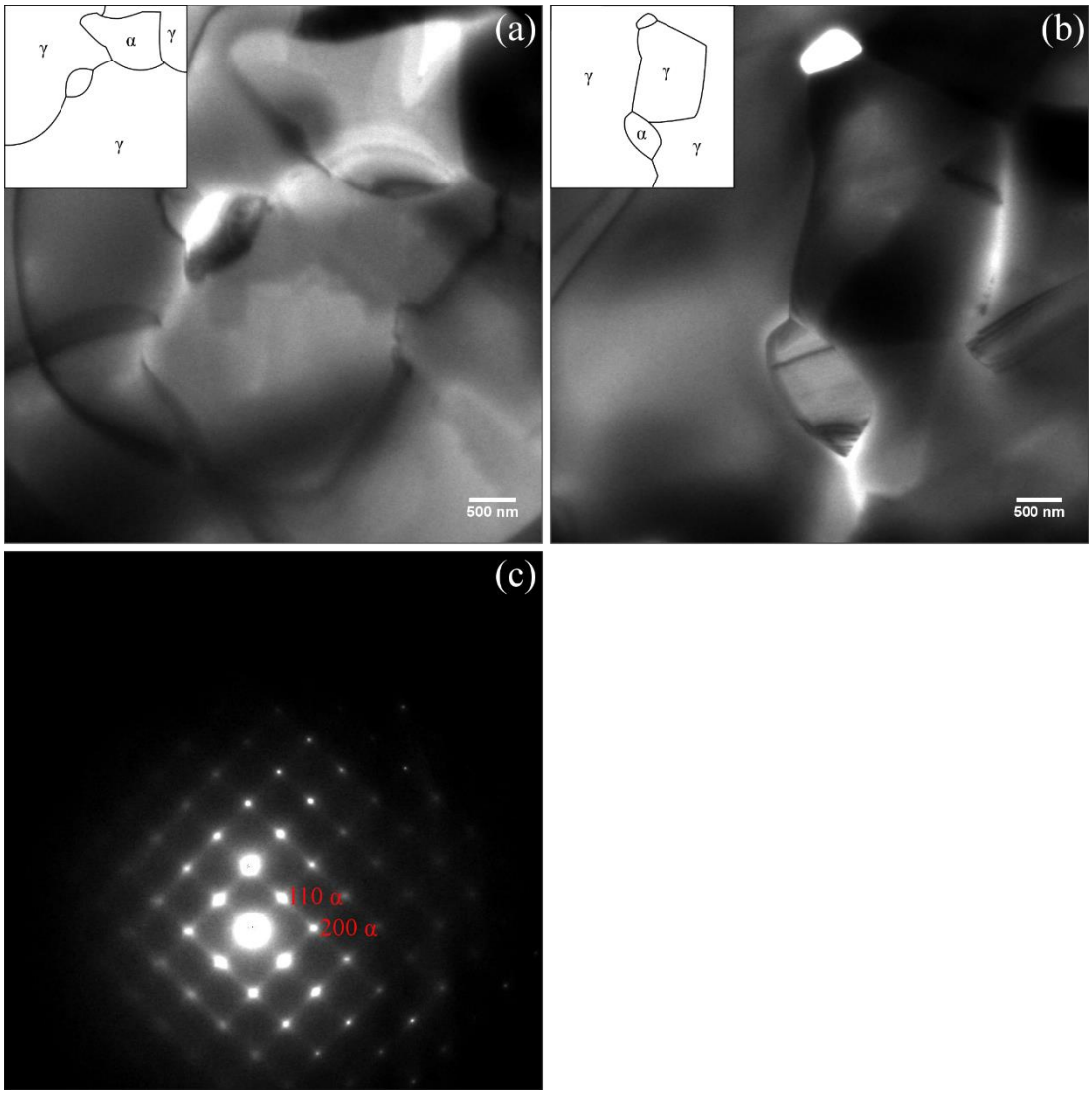

Figure 5.4: Bright field TEM of the Initial austenite-ferrite interfaces in (a) specimen 5.1 at 789°C, (b) specimen 5.2 at 800°C and (c) [001] zone axis selected area diffraction pattern for the ferrite grain in (b) . No defined orientation relationship was identified for these grains. Unlabelled grains could not be identified.

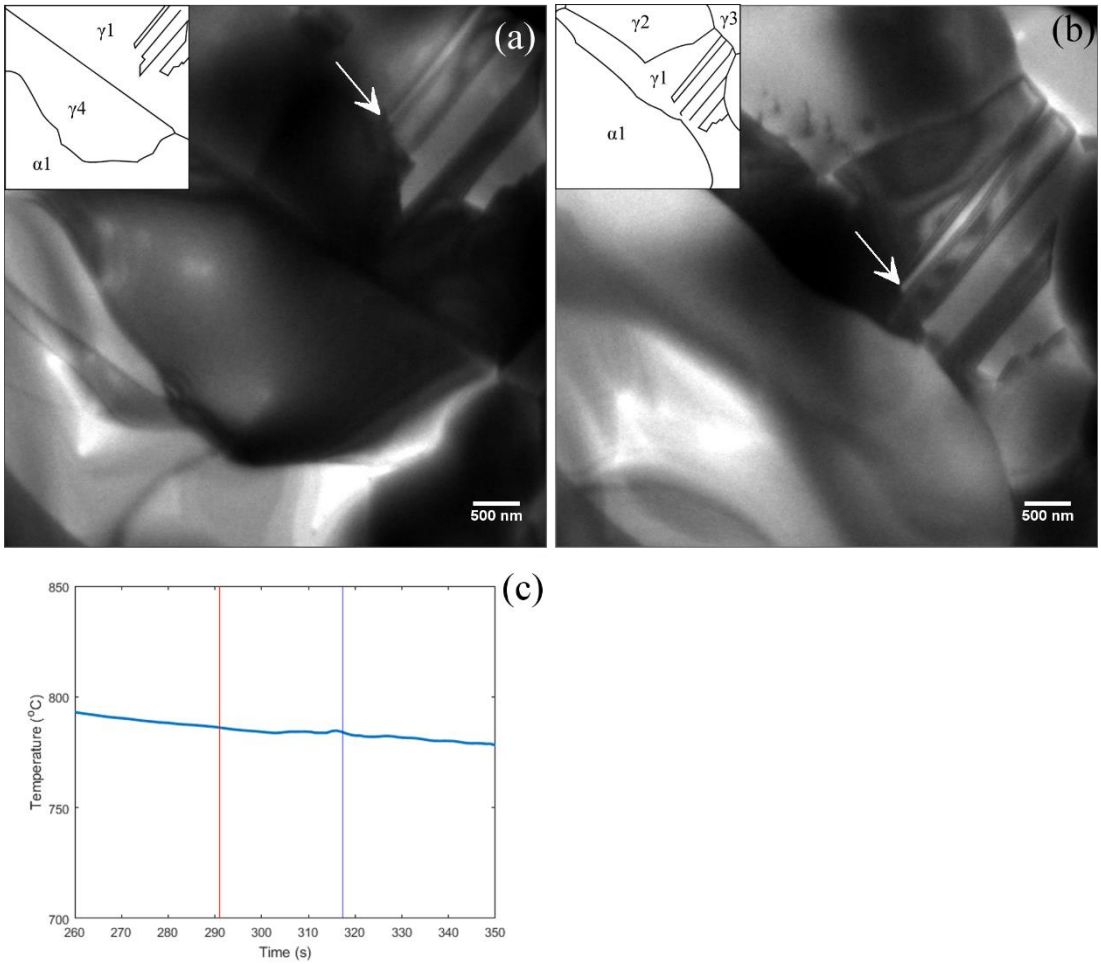

Figure 5.5: Bright field TEM of the Interaction of the interface with existing twin boundaries in the austenite. (a) The migration of the interface is briefly retarded ahead of a twin boundary normal to the growth direction at 786°C (b) Interaction with twin boundaries parallel to the growth direction at 784°C and (c) showing the time-temperature position of each frame. Vertical lines, from left to right, indicate the time depicted in frames (a)-(b). White arrows indicate twin boundary which is immobile between frames. (Specimen 5.1).

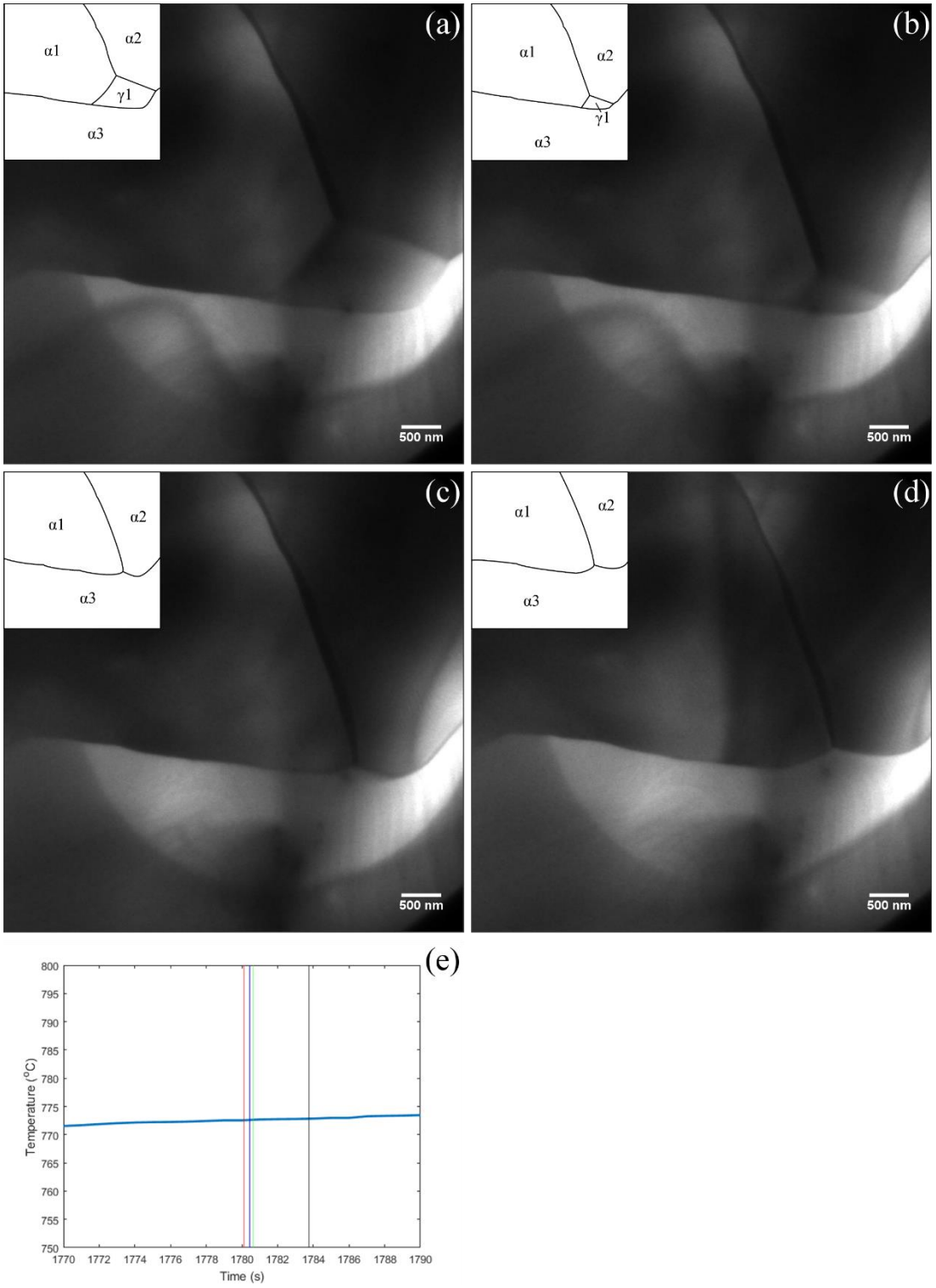

Figure 5.6: Bright field TEM of the end of the austenite to ferrite transformation (a) at 773°C, 1780.1 seconds (b) at 1780.4 seconds, (c) at 1780.6 seconds, (d) 1783.8 seconds at 773°C and (e) showing the time-temperature position of each frame. Vertical lines, from left to right, indicate the time depicted in frames (a)-(d). The transformation is completed by two mobile interfaces forming an α-γ-α triple point, whilst the third interface remains immobile. After the austenite grain is fully transformed, the grain boundary triple point migrates backwards establishing a new grain boundary shape. (Specimen 5.1).

For one of the interfaces observed in specimen 5.1, the complete transformation of an austenite grain was observed; Figure 5.6 shows this final transformation. The α3-γ1 interface remained static until the final point of the transformation. Before the austenite was completely transformed the triple point had angles close to 120^{o} for each of the three grains. After the transformation completed, there was a backward migration of the newly created grain boundary triple point. This increased the dihedral angle formed by the boundaries of grain α1 and reduced that of α3 by approximately 7^{o}.

This process of readjustment of triple point position was observed across multiple unsuccessfully tested specimens of this composition and for other steel compositions. This would appear to indicate that the final shape of incoherent grain boundaries seen in the TEM, after the completed transformation, is not just the result of passage of the interface during the transformation but is also due to small scale migration of the grain boundary in the immediate aftermath of the transformation.

5.4 Interface Position.

Figure 5.7 shows the interface position, against a fixed reference point, more or less perpendicular to the moving interface, for the most complete cycle. The stagnant stage and inverse transformation were both present alongside the normal transformation stages of austenite and ferrite growth. The stagnant stage was estimated to last for 26C on cooling, and 28C on heating, using the convention in the literature [4] to define the stagnant stage as the temperature range in which the interface was more or less immobile even whilst the temperature changed. For the obtained heating and cooling rate the stagnant stage duration was 199 and 197 seconds respectively. The corresponding inverse transformations were estimated to be 4C and 7C respectively.

The distance travelled by the interface during this cycle was 7.4 ± 0.1 μm. This is only a factor of ~2 different to that found in kinetic modelling performed by Chen et al. [87]. However, it should be noted that the T_1-T_2 temperature range is approximately 7^{o}C smaller in the present experiments. The interface displacement from the start to the end of the stagnant stage was 0.16 ± 0.05 μm on heating against 0.15 ± 0.06 μm on cooling. This minimal displacement would be effectively undetectable on a

macroscopic sample examined using dilatometry. The total distance travelled was 1.00 ± 0.05 µm on heating and 0.74 ± 0.05 µm on cooling.

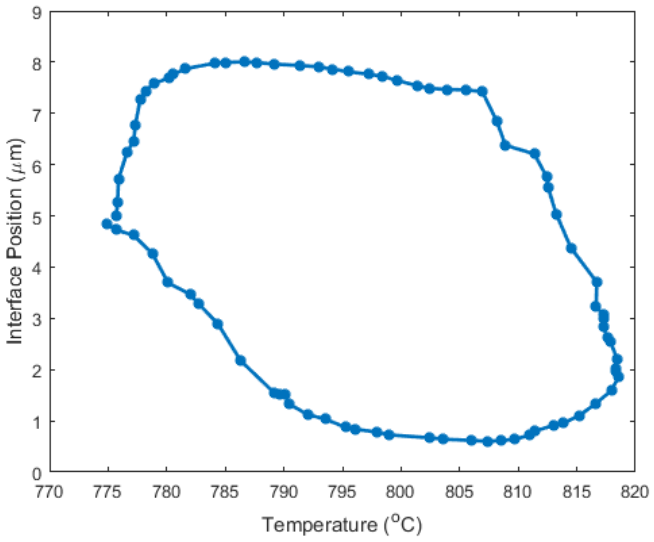

Figure 5.7: Graph of the interface position against temperature for the most complete cycle.

The development of the interface morphology during the inverse and stagnant stage whilst the specimen was cooled is shown in figure 5.8. The interface continued to migrate a short distance into the ferrite, before the direction reversed. This was accompanied by a change in the morphology, which resulted in the slight curvature of the interface becoming inverted.

Figure 5.9 shows the morphology of the interface as it develops during the stagnant stage whilst the foil was heated. In this case, the interface maintained a predominantly straight morphology, with some local segments deviating from this due to interactions with microstructural features (as in figure 5.9(a)), but there were no signs of intrinsic segmentation of the interface. The interaction of the interface with neighbouring microstructural features is discussed in more detail in chapter 5.7. After the end of the stagnant stage and the onset of the normal $\alpha \rightarrow \gamma$ transformation the interface can be seen to have developed a curved morphology, as shown in figure 5.9(d).

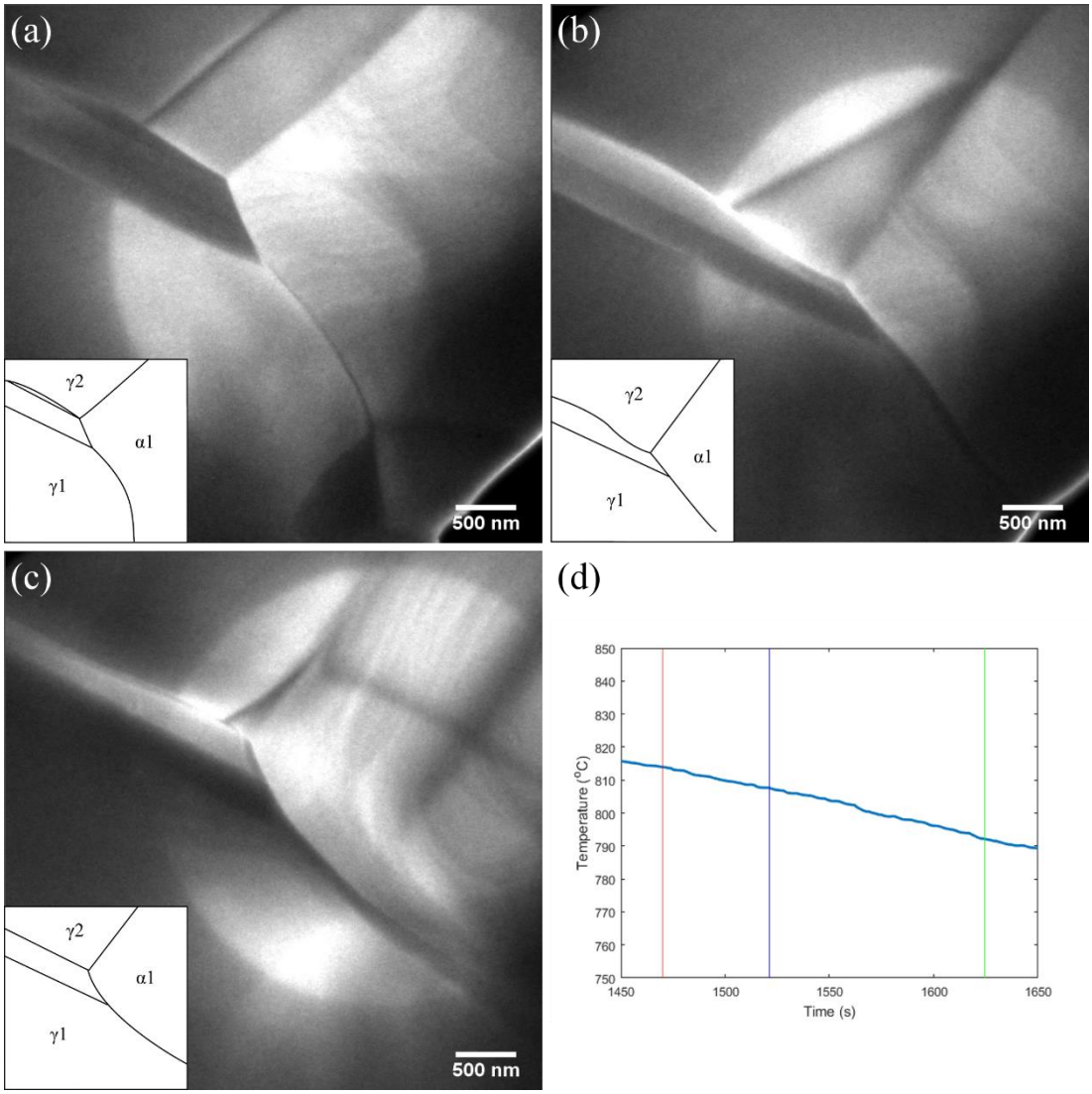

Figure 5.8: Bright field TEM of the Inversion of curvature during the stagnant stage on cooling (a) at 814°C, 1470.2 seconds (b) 1521.1 seconds at 808°C (c) 1624.3 seconds at 792°C and (d) showing the time-temperature position of each frame. Vertical lines, from left to right, indicate the time depicted in frames (a)-(c). Note that the beam has been condensed down. (Specimen 5.1).

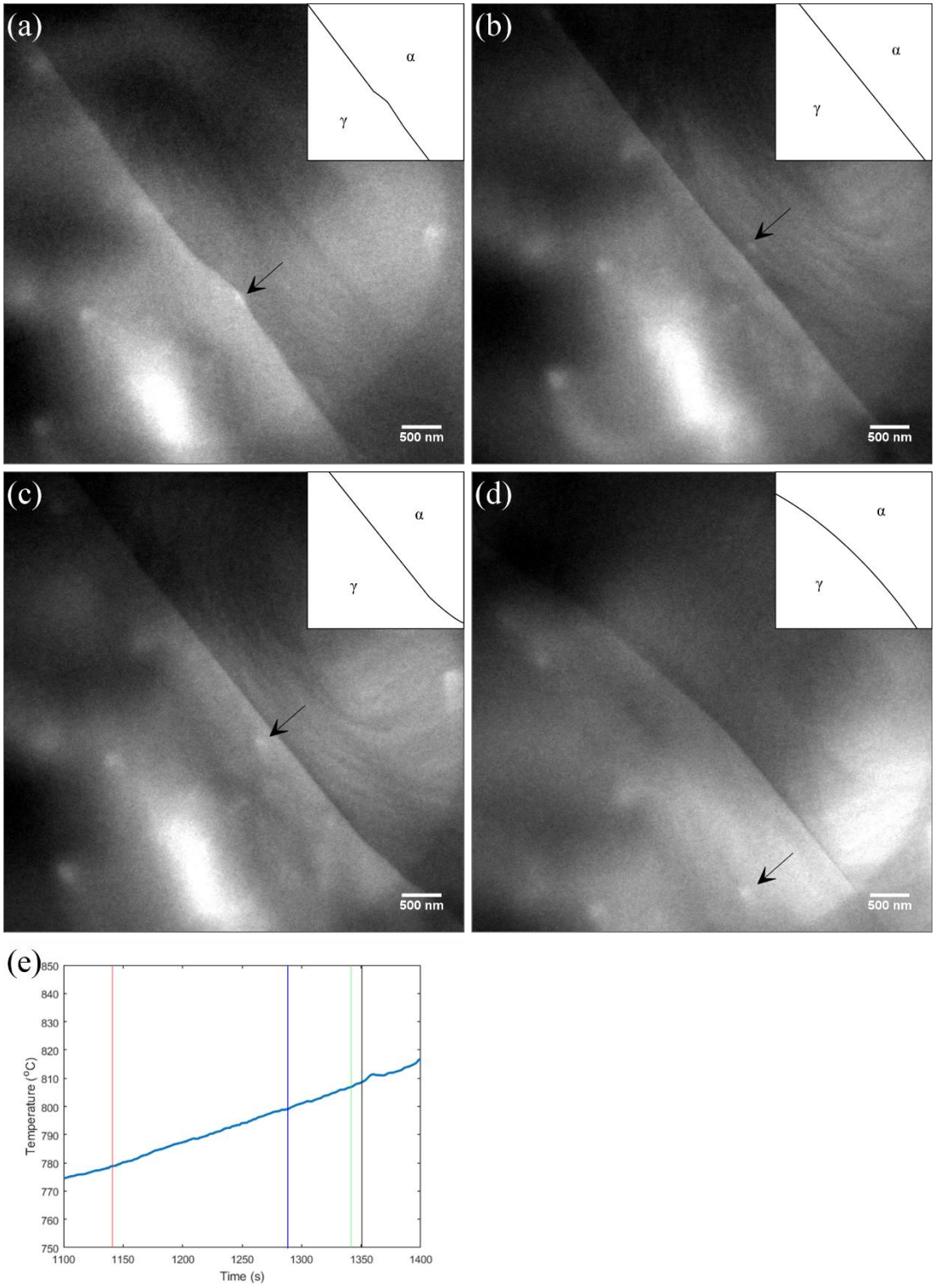

Figure 5.9: Bright field TEM of the morphology of the interface during the stagnant stage on heating at (a) 779°C (1141.4 seconds), the onset of the stagnant stage (b) at 1288.4 seconds (799°C) (c) at 1341.9 seconds (807°C), the end of the stagnant stage, (d) at 1350.5 seconds (808°C), showing the morphology at the beginning of the normal α→γ transformation and (e) showing the time-temperature position of each frame. Vertical lines, from left to right, indicate the time depicted in frames (a)-(d). Black arrows indicate particles, identified below, which are immobile between frames. (Specimen 5.1).

5.5 Interface Velocity.

Figure 5.10 shows the interface velocity corresponding to the interface shown in figure 5.7. The stagnant stage is particularly well defined with a period of low velocity, nearly 30°C long, before significant interface migration was resumed. On heating the velocity increased from <5 nm·s^{-1} after 807°C, indicating the start of the normal α→γ transformation. The interface continued to migrate with periods of acceleration and deceleration until the peak velocity of -560 nm·s^{-1} was reached at 817°C.

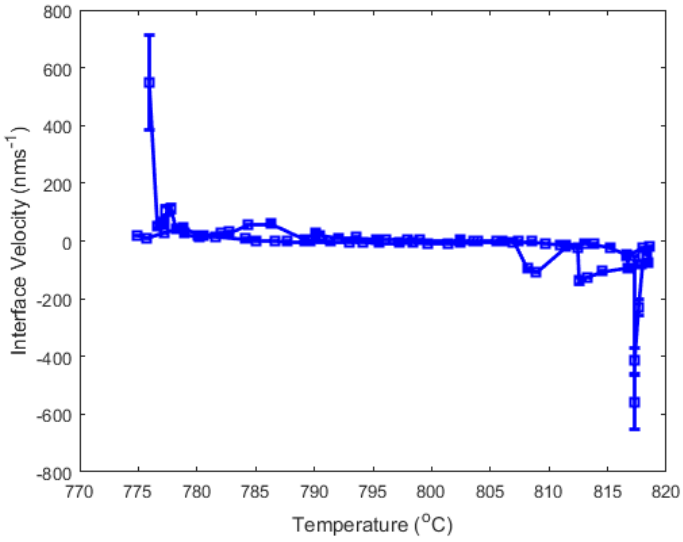

Figure 5.10: Graph of the interface velocity against temperature for the interface measured in figure 5.7 (note: the high velocity measurement at ~776°C was made during heating of the specimen, not cooling).

The interface velocity then decreased during the inverse α→γ transformation, dropping below 10 nm·s^{-1} after the specimen had cooled to 815°C, the start of the second stagnant stage. This period of low velocity continued until approximately 792°C, when the normal γ→α transformation began. There was an early increase in the velocity during cooling at approximately 789°C. It is likely that this led to a slight underestimate of the temperature range of the stagnant stage as it was caused by the reorienting of the interface near a triple point which began to migrate along an existing γ/γ grain boundary. This reorientation indicates that the change in position was not equal at all points along the interface. Once this reorientation was complete the interface migration initially slowed before once again increasing, reaching a peak of 113 nm·s^{-1} at 778°C.

5.6 General Observations: The Normal and Inverse Transformation.

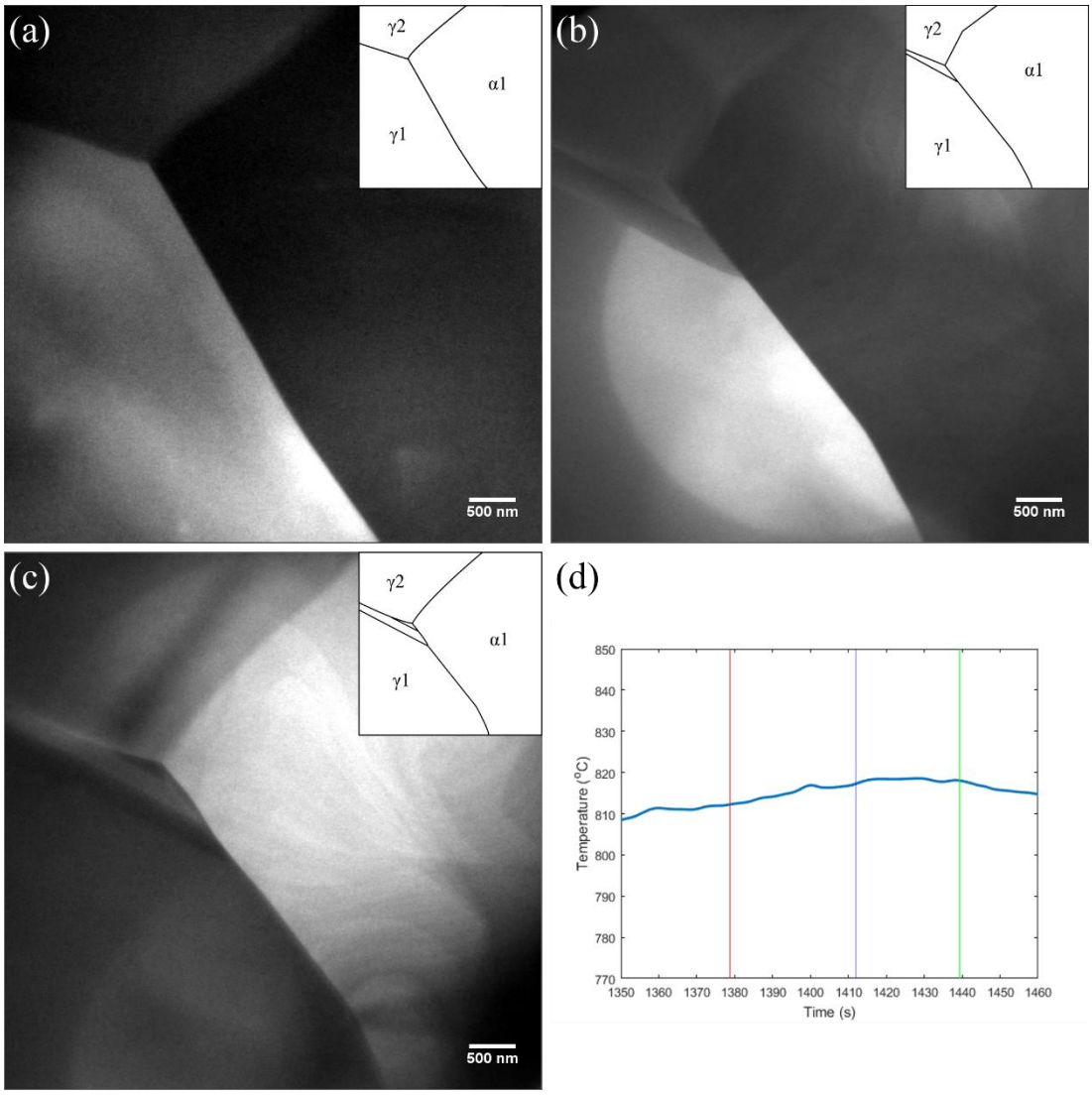

Figure 5.11: Bright field TEM of the interface morphology during the ferrite to austenite transformation (a) at 1378.7 seconds (812°C) (b) at 1412.1 seconds (817°C), (c) at 1439.3 seconds (818°C) and (d) showing the time-temperature position of each frame. Vertical lines, from left to right, indicate the time depicted in frames (a)-(c). (Specimen 5.1).

A set of interface images taken during the normal ferrite to austenite transformation is shown in figure 5.11. Comparing figure 5.11(a) with figure 5.9(d) the interface re-established a straighter morphology, which was maintained for part of the normal α→γ transformation. The interface became kinked towards the end of the normal α→γ transformation and throughout the inverse α→γ transformation. As noted above this curvature became inverted during the stagnant stage, as the direction of motion reversed.

The austenite to ferrite transformation for the same two interfaces is shown in figure 5.12. Between these two interfaces there was a significant difference in migration velocity during the austenite to ferrite transformation. The rapid migration of the adjacent interface (the upper interface shown in figure 5.11), led to the establishment of a long, predominantly straight lower interface, with a curved segment at adjacent to the triple point. This also resulted in a different direction of migration compared to the previous cycle.

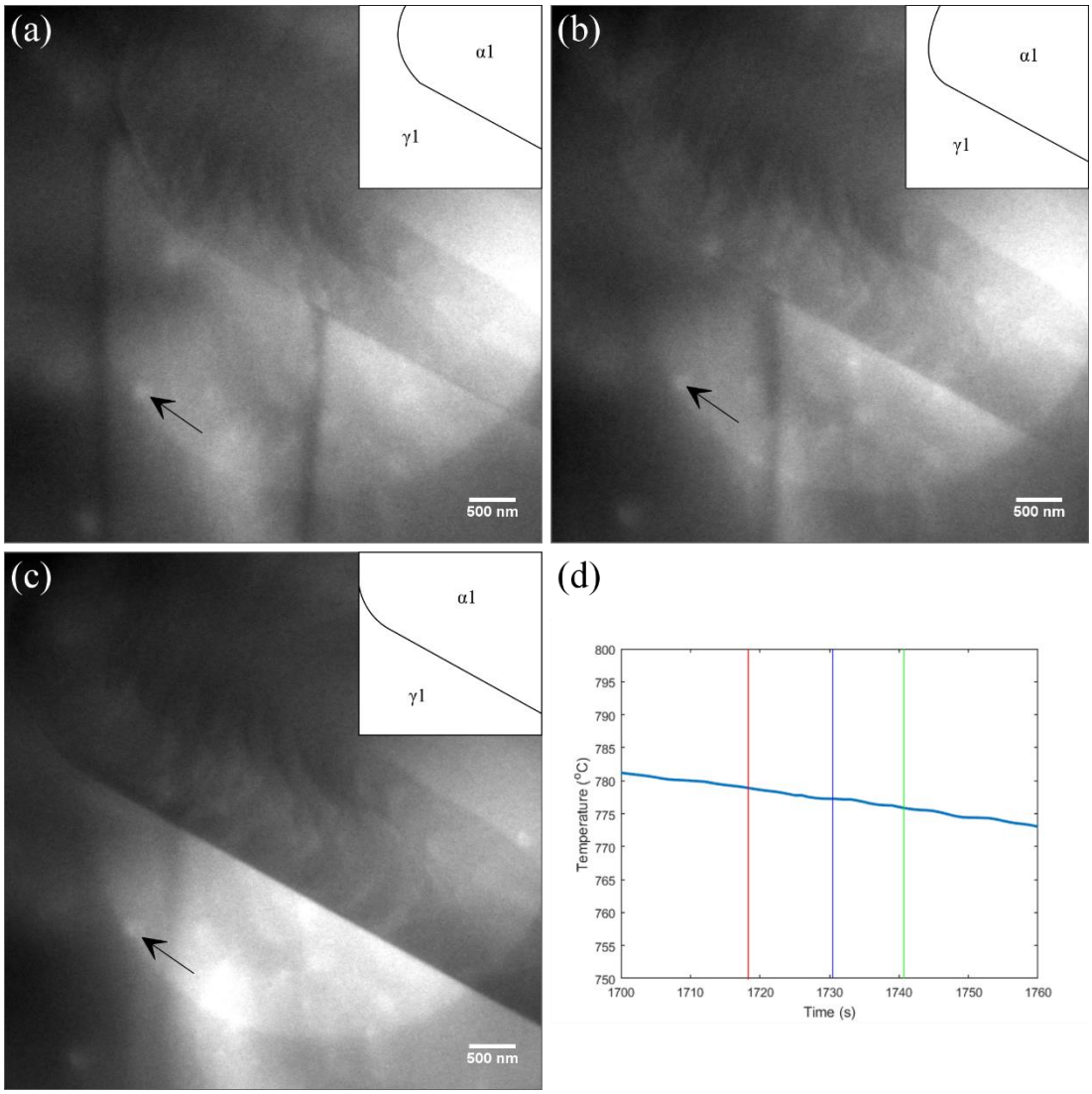

Figure 5.12: Bright field TEM of the interface morphology during the austenite to ferrite transformation (a) at 1718.32 seconds (779°C) (b) at 1730.5 seconds (777°C), (c) at 1740.7 seconds (776°C) and (d) showing the time-temperature position of each frame. Vertical lines, from left to right, indicate the time depicted in frames (a)-(c). Black arrows indicate a particle which was immobile between frames. (Specimen 5.1).

This predominantly straight morphology for most of the γ1/α1 interface was maintained during the normal γ→α transformation. However, another interface, which was between the same ferrite grain but a different neighbouring austenite grain, migrated with an undulating motion and an irregular morphology. This interface is shown in figure 5.13.

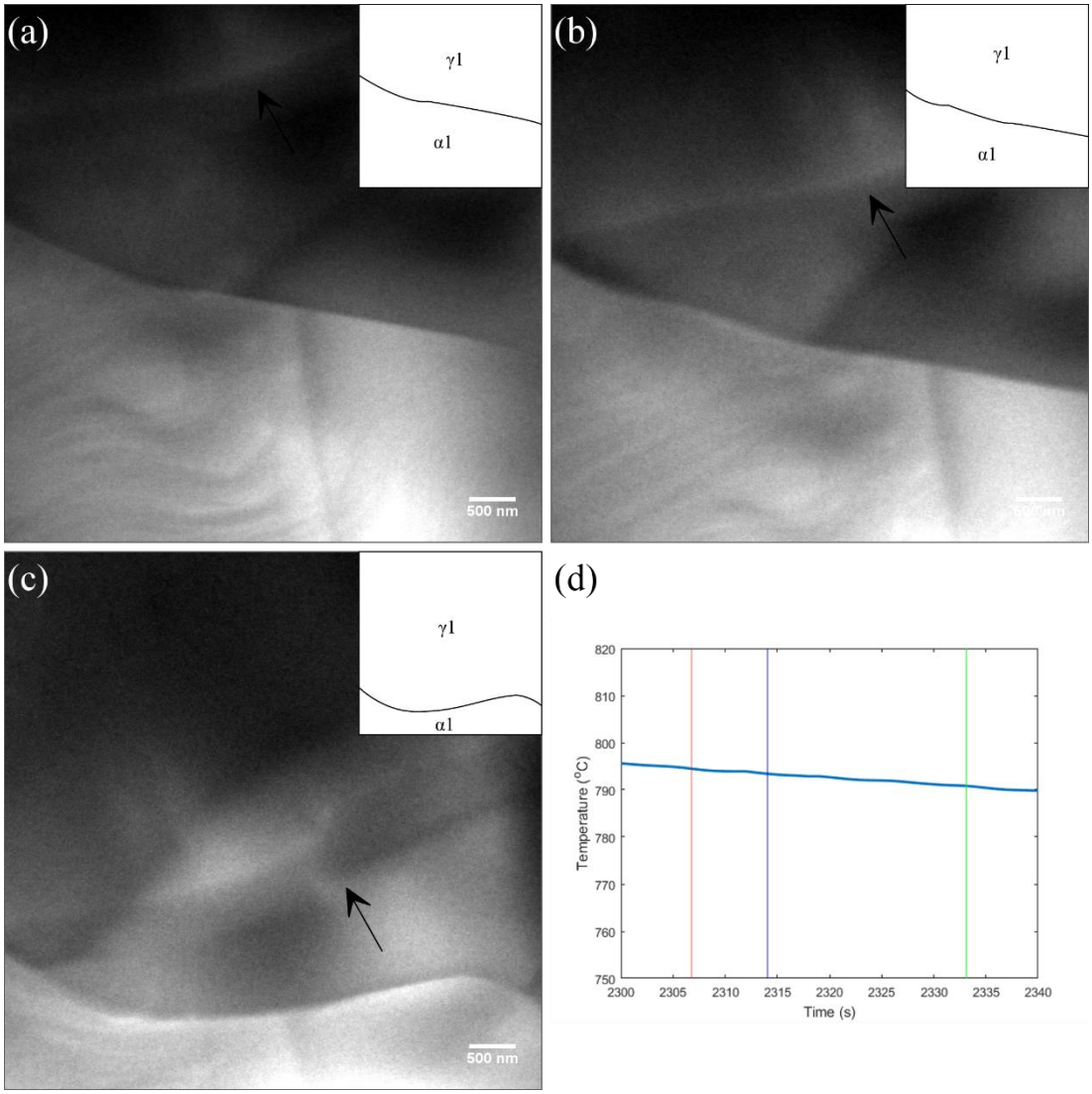

Figure 5.13: Bright Field TEM of the irregular morphology of an interface during the austenite to ferrite transformation (a) at 2306.7 seconds (794°C), (b) at 2314.1 seconds (793°C), (c) at 2333.1 seconds (791°C) and (d) showing the time-temperature position of each frame. Vertical lines, from left to right, indicate the time depicted in frames (a)-(c). Black arrows indicate a twin boundary which was immobile between frames. (Specimen 5.1).

In specimen 5.2 it was possible to observe the presence of dislocations in the austenite during cyclic transformations, as shown in figure 5.14. There was no apparent interaction with the interface during the time that the dislocations were visible, and the

dislocations remained static. Potentially these dislocations may have been emitted during the transformation, much like the process observed by Onink et al. [122], but the actual emission was not captured in the present study.

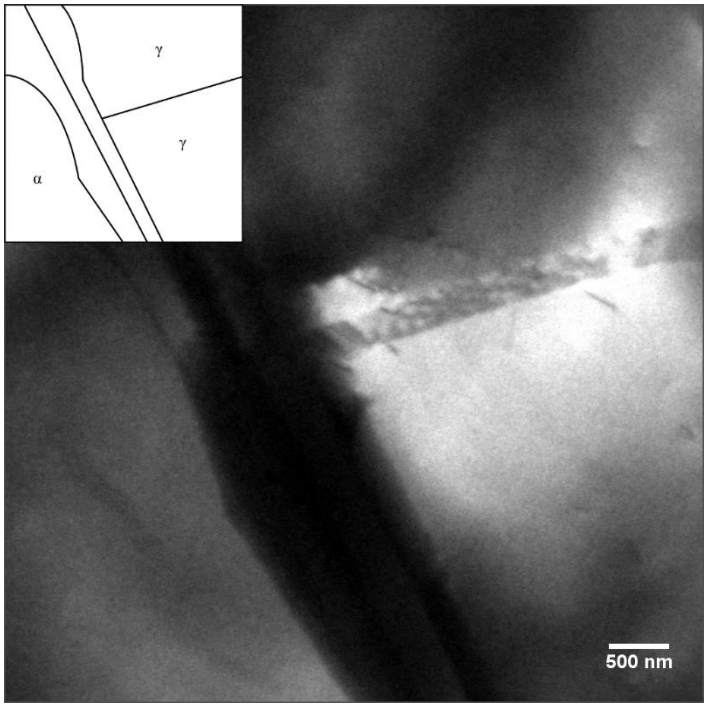

Figure 5.14: Bright field TEM of dislocations in the austenite at 778°C. (Specimen 5.2).

5.7 General Observations: Interface Pinning.

Figure 5.15 shows the interaction of the interface with an unidentified particle with estimated dimensions of 220 by 140 nm. This took place during the stagnant stage which occurred on heating during the first cycle of specimen 5.1. There is a localised inhibition of interface migration around the particle, developing over a period of approximately 20 seconds, before the interface escapes. During this period the temperature nominally increased by 2.5C.

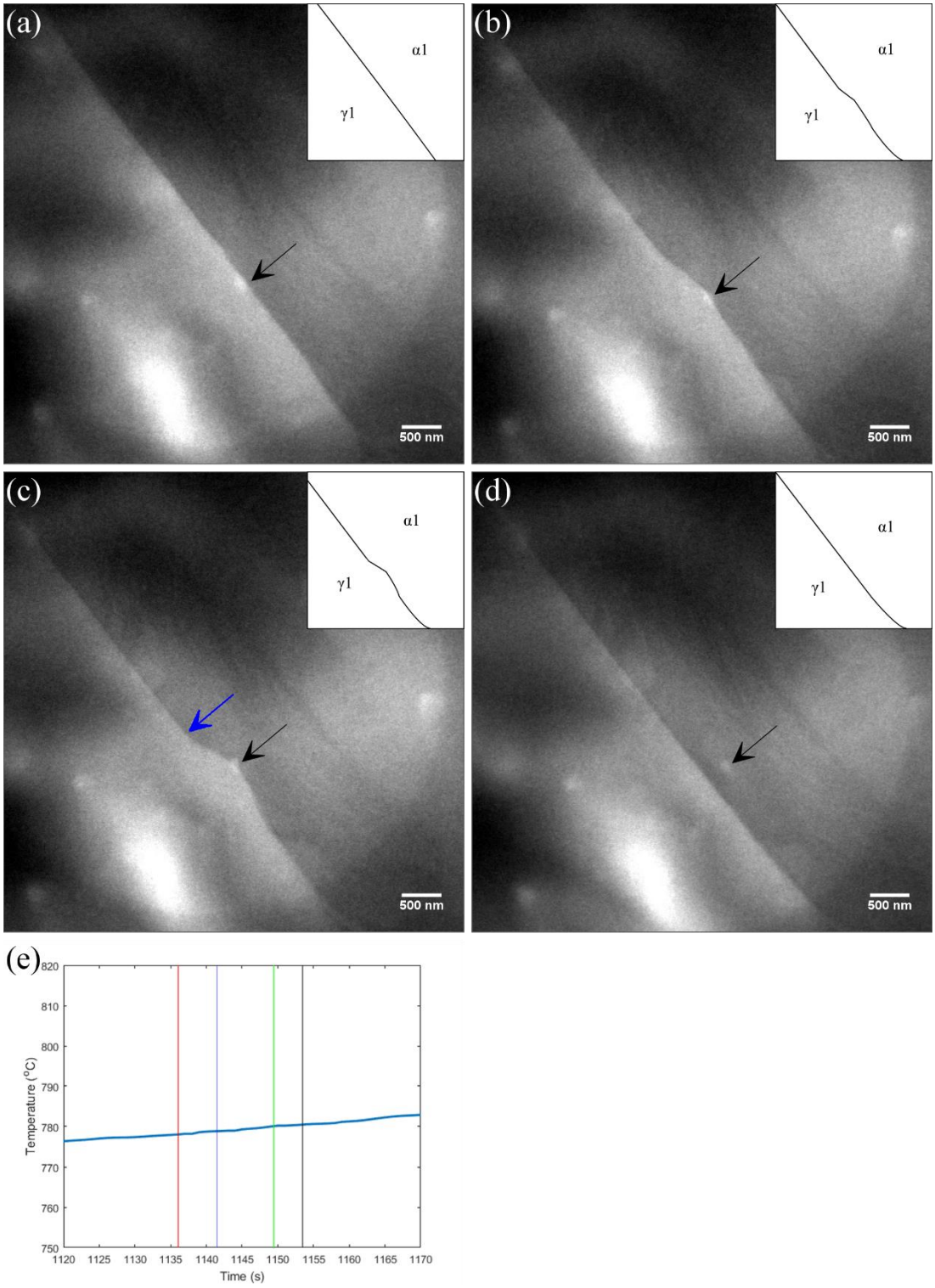

Figure 5.15: Bright field TEM of the interaction of the interface with an unidentified particle (a) at 1136.1 seconds (778°C), (b) at 1141.4 seconds (779°C), (c) at 1149.4 seconds (780°C), (d) at 1153.5 seconds (780°C) and (e) showing the time-temperature position of each frame. Vertical lines, from left to right, indicate the time depicted in frames (a)-(d). Black arrows indicate the particle, which is immobile between frames, the blue arrow indicates the reference point used for the measurements in figure 5.16. (Specimen 5.1).

Figure 5.16 shows how the interface developed during this period of interaction. In particular it shows the difference in position between the interface at the point it hits the inclusion (black arrow) and the position of the interface where the pinning effect appears to end (blue arrow). The creation of dislocations during this process was not observed. The difference in position between these two points (measured in the direction of interface motion) is shown in figure 5.15. This figure provides a unique insight into the interface pinning and release kinetics. These observations and a comparison with theoretical predictions are discussed in more detail in section 5.9.

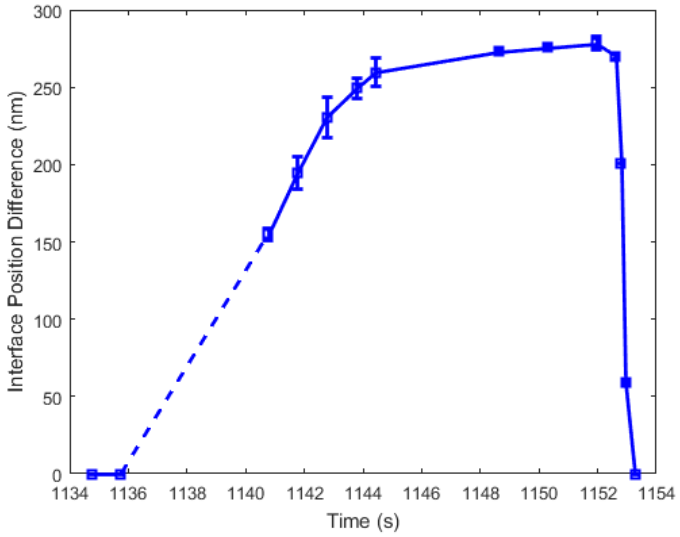

Figure 5.16: Graph of the relative difference in interface position for the pinned and unpinned section of the interface against time. The precise start time of the pinning effect could not be identified, and so is indicated by a dashed line.

The pinning force, F, exerted by the particle on the interface was calculated using equation 5.1 [173]:

$$F = \gamma \sin(\theta) \cdot 2\pi r cos(\theta) \qquad (5.1)$$

Where r is the particle radius, γ is the austenite-ferrite interface energy and θ is the angle of the interface where it intersects the particle.

An interfacial energy of 0.8 $J \cdot m^{-2}$ was used [174]. The pinning force increased over time to a maximum force of 181 ± 25 $nJ \cdot m^{-1}$ as measured immediately before the interface was released. The development of the pinning force over time is shown in figure 5.17.

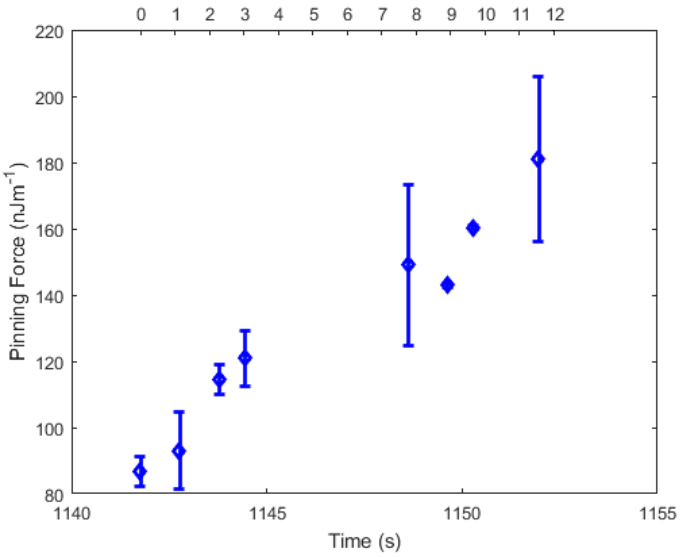

Figure 5.17: Showing the increase in the pinning force as a function of time. Top scale indicates the time (in seconds) from the first measurement of pinning force.

After cycling, the foils were investigated at room temperature to determine the identity of the particles seen in the video. Multiple particles, similar in appearance to those seen in the video during CPPT heat treatment were identified in the thermally cycled foils using TEM-EDS, figure 5.18(a) shows a typical example of these particles.. The majority of particles were found to be enriched with Al and O compared to the bulk composition. These were likely aluminium oxides particles embedded in the foil but without through thickness.

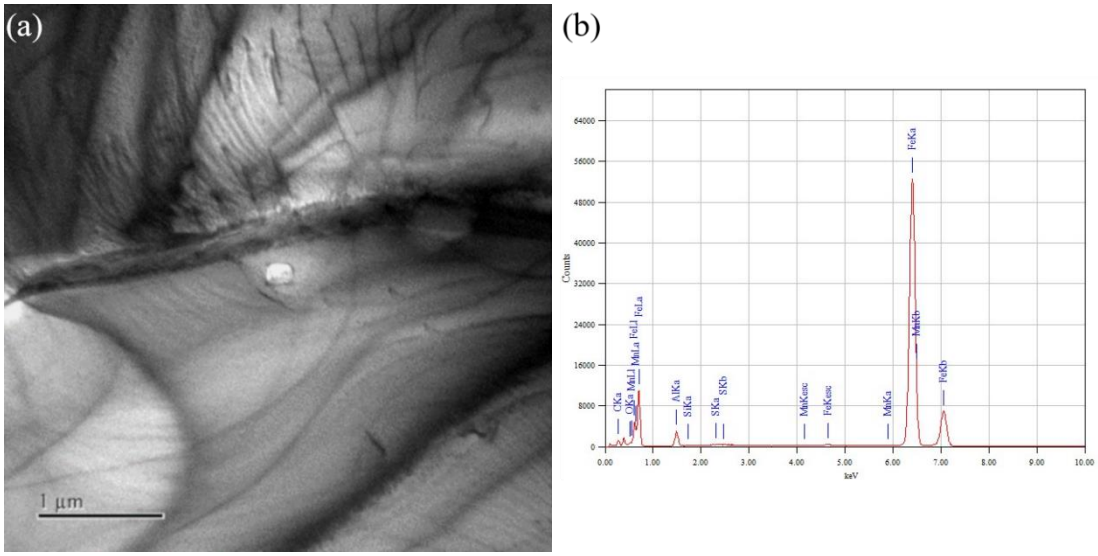

Figure 5.18: (a) Bright field TEM of a particle found in the Fe-0.1C-1Mn steel after thermal cycling and (b) EDS spectra from the particle.

5.8 Kinetic Modelling.

Figure 5.19 shows the position and velocity of the interface during thermal cycling as calculated using the Thermo-Calc/DICTRA [145] software. The temperature range of the normal and inverse transformations and the stagnant stage is shown below in table 5.2. There is surprising qualitative agreement between the TEM results (figures 5.7 and 5.10) and the DICTRA calculations. In both cases the transformation starts with a forward movement (as a result of the inverse transformation), a stage in which migration is slow, followed by an acceleration of the interface near the final T_2 temperature. There is a relatively slow reduction velocity during the stagnant stage on cooling, followed by a well-defined stagnant stage during the transformation to ferrite. This leads to a rapid acceleration of the interface below 780^{o}C which peaks quickly (29nms^{-1} at 777^{o}C) before the migration rate falls off towards T_1. The most significant difference between the experiment and calculation is the level of stagnation during the heating cycle. In the case of the TEM experiments stagnation is much more complete, whilst DICTRA predicts only a lower velocity.

There is, however, a significant difference in terms of the distance migrated by the interface. In figure 5.18(a) the total distance moved during the cycle is 0.82 μm. This is approximately a factor of 10 smaller than that observed in the TEM. Reinterpretation of CPPT dilatometry data from Chen and van der Zwaag [3] and Farahani et al. [175] (showing sample dilations of 3-6 μm) and assuming a nuclei density of $N^* = 6*10^{13}$, yielded an estimate of the maximum displacement distance of the interface during cycling of approximately 3.6 and 4.0 μm respectively. This is approximately a factor of 2 different to the migration distance observed in the TEM, a comparable difference to that found between dilatometry and the TEM observations for steels containing 0.5wt% Mn in the previous chapter.

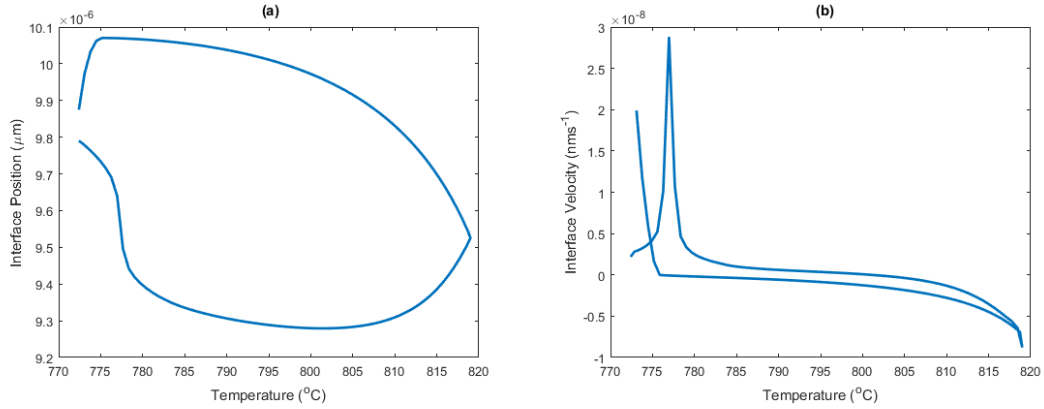

Figure 5.19: Graphs of (a) the position and (b) the velocity of the interface against temperature during thermal cycling obtained using DICTRA.

Table 5.2: Table of the estimated temperature range for each feature of a cyclic partial phase transformation on heating and cooling.

Feature	Heating	Cooling
Normal Transformation	19C	9C
Inverse Transformation	3C	7C
Stagnant Stage	25C	30C

5.9 Discussion.

Comparing the interface behaviour of the observed interface in the TEM with that predicted using kinetic modelling, there is good agreement in behaviour on heating. The onset of the stagnant stage is comparable in both cases: 776ºC for DICTRA, compared to 779ºC in the case of the TEM observations. The normal $\gamma \rightarrow \alpha$ transformation is more well-defined in the case of the TEM observations, with significant acceleration of interface migration at 807ºC, compared to a more gradual acceleration of the interface in the DICTRA simulation. The total temperature range of the stagnant stage is approximately 28C for the TEM observations on heating against 25C. This disparity is likely due to the fact that the stagnant stage predicted using DICTRA is not as well defined. On cooling the stagnant stage is estimated to be 26ºC for TEM against 30C for DICTRA, although as discussed above the TEM observation may have produced a small underestimate due to the rapid migration of a triple point adjacent to the measured length of the interface.

Figure 5.20 shows the temperature range of the stagnant stage as predicted by Chen et al. [7], based on simulations of Fe-0.02C-XMn (where X = 0.1, 0.2 & 0.3). Also shown is the expected stagnant stage temperature range, adjusted for the heating/cooling rates achieved in the experiments presented in this chapter. For the 0.5Mn steel reported in chapter 4 there is good agreement between the observed and expected stagnant stage temperature range. Agreement remains good in the present experiments where the observed stagnant stage temperature range is, on average, 10% shorter than expected.

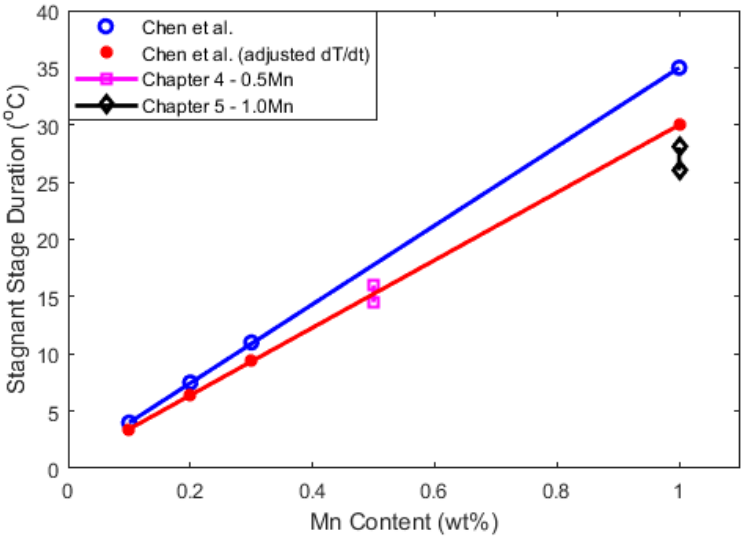

Figure 5.20: Graph of stagnant stage temperature range against Mn content, comparing predicted stagnant stage temperature range with TEM observations.

Part of the disparity may arise due to differences in the carbon concentration, 0.02 wt% for Chen et al. compared with 0.094 wt% in this chapter. Furthermore, the different composition means that slightly different T_1 and T_2 temperatures had to be used.

The morphology of the interface showed similar long-term variations as reported in chapter 4 for the 0.5 wt% Mn steel, where the interface was more regular during the stagnant stages, either being straight or smoothly curved, with some variation caused by interaction with microstructure features. During the normal transformation the primary interfaces under observation shifted more or less smoothly between a straight and curved morphology, although some interfaces with a wave-like character were observed. Compared to chapter 4 the main interfaces observed during the normal transformations appeared to be more regular in the specimens containing 1wt% Mn.

This may indicate that the greater Mn concentration at the interface favours more regular interface morphologies, but the effect, if present at all, is small.

The qualitative agreement between the distance migrated by the interface in the TEM and that predicted by DICTRA is poor, being a factor of 10 times higher in the TEM observations. However, this difference is reduced to a factor of ~2 when the compared with the interface migration during CPPT dilatometry experiments. This is approximately the same difference as found for 0.1C-0.5Mn steels in the previous chapter.

During thermal cycling an example of the interface interacting with and being pinned by an unidentified particle was observed. A theoretical treatment of the interaction of migrating grain boundaries with particles was first outlined by Zener [176] [177]. Since this effect arises from the reduction in interfacial energy when the grain boundary intersects the particle, similar considerations might be expected to apply to the interaction of migrating interphase boundaries and particles/precipitates [178]. Some differences might be expected to arise due to the different origins of the driving force for the phase transformation and grain boundary migration, and the diffusion-controlled nature of the transformation.

Experimental studies of the δ-ferrite to austenite and α-ferrite to austenite transformations indicate that the transformation interfaces interact with particles in the parent phase [179] [180]. Transformation kinetics were found to be retarded in a similar fashion to Zener pinning during grain growth [178] [179]. A minor (and not applicable to the present experiment) difference between the current observations and the prediction of interface pinning by the phase field model by Sato et al. [178] is that before the interface intersects the particle there is a local retardation of interface migration because of carbon diffusion being inhibited by the particle. The magnitude of the effect was dependent not just on the size and distribution of the particles but also by the relative interfacial energies between the particle and each phase [181]. It is important to note that the model is 2D and therefore the predicted local retardation may differ from a three-dimensional case.

However, it is important to consider that interfacial conditions are different in the present experiment compared to the cases discussed above. The interaction occurred at the onset of the stagnant stage, meaning that a significant interfacial enrichment of

Mn is expected to be present [3, 82]. In many respects this was advantageous as it made the pinning observations easier. It can be seen from figure 5.16 that at approximately 1144 seconds the rate at which the apparently unpinned part of the interface was migrating slowed. This is attributed to the end of the inverse transformation and the onset of the stagnant stage.

The migration of a newly formed grain boundary triple point, observed in figure 5.6, indicates that final boundary shape after the austenite to ferrite transformation may be influenced by both the phase transformation itself and subsequent adjustment of grain boundaries after the transformation is complete. The driving force for this backward migration is likely the reduction in the total surface energy of the three grain boundaries in contact and leads to a reduction of the angle formed between the two boundaries of each grain at the triple point. For the present experiment, the change was approximately 7°. The angle between two grains meeting at a triple point is 120° under equilibrium conditions and when the grain boundary energies are equal [182] [183]. In practice this is unlikely to be the case, as grain boundary energy varies with lattice misorientation and grain boundary plane orientation [184] [185]. In the present experiments, ferrite grains were most commonly (in fact, almost exclusively) found with the [001] direction parallel to the electron beam, indicating that the grain boundaries in question are most likely tilt boundaries. Studies calculating the grain boundary energy for α-Fe using molecular dynamics indicate that the energy for <100> symmetric tilt grain boundaries is up to 1.2 $J \cdot m^{-2}$ [186] [187], with a range of 0.5 $J \cdot m^{-2}$ including low angle grain boundaries [188].

5.10 Chapter Summary.

The results of successful cyclic partial phase transformation experiments on a 0.1C-1.0Mn steel using in-situ hot stage TEM are presented. In addition to some special observations of interface behaviour due to interactions with microstructural features, the in-situ observations confirmed the occurrence of stagnant, regular and inverse transformation behaviour during the appropriate stages of the thermal cycle within the intercritical domain. No radically different observations were made in comparison to those reported in chapter 4 for a 0.1C-0.5Mn steel.

The stagnant stage was found to be 26 and 28C, for cooling and heating respectively. This is close to that predicted by Chen et al. [7] when the different heating/cooling rates are taken into consideration. The normal and inverse transformations were also observed, with reduced temperature range in the case of the normal transformations compared to the 0.1C-0.5Mn steel, as well as with a reduced migration distance.

The interface morphology showed less variation than for the low Mn steel, with predominantly straight or smoothly curved interfaces observed during the stagnant stage and during the normal transformation. A straight interface was more prevalent during the austenite to ferrite transformation. However, some cases of more irregular, wave-like morphologies for the moving interface were encountered. Most often the irregularity could be linked to the presence of adjacent microstructural features such as twin boundaries, triple points or inclusions.

In addition, the increased carbon concentration would be expected to lower the A_{e3} temperature by stabilising the austenite. The temperature range of the $\alpha + \gamma$ two phase region is also reduced due to carbide formation as the carbon content is increased.

When comparing with kinetic modelling, there was qualitative agreement with the behaviour of interface. The temperature range of the cyclic partial phase transformation features were in reasonable agreement between TEM and DICTRA. The quantitative difference between the distance migrated as predicted by DICTRA and observed in the TEM experiments is a factor of approximately 10. However, this disparity is reduced to a factor of approximately 2 when the interface motion is estimated from dilatometry experiments.

6. Cyclic Partial Phase Transformation Experiments: Fe-XC-1.5Mn-0.14Si (where X = 0.183, 0.263 & 0.330).

6.1 Introduction.

The final set of cyclic experiments were performed on steels with a Mn concentration of 1.5 wt% and Si concentration of 0.14 wt %. The C concentration of these alloys was 0.183 wt%, 0.263 wt% and 0.33 wt%. This selection of alloys allowed for a comparison on the effect, if any, of changing carbon concentration on interface behaviour as well as providing a higher manganese composition compared to the alloys investigated in the previous chapters. The increased carbon content in the steels will have both thermodynamic and kinetic effects. Firstly, the increased carbon will reduce the temperature range of the two phase $\alpha+\gamma$ region primarily by lowering the A_3 temperatures due to the austenite stabilising nature of carbon. Secondly, all other factors being equal, it will reduce the rate of the austenite to ferrite transformation compared to steels with a smaller wt % of carbon.

The increased Mn concentration leads to an expectation that the temperature range of the stagnant stage increases in comparison with the 0.1C-0.5Mn and 0.1C-1Mn alloys. Previously the stagnant stages were estimated at 15-16C and 26-28C respectively. With a specimen containing 1.5 wt% Mn the maximum expected temperature range of the stagnant stage would be 45C. Furthermore, the velocity of the interface migration is expected to be reduced, with a corresponding reduction in the total distance migrated by the interface over the course of the cycle.

Within this chapter it was expected that the increased carbon concentration should also result in slower interface migration. Studies of the interaction between substitutional and interstitial alloying elements suggest that that carbon plays an important role in the segregation of Mn to austenite-ferrite interfaces [83] [84]. This indicates that an increase in the carbon concentration may also have the effect of increasing the temperature range of the stagnant stage. However, the magnitude of this effect may be limited. Chen et al. [7] used kinetic modelling in steels with a composition of Fe-0.02C-XMn (where X=0.1, 0.2, 0.3) steels to estimate the dependence of stagnant stage temperature range on Mn composition. This dependence is 35C per wt% Mn at

10^{o}C/min heating and cooling rate and, adjusting for the different heating and cooling rate, also predicted the stagnant stage temperature range in the dilatometry and TEM observations report in chapter 4, despite an increase in C content.

The morphological development of the interface is expected to remain similar to that seen for the previous compositions. The transition from LENP to LEP kinetics was observed to impose a more regular interface morphology, generally straight or smoothly curved, and similar observations are expected. During the normal transformation, where LENP kinetics are dominant, more variation is expected. In the Fe-0.1C-1Mn steel both regular and more irregular or wavelike interfaces were observed. This indicates that during this part of the thermal cycle, morphology is affected by local interfacial conditions which are not necessarily homogeneous across all interfaces.

This chapter presents not only the results from cyclic partial phase transformation experiments on Fe-XC-1.5Mn alloys but also includes a general discussion bringing together an assessment of interface behaviour across all of the compositions investigated using cyclic heat treatments.

6.2 Experimental Outline.

A total of 5 successful experiments were performed on the three compositions, which are outlined in table 6.1 below. In addition, there were a significant number (~10) of specimens which did not result in thermal cycling in the two-phase region. As with chapter 5, this may not necessarily indicate that the specimens were not undergoing cyclic partial phase transformations, only that no such interface migration was observed in the electron transparent region of the specimen.

Table 6.1: Table of Specimen number, composition and outcome.

Specimen Number	Wt% C	Notes
6.1	0.183	Success
6.2	0.183	Success
6.3	0.263	Success
6.4	0.33	Success
6.5	0.33	Success
6.6	0.183	Abnormal grain growth, no cyclic interface

Figure 6.1 below shows the heat treatment to which each of the three compositions were subjected. Anticipating a longer stagnant stage (up to 45C), a T_2-T_1 temperature range of 55^{o}C was used for the 0.183C-1.5Mn-0.14Si specimens. The T_1 and T_2 temperatures selected were 734^{o}C and 789^o respectively. These were chosen based on the same considerations as for the Fe-0.1C-0.5Mn and Fe-0.1C-1.0Mn specimens, in particular, both temperatures are within the two-phase $\alpha+\gamma$ region, at both temperatures the transformation is expected be governed by LENP kinetics, and the change in the equilibrium volume fraction of ferrite is approximately 0.4. For the 0.263C-1.5Mn-0.14Si specimens the T_1 and T_2 temperatures were 729^{o}C and 779^{o}C respectively. These temperatures were selected because the temperature range (50C) was still expected to be larger than the anticipated stagnant stage temperature range, whilst maintaining the change in equilibrium volume fraction of ferrite at approximately 0.4. Finally, specimens 6.4 and 6.5 used a temperature range of 40C, with T_1 and T_2 selected as 720^{o}C and 760^{o}C respectively. This reduction was to avoid carbide formation predicted in the equilibrium phase diagram on Thermo-Calc. In this case the change in the equilibrium volume fraction of ferrite was approximately 0.35.

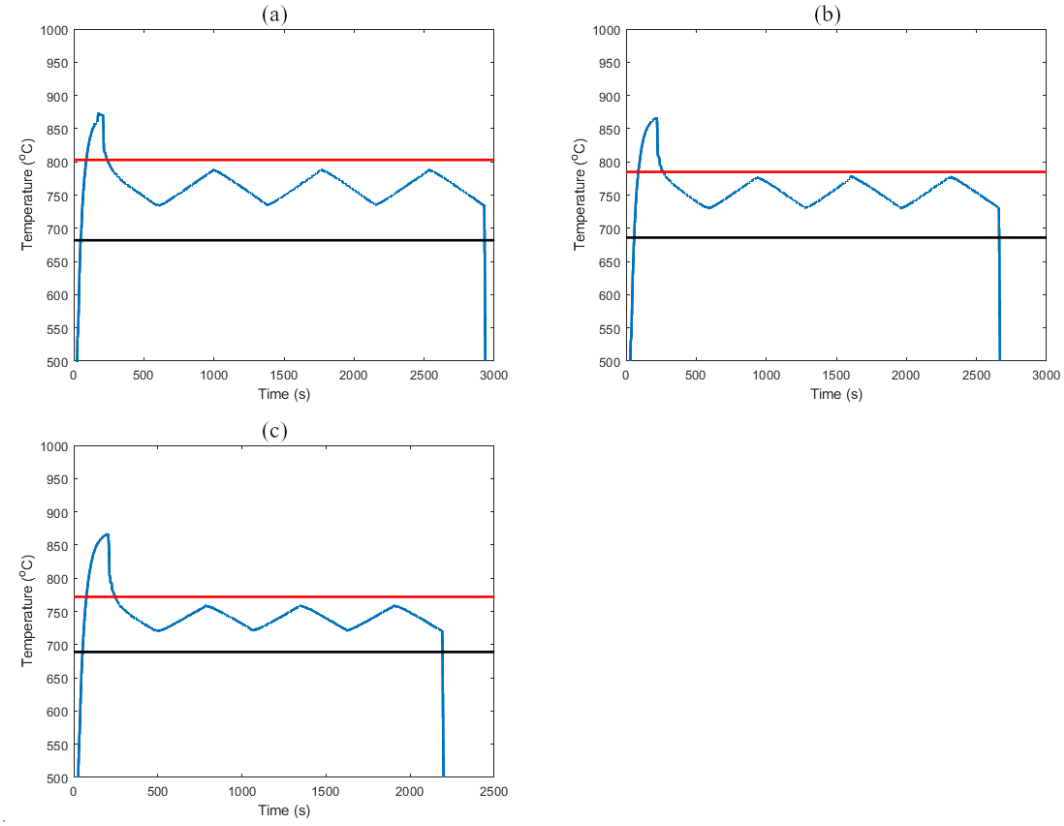

Figure 6.1: Graphs of temperature against time for the Imposed heat treatments used for (a) specimens 6.1, 6.2 & 6.3 (0.183 wt% C), (b) specimen 6.3 (0.263 wt% C) and (c) specimens 6.4 and 6.5 (0.330 wt% C). The upper and lower limits of the two phase region are indicated, respectively, by red and black horizontal lines.

Although the different temperature ranges limit the validity of direct comparisons between compositions, particularly the migration distance, it can be further justified on two grounds. Firstly, the results from the Fe-0.1C-0.5Mn experiments in chapter 4 show good agreement, once differences in heating/cooling rates are accounted for, with those of Chen et al [7] [82]. This is despite the temperature range in the TEM experiments being ~7-10^{o}C lower than those of Chen et al. and so suggests that the stagnant stage temperature range is not strongly dependent on temperature difference between T_1 and T_2. Instead, the reduction in the temperature range was expected to reduce only the normal and inverse transformation. Secondly, the main objectives of the experiments were to observe a transition between LE-NP and LE-P kinetics and to record the behaviour of the interface during this transition as well as during the normal transformation. Figure 6.2 shows examples of the starting microstructures in each of the three compositions investigated, predominantly consisting of a dual ferrite and pearlite microstructure.

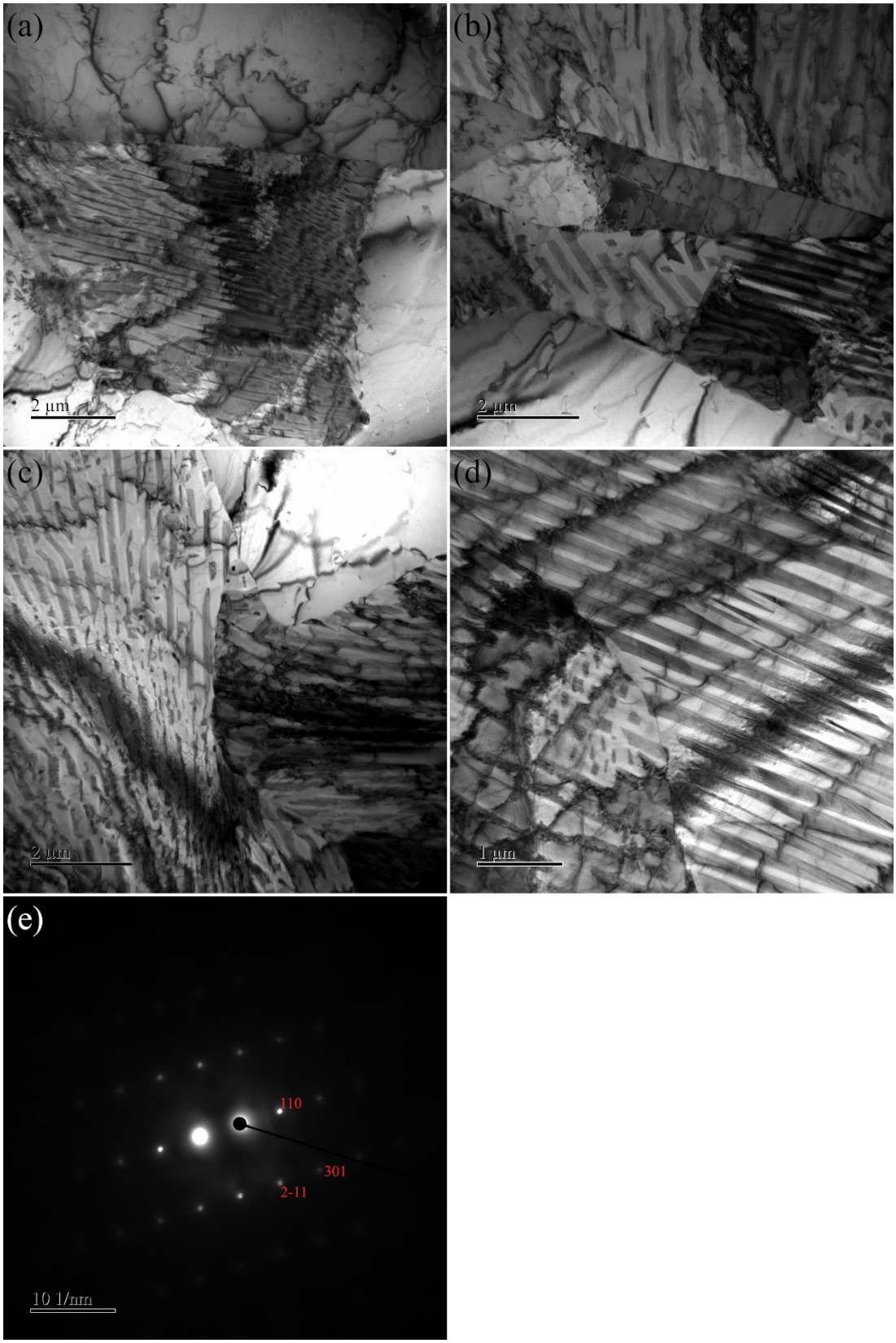

Figure 6.2: Bright field TEM of the starting microstructures of the mixed ferrite and pearlite microstructures for (a) Fe-0.183C-1.5Mn-0.14Si (b) Fe-0.263C-1.5Mn-0.14Si, (c) Fe-0.33C-1.5Mn-0.14Si, (d) the boundary between two pearlite colonies in Fe-0.33C-1.5Mn-0.14Si and (e) selected area diffraction pattern showing the absence of surface oxide for Fe-0.183C-1.5Mn-0.14Si.

6.3 Austenite Microstructure and Initial Interface Formation.

As with the previous compositions the austenite microstructure which formed on heating showed a mixture of incoherent grain boundaries with a number of growth twins within the austenite grains. Examples of this are shown in figure 6.3.

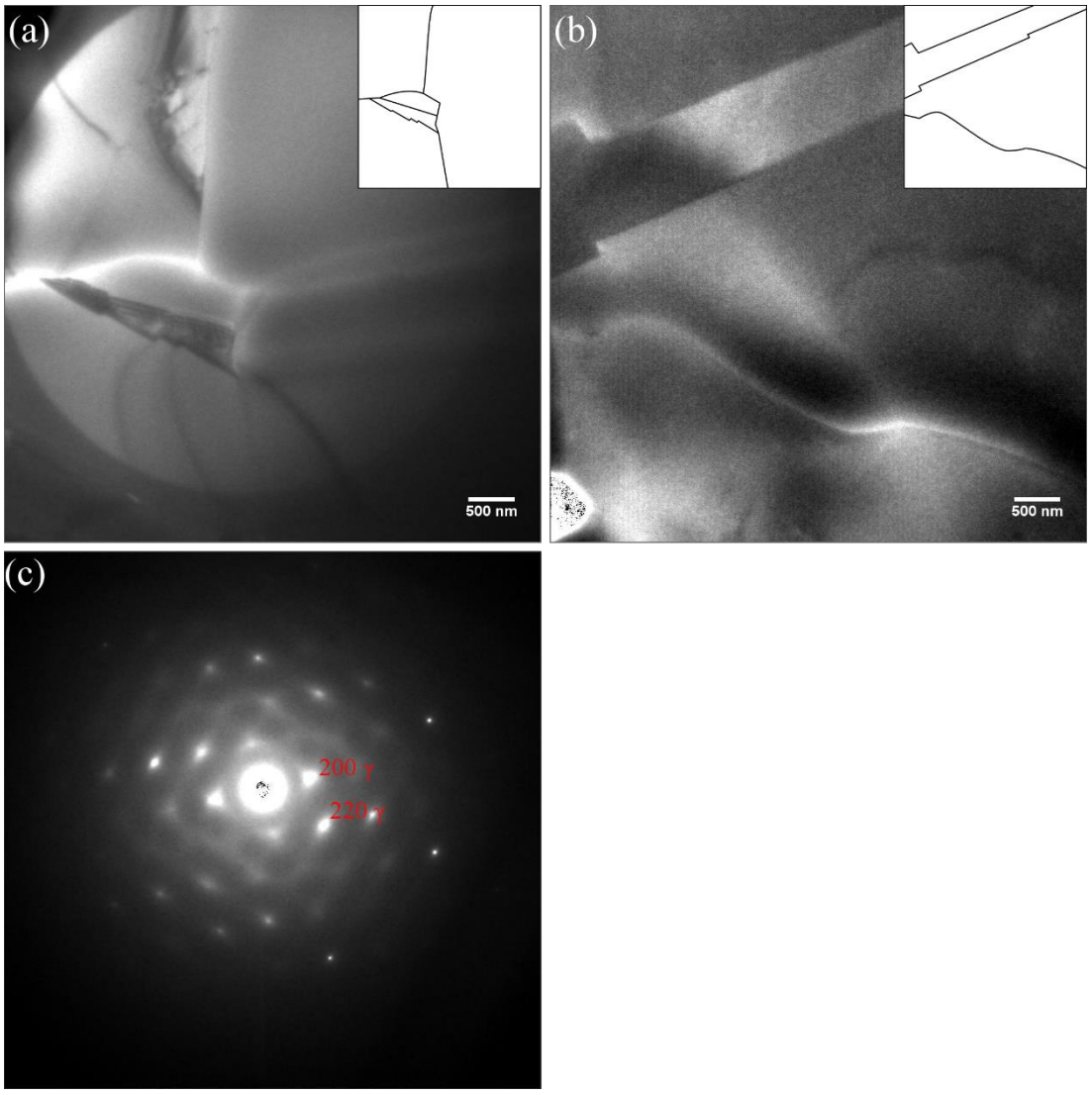

Figure 6.3: Bright field TEM of the Austenite microstructures in (a) specimen 6.1 at 859°C, (b) specimen 6.4 at 750°C, with curved grain boundaries and straight twin boundaries clearly visible in the austenite and (c) a austenite diffraction pattern along the [001] zone axis from specimen 6.3 at 750°C.

On cooling, the initial austenite-ferrite interface was captured for multiple specimens, shortly after the nucleation of the ferrite, as shown in figure 6.4. These early ferrite grains contained a mixture of straight and curved interfaces. A complete set of

diffraction patterns could not be obtained for all grains adjacent to the ferrite and consequently no OR was identified between those adjacent ferrite and austenite grains for which diffraction patterns were obtained.

One additional feature of note was the observation of significant lateral mode growth by the migration of ledges in one of the grains (figure 6.4(a)). This process is shown in figure 6.5. All growth of the ferrite grain during this period occurred as a result of the movement of these ledges. Visible ledges were apparent with a range of heights, with the two largest of 38 ± 4 nm and 70 ± 2 nm. These ledges did not necessarily form right angles suggesting that they may be composed of a collection of smaller ledges.

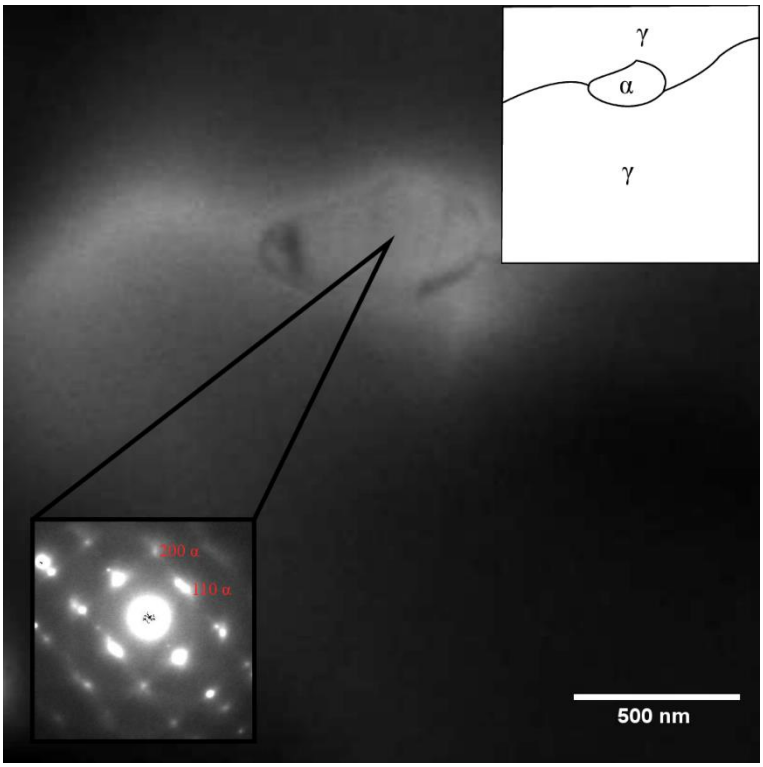

Figure 6.4: Bright field TEM of the Initial observations of austenite-ferrite interfaces in specimen 6.1 at 770°C. This ferrite grain was first observed shortly after nucleating on an austenite grain boundary.

Although only observed for a short time, the ledges did not appear to migrate with constant velocity, but showed distinct stages of mobility and immobility, the distinct mobile periods often lasted less than a second but with a relatively high velocity (up to ~300 $nm \cdot s^{-1}$). After this period of observation, the austenite-ferrite interface was eliminated by a second ferrite grain which grew with a much higher interface velocity in the normal mode.

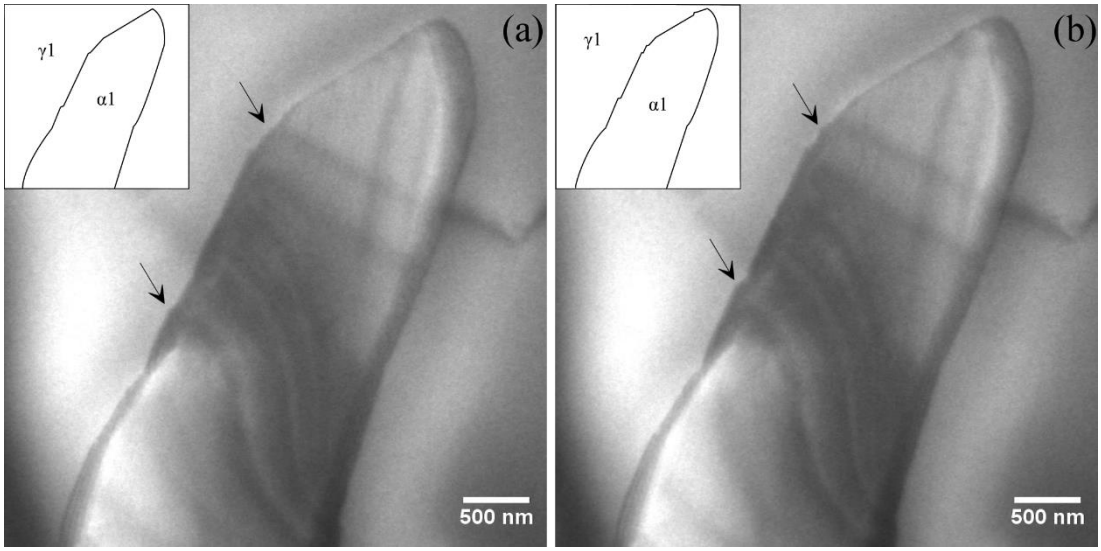

Figure 6.5: Bright field TEM of the ledge migration in specimen 6.1 (a) at 577.0 seconds (744°C) and (b) at 577.7 seconds 744°C). Black arrows, highlight the presence of mobile ledges on the left side of the grain. (Specimen 6.1).

6.4 Interface Position.

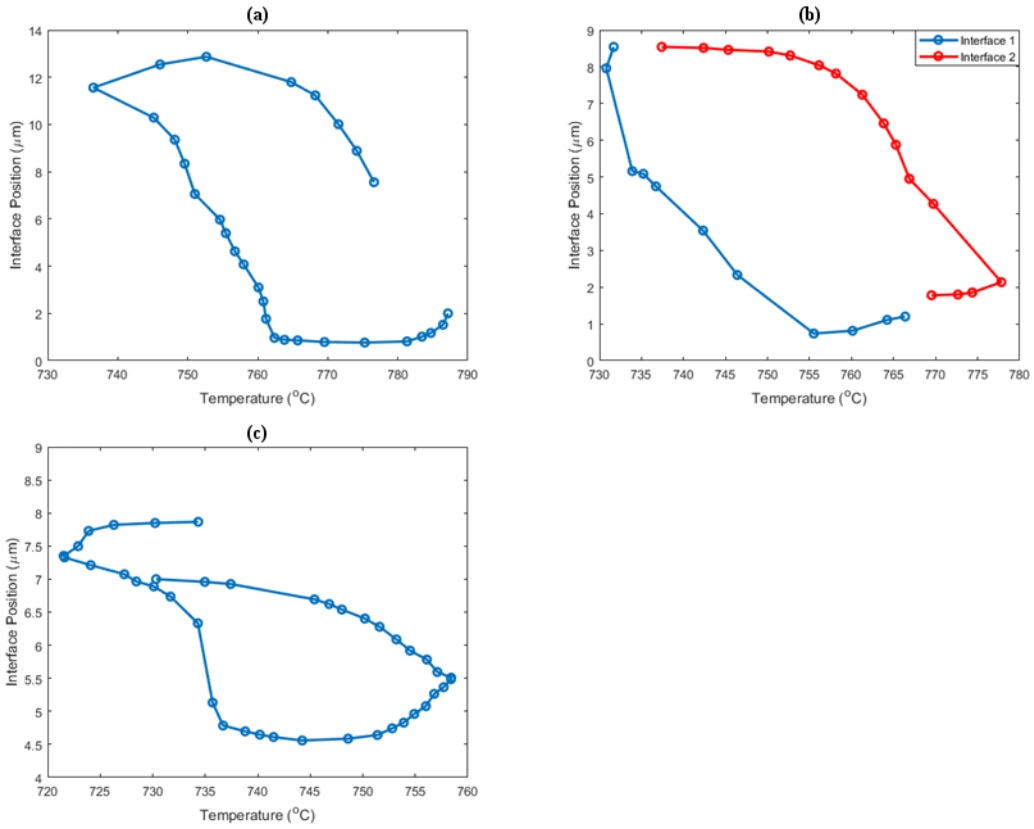

Figure 6.6: Graphs of the development of the interface position as a function of temperature during cyclic heat treatments for (a) specimen 6.1 (0.183 wt% C), (b) specimen 6.3 (0.263 wt% C) and (c) specimen 6.4 (0.330 wt% C). In all three compositions, distinct stagnant stages as well as inverse and normal transformations on both heating and cooling can be observed.

Figure 6.6 shows the most complete plot of interface position for a single heating and cooling cycle for all three compositions. In table 6.2 the estimated temperature range of each stage of the cycle, and the stagnant stage duration, is shown. There is only a small variation (2-3C) in the temperature range of the stagnant stage between specimens with a different carbon concentration.

Table 6.2: Table of the estimated temperature range of each transformation stage for all compositions in this chapter. Estimated from specimens 6.1, 6.3 and 6.4.

Stage	0.183 wt% C	0.263 wt% C	0.330 wt% C
Heating			
Inverse α→γ	4°C	1°C	2°C
Stagnant Stage	25°C	24°C	23°C
Normal α→γ	23°C	22°C	12°C
Stagnant time	187s	190s	181s
Cooling			
Inverse γ→α	4°C	3°C	4°C
Stagnant Stage	21°C	19°C	18°C
Normal γ→α	27°C	25°C	15°C
Stagnant time	153s	146s	131s

The total distance travelled by the interface during each cycle was 12.1 ± 0.5 μm for the 0.183C-1.5Mn steel and 7.8 ± 0.2 μm in the case of the 0.263C-1.5Mn steel. For the 0.33C-1.5Mn steel the total migration distance was 3.3 ± 0.2 μm. Of this the normal γ→α transformation accounted for 10.6 ± 0.4, 7.2 ± 0.2 and 2.6 ± 0.2 μm, in order of ascending carbon concentration.

These migration distances are not directly comparable due to the different temperature ranges. The estimated stagnant stage temperature range for all three specimens is approximately 23-25C on heating and 18-21C on cooling, meaning that the main difference between compositions is the temperature range of the normal transformation, and therefore the distance migrated. Comparing the normal transformation during equivalent temperature ranges is not strictly valid due to the changing velocity behaviour of the interface. However, in specimen 6.4 the normal α→γ transformation lasted from 722-737°C (i.e. 15C), migrating 2.6 μm. For specimen 6.1 the interface migrated 8.4 μm during the initial 15°C of the normal α→γ

transformation. This is in line with the expectation of higher interface migration velocity at lower carbon concentration.

The distance migrated during the inverse $\alpha \rightarrow \gamma$ transformation was 0.83 ± 0.07, 0.3 ± 0.2 and 0.55 ± 0.03 μm for specimens 6.1, 6.3 and 6.4 respectively. As with the migration during the normal transformation this is affected by the T_2 to T_1 temperature range. During the inverse $\gamma \rightarrow \alpha$ transformation the distance migrated by the interface was 0.17 ± 0.09, 0.6 ± 0.7 and 0.4 ± 0.08 μm.

From the start to the finish of the stagnant stage on heating, the interface displacement for specimens 6.1, 6.3 and 6.4 was 0.4 ± 0.03, 0.5 ± 0.03 and 0.26 ± 0.06 μm respectively. The comparable displacements on cooling were 0.05 ± 0.05, 0.46 ± 0.08 and 0.18 ± 0.04 μm. Similarly, the total distance migrated by the interface during this period for specimen 6.1 was 1.1 μm on heating and 0.46 μm on cooling. For specimen 6.3 this was 0.5 and 0.46 μm, and for specimen 6.4 it was 0.5 and 0.63 μm.

As with the previous compositions the morphological development of the stagnant stage differed between the stagnant stage on heating and on cooling. There were some broad similarities between compositions in each of these two stagnant stages.

On cooling, parts of the interface were slowly restructured over the course of the stagnant stage. This typically took the form of an inversion of curved sections of the interface as shown in figure 6.7. This did not necessarily affect the whole interface under observation but was particularly apparent in segments that were curved rather than straight. As can be seen in figure 6.7, neighbouring segments separated only by twin boundaries, inverted separately.

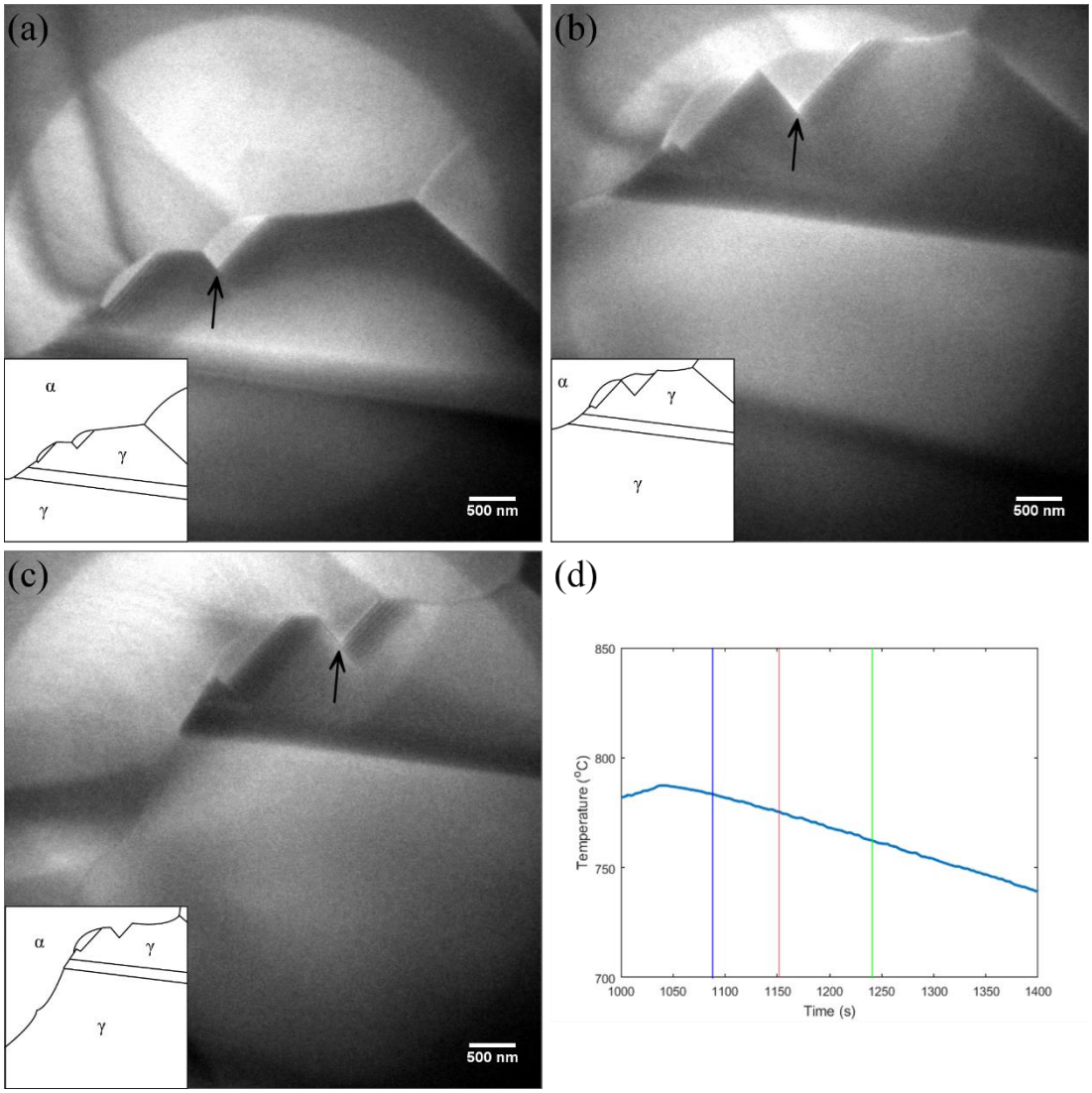

Figure 6.7: Bright field TEM of the development of the interface during the stagnant stage on cooling (a) at 1088.0 seconds (783°C), (b) at 1151.5 seconds (775°C), (c) at 1241.0 seconds (762°C) and (d) showing the time-temperature position of each frame. Vertical lines, from left to right, indicate the time depicted in frames (a)-(c). Black arrows indicate features (in this case a facetted boundary) which are immobile between frames. (Specimen 6.1).

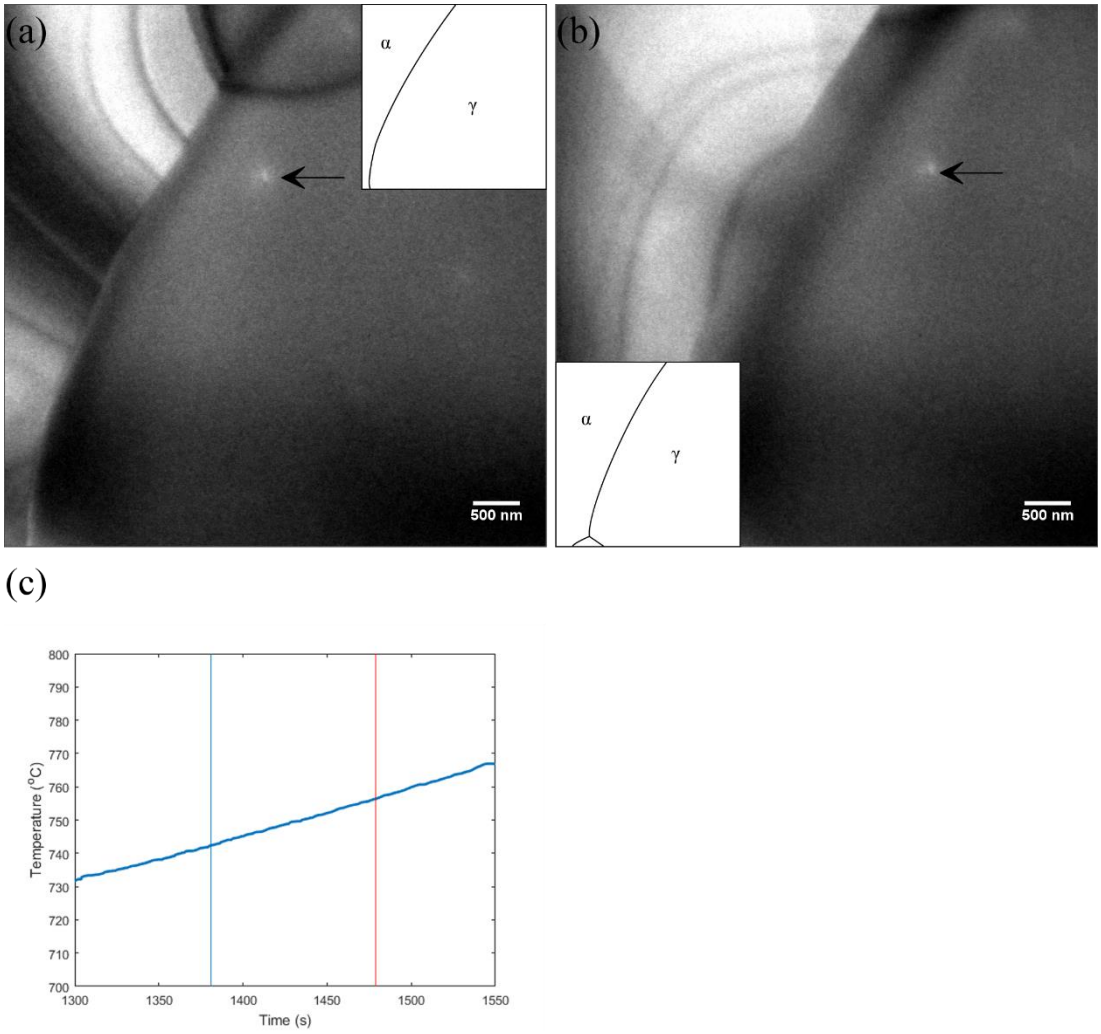

Figure 6.8: Bright field TEM of the stagnant stage on heating (a) at 1381.4 (742°C), (b) at 1479.2 seconds (756°C) and (c) showing the time-temperature position of each frame. Vertical lines, from left to right, indicate the time depicted in frames (a)-(b). Black arrows indicate a particle which was immobile between frames. (Specimen 6.3).

In contrast, during the stagnant stage on heating, the interface demonstrated a more stable morphology, which is particularly apparent in a second interface in specimen 6.3, shown in figure 6.8. Specimen 6.4, containing 0.330 wt% C, displayed the most disordered interface during the stagnant stage as shown in figure 6.9. However, this disorder increased as the stagnant stage ended, and the normal α→γ transformation began, as shown in figure 6.9(c).

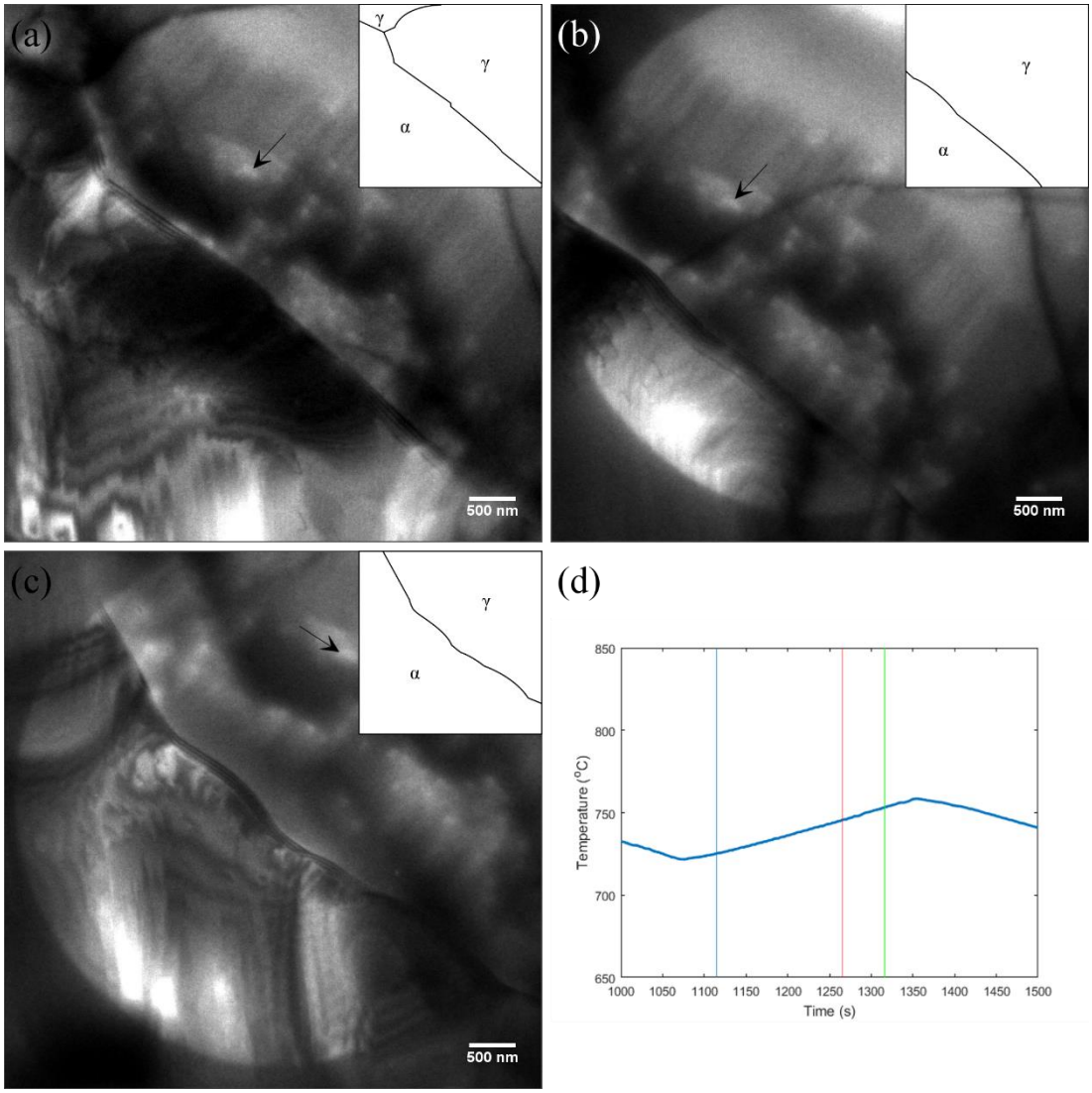

Figure 6.9: Bright field TEM of the development of interface morphology in specimen 6.4 (a) at 1115.3 seconds (725°C), (b) at 1265.4 seconds (745°C) at the end of the stagnant stage, (c) at 1315.8 seconds (753°C) during the normal α→γ transformation and (d) showing the time-temperature position of each frame. Vertical lines, from left to right, indicate the time depicted in frames (a)-(c). Black arrows indicate features which are immobile between frames. (Specimen 6.4).

6.5 Interface Velocity.

Figure 6.10 shows the interface velocities associated with the interfaces from figure 6.6 Velocities show the same qualitative behaviour as found in the previous compositions. The interface velocity increased as the temperature was increased during the ferrite to austenite transformation, peaking just before the T_2 temperature in each case. The peak velocities were -72 nm·s^{-1} for 0.183 wt% C, and -22 nm·s^{-1} for 0.330 wt% C. Similarly during the austenite to ferrite transformation the peak velocity

occurred soon after the transformation began for the 0.183wt% C and 0.330wt%C. This occurred at 761°C for specimen 6.1 and 735°C for specimen 6.4, with peak velocities of 154 nm·s^{-1} and 118 nm·s^{-1} respectively.

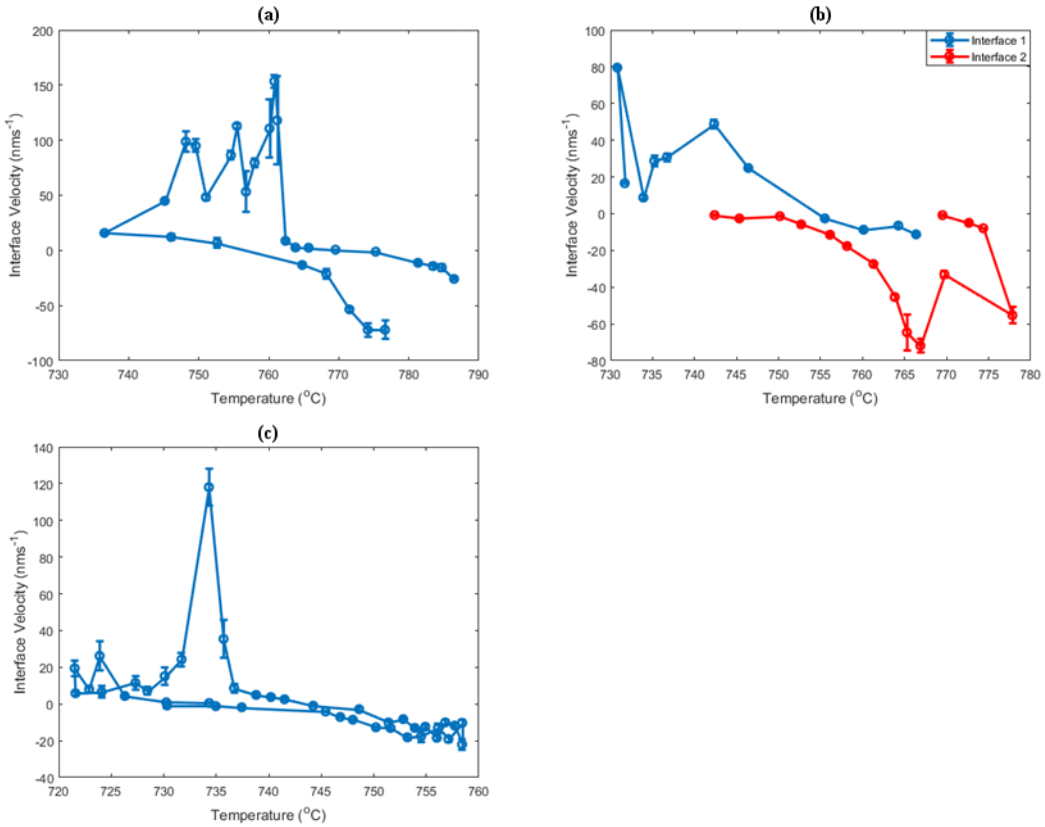

Figure 6.10: Graphs of the development of interface velocity as a function of temperature during cyclic heat treatment for (a) specimen 6.1 (0.183 wt% C), (b) specimen 6.3 (0.263 wt% C) and (c) specimen 6.4 (0.330 wt% C). Periods of normal and inverse transformation can be clearly distinguished from the stagnant stage.

Specimen 6.3 with 0.263 wt% C has a peak velocity at the T_1 temperature, which was 79 nm·s^{-1}. However, it was preceded by a very low interface velocity measurement (9 nm·s^{-1}). This is significant as the low velocity measurement occurred as the interface returned to the starting position it occupied during the initial formation of the interface, and may interact with the residual Mn spike. Figure 6.11 shows the interface shortly after observation had begun, with the position at which the low velocity measurement was made. A distinctively shaped region of dark contrast, potentially caused by thermal grooving can be seen, as well as several unidentified inclusions. These inclusions have a similar position in relation to the dark region indicating that the position had remained stable between the two images (i.e., that it is caused by a real

feature and not, for example, the foil bending). The situation is further complicated by the presence of several unidentified inclusions approximately 500-600 nm ahead of the previous interface position, which the interface was observed to interact with.

For this reason, it is likely that the 79 $nm \cdot s^{-1}$ peak velocity is due to the motion of the interface as it escapes the influence of the residual Mn spike and the inclusions. For comparison with the peak velocity of the other compositions, the earlier peak velocity of 49 $nm \cdot s^{-1}$ occurred at 742°C is therefore more appropriate. Similarly the early peak in the velocity on heating at 767°C was observed to be due to pinning by microstructural features and therefore is not considered to be the peak velocity of an unaffected interface. Instead the peak velocity is considered to occur at the T_2 temperature (in line with original expectations) and is -55 $nm \cdot s^{-1}$.

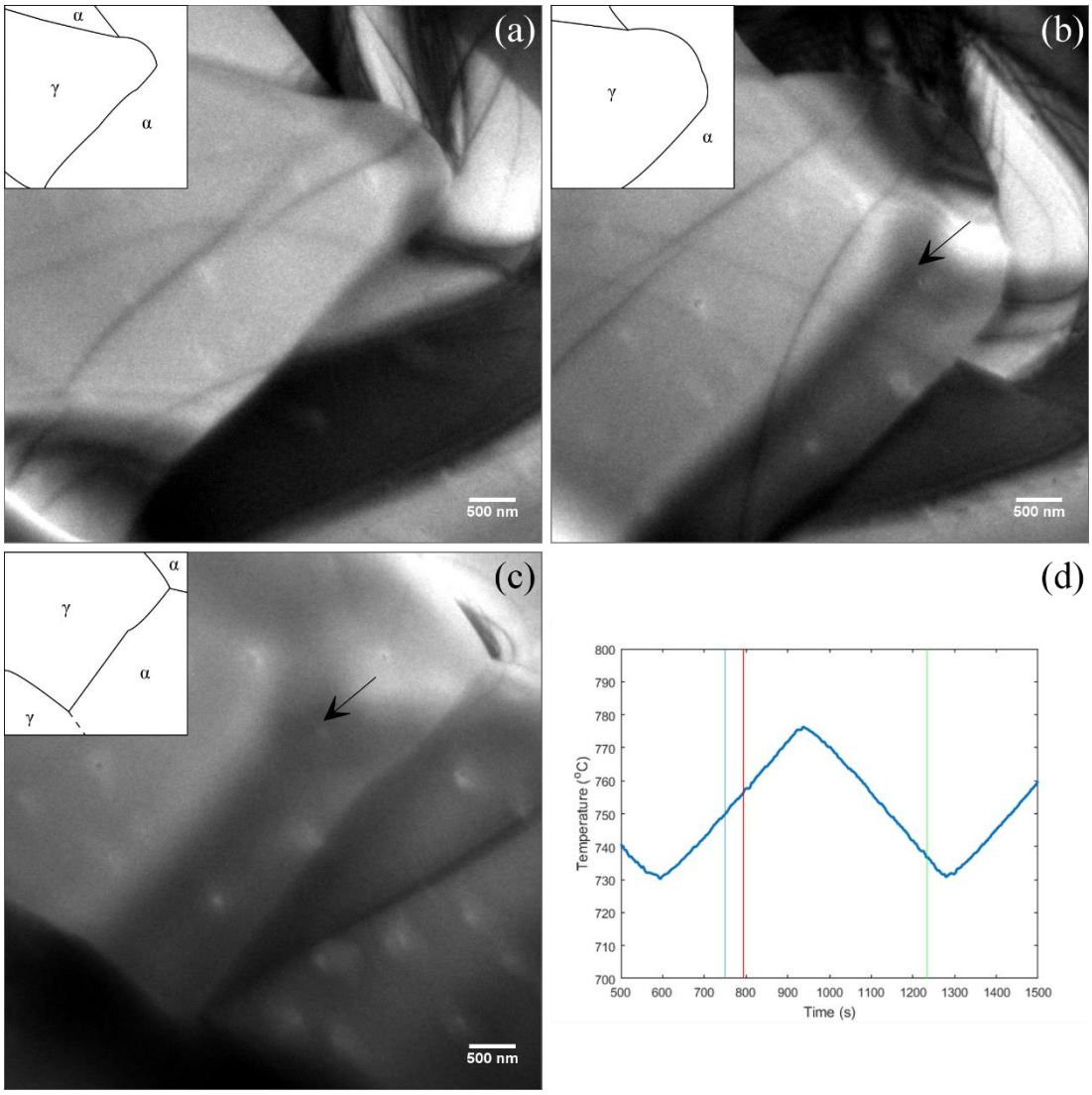

Figure 6.11: Bright field TEM of the return of the interface to a previous position (a) 749.2 seconds (750°C), (b) at 794.3 seconds (756°C), (c) the return of the interface at 1232.8 seconds (737°C) and (d) showing the time-

temperature position of each frame. Vertical lines, from left to right, indicate the time depicted in frames (a)-(c). Black arrows indicate the previous position of the interface which was immobile between frames. (Specimen 6.3).

The peak measured velocities decreased with increasing carbon concentration for both normal transformations, as originally anticipated.

6.6 General Observations.

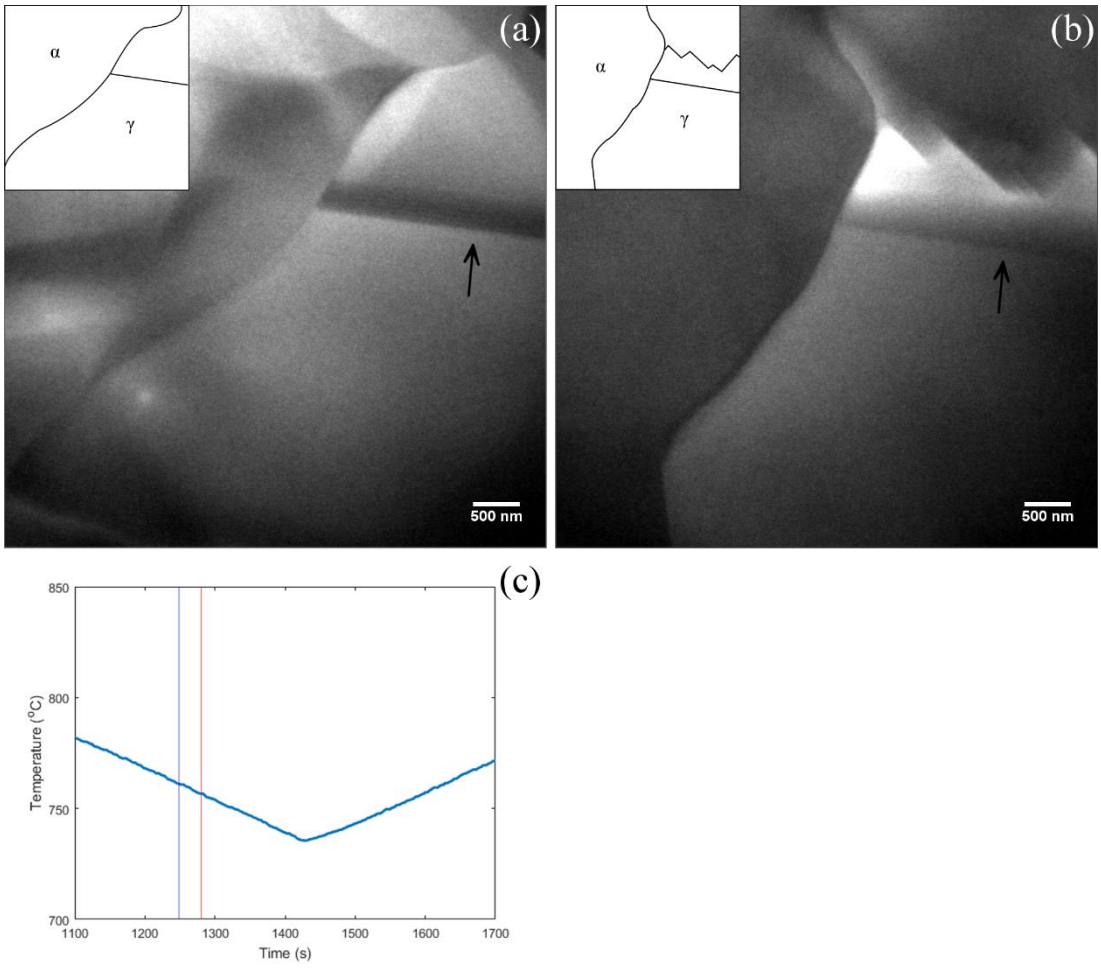

Figure 6.12: Bright field TEM of the development of the interface during the normal austenite to ferrite transformation (a) at 1247.8 seconds (761°C), (b) at 1280.6 seconds (757°C) and (c) showing the time-temperature position of each frame. Vertical lines, from left to right, indicate the time depicted in frames (a)-(c). Black arrows indicate a feature which appears in both frames, however, the field of view was moved sufficiently that this does not indicate a common position. (Specimen 6.1).

The normal γ→α transformation in the 0.183C specimens began from a curved interface as a result of the development during the cooling stagnant stage. This interface showed a constantly developing morphology developing a wave-like character as in figure 6.12. In contrast, the ferrite to austenite transformation did not

show this variation in interface morphology. In this case the sections of interface under observation maintained a regular morphology with parts slowly switching between straight and curved, as can be seen in figure 6.13.

In contrast the 0.263C specimens showed predominantly curved or straight interfaces during both the austenite to ferrite and ferrite to austenite transformations. Although development predominantly consisted of shifting between a curved or straight interface, some wave-like morphologies were observed. The structure of the interface was also influenced for both compositions by the presence of inclusions, which had a pinning effect similar to that shown in chapter 5.

In the case of the 0.33C specimens, the interface shifted between the competing morphologies. Figure 6.14 shows this development during the normal $\alpha \rightarrow \gamma$ transformation and into the inverse $\alpha \rightarrow \gamma$ transformation.

There were some inconsistencies in interface structure and migration behaviour between cycles in a single specimen. In chapter 4, this was found to be due to the behaviour of triple points which could be laterally displaced as neighbouring grains grew at different rates as well as by rapid motion along existing grain boundaries. In addition, differences in interface structure were observed, with the most apparent cause being the segmentation of the interface as a result of twin boundaries immediately behind or intersecting the interface. These twin boundaries did not necessarily form or form in the same location once the interface returned to its previous position.

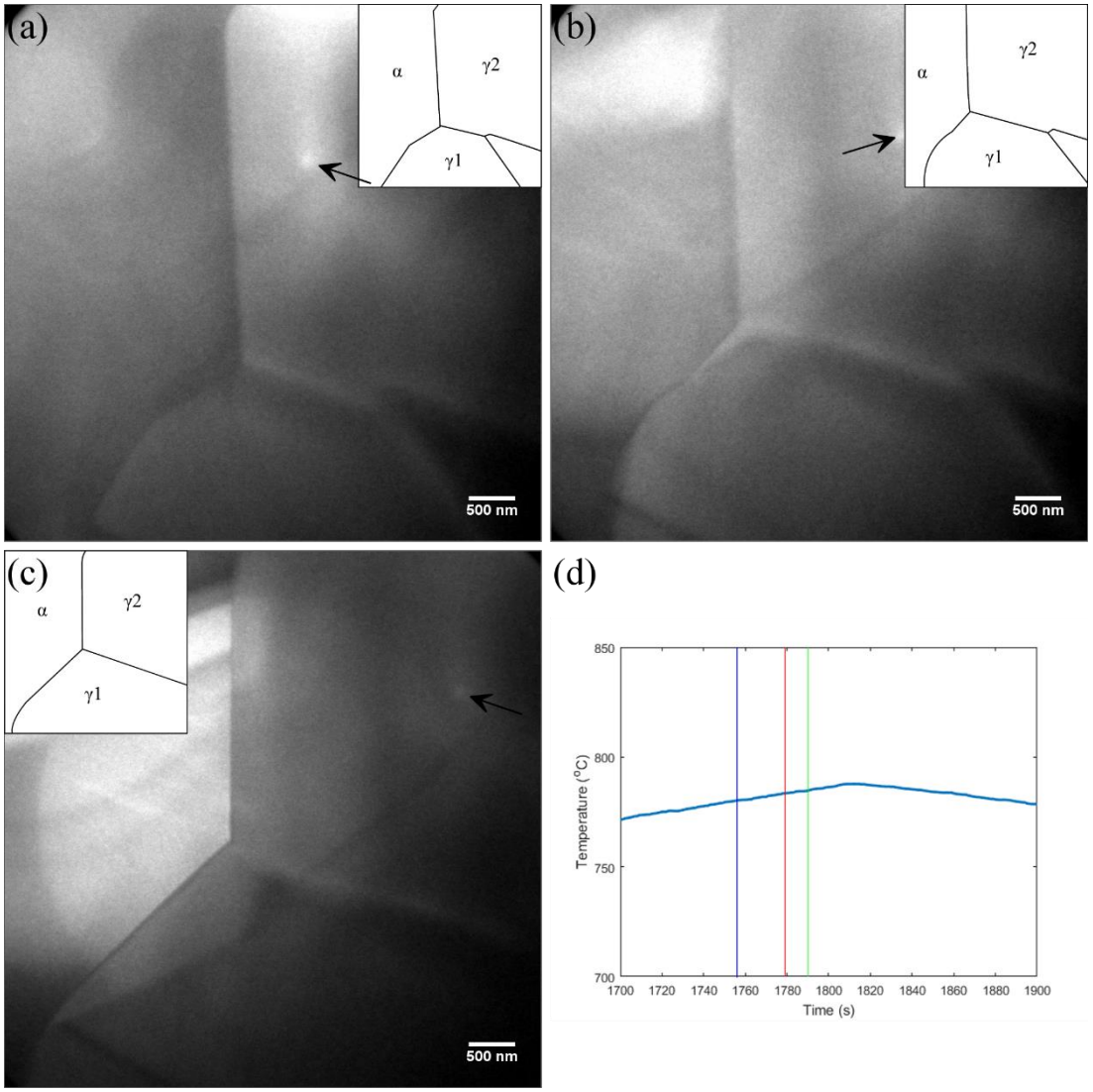

Figure 6.13: Bright field TEM of the development of the interface morphology during the normal α→γ transformation (a) at 1756.8 seconds (780°C), (b) at 1778.6 seconds (784°C), (c) at 1790.4 seconds (785°C) and (d) showing the time-temperature position of each frame. Vertical lines, from left to right, indicate the time depicted in frames (a)-(c). Black arrows indicate a particle which was immobile between frames. (Specimen 6.1).

Similar phenomena were observed in the present specimens, an example of which is specimen 6.1 where the final structure of the interface after one cycle is affected by both the absence of twin boundaries in the austenite and by the migration of a neighbouring austenite grain moving the shared grain boundary. This is shown in figure 6.15.

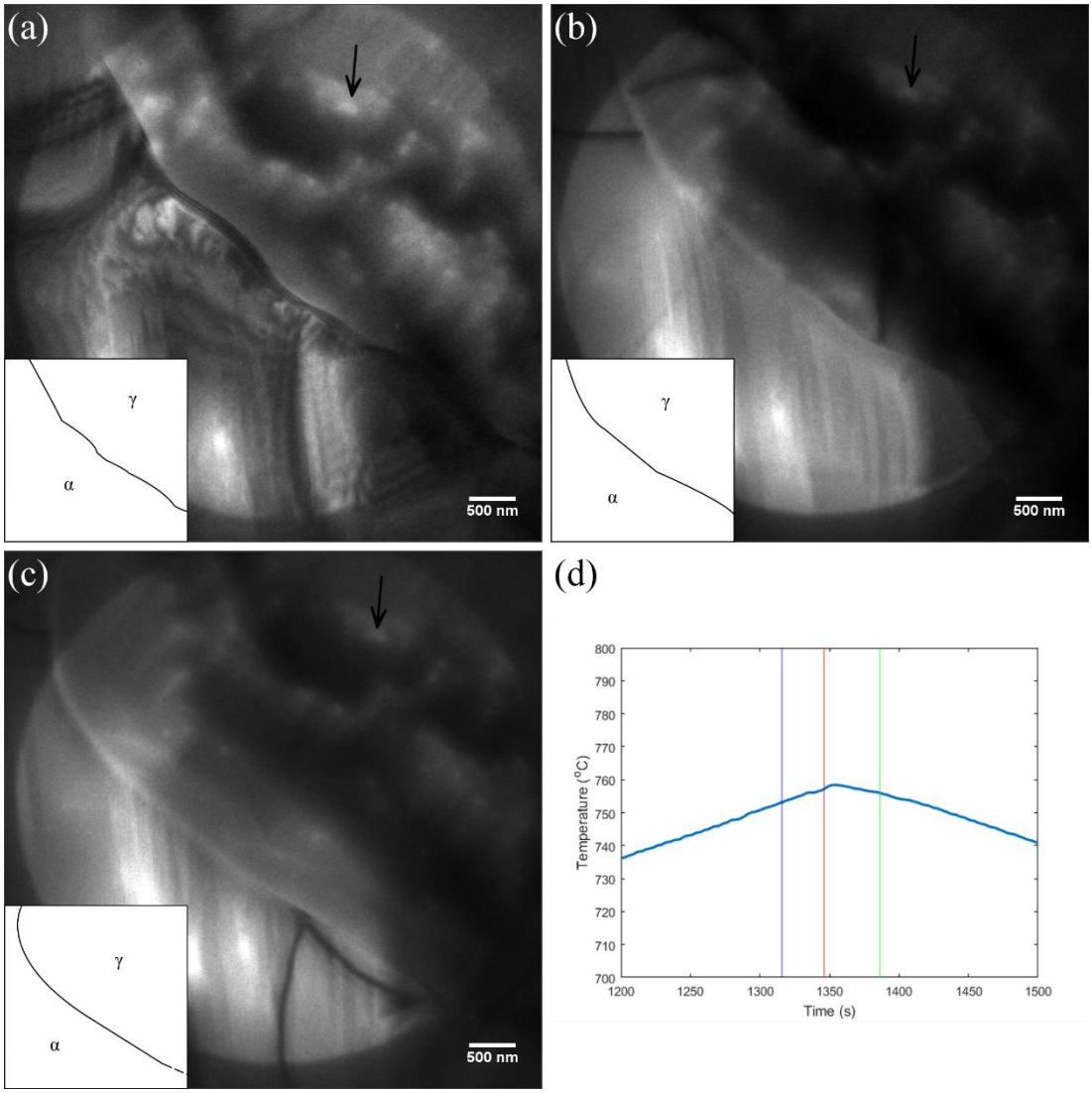

Figure 6.14: Bright field TEM of the development of the interface morphology during the normal and inverse α→γ transformation (a) at 1315.8 seconds (753°C), (b) at 1345.6 seconds (757°C), (c) at 1385.5 seconds (756°C) and (d) showing the time-temperature position of each frame. Vertical lines, from left to right, indicate the time depicted in frames (a)-(c). Black arrows indicate features which are immobile between frames. (Specimen 6.4).

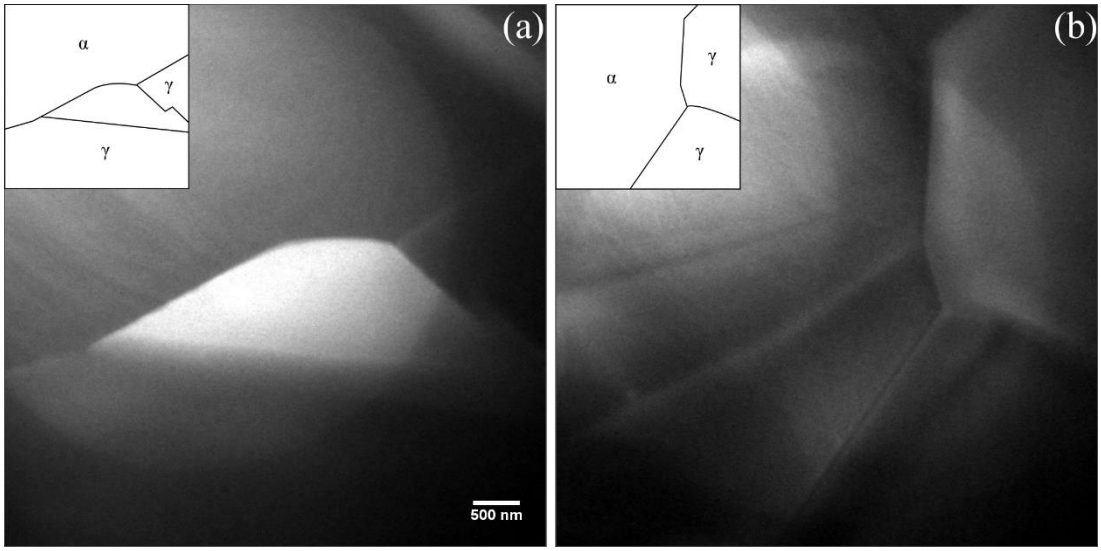

Figure 6.15: Bright field TEM of the variation between cycles in specimen 6.1 at (a) 787°C (1035.9 seconds) where two twin boundaries intersect the interface and (b) 787°C (1810.6 seconds), with the twin boundaries absent. (Specimen 6.1).

After cycling, the foils were investigated at room temperature to determine the identity of the particles seen in the video. As in the case of the particles observed in chapter 5, the particles showed increased levels of Al, indicating that these were likely aluminium oxides which were embedded in the foil but without penetrating through the full thickness of the foils.

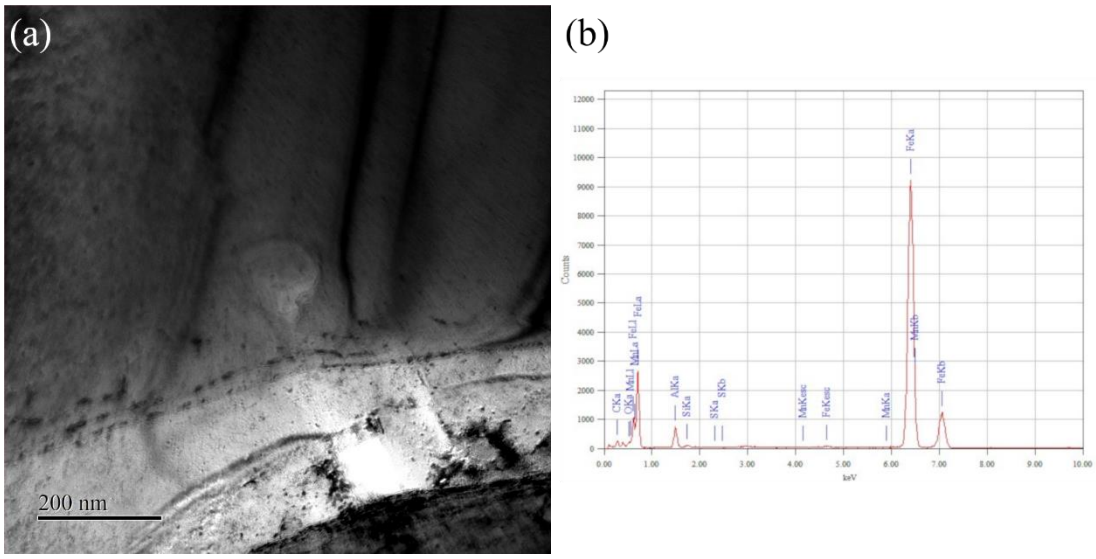

Figure 3.16: (a) Bright field TEM of a typical particle found in the Fe-0.33C-1.5Mn-0.14Si specimens (b) EDS spectra of the particle.

6.7 Kinetic Modelling and Dilatometry.

The heat treatments were modelled using the well-known DICTRA software [145], and the resulting development of the interface position over the course of the cycle is shown in figure 6.17 below. The austenite grain size was chosen as 25 μm, using the standard local equilibrium assumptions. The starting position of the interface is the position reached by the interface during initial cooling. The total migration distance predicted for steels containing 0.183, 0.263 and 0.330 wt% carbon was (excluding the first austenite to ferrite transformation) 100 nm, 85 nm and 30 nm respectively.

In order to compare the validity of the DICTRA predictions with the very different observations found during the TEM experiments, a specimen of 0.330C-1.5Mn-0.14Si steel was subjected to the same heat treatment used for specimens 6.4 and 6.5 in the TEM using dilatometry. In Chapter 4, the interface velocities extracted from dilatometry were comparable to that predicted by DICTRA. The results of the experiment are shown below in figure 6.18. There was very little dilation of the specimen during thermal cycling, with no easily distinguished normal transformation.

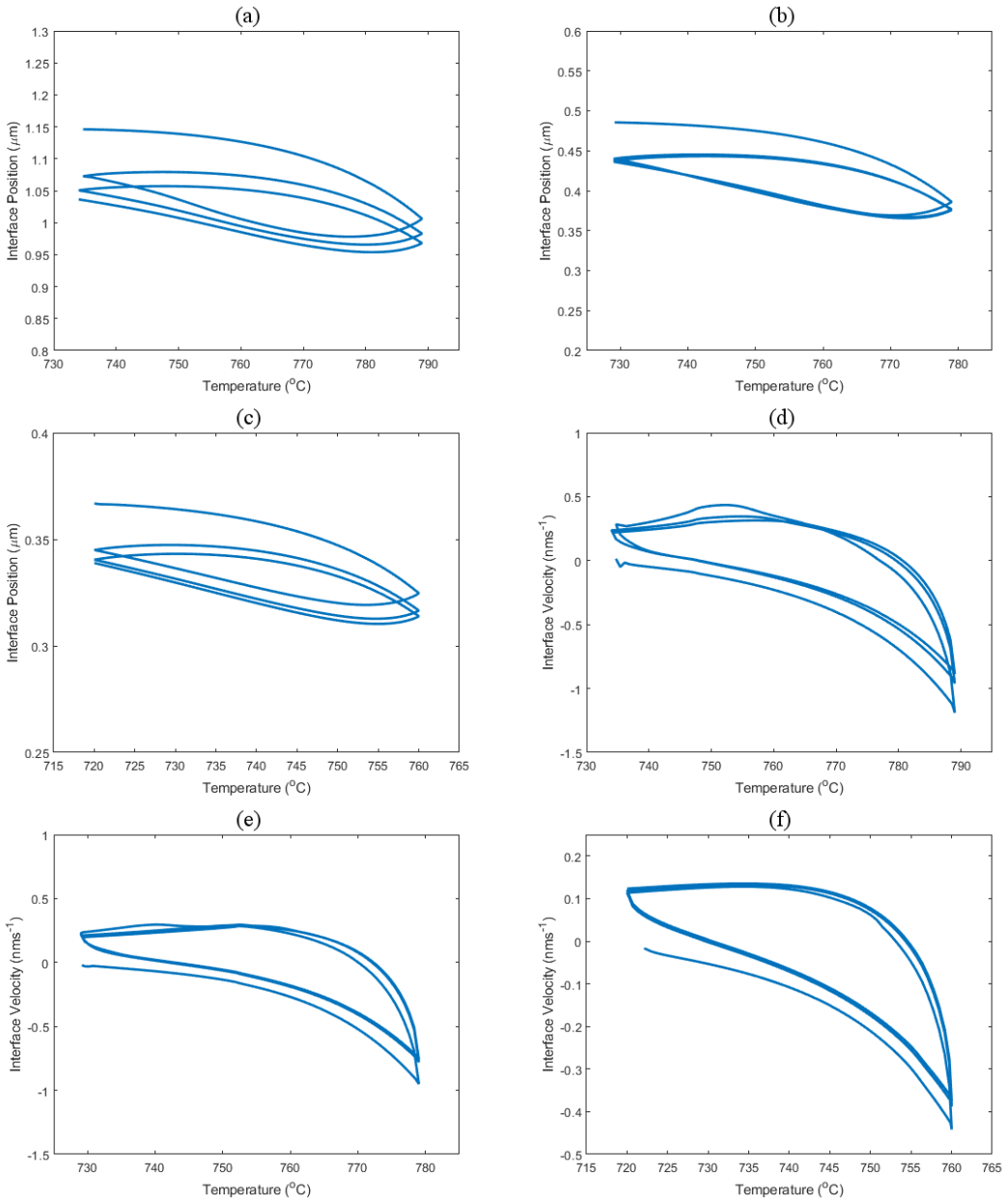

Figure 6.17: Graphs of the interface position against temperature for (a) 0.183 wt% C (b) 0.263 wt% C and (c) 0.330 wt% C and the velocity against temperature for the simulated heat treatments for (d) 0.183 wt% C (e) 0.263 wt% C and (f) 0.330 wt% C. The austenite to ferrite transformation has positive velocity and displacement.

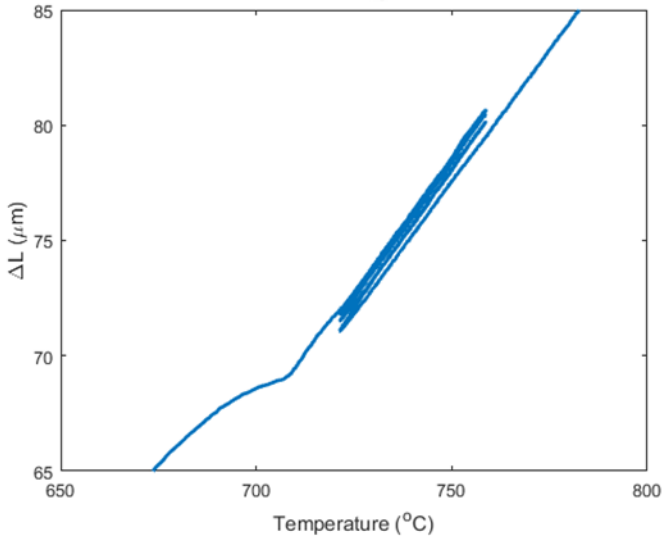

Figure 6.18: Graph of dilation against temperature for the 0.33C-1.5Mn-0.14Si cyclic heat treatment, very little transformation of the material is observable over the temperature range of the thermal cycle.

Figure 6.19 shows an optical micrograph of the microstructure found in the dilatometry specimen after heat treatment. It consisted predominantly of bainitic ferrite formed on cooling at the end of the cycle with very little proeutectoid ferrite apparent. This, the negligible dilation during heat treatment and the very small predicted interface movement from DICTRA, indicates that the behaviour observed in the TEM experiments is unlikely to be an accurate reflection of interface behaviour in the bulk. Furthermore this indicates that the likely stagnant stage temperature range experienced by the specimen on the order of 40ºC or higher, which would be in agreement with the results of Chen and van der Zwaag [3].

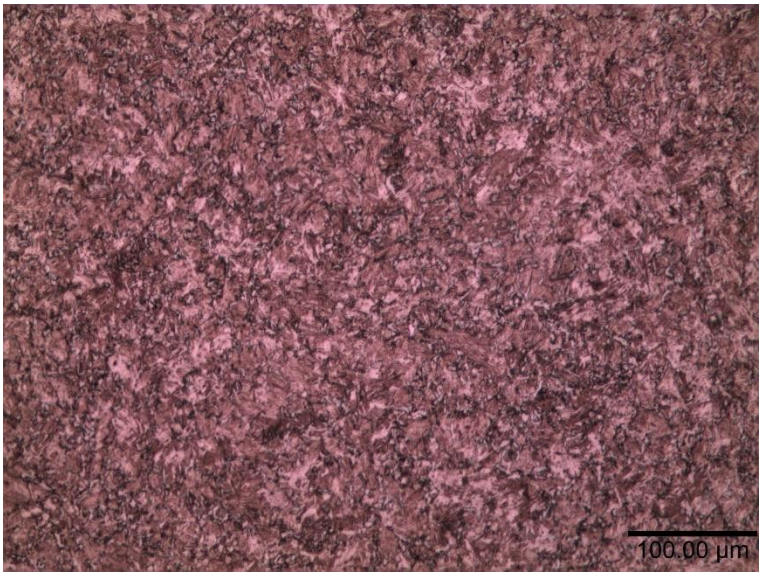

Figure 6.19: Optical micrograph of the microstructure of the 0.33C-1.5Mn-0.14Si steel specimen subjected to cyclic heat treatment using dilatometry and etched with 2% Nital. This microstructure contains very little ferrite, confirming that there was no transformation in the cycled temperature range.

6.8 Discussion.

The effect of the change in carbon concentration across the three compositions does not appear to have had a significant impact on the temperature range of the stagnant stage. Although the different heat treatments do not lend themselves well to direct comparison, the increase in carbon concentration does appear to have had the expected effect on slowing down the transformation kinetics, as can be seen by comparing the migration distance and peak velocities.

There are some disparities between the TEM observations and the bulk and simulation results, with the TEM experiments displaying a stagnant stage on the order of 20^{o}C shorter than expected. Despite these discrepancies between the TEM, bulk experiments and simulations, the 1.5 wt% Mn specimens all displayed a clearly defined stagnant stage in the TEM, which differed by only 2-3C across carbon compositions. As indicated in previous chapters there are some temperature differences between individual specimens, possibly as the result of variations in the quality of thermal contact between specimen and hot stage. In addition, in some cases contrast conditions make it difficult to precisely determine the start and end temperatures of each stage of the cyclic transformation. When these factors are considered a difference of 2-3C between specimens cannot be taken to represent

significant differences in stagnant stage temperature range as the carbon content is varied. This is broadly in agreement with the results of the previous chapters. The stagnant stage temperature range of the 0.1C-0.5Mn steel, for example, is in close agreement, when adjustments are made for the different heating and cooling rates, with that predicted by Chen et al. [7] using a lower carbon concentration of 0.02C-XMn (where X = 0.1, 0.2, 0.3).

However, atom probe tomography studies by van Landeghem et al. [84] and Langelier et al. [83] suggest that the segregation of Mn to the austenite-ferrite interface is primarily driven by C-Mn interactions. Song et al. [85] also show that C segregation at the interface can affect the distribution of Mn in Fe-0.19C-1.42Si-2.02Mn steels during quench and partitioning. Similarly, Ab initio simulations by Wicaksono and Militzer [86] also show co-segregation of C-Mn to Σ3 grain boundaries in bcc iron. Cyclic transformations reported by Farahani et al. [8] show that the concentration of C and N interstitials affects the stagnant stage temperature range.

It would therefore be expected that the present experiments show an increasing stagnant stage temperature range with increasing carbon concentration. That this is not seen can partially be attributed to the sensitivity of stagnant stage temperature range to carbon content. Farahani et al. [8] showed that stagnant stage temperature range is less sensitive to carbon concentration than to nitrogen, with a predicted increase of approximately 5C when C is increased from 0.1 wt% to 0.3 wt% with a heating/cooling rate of 60C/min. In the current experiments, with a heating rate of ± 8.4C/min and assuming that the effect is independent of Mn concentration, this would correspond to an increase of ~3ºC. This would be further reduced since the carbon concentration varies by 0.15 wt% in the present experiments. This would be difficult to distinguish under the experimental conditions used. The relatively small size predicted for this effect also accounts for the good agreement between the predictions of Chen et al. [7] and the TEM experiments in chapters 4 and 5.

One other feature of the experimental results reported in this chapter which is of interest is the apparent retardation of interface migration on its return to a previous position, as reported in chapter 6.5. In particular, as the interface returned to its previous position there was a sharp decrease in interface velocity followed by an acceleration of the interface as it migrated across and beyond its initial position. This

suggests that there may be some interaction with a residual Mn spike left in the austenite as a result of the austenite to ferrite transformation in the previous cycle.

This residual spike develops a specific Mn concentration profile in which the spike is preceded by a region in which there is a Mn depleted region ahead of the spike itself, where there is significant enrichment of the interface. DICTRA simulations indicate that for a 0.1C-0.5Mn steel the Mn composition profile at the T_2 temperature (figure 4.7) consists of a zig-zag in Mn concentration with a distance of approximately 600 nm between the maximum and minimum concentrations (in agreement with simulations performed by Chen et al. [7]). By the time the interface returns to the location of the residual spike, the width of the Mn enriched region is of the order of 1.2 μm (i.e. ~600 nm each side of the final position of the interface).

However, the situation is complicated by the presence of two inclusions in the austenite which interacted with the interface. These inclusions are located in approximately the same position as the Mn enriched region is expected to begin, around 5-600 nm from the initial position of the interface. The interface can be seen to undergo a minor change in shape as the interface migrated beyond these inclusions, which is associated with the lowest velocities all along the interface and indicates some pinning effect being exerted. The result is that the interface accelerated across the position it occupied during the stagnant stage of a previous cycle.

Although it is possible that there was some interaction of the interface with the residual Mn spike, it appears that the behaviour at this time is dominated by the effect of pinning by inclusions. However, this also means that it is not possible to explicitly rule out some interaction with the Mn spike.

The primary reasons for this is that changing the shape of the interface as a result of pinning will reduce the pinning effect of the Mn spike. Since only a relatively small length of the interface will cross the residual spike at a particular moment, the pinning force is reduced compared to a situation where the interface retained its morphology.

A secondary reason why the pinning effect of the residual Mn spike would be less apparent is because the interface crosses the location of the spike when it escapes from the influence of the pinning. Therefore, the interface is expected to have a high driving

force for further migration which may therefore make it difficult to observe the pinning effect of the residual Mn.

6.9 General Discussion.

Across all compositions the three transformation stages associated with CPPT heat treatments can be distinguished. The normal $\alpha \rightarrow \gamma$ and $\gamma \rightarrow \alpha$ transformations occur during periods of heating or cooling respectively. When the T_2 temperatures were reached and the specimen began cooling, the ferrite to austenite transformation continued for a time, as did the austenite to ferrite after reaching the T_1 temperature. This corresponds to the inverse transformation identified by Chen et al. using dilatometry and kinetic modelling. Finally there was a stage in where there was no significant interface migration, which corresponded to the stagnant stage. For all five compositions, the interface migration behaviour over the full temperature range of the stagnant stage was characterised by sluggish movement rather than being completely static. In general, the interface migration was observed to change direction during the period identified as the stagnant stage.

The first comparison to make across all compositions is in the stagnant stage temperature range and how this compares with expectations. Figure 6.20(a) compares the temperature range of the stagnant stage observed in the TEM from that obtained from dilatometry by Chen and van der Zwaag [3] Fe-0.1C-XMn (where X= 0.5, 1.0 and 1.5 wt%) for the comparable Mn concentrations. Figure 6.20(b) compares the temperature range of the stagnant stage as a function of Mn content with that expected based on the simulations of Chen et al. [7].

It can be seen that there is very good agreement for the TEM observations in the 0.1C-0.5Mn steel with the results from dilatometry and simulations and remains reasonably good for the 0.1C-1Mn steel. A significant discrepancy appears when the Mn concentration is increased to 1.5 wt% for specimens of all three carbon concentrations. In this case the observed stagnant stage was approximately half that expected and was actually lower than that observed for the 0.1C-1Mn steels.

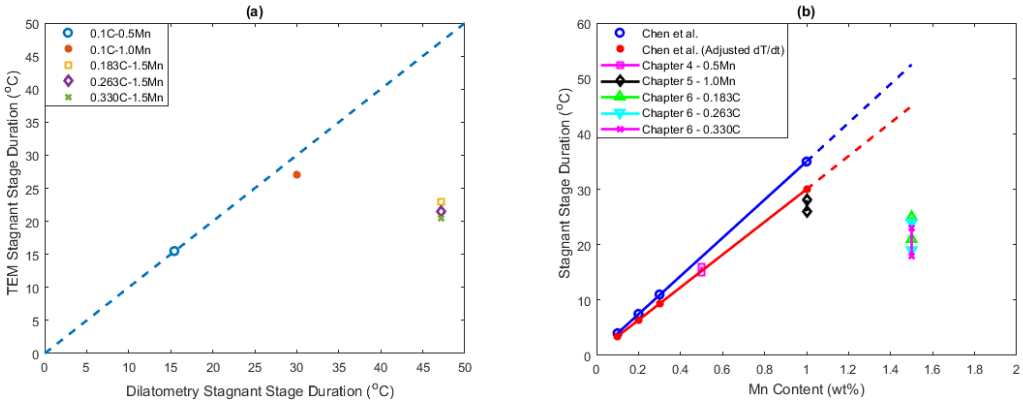

Figure 6.20: Graphs of (a) the average stagnant stage temperature range observed in the TEM against that found using dilatometry by Chen and van der Zwaag for Fe-0.1C-XMn (X=0.5,1.0,1.5) specimens (adjusted for heating/cooling rate) and (b) a comparison of the observed stagnant stage temperature range from TEM with that predicted by kinetic modelling.

That increasing Mn content increases the disparity between predicted and observed behaviour suggests that the concentration of Mn affects behaviour. Furthermore, Onink et al. [122] did not find significant disparities between calculated and measured growth rates during in situ TEM observations of the austenite to ferrite transformation in Fe-0.36C steels. This suggests that the disparity is not simply, for example, the result of surface diffusion of C accelerating the kinetics.

Farahani et al. [175] found a critical Mn concentration, between 1.5 and 2.0 wt%, at which the effective Mn concentration near the moving austenite-ferrite interface was locally increased, suppressing ferrite formation. As a result of limited backward migration of the interface during heating the zig-zag Mn profile formed at T_2 and the Mn spike formed at T_1 overlap, creating a region of increased Mn concentration.

Suppressed ferrite formation on cooling was in fact seen in the simulations and dilatometry performed for 1.5 wt% Mn specimens in this chapter. However, this was not the case for the TEM observations, indicating that interfacial conditions differed from the bulk during in situ experiments.

The morphology and behaviour of the interface during the stagnant stage was qualitatively consistent across all Mn compositions. On heating the stagnant stage demonstrated a stable morphology which was not totally static but migrated slowly throughout this period. The morphology at lower Mn compositions became more irregular once the stagnant stage ended and the normal $\alpha \rightarrow \gamma$ transformation began. On

cooling the stagnant stage exhibited a slow reshaping of the interface, typically in the form of the inversion of any curvature.

This inversion of the interface during the stagnant stage on cooling may be the result of the use of thin foil specimens. Typically, the ferrite was seen to first nucleate close to (but not at the edge of) the hole in the foil. Consequently, the direction of migration was away from the centre of the foil and into the thicker regions during the austenite to ferrite transformation. This means that the density of grain boundaries increased as the foil was heated and the ferrite to austenite transformation progressed. This increased number of grain boundaries and the shorter austenite/ferrite interfaces may have resulted in the edges of the interface experiencing a pinning effect resulting in bowing around the unpinned central lengths of interface.

In general, the stability of the interface during the stagnant stage may be due to the Mn enrichment at the interface and the greater role this plays in determining the transformation kinetics. Since diffusivity of Mn in austenite is several orders of magnitude smaller than for C [189], any perturbations which develop, so long as they maintain local equilibrium at the interface, will necessarily be smaller.

Considering the displacement of the interface during the stagnant stage the displacement falls within the range of 150-500 nm for all compositions, except for 50nm measured for specimen 6.1. The DICTRA simulations show that for up to 1 wt% Mn the displacement of the interface during the stagnant stage is of the order of 50-100 nm. For the 1.5 wt% Mn specimens the corresponding displacement is likely to be approximately 100 nm or higher, as this is the maximum displacement during cycling. Part of this variation can be attributed to limitations in how precisely the start and end of the stagnant stage could be determined. These displacements would be difficult to observe using other techniques such as CLSM or dilatometry.

During the stagnant stage the interface velocities developed by first decreasing, before the interface migration reversed direction and the interface began to accelerate. The lowest velocities measurements were on the order of 0.1-1 $nm \cdot s^{-1}$. The distance migrated at the lowest measured velocity was of the order of 20-30 nm for all specimens. This is at the lower limit of what can be confidently measured given the magnification used and the contrast conditions.

During the normal transformation it is useful to compare the peak velocities and the temperatures at which they occurred, this is shown in figure 6.21 below. The 0.5 and 1.0 wt% Mn specimens showed high peak interface velocities on both heating and cooling. On cooling (the normal γ→α transformation) this was 450 nm·s^{-1} and 113 nm·s^{-1} respectively, occurring at 816°C and 779°C. This shows excellent (within ~2°C) agreement with the temperature at which the peak velocity occurs in the DICTRA simulations. On heating (the normal α→γ transformation) the peak velocities were -300 nm·s^{-1} and -560 nm·s^{-1}. For 1.0 wt% Mn this occurred slightly before the T_2 temperature of the cycle 2°C early). As discussed above, the growth direction and distribution of the two phases was affected by the nucleation of ferrite close to the hole in the thin foil. It is possible, therefore, that the peak velocity occurred early as a result of impingement as the austenite grew into the relatively small ferrite grains. In other cases, such as the 0.5 wt% Mn specimens, unusually high velocities could be linked to nearby rapidly migrating triple points.

When the peak velocities of the 1.5 wt% Mn specimens are considered it can be seen that these are typically slower than those measured in the lower manganese specimens, but also tend to decrease with increasing levels of carbon.

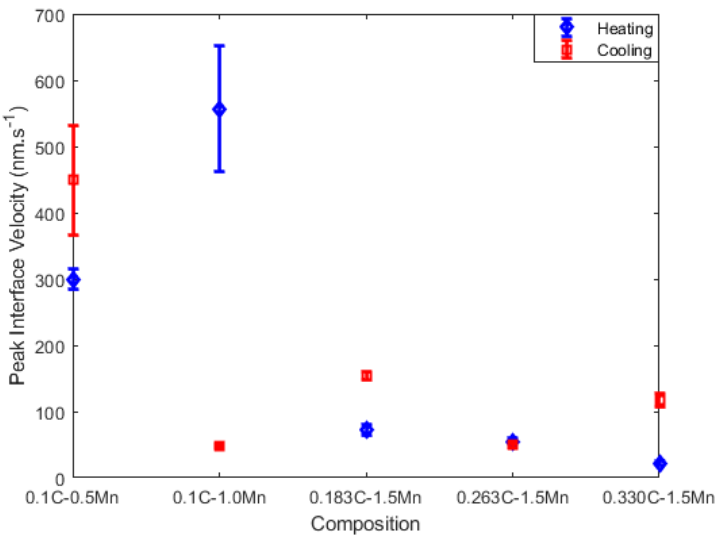

Figure 6.21: Graph of the peak velocities on heating and cooling for each composition.

In general, the present TEM observations during the normal transformation showed similar behaviour to that observed in hot stage TEM studies by Purdy [137] and Onink et al. [122]. Nishimura et al. [190] observed a non-planar, constantly evolving δ/γ

interface morphology using in situ X-ray imaging during massive-like transformation of Fe-0.3C-0.6Mn-0.3Si, on a larger length scale than the TEM observations.

There were only two observations of lateral-mode growth in the experiments reported within this thesis. Onink et al. reported more frequent observations of lateral mode growth during in situ TEM experiments on Fe-C steels. The observation in this chapter is a much clearer example than the ledges that were seen to form and migrate in the 0.1C-0.5Mn steel. The mobility of the facetted interface was low compared to the unfaceted interfaces which were observed within the steel, with the result that the majority of the surrounding austenite was transformed as a result of the unfaceted interface. Unfortunately this occurred before the orientation relationship between the faceted ferrite grain and the neighbouring austenite could be determined.

The ledges observed in the 0.1C-0.5Mn steel are a less clear example of lateral mode growth. Here the ledges formed on a migrating austenite-ferrite boundary during a period of austenite growth. There was a dislocation present in the austenite immediately behind the ledge indicating that the ledge may be more properly described as a disconnection [81]. In addition to the lateral movement of the ledge there was also some simultaneous normal movement of the interface as a whole.

The variation in the interface morphology did not correlate perfectly with interface velocity but in general during the normal transformation the interface morphology changed more rapidly leading in some cases to a wave-like or undulating movement. Examples of this can be seen in figure 4.20 for the 0.1C-0.5Mn specimens and figure 5.13 for the 0.1-1Mn specimen. Figure 4.10 shows how the interface became more irregular after the onset of the normal transformation for 0.1C-0.5n steels. In these cases the irregular interface could not necessarily be correlated with microstructural features. In comparison figures 6.9 and 6.14 show the change in the morphology for the 0.33C-1.5Mn steel from the stagnant stage on cooling, where the interface was predominantly (but not perfectly) straight, as in figure 6.9(a). A highly irregular interface developed during the normal $\gamma \rightarrow \alpha$ transformation, as in figures 6.9(c) and 6.14(a), before a more smoothly curved interface was established at the end of the inverse $\gamma \rightarrow \alpha$ transformation. In this case, the irregularity of the interface may have been increased by the presence of foreign particles in the foil.

6.10 Chapter Summary.

Successful cyclic partial phase transformation experiments were performed using in situ hot stage TEM on specimens containing Fe-XC-1.5Mn-0.14Si (where X = 0.183, 0.263 and 0.330) and are presented in this chapter. The qualitative behaviour of the interface is comparable with that observed in the previous chapters, with a more regular interface morphology during the stagnant stage than during the normal transformation. In addition, when a wave like interface morphology was observed, it appeared less pronounced than in the 0.1C-0.5Mn and 0.1C-1Mn steels.

However, there were also significant disparities between the TEM observations and the observations expected from bulk data and kinetic modelling. The interface migrated over a longer distance (a factor of 100x further) and with greater interface velocities. Unlike in simulated phase transformations, distinct normal and inverse transformations as well as a stagnant stage could be observed. The temperature range of this stagnant stage was 18-21C across all three carbon concentrations on cooling and 23-25C on heating.

There was no apparent increase in the temperature range of the stagnant stage with increased carbon content. Although this was expected based on the co-segregation of C and Mn to austenite-ferrite interfaces, under the chosen experimental conditions, the increase may be less than 3C. Within the limitations of the technique it would be difficult to determine that differing carbon concentration was responsible for differences of between specimens of this size.

7. Conclusions.

Following the in situ TEM experiments, the following conclusions are presented. These are divided into three parts, covering general conclusions relating to the use of in situ hot stage TEM experiments to study phase transformations, what can be concluded from the results of these experiments with respect to cyclic partial phase transformations and, briefly, some preliminary conclusions on the observations of bainite growth as reported in chapter 7.

7.1 Cyclic Partial Phase Transformations.

1. There was good agreement between the migration of the interface during cyclic partial phase transformation experiments using hot stage TEM and the CPPT behaviour found in dilatometry experiments and predicted by kinetic modelling. The interfaces were observed to display all the distinctive features of CPPT experiments including the normal and inverse transformations and a stagnant stage on both heating and cooling. Up to 1% Mn, there was semi-quantitative agreement with the bulk for variations in the interface velocity for non-stagnant stages of the transformation cycle, with a good agreement between the temperature at which peak velocities occur. In situ hot stage TEM offers a method to semi-quantitatively investigate the transformation behaviour of steels on the level of the individual interface.

2. The interface migration behaviour observed in the TEM did not include any unforeseen behaviour based current knowledge of phase transformations. That is, there was no unique behaviour observed as a consequence of the specimen being subjected to cyclic partial phase transformations.

3. The stagnant stage was found to be the result of the behaviour of individual interfaces and not the nucleation of new grains. This confirms that the transformation behaviour during cyclic partial phase transformations is the

result of local conditions at the austenite-ferrite interfaces. In general, it was rare to observe new grains at any time during thermal cycling other than the initial cooling. This agrees with the metallographic and HT-CLSM evidence of Chen et al. [88]

4. TEM observations made detailed observations of the morphology of the interface possible, and indicate that it is affected by the transformation kinetics. During the stagnant stage, when Mn is partitioned, the interface was predominantly found to have a more stable morphology, often one which was predominantly straight or smoothly curved. In comparison, during the normal transformation, when the interface was governed by LENP kinetics, the interface demonstrated more variability. In some cases a straight morphology was maintained, whilst in others migration was accompanied by a constantly developing, wave-like, morphology.

5. The morphology of the interface is influenced by the presence of microstructural features which can lead to the formation of complex or segmented boundaries. Twin boundaries were frequently found to be responsible for the segmentation of the interface. This arises where twin boundaries intersect the interface leading to a change in the equilibrium shape of the resulting interface-twin boundary triple point.

6. The interface continued to migrate at low velocity during the stagnant stage, with the total displacement measured during the stagnant stage between 50 and 500 nm. This would be difficult to detect using dilatometry and was not observed by HT-CLSM [88]. During the stagnant stage on heating the morphology was found to be stable. On cooling the evolution of the morphology was affected by the shorter length of the interface. The ends of the interface were pinned at grain boundaries and so further migration at the unpinned centre had the effect of altering the curvature of the interface. This

may be an artefact arising from thin foil specimens as the ferrite nucleated preferentially in thinner regions of the foil.

7. Up to 1 wt% Mn there is good agreement on the temperature range of the stagnant stage between the TEM observations and the predictions of Chen et al. [4], as well as with dilatometry. Agreement is excellent for the Fe-0.1C-0.5Mn specimens, and within ~10% for the Fe-0.1C-1Mn specimens. It is concluded from this that the conditions and chemistry at the interface are comparable in both the thin foil specimens used in the present experiments and in the bulk.

8. Up to 1 wt% Mn the interface migration is a factor of ~2 higher than that estimated from dilatometry and from simulations by Chen et al. [4] and Farahani et al. [175]. One reason for this disparity is that dilatometry averages the migration of many hundreds of grains, in comparison to the single interface followed in a TEM experiment. A second reason is that the impingement conditions may differ in the TEM. The ferrite nuclei preferentially nucleated in the thinner regions of the specimen and grew primarily away from the central hole. Therefore the effect of soft impingement may have been reduced.

9. The pinning of the interface by inclusions was observed in situ. The behaviour of the interface during the pinning process is in qualitative agreement with existing 2-D models of the process [178], once allowance is made for the transition from LENP to LEP kinetics. The maximum pinning force experienced by the austenite-ferrite interface in the Fe-0.1C-1Mn steel found in chapter 5 was calculated to be $F_{pinning} = 181 \pm 25$ nJ·m^{-1}.

10. There was good reversibility between cycles. The interface migrated over approximately the same path during thermal cycling with only minor changes in the orientation of the interface within the frame. However, there were some visible differences in the structure of the interface between cycles. A major

reason for this is that although twin boundaries were frequently seen to form in the austenite during the ferrite to austenite transformation, these twins did not necessarily occupy the same position from cycle to cycle. In addition, the number of twins formed varied from cycle to cycle. The reversibility of the interface was previously based on the HT-CLSM observations of Chen et al. [88]. The current observations confirm this reversibility at higher resolution and consequently more detail in terms of the surrounding microstructure.

7.2 Hot Stage TEM Experiments.

1. The TEM foils did not significantly decarburise over the timescale of the experiment. Had significant decarburisation occurred, this would have been accompanied by an increase in the amount of ferrite from cycle to cycle. For those interfaces where the interface position could be correlated across multiple cycles there was no persistent change in the interface position that would indicate an increase in the quantity of ferrite.

2. The TEM observations suggest that electron beam heating effect in the prevailing experimental conditions was small. Ferrite grains were never observed to nucleate within the field of view, indicating that the areas under observation may have experienced a local temperature increase. However, at no point was the direction of interface motion reversed when the stage was moved to view a new area with the electron beam. This indicates that the observed kinetics were not strongly affected by heating from the electron beam.

3. Thermal grooving was observed in some cases and was seen to affect the behaviour of the austenite-ferrite interface, particularly in the thinnest regions of the foil. This is not taken to have a significant effect on the overall transformation kinetics as the presence of severe thermal grooving could be directly observed from the TEM videos, and also produced distinctive interface

behaviour. Consequently, it was possible to eliminate interfaces which had been affected by the presence of thermal grooves from further analysis.

4. The surface diffusion coefficient, D_s, in Fe-0.1C-1.6Mn-0.5Mo specimens was estimated using the width of the thermal grooves found of the thin foil surface after heat treatment. At 870°C, the highest temperature, D_s was estimated to be on the order of 10^{-5} $cm^2 \cdot s^{-1}$. This is within the range expected from estimates of D_s found in the literature [149, 150, 151, 129].

7.3 Appendix A: Bainite Transformation.

1. The transformation from austenite to bainitic ferrite was observed at 300°C after austenitisation in the TEM. Lengthening behaviour was found to be discontinuous, with maximum measured velocities of 1,700 $nm \cdot s^{-1}$ and 4,300 $nm \cdot s^{-1}$, but with lower average lengthening rates of 230 $nm \cdot s^{-1}$ and 290 $nm \cdot s^{-1}$. This discontinuous lengthening behaviour is in contrast to continuous lengthening reported in the literature for in situ experiments. The thickening behaviour was found to be continuous, with the rate of thickening proportional to $t^{-1/2}$. The average velocities are of comparable order of magnitude to the <1 $\mu m \cdot s^{-1}$ growth rates found by Hu et al. [98] for a superbainitic steel containing 0.4 wt% C, 2.81 wt% Mn and 2 wt% Si, transformed at 330°C.

2. Bainitic ferrite plates were close to the expected K-S orientation relationship with the adjacent austenite. This indicates that the crystallography of the transformation remained unaffected by use of thin foil specimens.

3. During the lengthening of the bainitic plates, changing contrast was observed at the plate tip. In general this contrast became stronger during periods of lengthening and faded during periods of immobility. This suggests that the discontinuous lengthening behaviour of bainitic ferrite plates may originate with the build-up and relaxation of transformation stresses at the plate tip.

7.4 Future Work.

1. The observation of the interface crossing its previous position during the austenite to ferrite transformation as reported for the 0.263C-1.5Mn-0.14Si steel in chapter 6 was complicated by the interaction of the interface with other nearby microstructural features. Therefore one avenue of future work would be to observe this phenomenon in isolation. This could be achieved using the Fe-0.1C-0.5Mn and Fe-0.1C-1.0Mn specimens as these demonstrated that interfacial conditions were representative of the bulk. The heat treatment could be modified to ensure that the interface crosses the position occupied at the end of a previous cycle. This could be achieved by changing the thermal cycle from T_1-T_2-T_1 to T_1-T_2-T_3, where $T_3 = T_1 - 20^oC$.

2. Where possible the final position of the interface during the stagnant stage should be investigated using chemical analysis such as EDS, in order to directly link local chemistry to observed behaviour.

3. The observations for the steels containing 1.5 wt% Mn differ significantly from the bulk, whilst the lower Mn specimens showed much stronger agreement both in terms of the stagnant stage temperature range and the distance migrated. Further work is necessary to determine the precise mechanism responsible for this. A good starting point would be to examine steels containing intermediate levels of Mn with the aim of determining whether the discrepancy is the result of an abrupt change or a slow divergence.

4. The observation of the formation of bainite reported in chapter 7 was the result of a single successful experiment. In this case further work is necessary in order to ensure that the experiment can be performed successfully again and that the resulting observations are consistent and representative of bulk processes.

9. References

[1] H. K. D. H. Bhadeshia and R. W. K. Honeycombe, in *Steels: microstructure and properties*, Amsterdam, Elsevier, Butterworth-Heinemann, 2006, p. 1.

[2] M. Gouné, F. Danoix, J. Ågren, Y. Bréchet, C. Hutchinson, M. Militzer, G. Purdy, S. van Der Zwaag and H. Zurob, "Overview of the current issues in austenite to ferrite transformation and the role of migrating interfaces therein for low alloyed steels," *Materials Science & Engineering R,* pp. 1-38, 2015.

[3] H. Chen and S. van der Zwaag, "An Overview of the Cyclic Partial Austenite-Ferrite Transformation Concept and Its Potential," *Metallurgical and Materials Transactions A,* vol. 48, pp. 2720-2729, 2017.

[4] H. Chen, B. Appolaire and S. van der Zwaag, "Application of cyclic partial phase transformations for identifying kinetic transitions during solid-state phase transformations: Experiments and modeling," *Acta Materialia,* vol. 59, pp. 6751-6760, 2011.

[5] H. Chen and S. van der Zwaag, "Application of the cyclic phase transformation concept for investigating growth kinetics of solid-state partitioning phase transformations," *Computational Materials Science,* vol. 49, no. 4, pp. 801-813, 2010.

[6] S. E. Offerman, N. H. v. Dijk, J. Sietsma, S. Grigull, E. M. Lauridsen, L. Margulies, H. F. Poulsen, M. T. Rekveldt and S. v. d. Zwaag, "Grain Nucleation and Growth during Phase Transformations," *Science,* vol. 298, pp. 1003-1005, 2002.

[7] H. Chen, M. Gouné and S. van der Zwaag, "Analysis of the stagnant stage in diffusional phase transformation starting from austenite-ferrite mixtures," *Computational Materials Science,* vol. 55, pp. 34-43, 2012.

[8] H. Farahani, H. Zurob, C. R. Hutchinson and S. van der Zwaag, "Effect of C and N and their absence on the kinetics of austenite-ferrite phase transformations in Fe-0.5Mn alloy," *Acta Materialia,* vol. 150, pp. 224-235, 2018.

[9] D. A. Porter, K. E. Easterline and M. Y. Sherif, in *Phase Transformations in Metals and Alloys*, Boca Raton, CRC Press, 2009, pp. 383-384.

[10] H. K. D. H. Bhadeshia and R. W. K. Honeycombe, "Steels: microstructure and properties," Amsterdam, Elsevier, Butterworth-Heinemann, 2006, pp. 7-8.

[11] H. K. D. H. Bhadeshia and R. W. K. Honeycombe, "Steels: Microstructure and Properties," Amsterdam, Elsevier, Butterworth-Heinemann, 2006, pp. 39-42.

[12] W. D. Callister, "Materials Science and Engineering: An Introduction," New York, Wiley, 1994, pp. 267-270.

[13] C. Garcia de Andres, F. G. Caballero, C. Capdevila and L. F. Alvarez, “Application of dilatometric analysis to the study of solid-solid phase transformations in steels,” *Materials Characterization,* no. 101-111, p. 48, 2002.

[14] H. K. D. H. Bhadeshia, “Diffusional Formation of Ferrite in Iron and its Alloys,” *Progress in Materials Science,* vol. 29, pp. 321-386, 1985.

[15] R. J. Dippenaar and R. W. K. Honeycombe, “The Crystallography and Nucleation of Pearlite,” *Proceedings of the Royal Society of London A,* vol. 333, pp. 455-467, 1973.

[16] M. Hillert, “The Formation of Pearlite,” in *Decomposition of Austenite by Diffusional Processes*, New York, Interscience Publishers, 1962, pp. 226-227.

[17] H. I. Aaronson, “The Proeutectoid Ferrite and the Proeutectoid Cementite Reactions,” in *Decomposition of austenite by diffusional processes*, New York, Interscience, 1962, pp. 387-545.

[18] H. K. D. H. Bhadeshia and R. W. K. Honeycombe, “Steels: microstructure and properties,” Amsterdam, Elsevier, Butterworth-Heinemann, 2006, pp. 42-44.

[19] H. K. D. H. Bhadeshia, “The bainite transformation: unresolved issues,” *Materials Science and Engineering A,* vol. 273, pp. 58-66, 1999.

[20] L. C. D. Fielding, “The Bainite Controversy,” *Materials Science and Technology,* vol. 29, no. 4, pp. 383-399, 2013.

[21] A. Cottrell, “An Introduction to Metallurgy,” London, Edward Arnold, 1975, pp. 263-266.

[22] C. R. Hutchinson, A. Fuchsmann and Y. Brechet, “The Diffusional Formation of Ferrite from Austenite in Fe-C-Ni Alloys,” *Metallurgical and Materials Transactions A,* vol. 35, pp. 1211-1221, 2004.

[23] W. C. Leslie, “The Physical Metallurgy of Steels,” Washington, Hemisphere, 1981, pp. 142-145.

[24] J. C. Villalobos, A. Del-Pozo, B. Campillo, J. Mayen and S. Serna, “Microalloyed Steels through History until 2018: Review of Chemical Composition, Processing and Hydrogen Service,” *Metals,* vol. 8, no. 5, p. 351, 2018.

[25] W. C. Leslie, in *The Physical Metallurgy of Steels*, Washington, Hemisphere, 1981, pp. 145-147.

[26] P. Gong, E. J. Palmiere and W. M. Rainforth, “Dissolution and precipitation behvaiour in steels microalloyed with niobium during thermomechanical processing,” *Acta Materialia,* vol. 97, pp. 392-403, 2015.

[27] H. K. D. H. Bhadeshia and R. W. K. Honeycombe, “Steels: microstructure and properties,” Amsterdam, Elsevier, Butterworth-Heinemann, 2006, pp. 71-74.

[28] H. I. Aaronson, W. T. Reynolds and G. R. Purdy, “Coupled-Solute Drag Effects on Ferrite Formation in Fe-C-X systems,” *Metallurgical and Materials Transactions A,* vol. 35A, pp. 1187-1210, 2004.

[29] H. Kitahara, R. Ueji, N. Tsuji and Y. Minamino, “Crystallographic features of lath martensite in low-carbon steel,” *Acta Materialia,* vol. 54, pp. 1279-1288, 2006.

[30] D. B. Williams and C. B. Carter, in *Transmission Electron Microscopy: A Textbook for Materials Science*, New York, Plenum Press, 1996, p. 285.

[31] H. Kitahara, R. Ueji, M. Ueda, N. Tsuji and Y. Minamino, “Crystallographic analysis of plate martensite in Fe-28.5 at.% Ni by FE-SEM/EBSD,” *Materials Characterization,* vol. 54, pp. 378-386, 2005.

[32] R. W. K. Honeycombe and H. K. D. H. Bhadeshia, “Steels: Microstructure and Properties,” 2nd ed., Oxford, Butterworth-Heinemann, 2003, p. 35.

[33] J. R. Bradley and H. I. Aaronson, “The Stereology of Grain Boundary Allotriomorphs,” *Metallurgical Transactions A,* vol. 8, pp. 317-322, 1977.

[34] J. R. Bradley, J. M. Rigsbee and H. I. Aaronson, “Growth Kinetics of Grain Boundary Ferrite Allotriomorphs in Fe-C Alloys,” *Metallurgical Transactions A,* vol. 8, pp. 323-333, 1977.

[35] R. A. Vandermeer, “Modeling Diffusional Growth During Austenite Decomposition to Ferrite in Polycrystalline Fe-C Alloys,” *Acta Metallurgica et Materialia,* vol. 38, no. 12, pp. 2461-2470, 1990.

[36] D. A. Porter, K. E. Easterling and M. Y. Sherif, in *Phase Transformations in Metals and Alloys*, Boca Raton, CRC Press, 2009, pp. 263-276.

[37] P. J. Clemm and J. C. Fisher, “The Influence of Grain Boundaries on the Nucleation of Secondary Phases,” *Acta Metallurgica,* vol. 3, pp. 70-73, 1955.

[38] J. W. Christian, “The Theory of Transformations in Metals and Alloys: Part I,” Oxford, Elsevier Science Ltd, 2002, pp. 422-479.

[39] J. W. Cahn, “The Kinetics of Grain Boundary Nucleated Reactions,” *Acta Metallurgica,* vol. 4, pp. 449-459, 1956.

[40] J. W. Christian, “The Theory of Transformations in Metals and Alloys: Part I,” Oxford, Elsevier Science Ltd, 2002, pp. 480-486.

[41] D. Wang, Y. Liu, C. Bao, W. Tan and Z. Gao, “Approaches for isochronal transformation kinetics model and their application to the crystallization of amorphous alloys,” *Applied Physics A,* vol. 96, pp. 721-729, 2009.

[42] H. Chen, Y. Liu, Z. Yan, Y. Li and L. Zhange, “Consideration of the growth mode in isochronal austenite-ferrite transformation of ultra-low-carbon Fe–C alloy,” *Applied Physics A,* vol. 98, pp. 211-217, 2010.

[43] M. Hillert and L. Hoglund, “Mobility of α/γ phase interfaces in Fe alloys,” *Scripta Materialia,* vol. 54, pp. 1259-1263, 2006.

[44] J. J. Wits, T. A. Kop, Y. van Leeuwen, J. Seitsma and S. van der Zwaag, “A study on the austenite-to-ferrite phase transformation in binary substitutional iron alloys,” *Materials Science and Engineering A,* vol. 283, pp. 234-241, 2000.

[45] G. P. Krielaart and S. van der Zwaag, “Kinetics of γ→α phase transformation in Fe-Mn alloys containing low manganese,” *Materials Science and Technology,* vol. 14, pp. 10-18, 1998.

[46] Y. C. Liu, F. Sommer and E. J. Mittemeijer, “Kinetics of the abnormal austenite-ferrite transformation behaviour in substitutional Fe-based alloys,” *Acta Materialia,* vol. 52, pp. 2549-2560, 2004.

[47] Y. C. Liu, F. Sommer and E. J. Mittemeijer, “Abnormal austenite–ferrite transformation behaviour in substitutional Fe-based alloys,” *Acta materialia,* vol. 51, pp. 507-519, 2003.

[48] Y. C. Liu , F. Sommer and E. J. Mittemeijer, “Abnormal austenite–ferrite transformation behaviour of pure iron,” *Philosophical Magazine,* vol. 84, no. 18, pp. 1853-1876, 2004.

[49] J. Zhu, H. Luo, Z. Yang, C. Zhang, S. van der Zwaag and H. Chen, “Determination of the intrinsic a/g interface mobility during massive transformations in interstitial free Fe-X alloys,” *Acta materialia,* vol. 133, pp. 258-268, 2017.

[50] J. W. Christian, “The Theory of Transformations in Metals and Alloys Part I,” 3rd ed., Oxford, Elsevier Science Ltd, 2002, pp. 486-508.

[51] C. Zener, “Theory of Growth of Spherical Precipitates from Solid Solution,” *Journal of Applied Physics,* vol. 20, pp. 950-953, 1949.

[52] J. S. Kirkaldy, “Theory of Diffusional Growth in Solid-Solid Transformations,” in *Decomposition of Austenite by Diffusional Processes*, New York, Interscience, 1962, pp. 39-122.

[53] H. K. D. H. Bhadeshia and R. W. K. Honeycombe, “Steels: microstructure and properties,” Amsterdam, Elsevier, Butterworth-Heinemann, 2006, pp. 47-52.

[54] M. Hillert and J. Agren, “On the definitions of paraequilibrium and orthoequilibrium,” *Scripta Materialia,* vol. 50, pp. 697-699, 2004.

[55] A. Van der Ven and L. Delaey, “Models for Precipitate Growth During the y -> a + y transformation in Fe-C and Fe-C-M Alloys,” *Progress in Materials Science,* vol. 40, pp. 181-264, 1996.

[56] J. S. Kirkaldy, “Diffusion in Multicomponent Metallic Systems: I. Phenomenological theory for substitutional solid solution alloys,” *Canadian Journal of Physics,* vol. 36, pp. 899-906, 1958.

[57] W. C. Leslie, in *The Physical Metallurgy of Steels*, Washington, Hemisphere, 1981, pp. 74-79.

[58] G. Purdy, J. Agren, A. Borgenstam, Y. Brechet, M. Enomoto, T. Furuhara, E. Gamsjager, M. Gouné, M. Hillert, C. Hutchinson, M. Militzer and H. Zurob, "ALEMI: A Ten-Year History of Discussions of Alloying-Element Interactions with Migrating Interfaces," *Metallurgical and Materials Transactions A,* vol. 42A, pp. 3703-3718, 2011.

[59] C. R. Hutchinson, H. S. Zurob and Y. Brechet, "The Growth of Ferrite in Fe-C-X Alloys: The Role of Thermodynamics, Diffusion, and Interfacial Conditions," *Metallurgical and Materials Transactions A,* vol. 37, pp. 1711-1720, 2006.

[60] A. Phillion, H. S. Zurob, C. R. Hutchinson, H. Guo, D. V. Malakhov, J. Nakano and G. R. Purdy, "Studies of the Influence of Alloying Elements on the Growth of Ferrite from Austenite under Decarburization Conditions: Fe-C-NI Alloys," *Metallurgical and Materials Transactions A,* vol. 35, pp. 1237-1242, 2004.

[61] H. S. Zurob, C. R. Hutchinson, A. Beche, G. R. Purdy and Y. J. M. Brechet, "A transition from local equilibrium to paraequilibrium kinetics for ferrite growth in Fe-C-Mn: a possible role of interfacial segregation," *Acta Materialia,* vol. 56, pp. 2203-2211, 2008.

[62] H. S. Zurob, C. R. Hutchinson, Y. Brechet, H. Seyedrezai and G. R. Purdy, "Kinetic transitions during non-partitioned ferrite growth in Fe-C-X alloys," *Acta Materialia,* vol. 57, pp. 2781-2792, 2009.

[63] H. Guo, G. R. Purdy, M. Enomoto and H. I. Aaronson, "Kinetic Transitions and Substitutional Solute (Mn) Fields Associated with Later Stages of Ferrite Growth in Fe-C-Mn-Si," *Metallurgical and Materials Transactions A,* vol. 37, pp. 1721-1729, 2006.

[64] J. Sietsma and S. van der Zwaag, "A concise model for mixed-mode phase transformations in the solid state," *Acta Materialia,* vol. 52, pp. 4143-4152, 2004.

[65] C. Bos and J. Sietsma, "A mixed-mode model for partitioning phase transformations," *Scripta Materialia,* vol. 57, pp. 1085-1088, 2007.

[66] M. Hillert, J. Odqvist and J. Agren, "Interface conditions during diffusion-controlled phase transformations," *Scripta Materialia,* vol. 50, pp. 547-550, 2004.

[67] M. Hillert, "Solute drag in grain boundary migration and phase transformations," *Acta materialia,* vol. 52, pp. 5289-5293, 2004.

[68] J. W. Cahn, "The impurity-drag effect in grain boundary motion," *Acta Metallurgica,* vol. 10, pp. 789-798, 1962.

[69] M. Hillert, "Solute Drag, Solute Trapping and Diffusional Dissipation of Gibbs Energy," *Acta Metallurgica,* vol. 47, no. 18, pp. 4481-4505, 1999.

[70] K. Lucke and K. Detert, "A quantitative theory of grain boundary motion and recrystallisation in metals in the presence of impurities," *Acta Metallurgica,* vol. 5, pp. 628-637, 1957.

[71] M. Hillert and B. Sundman, “A treatment of the solute drag on moving grain boundaries and phase interfaces in binary alloys.,” *Acta Metallurgica,* vol. 24, pp. 731-743, 1976.

[72] M. Hillert, J. Odqvist and J. Agren, “Comparison between solute drag and dissipation of Gibbs energy by diffusion,” *Scripta Materialia,* vol. 45, pp. 221-227, 2001.

[73] G. R. Purdy and Y. J. Brechet, “A solute drag treatment of the effects of alloying elements on the rate of the proeutectoid ferrite transformation in steels,” *Acta Metallurgica et materialia,* vol. 43, no. 10, pp. 3763-3774, 1995.

[74] M. Hillert, “Phase Equilibria, Phase Diagrams and Phase Transformations,” Cambridge, Cambridge University Press, 2008.

[75] J. W. Christian, “The Theory of Transformations in Metals and Alloys Part I,” Oxford, Elsevier Science Ltd, 2002, pp. 533-542.

[76] H. Zhao and E. J. Palmiere, “Effect of austenite grain size on acicular ferrite transformation in a HSLA steel,” *Materials Characterization,* vol. 145, pp. 479-489, 2018.

[77] F. Liu, F. Sommer, C. Bos and E. J. Mittemeijer, “Analysis of solid state phase transformation kinetics: models and recipes,” *International Materials Reviews,* vol. 52, no. 4, pp. 193-212, 2007.

[78] J. W. Christian, “The Theory of Transformations in Metals and Alloys Part I,” Oxford, Elsevier Science Ltd, 2002, pp. 480-482.

[79] D. A. Porter, K. E. Easterling and M. Y. Sherif, “Phase Transformations in Metals and Alloys,” vol. Boca Raton, Boca Raton, CRC Press, 2009, pp. 202-205.

[80] G. J. Shiflet, M. A. Mangan and W. G. Meng, “Growth by Ledges,” *Interface Science,* vol. 6, pp. 133-154, 1998.

[81] H. I. Aaronson, B. C. Muddle, J. F. Nie and J. P. Hirth, “Comparison of Interfacial Structure-Related Mechanisms in Diffusional and Martensitic Transformations,” *Metallurgical and Materials Transactions A,* vol. 33, pp. 2541-2547, 2002.

[82] H. Chen and S. van der Zwaag, “Indirect evidence for the existence of the Mn partitioning spike during the austenite to ferrite transformation,” *Philosophical Magazine Letters ,* vol. 92, no. 2, pp. 86-92, 2012.

[83] B. Langelier, H. P. Van Landeghem, G. A. Botton and H. S. Zurob, “Interface Segregation and Nitrogen Measurement in Fe–Mn–N Steel by Atom Probe Tomography,” *Microscopy and Microanalysis,* vol. 23, pp. 385-395, 2017.

[84] H. P. Van Landeghem, B. Langelier, D. Panahi, G. R. Purdy, C. R. Hutchinson, G. A. Botton and H. S. Zurob, “Solute Segregation During Ferrite Growth: Solute/Interphase and Substitutional/Interstitial Interactions,” *Journal of Materials,* vol. 68, no. 5, pp. 1329-1334, 2016.

[85] C. Song, H. Yu, L. Li and J. Lu, “Effect of carbon at interface of austenite on manganese segregation of low carbon and manganese steel,” *Materials Letters,* vol. 174, pp. 75-78, 2016.

[86] A. T. Wicaksono and M. Militzer, “Interaction of C and Mn in a Σ3 grain boundary of bcc iron,” *IOP Conf. Series: Materials Science and Engineering ,* vol. 219, p. 012044, 2017.

[87] H. Chen and S. van der Zwaag, “Analysis of ferrite growth retardation induced by local Mn enrichment in austenite created by prior interface passages,” *Acta Materialia,* vol. 61, pp. 1338-1349, 2013.

[88] H. Chen, E. Gamsjager, S. Schider, H. Khanbareh and S. van der Zwaag, “In situ observation of austenite-ferrite interface migration in a lean Mn steel during cyclic partial phase transformations,” *Acta Materialia,* vol. 61, pp. 2414-2424, 2013.

[89] H. K. D. H. Bhadeshia and R. W. K. Honeycombe, “Steels: microstructure and properties,” Amsterdam, Elsevier, Butterworth-Heinemann, 2006, p. 129.

[90] H. D. K. H. Bhadeshia, “Bainite in Steels: Theory and Practice,” Leeds, Maney Publishing, 2015, pp. 17-19.

[91] M. Takahashi, “Recent progress: kinetics of the bainite transformation in steels,” *Current Opinion in Solid State & Materials Science,* vol. 8, pp. 213-217, 2004.

[92] J. M. Oblak and R. F. Hehemann, “Structure and growth of Widmanstatten ferrite and bainite,” in *Transformation and Hardenability in Steels*, Ann Arbor, Climax Molybdenum, 1967, pp. 15-30.

[93] H. Matsuda and H. K. D. H. Bhadeshia, “Kinetics of the Bainite Transformation,” *Proceedings: Mathematical, Physical and Engineering Sciences,* vol. 460, no. 2046, pp. 1707-1722, 2004.

[94] H. K. D. H. Bhadeshia, “Bainite in Steels: Theory and Practice,” Leeds, Maney, 2015, p. 131.

[95] H. K. D. H. Bhadeshia, “Bainite in Steels: Theory and Practice,” Leeds, Maney, 2015, pp. 148-149.

[96] H. K. D. H. Bhadeshia and D. V. Edmonds, “The Mechanism of Bainite Formation in Steels,” *Acta Metallurgica,* vol. 28, pp. 1265-1273, 1980.

[97] H. Hu, G. Xu, Y. Zhang, Z. Xue and M. Zhou, “Dynamic Observation of Bainite Transformation in a Fe-C-Mn-Si Superbainite Steel,” *Journal of Wuhan University of Technology - Mater. Sci. Ed.,* vol. 30, no. 4, pp. 818-821, 2015.

[98] Z. Hu, G. Xu, H. Hu, L. Wang and Z. Xue, “In situ measured growth rates of bainite plates in an Fe–C–Mn–Si superbainitic steel,” *International Journal of Minerals, Metallurgy and Materials ,* vol. 32, no. 4, pp. 371-378, 2014.

[99] H. Yada, M. Enomoto and T. Sonoyama, “Lengthening Kinetics of Bainitic Plates in Iron-Nickel-Carbon Alloys,” *ISIJ International,* vol. 35, pp. 976-981, 1995.

[100] G. Mao, R. Cao, X. Guo, Y. Jiang and J. Chen, “In Situ Observation of Kinetic Processes of Lath Bainite Nucleation and Growth by Laser Scanning Confocal Microscope in Reheated Weld Metals,” *Metallurgical and Materials Transactions A,* vol. 48, pp. 5783-5798, 2017.

[101] P. Kolmskog, A. Borgenstam, M. Hillert, P. Hedstrom, S. S. Babu, H. Terasaki and Y. Komizo, “Direct Observation that Bainite can Grow Below MS,” *Metallurgical and Materials Transactions A,* vol. 43, pp. 4984-4988, 2012.

[102] S. Sainis, H. Farahani, E. Gamsjager and S. van der Zwaag, “An In-Situ LSCM Study on Bainite Formation in a Fe-0.2C-1.5Mn-2.0Cr Alloy,” *Metals,* vol. 8, p. 498, 2018.

[103] E. P. Butler and K. F. Hale, “Dynamic Experiments in the Electron Microscope,” Amsterdam, Elsevier/North-Holland Biomedical Press, 1981, pp. 109-124.

[104] M. L. Taheri, E. A. Stach, I. Arslan, P. A. Crozier, B. C. Kabius, T. LaGrange, A. M. Minor, S. Takeda, M. Tanase, J. B. Wagner and R. Sharma, “Current status and future directions for in situ transmission electron microscopy,” *Ultramicroscopy,* vol. 170, pp. 86-95, 2016.

[105] J. T. van Omme, M. Zakhozheva, R. G. Spruit, M. Sholkina and H. H. Perez Garza, “Advanced microheater for in situ transmission electron microscopy; enabling unexplored analytical studies and extreme spatial stability,” *Ultramicroscopy,* vol. 192, pp. 14-20, 2018.

[106] M. Canavan, D. Daly, A. Rummel, E. K. McCarthy, C. McAuley and V. Nicolosi, “Novel in-situ lamella fabrication technique for in-situ TEM,” *Ultramicroscopy,* vol. 190, pp. 21-29, 2018.

[107] H. Saka, T. Kamino, S. Arai and K. Sasaki, “In Situ Heating Transmission Electron Microscopy,” *MRS Bulletin,* vol. 33, pp. 93-100, 2008.

[108] D. B. Williams and C. B. Carter, “Transmission Electron Microscopy: A Textbook for Materials Science,” New York, Plenum Press, 1996, p. 61.

[109] B. Gale and K. F. Hale, “Heating of metallic foils in an electron microscope,” *British Journal of Applied Physics,* vol. 12, pp. 115-117, 1961.

[110] E. P. Butler and K. F. Hale, “Dynamic Experiments in the Electron Microscope H,” Amsterdam, Elsevier/North-Holland Biomedical Press, 1981, pp. 10-24.

[111] J. J. Laidler and B. Mastel, “Application of High-Voltage Electron Microscopy to the Study of Radiation Damage in Metals,” in *Physical apsects of electron microscopy and microbeam analysis*, New York; London, Wiley, 1975, pp. 103-128.

[112] E. P. Butler, “In situ experiments in the transmission electron microscope,” *Rep. Prog. Phys.,* vol. 42, pp. 833-895, 1979.

[113] M. Wilkens and K. Urban, “Studies of Radiation Damage in Crystalline Materials by Means of High Voltage Electron Microscopy,” in *High Voltage Electron Microscopy*, London , Academic Press, 1974, pp. 332-340.

[114] J. L. Martin and L. P. Kubin, “Discussion on the limitations of "in situ" deformation experiments in a high voltage electron microscope,” *Ultramicroscopy,* vol. 3, pp. 215-226, 1978.

[115] E. P. Butler and K. F. Hale, in *Dynamic Experiments in the Electron Microscope*, Amsterdam, Elsevier/North-Holland Biomedical Press, 1987, p. 16.

[116] W. W. Mullins, “Theory of Thermal Grooving,” *Journal of Applied Physics,* vol. 28, no. 3, 1957.

[117] D. J. Allen, “Thermal Grooving At Migrating Grain Boundaries,” *Scripta METALLURGICA,* vol. 16, pp. 5-9, 1982.

[118] V. T. Binh, M. Chaudier, J. C. Couturier, R. Uzan and M. Drechsler, “Grain boundary groove evolutions by surface self-diffusion on a plane and on a wire,” *Surface Science,* vol. 57, no. 1, pp. 184-204, 1976.

[119] W. W. Mullins and P. G. Shewmon, “The kinetics of grain boundary grooving in copper,” *Acta metallurgica,* vol. 7, pp. 163-170, 1959.

[120] P. J. Goodhew and D. A. Smith, “Grooving at grain boundaries in thin films,” *Scripta Metallurgica,* vol. 16, no. 1, pp. 91-94, 1982.

[121] W. W. Mullins, “The effect of thermal grooving on grain boundary motion,” *Acta Metallurgica ,* vol. 6, pp. 414-427, 1958.

[122] M. Onink, F. D. Tichelaar, C. M. Brakman, E. J. Mittemeijer and S. van der Zwaag, “An in situ hot stage transmission electron microscopy study of the decomposition of Fe-C austenites,” *Journal of Materials Sciences,* vol. 30, pp. 6223-6234, 1995.

[123] E. H. Yoffe, “A Dislocation at a Free Surface,” *Philosophical Magazine,* vol. 6, pp. 1147-1155, 1961.

[124] A. Couret, J. Crestou, S. Farenc, G. Molenat, N. Clement, A. Coujou and D. Caillard, “In situ deformation in T.E.M.: recent developments,” *Microscopy Microanalysis Microstructures ,* vol. 4, pp. 153-170, 1993.

[125] A. K. Head, “The Dislocation Image Force in Cubic Polycrystals,” *Physica status solidi (b),* vol. 10, no. 2, pp. 481-484, 1965.

[126] E. P. Butler and P. R. Swann, “In situ High Voltage Microscope Observations of Precipitation,” in *Physical aspects of electron microscopy and microbeam analysis*, New York; London, Wiley, 1975, pp. 129-148.

[127] C. Laird and H. I. Aaronson, “Mechanisms of formation of θ and dissolution of θ' precipitates in an Al-4% Cu Alloy,” *Acta Metallurgica,* vol. 14, no. 2, pp. 171-185, 1966.

[128] G. Thomas and M. J. Whelan, “Observations of Precipitation in Thin Foils of Aluminium+4% Copper Alloy,” *Philosophical Magazine,* vol. 6, pp. 1103-1114, 1961.

[129] E. Schmidt, Y. Wang and S. Sridhar, “A Study of Nonisothermal Austenite Formation and Decomposition in Fe-C-Mn Alloys,” *Metallurgical and Materials Transactions A,* vol. 37, pp. 1799-1810, 2006.

[130] P. Cotterill and P. R. Mould, “Recrystallization and Grain Growth in Metals,” London, Surrey University Press, 1976, pp. 291-292.

[131] H. K. Sehgal, E. P. Butler and P. R. Swann, “In situ observations of recrystallisation in pure aluminium,” *Scripta Metallurgica ,* vol. 9, pp. 165-170, 1975.

[132] B. Lehtinen and W. Roberts, “In situ observations of precipitation and recrystallization with a 1 MeV electron microscope,” *Journal of Microscopy,* vol. 97, pp. 197-208, 1973.

[133] J. G. Brons and G. B. Thompson, “A comparison of grain boundary evolution during grain growth in fcc metals,” *Acta Materialia,* vol. 61, pp. 3936-3944, 2013.

[134] R. Dannenberg, E. A. Stach, J. R. Groza and B. J. Dresser, “In-situ TEM observations of abnormal grain growth, coarsening, and substrate de-wetting in nanocrystalline Ag thin films,” *Thin Solid Films,* vol. 370, pp. 54-62, 2000.

[135] G. D. Hibbard, V. Radmilovic, K. T. Aust and U. Erb, “Grain boundary migration during abnormal grain growth in nanocrystalline Ni,” *Materials Science and Engineering A,* vol. 494, pp. 232-238, 2008.

[136] L. S. Darken and R. M. Fisher, “Some Observations on the Growth of Pearlite,” in *Decomposition of Austenite by Diffusional Processes*, New York, Interscience Publishers, 1962, pp. 249-288.

[137] G. R. Purdy, “The dynamics of transformation interfaces in steels-I. The ferrite-austenite interface in Fe-C-Mo alloys,” *Acta Metallurgica,* vol. 26, pp. 477-486, 1978.

[138] G. R. Purdy, “On the direct observation of the formation of ferrite in steels,” *Scripta Metallurgica,* vol. 21, pp. 1035-1038, 1987.

[139] M. Nemoto, “Growth of Bainite in an Iron-Nickel-Carbon Alloy,” in *High Voltage Electron Microscopy*, London, Academic Press, 1974, pp. 230-234.

[140] M. Kang, M.-X. Zhang and M. Zhu, “In situ observation of bainite growth during isothermal holding,” *Acta Materialia,* vol. 54, pp. 2121-2129, 2006.

[141] E. Schmidt, D. Soltesz, S. Roberts, A. Bednar and S. Sridhar, “The Austenite/Ferrite Front Migration Rate during Heating of IF Steel,” *ISIJ International,* vol. 46, pp. 1500-1509, 2006.

[142] J. Hamada, M. Enomoto, T. Fujishiro and T. Akatsuka, “In-Situ Observation of the Growth of Massive Ferrite in Very Low-Carbon Fe-Mn and Ni Alloys,” *Metallurgical and Materials Transactions A,* vol. 45, pp. 3781-3789, 2014.

[143] E. P. Butler and K. F. Hale, “Dynamic Experiments in the Electron Microscope,” Amsterdam, North-Holland Publishing Company, 1981, p. 131.

[144] A. T. W. Kempen, F. Sommer and E. J. Mittemeijer, “Calibration and desmearing of a differential thermal analysis measurement signal upon heating and cooling,” *Thermochimica Acta,* vol. 383, no. 1-2, pp. 21-30, 2002.

[145] J. O. Andersson, T. Helander, L. Hoglund, P. F. Shi and B. Sundman, “Thermo-Calc and DICTRA, Computational tools for materials science,” *Calphad,* vol. 26, pp. 273-312, 2002.

[146] Y.-K. Lee, “Empirical formula of isothermal bainite start temperature of steels,” *Journal of Materials Science Letters,* vol. 21, pp. 1253-1255, 2002.

[147] C. Capdevila, F. G. Caballero and C. Garcia de Andres, “Determination of Ms Temperature in Steels: A Bayesian Neural Network Model,” *ISIJ International,* vol. 42, pp. 894-902, 2002.

[148] S. Schönecker, X. Li, B. Johansson, S. K. Kwon and L. Vitos, “Thermal surface free energy and stress of iron,” *Scientific Reports,* vol. 5, p. 14860, 2015.

[149] G. E. Rhead, “Diffusion on Surfaces,” *Surface Science,* vol. 47, pp. 207-221, 1975.

[150] C. Wang, Z. Qin, Y. Zhang, Q. Sun and Y. Jia, “A molecular dynamics simulation of self-diffusionon Fe surfaces,” *Applied Surface Science,* vol. 258, pp. 4294-4300, 2012.

[151] H. Chamati, N. I. Papanicolaou, Y. Mishin and D. A. Papaconstantopoulos, “Embedded-atom potential for Fe and its application to self-diffusion on Fe(100),” *Surface Science,* vol. 600, pp. 1793-1803, 2006.

[152] M. Švantner, P. Vacikova and M. Honner, “Non-contact charge temperature measurement on industrial continuous furnaces and steel charge emissivity analysis,” *Infrared Physics & Technology,* vol. 61, pp. 20-26, 2013.

[153] W. C. Leslie, “The Physical Metallurgy of Steels,” Washington; London, Hemisphere, 1983, p. 244.

[154] B. Zhu, H. Chen and M. Militzer, “Phase-field modeling of cyclic phase transformations in low-carbon steels,” *Computational Materials Science,* vol. 108, pp. 333-341, 2015.

[155] H. Chen, B. Zhu and M. Militzer, “Phase Field Modeling of Cyclic Austenite-Ferrite Transformations in Fe-C-Mn Alloys,” *Metallurgical and Materials Transactions A,* vol. 47, pp. 3873-3881, 2016.

[156] H. Chen, R. Kuziak and S. van der Zwaag, “Experimental Evidence of the Effect of Alloying Additions on the Stagnant Stage Length During Cyclic Partial Phase Transformations,” *Metallurgical and Materials Transactions A,* vol. 44, pp. 5617-5621, 2013.

[157] Y. Liu, D. Wang, F. Sommer and E. J. Mittemeijer, “Isothermal austenite-ferrite transformation of Fe-0.04 at.% C alloy: Dilatometric measurement and kinetic analysis,” *Acta Materialia,* vol. 56, pp. 3833-3842, 2008.

[158] R. L. Higginson and C. M. Sellars, in *Worked Examples in Quantitative Metallography*, London, Maney Publishing, 2003, pp. 31-66.

[159] Y. C. Liu, F. Sommer and E. J. Mittemeijer, “The austenite-ferrite transformation of ultralow-carbon Fe-C alloy; transition from diffusion- to interface-controlled growth,” *Acta Materialia,* vol. 54, pp. 3383-3393, 2006.

[160] A. T. W. Kempen, F. Sommer and E. J. Mittemeijer, “The kinetics of the austenite–ferrite phase transformation of Fe-Mn: differential thermal analysis during cooling,” *Acta Materialia,* vol. 50, pp. 3545-3555, 2002.

[161] E. P. Butler and K. F. Hale, in *Dynamic Experiments in the Electron Microscope*, Amsterdam, Elsevier/North-Holland Biomedical Press, 1981, p. 138.

[162] H. K. D. H. Bhadeshia and R. W. K. Honeycombe, “The iron-carbon equilibrium diagram and plain carbon steels,” in *Steels: Microstructure and Properties*, Amsterdam, Butterworth-Heinemann, 2006, pp. 42-44.

[163] D. B. Williams and C. B. Carter, in *Transmission Electron Microscopy: A Textbook for Materials Science*, New York, Plenum Press, 1996, p. 295.

[164] O. Thullier, F. Danoix, M. Gouné and D. Blavette, “Atom probe tomography of the austenite-ferite interphase boundary composition in a model alloy Fe-C-Mn,” *Scripta Materialia,* vol. 55, pp. 1071-1074, 2006.

[165] F. J. Humphreys and M. Hatherly, in *Recrystallization and Related Annealing Phenomena*, Oxford, Pergamon, 1996, p. 144.

[166] Y. van Leeuwen, S. Vooijs, J. Sietsma and S. van der Zwaag, “The Effect of Geometrical Assumptions in Modeling SolidState Transformation Kinetics,” *Metallurgical and Materials Transactions A,* vol. 29, pp. 2925-2931, 1998.

[167] T. Lillo, M. R. Plichta and S. A. Hackney, “in-situ observations of intrinsic grain boundary structure during thermal cycling,” *Ultramicroscopy,* vol. 29, pp. 257-265, 1989.

[168] T. M. Lillo, S. A. Hackney and M. R. Plichta, “On the origins of ghost boundaries during in situ strain-induced grain-boundary migration,” *Ultramicroscopy,* vol. 37, pp. 294-309, 1991.

[169] K. R. Kinsman and H. I. Aaronson, “Influence of molybdenum and manganese on the kinetics of the proeutectoid ferrite reaction,” in *Transformation and Hardenability in Steels*, Arbor, MI, Ann Climax Molybdenum Co., 1967, p. 39.

[170] D. A. Porter, K. E. Easterling and M. Y. Sherif, in *Phase Transformations in Metals and Alloys*, CRC Press, 2009, pp. 117-121.

[171] S. G. Wang, E. K. Tian and C. W. Lung, “Surface energy of arbitrary crystal plane of bcc and fcc metals,” *Journal of Physics and Chemistry of Solids ,* vol. 61, pp. 1295-3000, 2000.

[172] J. Gautam, R. Petrov, L. Kestens and E. Leunis, “Surface energy controlled a–c–a transformation texture and microstructure character study in ULC steels alloyed with Mn and Al,” *Journal of Materials Science,* vol. 43, pp. 3969-3975, 2008.

[173] A. Harun, E. A. Holm , M. P. Clode and M. A. Miodownik, “On computer simulation methods to model Zener pinning,” *Acta Materialia,* vol. 54, pp. 3261-3273, 2006.

[174] Z. Yang and R. A. Johnson, “An EAM simulation of the alpha-gamma iron interface,” *Modelling and Simulation in Materials Science and Engineering,* vol. 1, pp. 707-716, 1993.

[175] H. Farahani, W. Xu and S. van der Zwaag, “Determination of mode switching in cyclic partial phase transformation in Fe-0.1C-XMn alloys as a function of the Mn concentration,” *Manuscript submitted for publication,* 2018.

[176] P. Cotterill and P. R. Mould, in *Recrystallization and Grain Growth in Metals*, London, Surrey Univserity Press, 1976, pp. 233-235.

[177] E. Nes, N. Ryum and O. Hunderi, “On The Zener Drag,” *Acta Metallurgica,* vol. 33, pp. 11-22, 1985.

[178] D. Sato, M. Ohno and K. Matsuura, “Phase-Field Simulations and Analysis of Effect of Dispersed Particles on Migration of Delta to Gamma Transformation Interface,” *Metallurgical and Materials Transactions A,* vol. 46, pp. 981-988, 2014.

[179] L. Chen, K. Matsuura, D. Sato and M. Ohno, “Effects of Second Phase Particle Dispersion on Kinetics of Isothermal Peritectic Transformation in Fe–C Alloy,” *ISIJ International,* vol. 52, no. 3, pp. 434-440, 2012.

[180] L. Chen, K. Matsuura, M. Ohno and D. Sato, “Effects of Second Phase Particles on Migration of α / γ Interface during Isothermal α to γ Transformation,” *ISIJ International,* vol. 52, no. 10, pp. 1841-1847, 2012.

[181] D. Sato, M. Ohno and K. Matsuura, “A role of interfacial energy balance in delta to gamma transformation kinetics in carbon steel with dispersed second phase particles analyzed by phase-field simulation,” *Computational Materials Science,* vol. 106, pp. 188-192, 2015.

[182] J. W. Christian , in *The Theory of Transformations in Metals and Alloys Part I*, Amsterdam, Elsevier Science Ltd, 2002, p. 331.

[183] A. C. F. Cocks and S. P. A. Gill, “A variational approach to two dimensional grain growth - I. Theory,” *Acta Materialia,* vol. 44, no. 12, pp. 4765-4775, 1996.

[184] S. Ratanaphan, D. L. Olmsted, V. V. Bulatov, E. A. Holm, A. D. Rollett and G. S. Rohrer, "Grain boundary energies in body-centred cubic metals," *Acta Materialia,* vol. 88, pp. 346-354, 2015.

[185] G. S. Rohrer, "Grain boundary energy anisotropy: a review," *Journal of Materials Science,* vol. 46, pp. 5881-5895, 2011.

[186] M. A. Tschopp, K. N. Solanki, F. Gao, X. Sun, M. A. Khaleel and M. F. Horstemeyer, "Probing grain boundary sink strength at the nanoscale: Energetics and length scales of vacancy and interstitial absorption by grain boundaries in α-Fe," *Physical Review B,* vol. 85, p. 064108, 2012.

[187] N. R. Rhodes, M. A. Tschopp and K. N. Solanki, "Quantifying the energetics and length scales of carbon segregation to α-Fe symmetric tilt grain boundaries using atomistic simulations," *Modelling and Simulation in Materials Science and Engineering,* vol. 21, p. 035009, 2013.

[188] M. A. Tschopp, M. F. Horstemeyer, F. Gao, X. Sun and M. Khaleel, "Energetic driving force for preferential binding of self-interstitial atoms to Fe grain boundaries over vacancies," *Scripta Materialia,* vol. 64, pp. 908-911, 2011.

[189] W. C. Leslie, in *The Physical Metallurgy of Steels*, Washington, Hemisphere, 1981, p. 79.

[190] T. Nishimura, K. Morishita, M. Yoshiya and H. Yasuda, "Kinetics of the δ/γ interface in the massive-like transformation in Fe-0.3C-0.6Mn-0.3Si alloys," *IOP Conf. Series: Materials Science and Engineering,* vol. 84, p. 012062, 2015.

[191] D. Zhang, H. Terasaki and Y. Komizo, "In situ observation of phase transformation in Fe-0.15C binary alloy," *Journal of Alloys and Compounds,* vol. 484, pp. 929-933, 2009.

[192] D. Zhang, H. Terasaki and Y. Komizo, "Morphological and Crystallographic Evolution of Bainite Transformation in Fe-0.15C Binary Alloy," *Microscopy Research and Technique,* vol. 73, pp. 67-70, 2010.

[193] H. D. K. H. Bhadeshia, in *Bainite in Steels: Theory and Practice*, Leeds, Maney Publishing, 2015, p. 33.

[194] J. Wang, S. van der Zwaag, Z. Yang and H. Fang, "Aspect ratio of bainite in steels," *Materials Letters,* vol. 45, pp. 228-234, 2000.

Appendix A: Bainitic Transformation.

7.1 Introduction.

In addition to the cyclic partial phase transformation experiments, multiple experiments were performed on Fe-0.307C-3Mn-1.5Si-0.15Mo steel specimens in order to investigate bainite growth using in situ TEM. The composition was chosen based on the continuous cooling transformation behaviour in the bulk which demonstrated a well-defined bay between the ferrite and bainite temperature domains, along with slow ferrite growth.

A number of studies have used hot stage confocal microscope experiments to make in situ observations of the transformation under both continuous cooling and isothermal conditions in Fe-0.15C [191] [192], Fe-C-Mn-Si [97, 101, 98] and in more complex steels with high nickel content [100] [99]. Kang et al. [140] used in situ TEM to observe bainite growth during isothermal holding. Measured lengthening rates in these experiments were typically found to be consistent with diffusion-controlled growth.

This chapter presents the results of a successful experiment in which the bainite transformation was observed during isothermal holding at 300^{o}C. As noted in Chapter 3, the calculated B_s temperature for the steel was 465^{o}C, and the calculated M_s temperature was 284^{o}C (557K).

The success rate of these experiments was low, with only one successful observation in 15 specimens. This was primarily because the majority of the austenite transformed into ferrite during the initial cooling, making it difficult to locate the remaining austenite.

7.2 Experimental Outline.

Figure A.1 shows the heat treatment to which the specimen was subjected to. The specimens were first heated at the maximum heating rate of 5 C/s, above the A_3 temperature for this composition of 775^{o}C, to 1030^{o}C (nominal) and held for 5 minutes to form austenite. The temperature was then lowered to 300^{o}C (nominal) with a target

cooling rate of 20C/s. Specimens were held at temperatures of 300-450°C for up 30 minutes. For the specimen in which a successful observation of bainite growth was made, the specimen was completely transformed after the initial cooling, with no bainite growth observed. In this case the specimen temperature was manually increased to re-austenitise it before being cooled to 300°C and held for at this temperature for the remaining time. It was during this period the growth of bainite plates was observed.

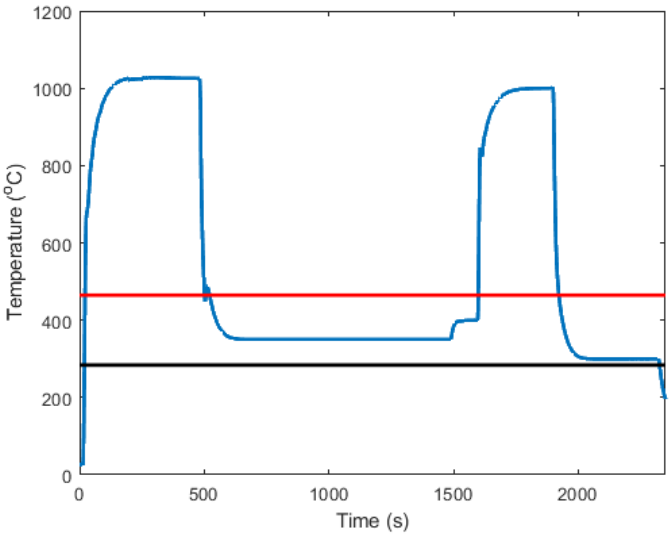

Figure A.1: Graph of temperature against time for the applied heat treatment for the successful specimen.

Representative starting microstructures of the specimens are shown in Figure A.2.

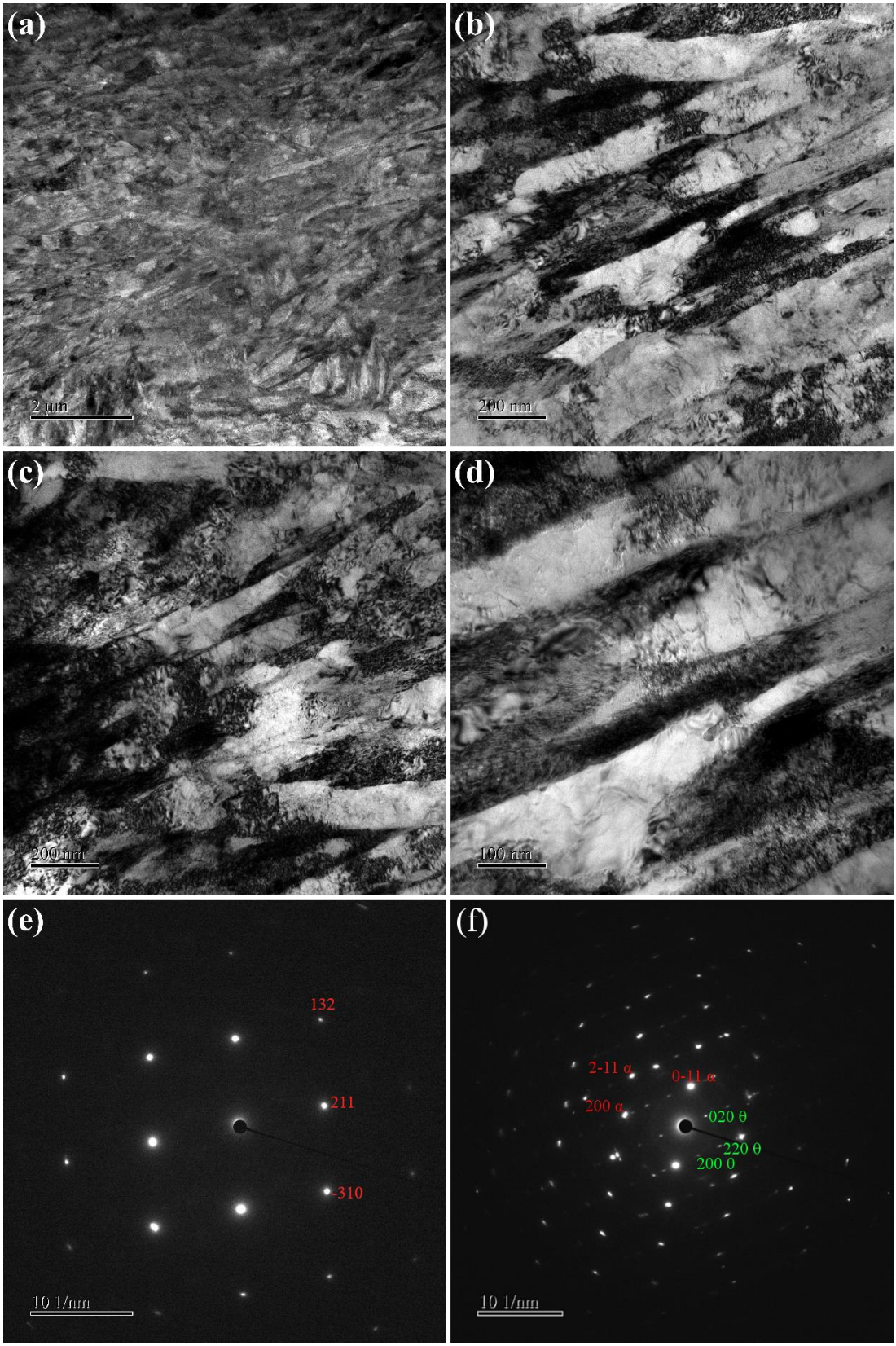

Figure A.2: (a)-(d) Bright field TEM of representative starting microstructures of the steel before heating, (e) Selected area diffraction pattern from the bainitic ferrite, showing that the foil surface is clear of oxidation and (f) selected area diffraction pattern with both the ferrite and Fe_3C spots.

7.3 Results.

After cooling, much of the specimen was transformed into ferrite, with a relatively small amount of remaining austenite. This austenite contained many dislocations with significant changes in contrast within the grain.

Two bainitic ferrite plates were observed to grow into this austenite. Figure A.3 shows the specimen when the first plate was initially observed. The orientation relationship of the bainite with the adjacent austenite was close to the K-S orientation relationship. This plate remained immobile for several seconds before the appearance of a bainitic ferrite plate, which rapidly grew to a length of 800 nm (in frame) before stopping. The first observed plate appeared to have nucleated on a twin boundary in the austenite, whilst the second plate originated close to where the twin boundary intersected the austenite grain boundary. As can be seen from Figure A.3(b) plate 2 grew across plate 1 indicating that they did not extend through the full thickness of the foil.

The angle between the growth directions of the two plates was 50^{o}. The growth directions of the two plates were parallel, or nearly parallel, to the (110) and (420) directions in the austenite. The length of the bainitic ferrite as a function of time is shown in Figure A.4. The growth of the bainitic ferrite was characterised by periods of relative immobility followed by rapid lengthening. Lengthening rates were typically 0-20 $nm \cdot s^{-1}$ during periods of relative immobility, before accelerating to velocities of >100 $nm \cdot s^{-1}$ with the maximum measured lengthening rates of 4,300 $nm \cdot s^{-1}$ and 1,700 $nm \cdot s^{-1}$ for plate 1 and 2 respectively. Growth was halted when the tip of the bainitic ferrite reached the austenite grain boundary.

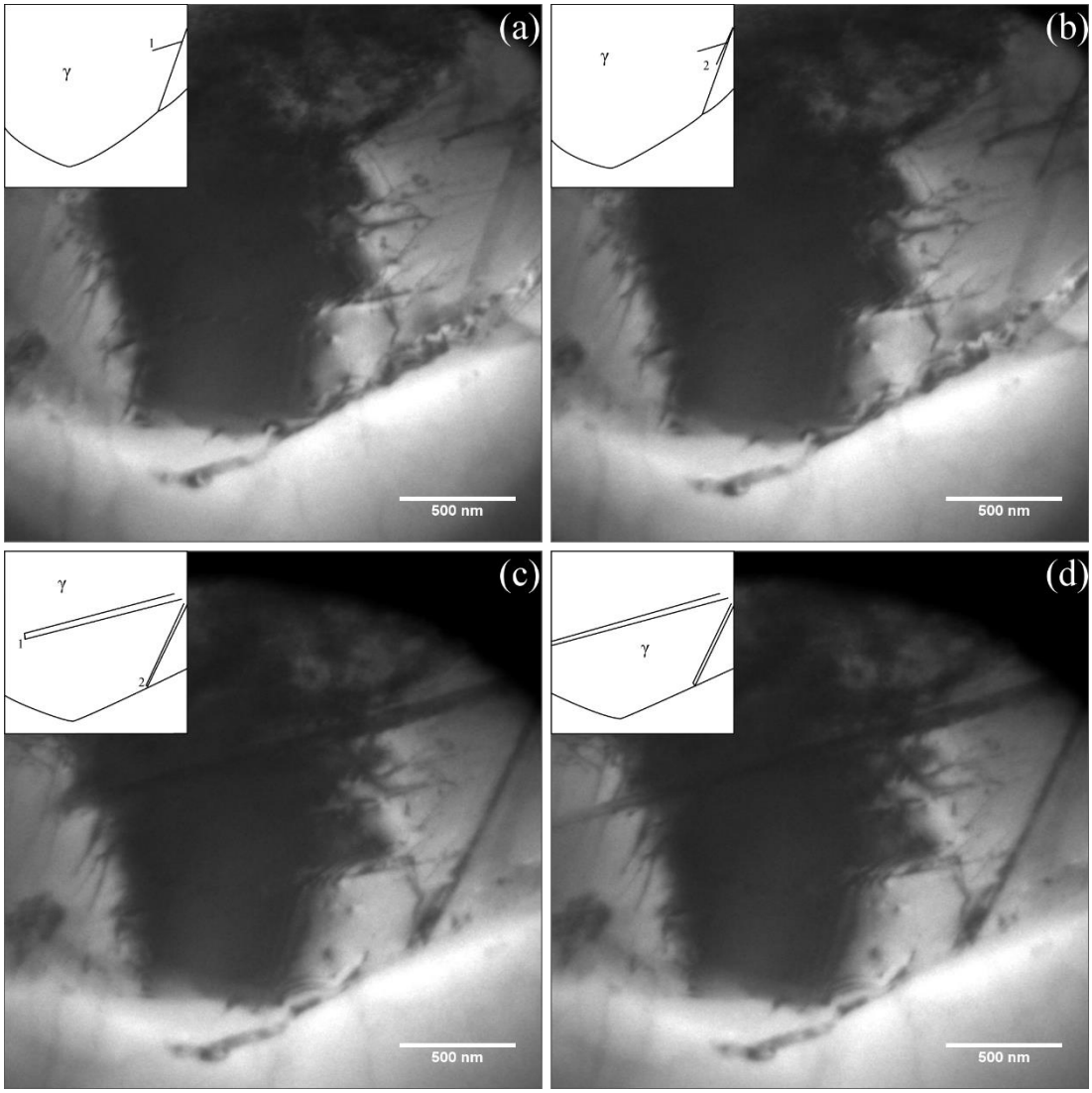

Figure A.3: Bright field TEM of the lengthening of bainitic ferrite plates in the austenite (a) at 2112.3 seconds, the initial observation (b) at 2113.6 seconds (c) at 2118.9 seconds and (d) the completed transforamtion at 2119.1 seconds.

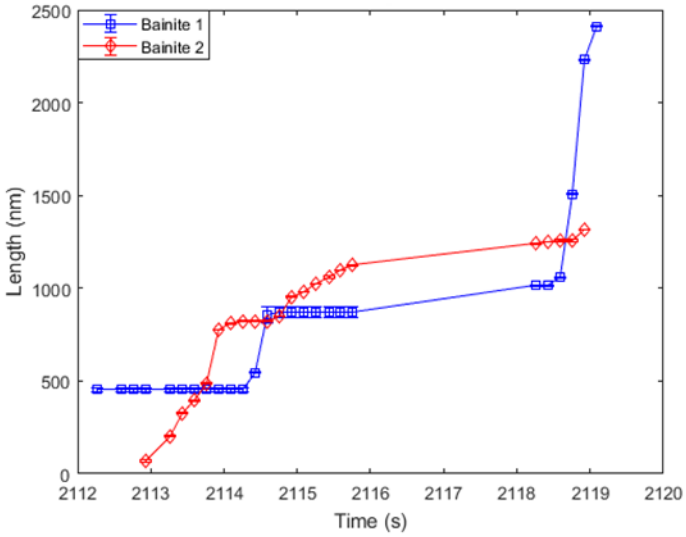

Figure A.4: Graph of the lengthening of the bainitic ferrite plates against time during isothermal holding at 300°C.

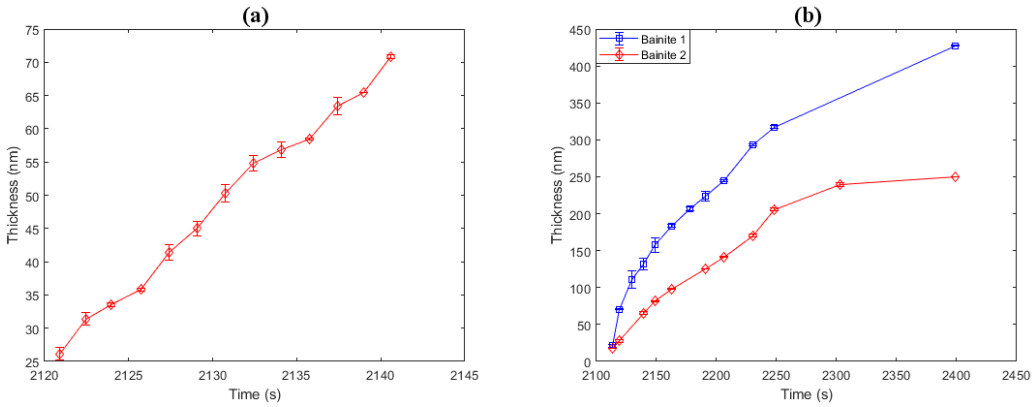

Figure A.5: (a) Graph of the thickening of bainitic ferrite plate 2 against time immediately after lengthening completed, (b) Graph of the lengthening of bainitic ferrite plates for the entire period of isothermal holding.

The first bainitic ferrite plate observed showed some thickening along its length after the first observed period of growth, whilst for the second thickening was more modest until it stopped lengthening. Figure A.5 shows the thickening (measured from the midpoint) of the bainitic ferrite from first observation and for the remaining 5 minutes of the isothermal holding. The plates thickened continuously as shown in Figure A.5(a), no ledges were observed at this time and thickening occurred simultaneously along the broad faces of the plates. During this time no other plates were observed to grow, although an additional plate (plate 3), shown in Figure A.6 was later found to have grown unobserved between plate 1 and the austenite grain boundary. The overall shape of the bainitic ferrite after thickening was a convex lens with a noticeable

discontinuity in plate 2 where thickening has been prevented by intersection with plate 3.

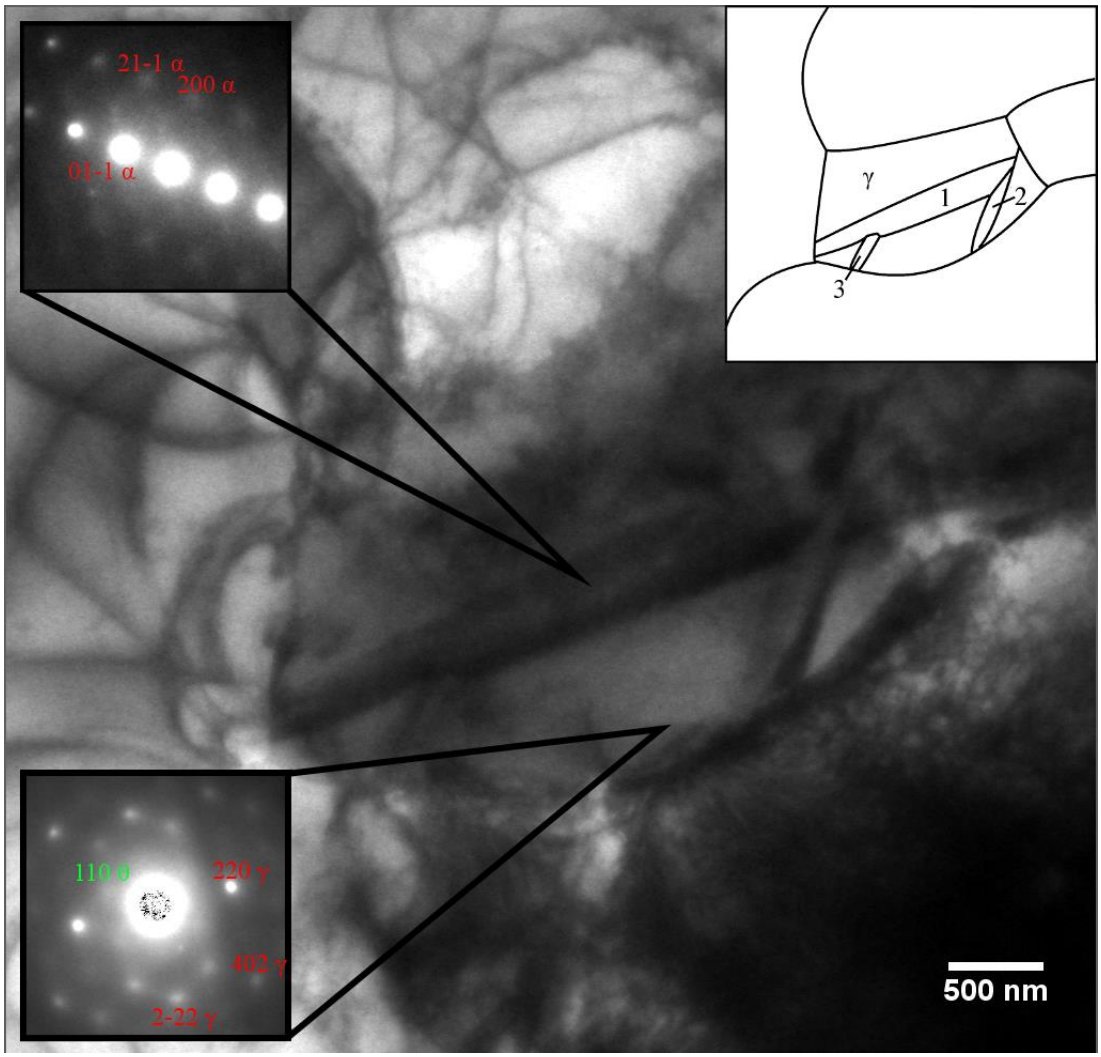

Figure A.6: Bright field TEM of the final microstructure after isothermal holding for approximately 5 minutes after the plates were first observed. Diffraction patterns indicate that plate was ferrite and the surrounding grain austenite, with Fe_3C carbides having formed on the austenite grain boundary.

The behaviour of dislocations in the austenite was highly localised. Visible dislocations in the austenite away from the bainite plates remained immobile throughout the period of observation. However, dislocations adjacent to the bainite plates were observed to move towards the tip of the plate during isothermal holding after lengthening had been completed. The actual lengthening of the plate was accompanied by changing contrast at the tip of the bainite, with increasing contrast as

the tip moved followed by reduced contrast until movement continued, this is shown in Figure A.7 for plate 2.

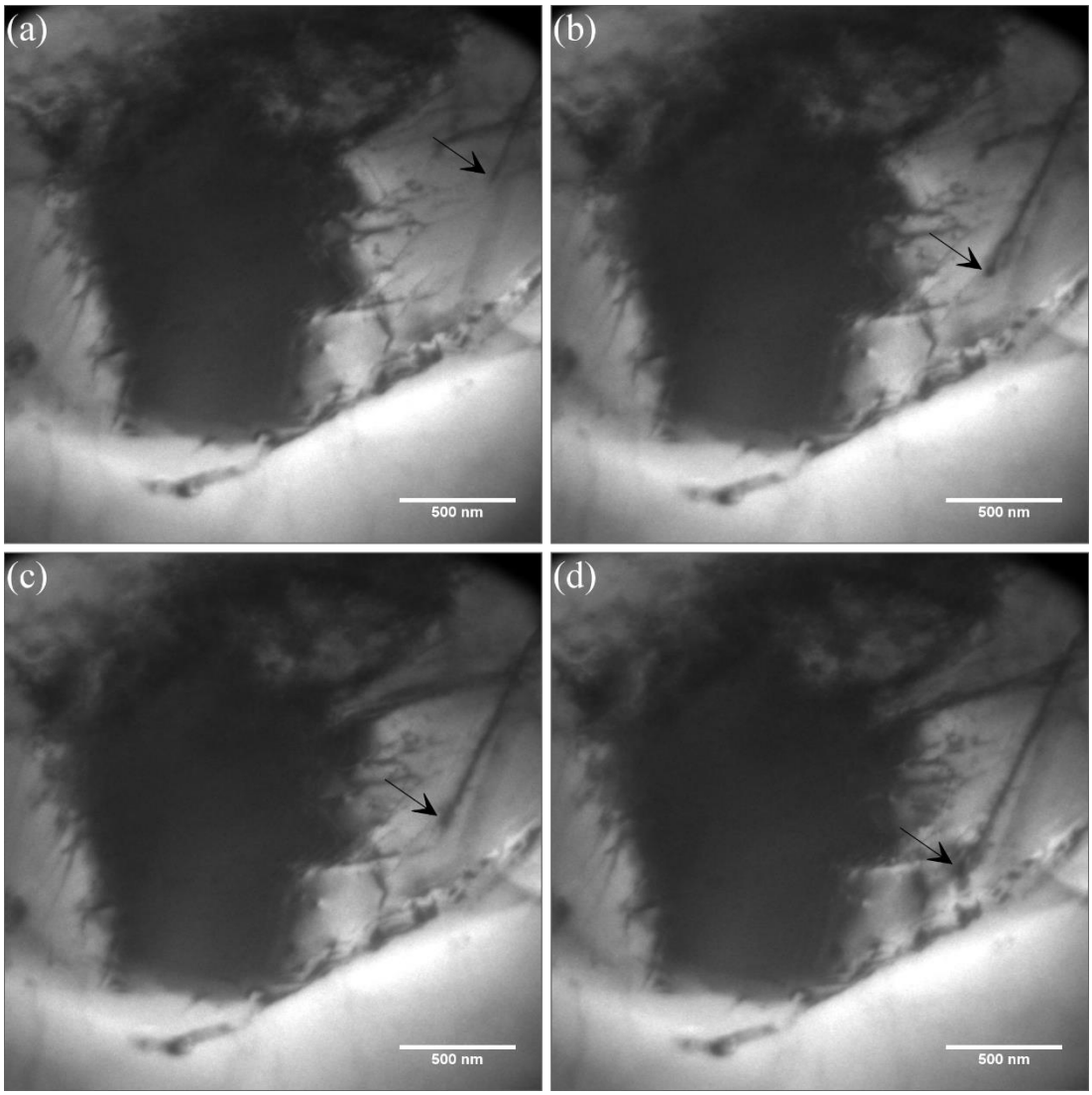

Figure A.7: Bright field TEM of the changing contrast at the tip of the bainite plate (a) at 2113.6 seconds, during the initial period of growth, (b) at 2114.3 seconds at the start of a period of relative immobility (c) at 2114.8 seconds, as the period of immobility ended and (d) at 2115.8 seconds and the start of a new period of immobility.

7.4 Discussion.

According to the nucleation-controlled model, the kinetics of the bainite transformation are governed by the nucleation and growth of individual sub units within a sheaf. After initially nucleating on the austenite grain boundary the subunit rapidly grows into the austenite before being halted by transformation stresses ahead

of the newly formed bainite, followed by the nucleation of additional subunits [93] [91].

As expected plate 2 nucleated at the austenite grain boundary, in this case close to where it intersected with a pre-existing twin boundary. Bainite nucleation at grain boundaries is also observed in multiple in situ CLSM studies [191] [97] [100]. Somewhat unexpectedly, due to its relatively low interfacial energy, plate 1 appeared to have nucleated along a twin boundary. However, Mao et al. [100] observed nucleation of bainite laths along twin boundaries at lower (362^{o}C) temperatures using CLSM. The bainitic ferrite is close to the Kurdjumov-Sachs orientation relationship with the adjacent austenite, as expected for bainite [193].

The lengthening of the bainite plates was not constant but showed distinct periods of growth and immobility. As a result, the average growth rates of the two plates range between 290 and 230 nm·s^{-1}, for plate 1 and 2 respectively, whilst the maximum measured growth rates were as high 4,300 nm·s^{-1} and 1,700 nm·s^{-1}. It could be seen particularly clearly for plate 2 that there was changing contrast at the tip of the growing lath, indicating localised bending of the foil. This contrast increased as the lath grew, before becoming less intense in the period leading up to further movement. This suggests that the localised build-up of stress at the growth tip was responsible for slowing and then halting growth. As a result, the average growth rate is an order of magnitude lower than the maximum growth rate during the periods of mobility. Average growth rates are comparable with the <1 μm·s^{-1} growth rates found by Hu et al. [98] for a superbainitic steel containing 0.4 wt% C, 2.81 wt% Mn and 2 wt% Si, transformed at 330^{o}C.

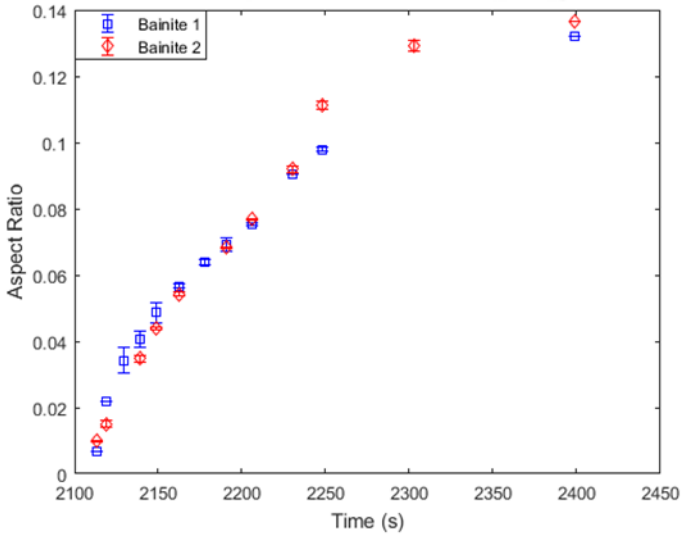

Figure A.8: Graph of the development of the aspect ratio over time.

During lengthening both plates underwent some minor thickening, but the majority of the thickening took place during the remaining isothermal holding time. The rate of thickening was proportional to $t^{-1/2}$ and during the observed period was on the order of 1-10 nm·s^{-1}. Using the total length and thickness information from Figure A.5, the evolution of the aspect ratio can be determined, as shown in Figure A.8. This shows that the aspect ratio is approximately 0.03 for both plates in the period immediately after growth ceased, increasing to 0.13-0.14 after thickening completed. The initial aspect ratio is close to the most frequent value found by Wang et al. [194] for lower bainite. The final shape of each plate was a convex lens, with a deviation at the tip of plate 1, where plate 3 intersected, indicating that plate 3 prevented thickening at this location.

7.5 Chapter Summary.

The austenitisation and partial transformation to bainite was observed in situ using hot stage TEM for a Fe-C-Mn-Si-Mo steel. The bainitic ferrite plates were observed to grow across the austenite grain with distinct periods of mobility and immobility. Maximum velocities of this lengthening for each plate were 1,700 and 4,300 nm·s^{-1}. Most thickening of each plate occurred after lengthening had been halted, with the rate

of thickening decreasing as isothermal holding continued. The aspect ratio increased from ~0.03 to ~0.13 during this period.

The bainite was found to have an orientation relationship with the adjacent austenite which was close to the Kurdjumov-Sachs orientation relationship and the two observed plates grew with a 50^{o} difference in growth direction.

Little dislocation motion was observed in the austenite in general, although there was observed motion along the length of the bainite laths during the time it was under observation. The lengthening of the plate was associated with changing contrast conditions at the tip indicating that there was localised bending of the foil ahead of the tip of the bainite. This may indicate that the change in lengthening rate was associated with the build-up and relaxation of stress at the plate tip. In contrast the thickening of each plate was observed to be a continuous process.

The present observations are, however, from a single experiment and therefore further observations are necessary to confirm their representativeness.